AN INVESTIGATION OF ELECTROMAGNETIC RIG – GENERATED STRONG MAGNETIC FIELDS

By

NASSER BASHIR EKREEM

A thesis submitted for the degree of
Doctor of Philosophy

Faculty of Engineering and Computing

School of Mechanical and Manufacturing Engineering

Dublin City University
January 2009

Supervisors

Dr. Tim Prescott
Dr. A. G. Olabi
Prof. Saleem Hashmi

PhD 2009

Declaration

I hereby certify that this material which I now submit for assessment on the programme of study leading to the award of PhD is entirely my own work and has not been taken from the work of others save and to the extent that such work has been cited and acknowledged within the text of my work.

Signed: ID No.: 54149932

Date: ----------------------------

Publications

This work has been disseminated through the following publications.

Selected Peer Reviewed Journals:

- **N. B. Ekreem,** A. G. Olabi, T. Prescott, A. Rafferty, and M.S.J. Hashmi, An Overview of Magnetostriction, Its Use and Methods to Measure These Properties, Journal of Materials Processing Technology, Vol. 191, 2007, 96-101.
- **N.B. Ekreem**, A. Rafferty, S. A. Mazlan, T. Prescott, and A.G. Olabi, Measurement and FEMM Modelling of Experimentally Generated Strong Magnetic Fields, submitted to the Journal of Smart Materials and Structures.
- **N.B. Ekreem**, A. Rafferty, S. A. Mazlan, T. Prescott, and A.G. Olabi, An Investigation of Electromagnetic-Rig Generated Strong Magnetic Fields, submitted to the Journal of Applied Physics-D.

Conferences:

- **N. B. Ekreem**, A. Rafferty, S. A. Mazlan, T. Prescott, and A.G. Olabi, Prediction of Strong Magnetic Fields Using Computational FEMM Modelling, presented in the International Conference on Simulation Based Engineering and Sciences, Venice, Italy, October 16-17, 2008.
- **N. B. Ekreem,** T. Prescott, A. G. Olabi, and A. Rafferty**,** Design Optimization for Generating a High Static Magnetic Field, Proceeding of the 24th Internal Manufacturing Conference , Waterford Institute of Technology, 2007, 329-336.
- **N. B. Ekreem**, A. Rafferty, S. A. Mazlan, T. Prescott, and A.G. Olabi, Prediction and Measurement of Magnetic Fields Using Computational FEMM Modelling, will be presented in the IV Eccomas Thematic Conference (Smart Materials and Structure), Porto, Portugal, 13-15 July, 2009.

Posters:

- **N. B. Ekreem,** A. G. Olabi, T. Prescott, and A. Rafferty, An Enhancement of Magnetic Properties of Cobalt Ferrite by Magnetic Annealing, 1st Mechanical and Manufacturing Engineering Symposium, DCU, Dublin, Ireland, December 20, 2006.

Dedication

To My Beloved Wife
(Suad Girbi)

&

Children
(Mahmoud, Soheib Ahmed And Seraj)

The source of all the good in me

Acknowledgments

I am grateful to Almighty Allah from the core of my heart for the fulfilment of my desire for the completion of the thesis. Completing a Ph.D. is truly a marathon event, and I would not have been able to complete this journey without the aid and support of countless people over the past four years.

Numerous people deserve recognition for contribution, large and small, which made it possible for me to complete this dissertation. A special thanks to my supervisors Dr. Tim Prescott, and Dr. A.G. Olabi for providing the impetus for me to pursue this work, for monitoring and guiding me through the academic process and most importantly, for having confidence in me. I also would like to extend my thanks to Dr. Aran Rafferty for his assistance in technical support.

I am indebted to the Libyan Government for providing me the scholarship in order to achieve this dream.

I also thank some of my fellow PhD students and friends; Walid, Esam, Ayad, Helen, Ahmed, Khalid, Andrew, Othgon and especially my best friend Saiful Amri Mazlan. They have each helped make my time in the PhD program more fun and interesting. I apologize for the so many names not included here; this only means that you are closer to my heart than you are to my mind.

I would like to sincerely thank all my wonderful family and friends for their support throughout my education. Your thoughtfulness, friendship, and love have made it possible.

Finally, I am eternally grateful for the patience, understanding, and encouragement of my wife Suad Girbi, and my lovely children Mahmoud, Soheib, Ahmed, and our new baby boy Seraj.

Abstract

In this thesis, two alternative solenoid designs are presented: “Air-core” coil design and “C-shape” coil design. The coils were designed to be capable of generating strong and static magnetic fields in various samples of magnetic materials. In the case of the first design, the sample would be placed in the central air space. In the second design, the sample would be placed in part of the “jaws” of the “C” shape. It was intended that the rig would be used to measure the magnetostriction strain of annealed cobalt ferrite and Terfenol-D based materials. It was thought that magnetic flux densities of the order 1.6 tesla would be needed in the air-gap. However after carrying out preliminary calculations for the air-core design, it was realized that very high electrical currents would be required, with the result that complex systems would be needed to remove the heat being generated. This design was therefore abandoned.

The “C-shape” coil design was completed allowing for fabrication and experimental performance measurement.

The thesis also presents comparisons between the experimentally generated magnetic field strengths and values generated from modelling the structures using Finite Element Method Magnetics (FEMM) software. It had been assumed that the experimental measurements would be almost the same as the original design calculations and predictions of the software. However the experimental results fell far short of both the calculated magnetic field strengths and the values predicted by the software. Magnetic flux densities in the range of 1.03 tesla were achieved.

The discrepancies could be due to changes in the magnetic properties of the core material. Drilling and machining of these components could have produced skin effects and other regions of poor magnetic properties. The effects could be exaggerated or diminished, depending on the exact configuration of the “C” shape.

List of Tables

List of Figures

FIGURES OF CHAPTER 2

FIGURES OF CHAPTER 3

FIGURES OF CHAPTER 4

FIGURES OF CHAPTER 5

FIGURES OF CHAPTER 6

Table of Contents

CHAPTER 3: COIL DESIGN PROCEDURES

CHAPTER 4: EXPERIMENTAL WORK PROCEDURE AND RESULTS

CHAPTER 5: MAGNETIC FIELD SIMULATION OF THE C-SHAPE CIRCUIT

CHAPTER 1

INTRODUCTION

1.0 Introduction

This project owes its origin to a research project called IELAS (contract number GRD2-2000-30207) performed under the Competitive and Sustainable Growth Research Programme of the European Commission.

A new method of alternating current measurement based on magnetostrictive material, can be introduced which will operate with mechanical waves.

The instrument transformers are traditional devices for the measurement of voltage and electrical currents, and have been key elements within the modern systems of generation, transmission, and distribution of electrical energy. Their principle of operation is based on magnetic flux variation. However these instruments are still manufactured with almost the same technological principles and methods as four decades ago. In fact, the size of these devices has become large, heavy, and expensive when used in high power application such as 400 kV.

The proposed system consists essentially of a current sensor and the associated modules. The current sensor is formed by an emitter, and a receiver. The emitter is based on magnetostrictive materials that generate mechanical wave under the alternate magnetic field induced by the primary current to be measured. Thus the 50 Hz, or 60 Hz, electrical signals are converted into elastic (mechanical) waves that propagate through a coupling structure until they reach the receiver. The receiver is based on piezoelectric materials. These materials have the property of inverse conversion of energy; thus the mechanical waves are transformed into electrical signals in the receiver. These electrical signals from the receiver are then amplified and compensated through electronic circuits.

From the commercial point of view, Terfenol–D is the most frequently used magnetostrictive material; this is due to its high magnetostrictive coefficient. For many potential applications, speed of response and operation at high frequencies are important, and Terfenol–D suffers from the problem of eddy currents, which are electric currents produced in the material by the effect of the varying magnetic field. Therefore within the material, the local magnetic field strength will be decreased, and a delay in reaching the point where the maximum occurs. They lead to power loss and they limit the frequency at which the material can operate.

A solution to reduce eddy currents is the use of another magnetostrictive material with a greater electrical resistivity, which can be used to give a response (in the form of a mechanical elastic wave) and preserve the features of the original excitation current more faithfully.

One material which falls into this category is cobalt ferrite ($CoFe_2O_4$) which has a very high electrical resistivity of $1\times10^{7}\ \Omega\,\mathrm{cm}$ when compared to Terfenol D, which has electrical resistivity of $58\times10^{-6}\ \Omega\,\mathrm{cm}$, although it has a smaller magnetostrictive coefficient. Cobalt ferrite can be enhanced by heat treatment, in the presence of high static magnetic field for a long period of time, a process which has been previously shown by Bozorth et al. and Lo et al. to greatly increase the magnetostriction of cobalt ferrite [1 - 2].

Magnetostriction is a property of ferromagnetic materials such as iron, nickel, cobalt and others. When placed in a magnetic field, these materials change shape and/or size. The physical response of a ferromagnetic material is due to the presence of magnetic moments, and can be understood by considering the material as a collection of tiny permanent magnets, or domains. Each domain consists of many atoms. When a material is not magnetized, the domains are randomly arranged. When the material is magnetized, the domains are oriented with their axes approximately parallel to one another.

1.1 Research objective

The main objective of this study is to investigate the suitability of new electromagnetic rig for the electromagnetic characterization of magnetostrictive materials. More specifically, the aims of this study can be summarized as follows:

A. To design and build an apparatus to generate strong and static magnetic field which can be used to measure the magnetostrictive strain of annealed cobalt ferrite and Terfenol-D based materials.

B. To develop an adequate cooling system for the rig in order to minimize the undesirable effects of the heat generated by the coils.

C. To compare between experimentally generated magnetic field strengths and computationally modelled field strengths.

D. To use a computational method to simulate the magnetic fields generated by the coils, and by introducing design variants into the models, to achieve the highest possible magnetic field strengths, which can be generated in practice by the chosen approach.

E. To investigate the influence of different factors such as different configurations, differently shaped corner components in the magnetic circuit, different magnetic properties of the core materials, and regions of poor magnetic properties such as skin effects, on the efficiency of the electromagnetic rig.

1.2 Structure of thesis

This thesis is organized in seven chapters. This chapter discusses the background of the research topic and aims of the study. Each chapter in this thesis ends with a brief summary outlining the achievements and findings that were established. The remainder of this thesis is organized as follows:

Chapter 2: The theoretical background and literature review of related research topics are elaborated in this chapter.

Chapter 3: This chapter covers coil design procedures

Chapter 4: All the experimental work procedures associated with the results are detailed.

Chapter 5: This chapter presents the simulation results of the magnetic fields generated by The C-shape design using different configurations.

Chapter 6: This chapter is furnished with results and discussions of each factor that contributes to the effects on the performance of the electromagnetic rig.

Chapter 7: Chapter 7 presents an overall discussion of the study and concludes with highlighting the most important findings and recommendations for future research work.

CHAPTER 2

LITERATURE REVIEW

2.0 Introduction

Many modern technological devices rely on magnetism and magnetic materials; these include electrical power generators and transformers, electrical motors, radios televisions, telephones, and computers.

Iron, nickel, and cobalt are well known examples of materials that exhibit magnetic properties. Most substances are influenced to one degree or another by the presence of magnetic field. This chapter provides a brief description of the origin of magnetic fields and discusses types of magnetic materials and their properties, and the generation of high magnetic fields. Also a description of magnetostriction effects and an explanation why they occur is covered. It lists a number of devices where the properties have been put to use, and describes a range of methods which have been used to measure these properties. Finally, magnetic annealing of cobalt ferrite is elaborated in the last section of this chapter followed by a brief summary.

2.1 Magnetic behaviour of materials

Magnetism is one of the phenomena in which materials assert an attractive force or the only phenomenon in which materials assert a repulsive force or influence on some other materials. The force acts at a distance and can be analysed in terms of magnetic fields. This force can act strongly in ferromagnetic materials. These are some of the transition elements such as iron, nickel and cobalt, some rare earth elements, and various chemical compounds containing these elements.

A magnet is an object or material that attracts certain metals, such as iron, nickel and cobalt. It can also attract or repel another magnet. All magnets have North-seeking (N) and South-seeking (S) poles. The magnetic force strongly attracts an opposite pole of another magnet and repels a like pole.

There are three types of magnets which can attract other pieces of iron or steel i.e. permanent magnets, temporary magnets and electromagnets. A permanent magnet often called a hard magnet retains number of magnetic properties permanently and only loses them under special demagnetising circumstances. These properties include a high remanence, a high permeability, a high coercive field, a large hysteresis loop, and require high electrical power to achieve a complete cycle [3]. Temporary magnets are those that act like a permanent magnet when they are within a strong magnetic field, but they loose their magnetism when the magnetic field disappears. They have a narrow hysteresis loop, and hence they can be more easily magnetised and demagnetized. Electromagnets are produced by wrapping a coil of wire around a spool. Inside this spool there may be a magnetic material such as soft iron, or there may be a non-magnetic material such as air. They act like a permanent magnet when current is flowing in the wire. The strength and polarity of the magnetic field created by the electromagnet are adjustable by changing the magnitude of the current flowing through the wire and by changing the direction of the current flow.

2.1.1 Magnetic dipoles and magnetic moments

The magnetic behaviour of materials is determined primarily by their electronic structures, which provide magnetic dipoles. Interactions between these dipoles determine the type of magnetic behaviour that is observed. Magnetic behaviour can be modified by composition, microstructure, and processing of these basic materials.

Magnetic dipoles are found to exist in all magnetic materials, and may be thought of as small bar magnets composed of north and south poles [4]. Pre-existing magnetic dipoles within the material are oriented in various directions, but they are influenced when external magnetic fields are generated. Within a magnetic field, forces may exert torques that tends to orient the dipoles along the field.

The physical cause of magnetism in objects is the atomic magnetic dipole associated with individual electrons. On an atomic scale, magnetic dipoles, or magnetic moments, are a result of two kinds of movement of electrons [4]. One is related to the orbital motion of an electron around a nucleus; being a moving charge, an electron may be considered to be a small current loop, generating a very small magnetic field, resulting in an orbital magnetic dipole along its axis of rotation, as schematically illustrated in figure 2.1(a). The second source of magnetic moment is called the spin dipole, which originates from this electron spin. It is directed along the spin axis as shown in figure 2.1(b). Spin magnetic moments may be only in "up" direction or in "down" direction. Thus each electron in an atom may be thought of as being a small magnet having permanent orbital and spin magnetic moments.

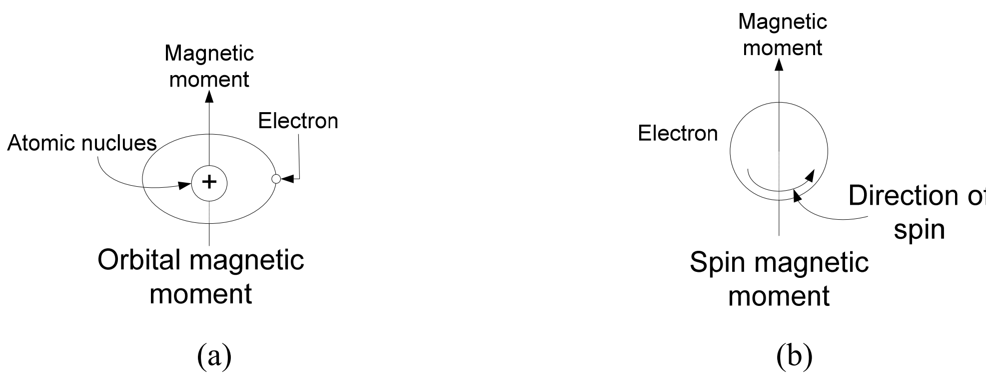

Figure 2.1: Magnetic moments associated with (a) an orbiting electron and (b) a spinning electron [4].

The overall magnetic moment of the atom is the net sum of all of the magnetic moments of the individual electrons. In each individual atom, orbital moments of almost all electron pairs cancel each other; this also holds for spin moments. Thus, in the case of an atom with a completely filled electron shell or sub-shell, the magnetic moments normally completely cancel each other out; therefore the whole material is not capable of being permanently magnetized. Only atoms with partially filled electron shells have a magnetic moment, whose strength depends on the number of unpaired electrons [5]. The differences in configuration of the electrons in various elements thus determine the nature and magnitude of the atomic magnetic moments, which in turn determine the differing magnetic properties of various materials.

2.1.2 Magnetic field around a current carrying conductor

When a conductor carries an electric current I (amperes), a magnetic field is produced about that conductor [6]. If a compass is placed in the vicinity of this conductor, its needle will align itself at right angles to the conductor, indicating the presence of a magnetic field.

A cross-sectional view of a conductor that is carrying current toward the observer is illustrated in figure 2.2(B). Notice that the direction of current is indicated by a dot, representing the head of the arrow. A conductor that is carrying current away from the observer is illustrated in figure 2.2(C). Note that the direction of current is indicated by a cross, representing the tail of the arrow. Also note that the magnetic field around a current carrying conductor is perpendicular to the conductor, and that the magnetic lines of force are equal along all parts of the conductor.

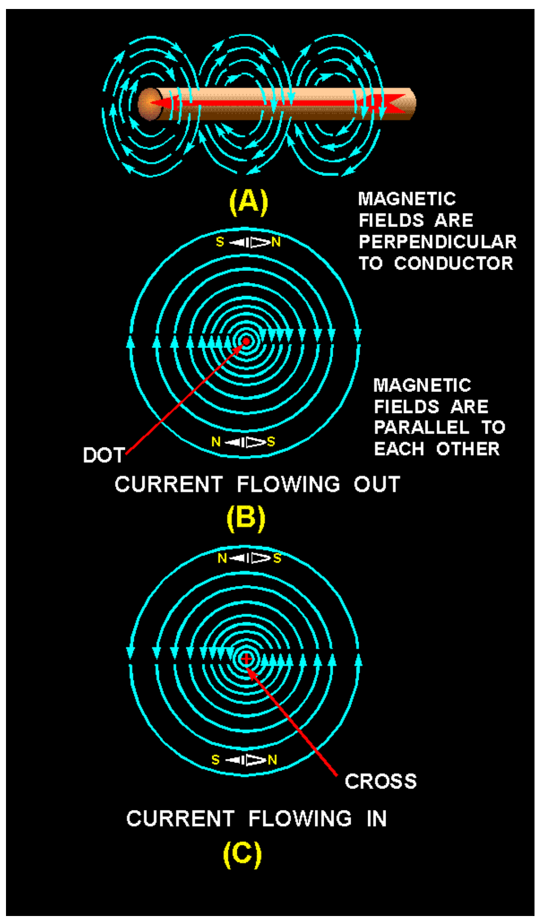

Figure 2.2: Magnetic field around a current-carrying conductor [7].

If two parallel and adjacent conductors are carrying currents in the same direction as shown in figure 2.3, the fields about the two conductors aid each other. Conversely, if the two conductors are carrying currents in opposite directions, the fields about the conductors repel each other.

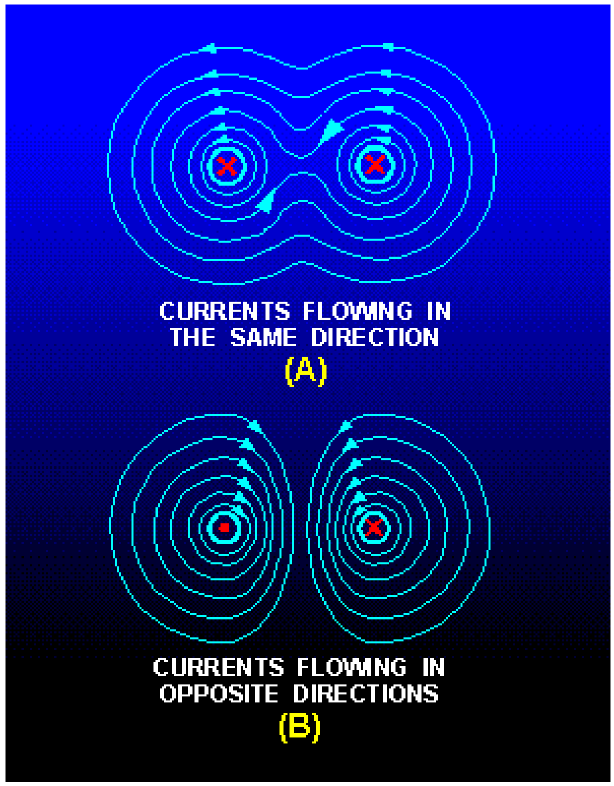

Figure 2.3: Magnetic fields around two parallel conductors [7].

2.1.3 Magnetic field produced by a current carrying coil

In order to increase the magnetic field strength, a coil of N turns can be constructed as depicted in figure 2.4. The coil is formed by wrapping a conductor around an iron core or coil spool. The magnetic field strength is directly proportional to the number of turns as well as the current it carries. The magnetic field around each turn of wire links with the fields produced in the adjacent turns when a current passes through the coil. The combined influence of all the turns produces a two pole field similar to that of a simple bar magnet. One end of the coil is a north pole and the other end is a south pole.

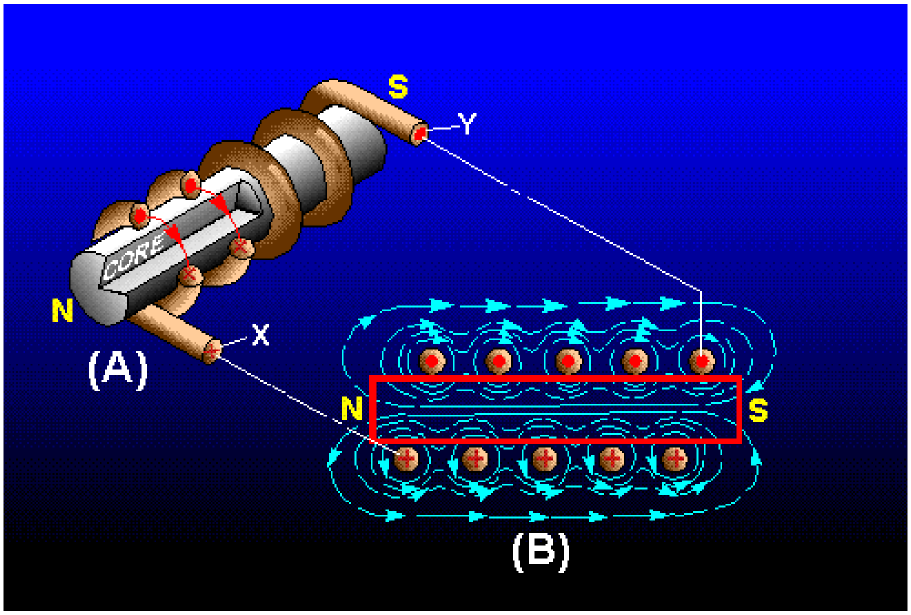

Figure 2.4: Magnetic field produced by a current carrying coil [7].

If the coil is constructed around a spool (air-core) as depicted in figure 2.5, the magnetic field strength of the coil can be estimated using the following formulae [8]:

$$\frac{B}{H} = \mu \rightarrow \frac{B}{\mu} = H \qquad (2\text{-}1)$$

where:

B is the flux density

H is the magnetic field strength

μ is the magnetic permeability constant

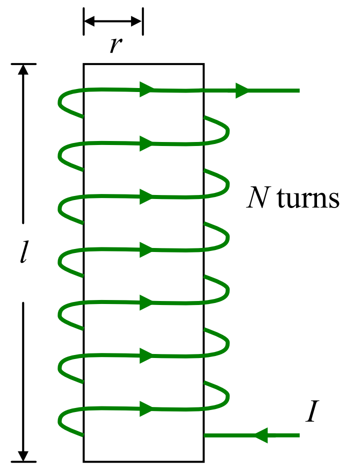

Figure 2.5: Schematic of a basic solenoid coil wound around spool.

The maximum flux density B will be at the centre of the coil given by [9]:

$$B = \frac{\mu NI}{\sqrt{4r^2 + l^2}} \tag{2-2}$$

Therefore:

$$\frac{B}{\mu} = \frac{NI}{\sqrt{4r^2 + l^2}} \tag{2-3}$$

where:

N is the number of loops or turns of windings

I is the current flow through the coil

r is the effective radius of the coil

l is the length of the coil

Combining equations (2-8) and (2-10) yields:

$$H = \frac{NI}{\sqrt{4r^2 + l^2}} \tag{2-4}$$

2.1.4 Domain structure and hysteresis loop

Domains are regions in the material in which all the dipoles are aligned [10]. Adjacent domains are separated by domain boundaries or walls called Bloch walls. The Bloch walls are narrow zones in which the direction of the magnetic moment gradually and continuously changes from that of one domain to that of the next. Normally domains are microscopic in size, and for a polycrystalline specimen, each grain may consist of more than a single domain. Thus, in a microscopic piece of material, there are a large number of domains, and each has a different magnetization orientation. The magnitude of the Magnetization, *M*, field for the entire solid is the vector sum of the magnetizations of all domains. In a material that has never been exposed to a magnetic field, the individual domains have a random orientation. The net magnetization in the material as a whole is zero.

Hysteresis loop demonstrates the relationship between *B* and *H*, and provides information about the magnetic properties of a material. An example of the hysteresis loop for a ferromagnetic material is shown in figure 2.6.

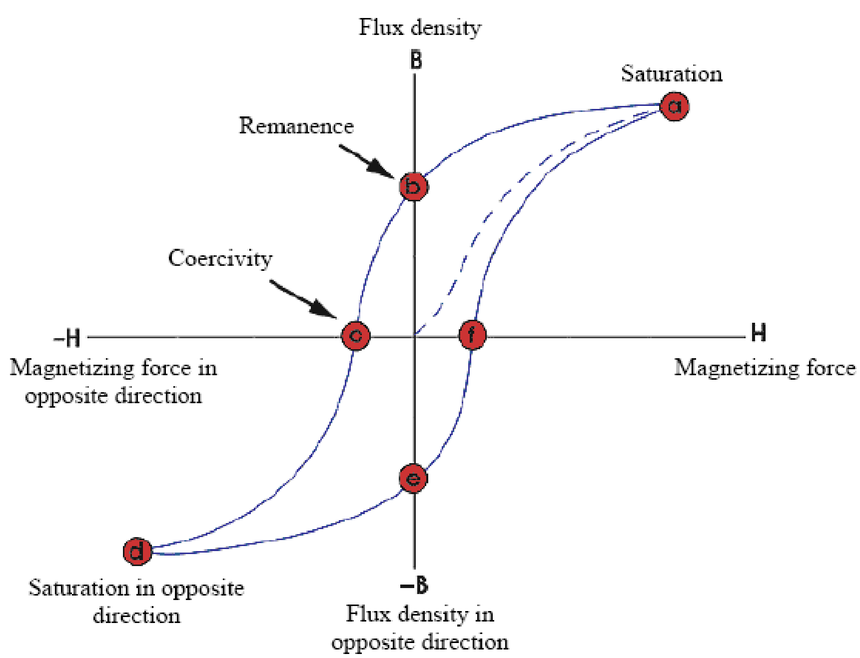

Figure 2.6: Magnetic flux density versus magnetic field strength [10].

The loop is generated by measuring the magnetic flux *B* of a ferromagnetic material while the magnetizing force *H* is changed. A ferromagnetic material that has never been previously magnetized or has been thoroughly demagnetized will follow the dashed line as *H* is increased. When a magnetic field is imposed on the material, domains that are nearly aligned with the field grow at the expense of unaligned domains [4]. Initially the domains grow with difficulty, and relatively large increases in the field are required to produce even a little magnetization. As the field increases in strength, favorably oriented domains grow more easily. Eventually, at point "a" almost all of the magnetic domains are aligned and an additional increase in the magnetizing force will produce very little increase in magnetic flux. The material has reached the point of magnetic saturation.

Hysteresis behavior may be explained by the motion of domains walls. Upon reversal of the field direction from saturation (from point "a" to point "b"), the process by which the domain structure changes is reversed. First there is a rotation of a single domain with the reversed field. Next, domains having magnetic moments aligned with the new field form and grow at the expense of the former domains. Critical to this explanation is the resistance to the movement of domain walls that occurs in response to the increase of the magnetic field in the opposite direction; this accounts for the lag of *B* with *H*, or the hysteresis. When *H* is reduced back down to zero, the upper section of the curve is followed. At point "b", it can be seen that some magnetic flux remains in the material even though the magnetizing force is zero. This is referred to as the point of retentivity on the graph and indicates the remanence or level of residual magnetism in the material. As the magnetizing force is reversed, the properties follow the curve to point "c", where the flux has been reduced to zero. This is called the point of coercivity on the curve. The reversed magnetizing force has flipped enough of the domains so that the net flux within the material is zero. The force required to remove the residual magnetism from the material, is called the coercive force or coercivity of the material.

As the magnetizing force is increased in the negative direction, the material will again become magnetically saturated but in the opposite direction at point "d". Reducing *H* to zero brings the curve to point "e". It will have a level of residual magnetism equal to that achieved in the other direction. Increasing *H* back in the positive direction will return B to zero. Notice that the curve does not pass through the origin of the graph because some force is required to remove the residual magnetism. The curve will take a different path from point "f" back to the saturation point where it with complete the loop.

On the other hand, when the value of H is increased back to zero, the curve moves from point S' to point $-B_r$, which has the same value of B_r in the other direction. This is because they have the same amount of the residual magnetism. The curve moves to H_c when H is given a positive value at zero value of B. Further increases of H will result the curve to move back to point S, where the curve completes the loop.

Figure 2.7 shows typical hysteresis loops for hard and soft magnetic materials. The shape and size of the hysteresis loop greatly depends on the type of the material. The loop will be narrow if the material is easily magnetized. On the other side, the loop will be wide if the material does not get magnetized easily. In addition, different types of magnetic materials will saturate at different values of magnetic flux density, which is affecting the height of the loop. The loop area also depends upon the maximum flux density that is established in the material.

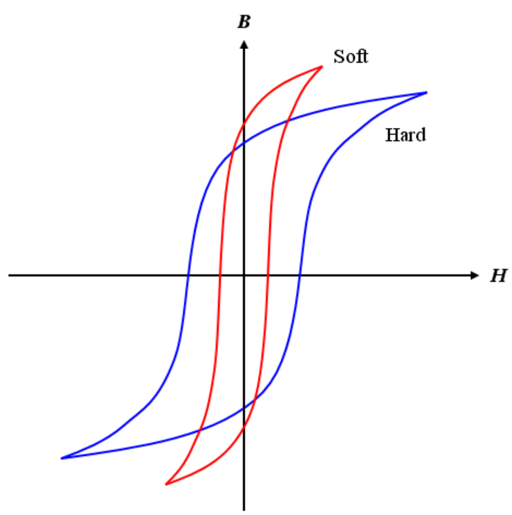

Figure 2.7: Hysteresis loops for soft and hard magnetic materials [11].

Table 2.1 gives the magnetic properties of hard and soft magnetic materials. The permanent magnets are made from hard magnetic materials such as steel, cobalt steel and carbon steel. The magnet is quite strong since these materials have high remanence. They are difficult to be demagnetized by removing the magnetic fields due to their high coercivity. The electromagnets or temporary magnets are made from soft magnetic materials such as soft iron. They can be easily demagnetized and produce strong magnets since these materials have low coercivity and high saturation flux density, respectively. For instance, transformer cores are made from soft magnetic materials since they have narrow hysteresis loop (smaller hysteresis loop area). When a transformer is in use, its core is taken through many cycles of magnetization. The energy lost as heat in reversing the magnetization of the material (hysteresis loss) is proportional to the area of the hysteresis loop.

Table 2.1: Comparison magnetic properties between soft and hard magnetic materials.

Magnetic Property	Soft Magnetic Material	Hard Magnetic Material
Hysteresis loop	Narrow	Large area
Remanence	High	High
Coercivity	Low	High
Saturation flux density	High	Good

2.1.5 Magnetic permeability and magnetisation

Magnetic permeability, μ, is a property of a specific medium through which the magnetic field strength, H, passes and in which the magnetic flux density, B is measured. It has dimensions of webers per ampere-meter (Wb/A-m) or henries per meter (H/m).

The magnetic field strength, H is the amount of magnetizing force which is inversely proportional to the length of a coil and directly proportional to the amount of electrical current passing through the coil. According to Ampere’s law, the line integral of H around a single closed path is equal to the current enclosed by the path. It is expressed by [12]

$$\oint H \cdot dL = I \tag{2-5}$$

where H is the magnetic field strength (Am^{-1}) and dL is the infinitesimal element of path length (m). An analogous relation with static electric field and the relation of magnetomotive force, equation (2-5) can also be written as

$$\oint H \cdot dL = I = F \tag{2-6}$$

where F is the magnetomotive force (mmf) is equal to the current enclosed (ampere-turn, At).

If the path of integration in equation (2-6) consists of a number of turns of wire each with a current in the same direction, equation (2-6) may be written as

$$\oint H \cdot dL = F = NI \tag{2-7}$$

In other word, if the magnetic field is generated by a cylindrical coil, then

$$H = \frac{NI}{L} \tag{2-8}$$

In this case, the unit of H can be written as either ampere-turns per metre (At/m) or simply ampere per metre (A/m).

The magnetic flux density B represents the magnitude of the internal field strength within a substance that is subjected to an external H field [13] and is given by,

In a vacuum

$$B = \mu_0 H \tag{2-9}$$

where, μ_0 is the permeability of a vacuum = $4\pi \times 10^{-7} \approx 1.257 \times 10^{-6}$ T.m/A. If there is a material, other than vacuum, in the middle of the magnetic fields, the magnetic flux density now is [3]

$$B = \mu H \tag{2-10}$$

Relative permeability μ_r (unitless) is used to measure the degree to which the material can be magnetized, where

$$\mu_r = \frac{\mu}{\mu_0} \tag{2-11}$$

Magnetization M is a property of some materials that describes the additional magnetic flux density residing in the material is given by [13],

$$B = \mu_0 H + \mu_0 M \tag{2-12}$$

where, M is the magnetization of a material (magnetic moment per unit volume, $A.m^2/kg$ or Wb.m/kg).

In general, a material becomes magnetized in response to an external field H and can be measured through susceptibility and permeability. Hence, M can be expressed as

$$M = \chi_m H \tag{2-13}$$

where χ_m is the magnetic susceptibility (unitless). Magnetic susceptibility is the degree of magnetization of a material in response to an applied magnetic field. Relative permeability and magnetic susceptibility are related as follows:

$$\mu_r = 1 + \chi \tag{2-14}$$

2.1.6 Types of Magnetism

Materials may be classified by their response to the externally applied magnetic fields as diamagnetic, paramagnetic, ferromagnetic, ferrimagnetic, and antiferromagnetic (table 2.2). These magnetic responses differ greatly in strength [9].

a. Diamagnetism

Diamagnetism is a very weak form of magnetism, and persists only while an external field is being applied to the material. Although the orbit and spin magnetic moments in such a materials cancel in the absence of external magnetic field, an applied field causes the spin moment to slightly exceed the orbital moment. The magnitude of the induced magnetic moment is extremely small, and in the opposite direction of the applied magnetic field. The relative permeability is less than unity, and the magnetic susceptibility is negative; that is, the magnitude of flux density, B, within a diamagnetic solid is less than a vacuum.

Table 2.2: Different types of magnetic behaviour.

Type of Magnetism	**Magnetic Behaviour**	**Magnetic Susceptibility**	**Examples** [3]
Diamagnetic	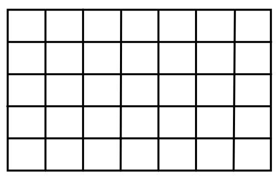	Small and negative	Copper, silver, gold and alumina
Paramagnetic	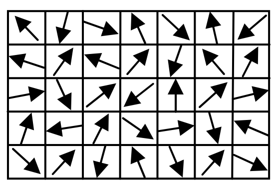	Small and positive	Aluminium, titanium and alloys of copper
Ferromagnetic	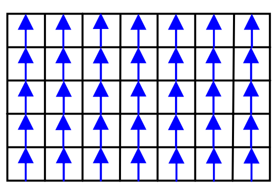	Very large and positive, function of applied field, microstructure dependent	Iron, nickel and cobalt
Anti-ferromagnetic	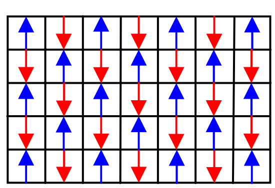	Small and positive	Manganese, chromium, MnO and NiO
Ferrimagnetic	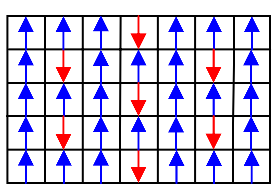	Large and positive, function of applied field, microstructure dependent	Ferrites

b. Paramagnetism

For some other materials such as Aluminium, and titanium, each atom possesses a permanent dipole moment due to incomplete cancellation of electron spin and/or orbital magnetic moments, resulting in a net magnetic moment for the atom even with no applied magnetic field. In the absence of the applied field, the orientation of these atomic magnetic moments is random, but when an external magnetic field is applied, they experience a torque which tends to align them with the direction of the field.

c. Ferromagnetism, ferrimagnetism and antiferromagnetism

Ferromagnetic materials such as iron, nickel, cobalt and some of the rare earth elements are considered to be the most important magnetic substances. The elementary magnetic dipoles inside the domains are all oriented in a direction parallel to each other [3]. They have high magnetic permeability, capable to become highly magnetic and have the ability to retain a permanent magnetic moment in the absence of an external field. If the magnetic moments of adjacent atoms are oriented in a direction antiparallel to each other, the material is said to be antiferromagnetic and appears to be nonmagnetic. Whereas, if magnetic moments are not equal and aligned opposite to each other so that there is a net magnetic moment (not equal to zero)such a material is said to be ferrimagnetic.

2.1.7 Types of magnetic materials

Ferromagnetic and ferrimagnetic are two types of materials that are widely used in magnetic components. They have different coercivity depending on their sizes or domains. The coercivity increases when the amount of particle of the magnetic materials increases. Therefore materials with a few or no domains have a high coercivity whilst those with many domains have low coercivity. The energy of the domains on either side of the walls (an interface separating magnetic domains) will increase with the application of a very low magnetic field. This low magnetic field produces zero coercivity where there is nothing to impede its motion. Under the pressure of the applied magnetic field, magnetization reversal occurs either by coherent rotation of the magnetic moments in the domain or by nucleation and growth of reverse domains. The coercivity of a crystal structure in a permanent magnet is usually very small. A crystal structure (also known as a lattice) is a set of atoms arranged in a particular way. However, due to imperfections in the structure such as inclusion [14] and dislocation [15], the crystal coercivity increases. These factors act as a barrier to the movement of domain boundaries.

Inclusions are small "holes" in the medium, usually formed by the entrapment of a foreign material. The inclusions are either nonmagnetic or having much smaller magnetization than their surroundings. Such inclusions impede the process of magnetization, having magnetic poles induced on their surface causing a reduction in the surface energy of the domain walls. On the other hand, a dislocation in the crystal lattice interacts with the domain walls. In some cases, the easy axes on two sides of the dislocation may be aligned differently. (In iron, the easy axes are all mutually perpendicular). If the dislocation is severe, the exchange interaction between atoms on the two sides of the wall may become negligible and a domain wall might not be able to cross the boundary.

a. Hard magnetic materials

Hard magnets, also referred to as permanent magnets, are magnetically saturated materials. As a result, once magnetized, these materials have a very large intrinsic coercivity and become permanent magnets [13]. At the atomic level, ferromagnetic materials exhibit a long-range ordering phenomenon which causes unpaired-electron spins to line up parallel to each other in a domain. A strong magnetic field exists within the domain, but as an entire material it has a small magnetic field because the domains are randomly oriented with respect to one another. An external magnetic field can cause the magnetic domains to line up with each other. As a result, the material is said to be magnetized.

One of the important factors in permanent magnets is called magnetic remanence of the material. This phenomenon occurs when the applied magnetic field is removed where a fraction of the saturation magnetization still remains [3]. A certain level of energy is required in order to force the domains back to the original condition. Normally, hard magnetic materials are used in the production of permanent magnets. The properties of ferromagnetic materials make them applicable to be utilized as a magnetic memory. Some of the compositions of the ferromagnetic materials will retain an imposed magnetization indefinitely such that the criteria of permanent magnets can be fulfilled.

b. Soft magnetic materials

Soft magnetic materials require a very small magnetizing field to become magnetized. For instance, a magnetic field is created when a current is passed through a wire wound around a soft magnetic core. They have a low coercivity and once the magnetizing field is removed, the flux density essentially goes to zero. Alternating current (AC) or direct current (DC) electrical circuits can be used in order to generate a magnetic field or to create a force. Permeability is the main consideration for the material selection in the DC application, whereas the saturation magnetization may then be significant. This would be the case, for example, in shielding applications where the flux must be channelled through the material, and can also be utilized to amplify the flux generated by an electric current [3]. Energy loss is the most critical factor in the system for AC applications as the material is cycled around its hysteresis loop. The energy loss can originate from three different sources such as hysteresis loss, eddy current loss and anomalous loss (magnetic losses in soft magnetic material) [13]. Hysteresis losses can be reduced by the reduction of intrinsic coercivity with a consequent reduction in the area within the hysteresis loop. An eddy current is a swirling current set up in a conductor in response to a changing magnetic field. Eddy current losses can be reduced by decreasing the electrical conductivity of the material. Because of the skin effect at a higher frequency which can influence the overall conductivity, it also can be reduced by laminating the material. Finally, anomalous losses can be reduced by having a completely homogeneous material, so that there is no obstruction to the motion of the domain walls [16].

2.1.8 Mechanical effects which cause the magnetic properties to become poorer

Magnetic materials are frequently are subject to machining to obtain complex shapes and high dimensional precision. These operations alter the magnetic properties, and thereby affect their performance when applied in certain application.

The property changes depend mainly on the alloy, on the type of and degree of machining, and on the thickness of the machined parts.

A. Bass investigated the turning and drilling operations on the magnetic properties of several soft magnetic toroidal rings [17]. Results showed that the coercive force increased with a reduction in thickness of the rings and that the remaining magnetic properties such as permeability and magnetic flux density decreased with a reduction in thickness. These properties decrease as the number of machining increase. The decrease in magnetic properties can be explained by the alteration of the material to a particular depth. This alteration could even be of smaller depth than in the solid materials because of the effect of the porosity acting as a barrier to the propagation of the dislocations as shown in figure 2.8.

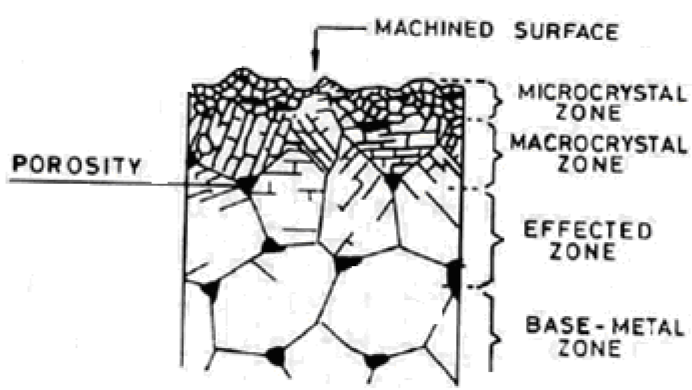

Figure 2.8: Surfaces changes caused by machining [17].

R. Maxime et al. also studied the effect of machining on the electromagnetic properties of soft magnetic materials [18]. It was observed that machining increased the electrical resistivity of the material up to 54%. The increase in resistivity can be explained by the removal of the more conducting surface layer, and therefore the permeability of the material decreased and the coercive force increased. Magnetic permeability and hysteresis losses are dependent upon the iron density of the material, the lower the density, the lower the permeability and the higher the hysteresis losses.

2.2 Magnetic circuit

Magnetic circuit is a closed path containing a magnetic flux. It is generally composed of magnetic elements such as permanent magnets, ferromagnetic materials and electromagnets, and may also contain an air gap and other materials [6]. Basically, there are kinds of magnetic circuits, series and parallel as shown in figure 2.9. This is analogous to electrical circuits, a magnetic series circuit is one in which the flux set up by the current carrying coil. In parallel circuit, there is more than one path for the flux to close.

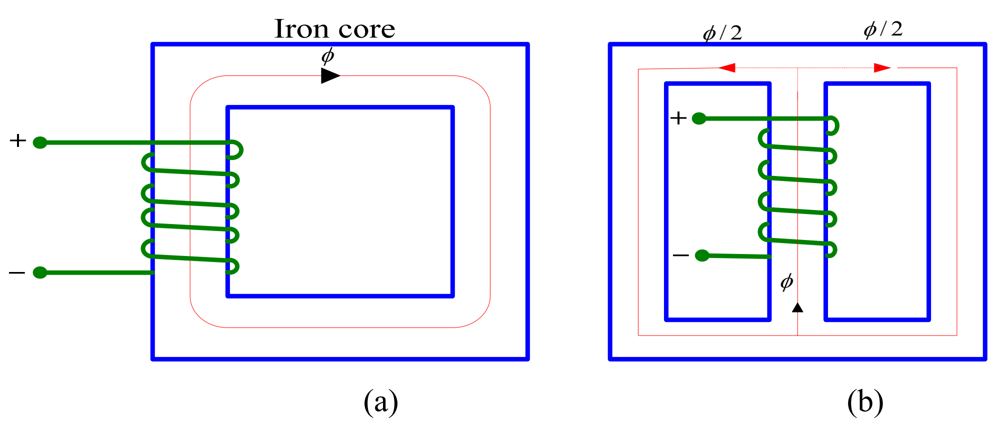

Figure 2.9: Examples of magnetic circuits: (a) series; (b) parallel [6].

If ϕ is the magnetic flux in the magnetic circuit, F is the magnetomotive force applied to the circuit, and $\Re$ is the reluctance of the circuit, then it follows from Ampere's law that [6]

$$\phi = \frac{F}{\Re} \tag{2-15}$$

This is analogous to Ohm's law in electrical circuits. Magnetic flux, magnetomotive force and reluctance are analogous to current, voltage and resistance respectively. It follows that:

$$\Re = \frac{l}{\mu A} \tag{2-16}$$

where:
A is the cross-sectional area of the flux path in meter square (m^2)
μ is the permeability of the material in henries/meter (H/m)
l is the length of the magnetic path in meters (m)

The reluctance of a magnetic circuit is directly proportional to the length of the magnetic path, and inversely proportional to its cross-sectional area. Thus equation 2-16 can be equated to Ohm's law for magnetic circuits. Low reluctance, like low resistance in electric circuits, is generally preferred.

In gapless magnetic circuits such as the circuit shown in figure 2.9, the required NI (number of turns times current) to produce a certain flux density B can be calculated using the following formula [9]:

$$NI = Hl \tag{2-17}$$

The corresponding H value can be taken from a B-H curve for the core material, and then B can be calculated as follows:

$$B = \frac{\mu NI}{l} = \frac{\mu NI}{2\pi r} \tag{2-18}$$

In some magnetic circuits especially those that contain air gaps, there is a tendency for the flux to leak out of the magnetic path or spread out in the air gap as illustrated in figure 2.10. Leakage flux is not very effective and requires greater magnetomotive force F to compensate for this leakage. Spreading out of the flux in the air gap is called a fringing leakage; it spreads out the flux over a relatively larger area if the air gap is large, and thus it reduces the magnetic flux density B in the air gap.

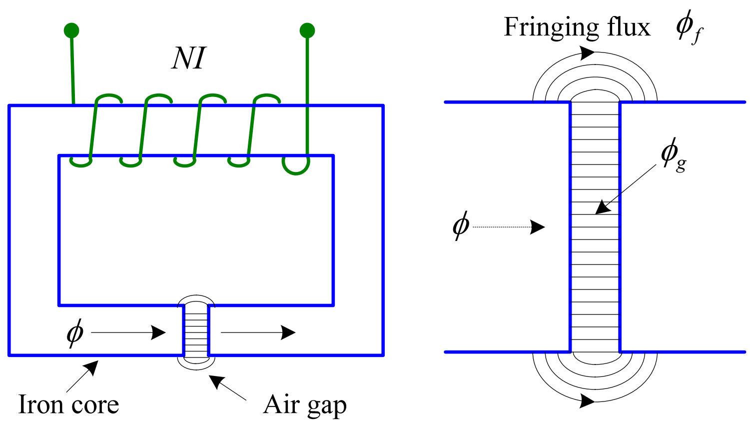

Figure 2.10: Leakage fluxes and fringing effect on flux in the air gap [19].

Air gaps are very commonly used in magnetic devices such as in rotating machines, and have an effect on the core characteristics. In designing machines with air gaps, it is desirable to have a gap of which is a little more than a mechanical clearance. The length of the core is not very critical.

Assuming the surface area of the iron core faces shown in figure 2.10 is large compared with the air gap width, and then fringing flux can be neglected. By the continuity of the normal component B, the flux density in the iron core is the same as the flux density in the air gap [9]. However, the magnetic field strengths in the air gap and in the iron core are different. They are related to the energy required to establish the magnetic flux and in iron this energy is very much smaller than that required in air.

The magnetic field strength in the air gap (H_g), and in the iron core (H_c) are given by:

$$H_g = \frac{B}{\mu_o} \tag{2-19}$$

$$H_c = \frac{B}{\mu_r \mu_o} \tag{2-20}$$

Ampere's circuital law of magnetism states that the line integral of magnetic field strength H around the magnetic circuit equals the total magnetomotive force F, or ampere-turns enclosed. That is [9]:

$$F = NI = \oint H.dl \tag{2-21}$$

If leakage flux is neglected, B and H in the iron core will be constant. Thus:

$$F = NI = \oint H.dl = H_{iron} l_{iron} + H_{gap} l_{gap} = \frac{Bl_{iron}}{\mu_r \mu_o} + \frac{Bl_{gap}}{\mu_o} \tag{2-22}$$

Referring to figure 2.10, magnetic poles of opposite polarity exist on either side of the air gap. Therefore they are attracted to each other and the effect of the magnetic field is such as to exert a force which tends to close the gap.

The density of energy w stored in a magnetic field is expressed as [9]

$$w = \frac{1}{2} \frac{B^2}{\mu} \tag{2-23}$$

Assuming that the air gap is small, and the field in the air gap is uniform, then the total energy W_m stored in the air gap is given by:

$$W_m = \frac{B^2 Ag}{2\mu_o} \tag{2-24}$$

where:

A = area of the air gap (m^2)

g = width of air gap (m)

If the iron core is flexible so that the air gap must be held open by a force F. If this force in increased so as to increase the air gap by an amount of Δg, while at the same time, the current in the coil has to be increased to maintain the flux density B constant around the magnetic circuit, then the energy stored in the air gap is increased accordingly by a small amount ΔW_m :

$$\Delta W_m = \frac{B^2 A}{2\mu_o} \Delta g \tag{2-25}$$

Energy can be expressed as force multiplied by distance, that is:

$$\Delta W_m = F \Delta g \tag{2-26}$$

where: F is equal to the attractive force between the magnetic pole pieces.
It follows that:

$$F \Delta g = \frac{B^2 A}{2\mu_o} \Delta g \tag{2-27}$$

Therefore, the required force (gap force) to hold the poles apart from each other is calculated as follows:

$$F = \frac{B^2 A}{2\mu_o} \tag{2-28}$$

2.3 Magnetostriction overview

The history of magnetostriction begins in the early 1840s when James Prescott Joule (1818-1889) positively identified the change in length of an iron sample as its magnetization change. Work continued with magnetostrictive, into the 20th century, resulting in an early magnetostrictive telephone, magnetostrictive oscillators, torque meter, and sonar [20].

During the early 1960's, a breakthrough in magnetostrictive materials occurred with the discovery of largest magnetostriction in rare earth elements terbium and dysprosium. The strains in these elements are of the order of 10,000 X 10^{-6}.

Unfortunately, from the point of view of making use of these rare earth metals in their elemental form, their magnetic properties only exist at low temperatures by their curie temperature (T_c), which is the temperature above which the material becomes non–magnetic. However this temperature limitation and the fact the field of piezoelectricity was gaining technical maturity hindered the development of magnetostrictive materials.
In the early 1970's, Art Clark and his co-workers at the Naval Ordinance Laboratory (NOL) in Maryland, USA have provided a new class of transducer materials capable of high room temperature strains. Highly magnetostrictive rare earths (R), principally samarium (Sm), terbium (Tb), and dysprosium (Dy), were combined with the magnetic transition metals nickel, cobalt and iron by direct compound synthesis and by rapid sputtering into amorphous alloys. The rare earth ferrite compounds (R-Fe) exhibit an increase in the Curie temperature with increasing rare earth concentration [21].
This unusual property facilitates huge room temperature magnetostrictions, of up to 3000 X $10^{-6,}$ particularly in the terbium ferrite compounds ($TbFe_2$), but large fields of over 2 MA/m are needed to bring these compounds to saturation.

Partial substitution of dysprosium for terbium in $TbFe_2$ resulted in improved magnetostriction and anisotropy properties. The appropriate composition is 27% $TbFe_2$ and 73% DyFe2 and the resulting compound $Tb_{0.27}Dy_{0.73}Fe_{1.9\text{-}1.95}$ has been available commercially since the 1980's under the name Terfenol-D (Ter = terbium, Fe = iron, N = Naval, O = Ordnance, L = Laboratory, and D = dysprosium).The highest room temperature magnetostriction for Terfenol-D is 1600 X10^{-6} at a moderate saturation field of 0.16 MA/m. At present Terfenol-D is widely used in different applications such as active noise and vibration control systems, low frequency under water communications (sonar), linear and rotational motors, ultrasonic cleaning, machining and welding, micro positioning, and the detection of motion, force and magnetic fields [22].

Terfenol-D is expensive, extremely brittle and the high content of rare earth metal makes the material extremely susceptible to corrosion. Terfenol-D also suffers from the problem of induced eddy currents, common to all metallic magnetic materials, which gives rise to ohmic losses and consequently decreases the performance (extension) of the magnetostrictive material [23]. The effect of eddy currents in Terfenol-D is a particularly severe because the material is very brittle and therefore difficult to laminate, as is done for example with transformer cores. Recently, this limitation has been addressed by the development of composite materials in which small particles of Terfenol-D are bonded with a nonconducting polymer binder [24]. However, despite some advantages, including easier machinability and moldability of specific sizes and shapes, magnetostrictive composites exhibit lower saturation magnetostriction than the monolithic material [25].

A magnetostrictive material will change shape when it is placed in a magnetic field. Most ferromagnetic materials exhibit some measurable magnetostriction. Since the phenomenon involves a bidirectional energy exchange between magnetic and elastic states, these materials provide a mechanism both for actuation and sensing applications. They are also successfully employed in a wide variety of devices for vibration control of mechanical equipment.

The nature of this effect is illustrated in figure 2.11. A rod of a magnetic material of length L is shown surrounded by a coil of wire carrying an electrical current so that a magnetic field, H, is produced along the rod. With the current flowing, the length of the rod increases by a small amount ΔL. The strain ΔL/L is called the magnetostriction (for which the symbol λ is used).

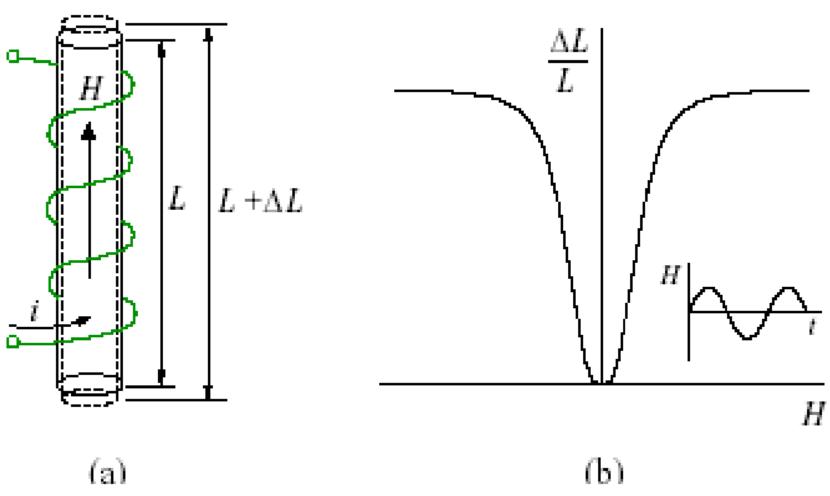

Figure 2.11: Joule magnetostriction (a) The changes in shape in response to the magnetic field H. H is proportional to the current that passes through the solenoid (b) The relationship between $\Delta L / L$ and H [26].

Figure 2.11(a) also shows that in addition to an increase in length in the direction of the field, there is a decrease in the perpendicular direction and as a result of this the volume of the rod remains essentially constant. Figure 2.11(b) also reveals two important features of magnetostriction: firstly for high values of H, λ eventually reaches a constant value λ_{sat}, indicating saturation, and secondly the sign of λ does not change when the field H becomes negative. The rod increases in length for both positive and negative values of the magnetic field strength. (Magnetostriction is therefore a second order effect) [24].

The principal magnetostrictive effects observed experimentally are: 1) The Joule effect. This can be an extension or a contraction in the same direction as the magnetic field or in some other direction. 2) The volume effect (volumetric expansion), a very weak effect. 3) The Wiedemann effect (a shear strain response to the magnetic field, analogous to the tensile or compressive strain produced in the Joule effect) [27]. In addition, inverse effects are also observed, such as the Villari effect. In this case there is a change in magnetic permeability in response to an applied stress. The inverse magnetostrictive effects are sometimes referred to as magneto mechanical effects. For most transducer applications the maximum force or movement are desired as outputs, and so the Joule effect or its inverse, the Villari effect are the most useful in technology. Therefore the discussion that follows will concentrate primarily on these effects. Information on other effects can be found in reference [28].

2.4 Physical origin of magnetostriction

The two largest contributions to magnetic effects arise because of the movements of unpaired electrons. Because electrons spin, a magnetic field is produced, and because electrons also move in orbitals around the atomic nucleus, another magnetic field is also produced. There is an interaction between these magnetic fields, which causes the spins of different unpaired electrons close to each other to align along the same direction, and there is also an interaction causing the orbitals to align also in the same direction, if there is freedom to do so [10].

However in crystalline solids the atoms are arranged in regular patterns and the distance between one atom or ion and its neighbours is fixed within certain limits. General attractive forces cause the atoms to approach each other and to be as close to each other as possible. However the limiting factor opposing this movement is the orbitals of the outer electrons of each atom or ion. The orbitals cannot cross over each other. Now, with the exception of the electrons involved in electrical conductivity in metals, it is among the outer electrons where unpaired electrons are likely to occur, and it is these same electrons that give rise to the magnetic properties of the material.

Electron orbitals are normally depicted as circular, but this is only true for the smallest and simplest of atoms or for the innermost electrons in more complex atoms. In the magnetic materials of greatest interest the outer electron orbitals are highly unsymmetrical, being elongated in one direction and flattened in another.
Also in crystal lattices the distance between an individual atom or ion and its nearest neighbour depends on where that neighbour is. For atoms arranged in a rectangular pattern, the nearest neighbour is the next atom in the row, but the nearest in a direction at 90º to that row may be further away, and the nearest in a direction at 45º to the row is likely to be even further away, and so on. There is therefore in most crystal lattices scope for accommodating electron orbitals which are elongated in one direction.
It follows that there are directions which are specific to certain crystals where it is easy to magnetise the material, and, as a result small groups of atoms or ions tend to organise themselves spontaneously into magnetic domains where the spins and orbitals of unpaired electrons are all aligned. However the domains cannot be very large because of energy considerations. Unless an external magnetic field is imposed on the material, energy is minimised where there are a large number of domains present in a sample of material, with the magnetic field in each domain orientated in a different direction.

When an external magnetic field is created, the domains which are aligned most closely with the external field will grow while all other domains will be reduced in size [29]. Depending on the orientation of the crystal, there will be some cases where electron orbitals cannot become aligned to the direction of the external magnetic field without a change taking place in the distances between the atoms or ions. These distances must increase to allow the orbitals to become aligned. These changes in length may cause the crystal structure to become elongated in the same direction as the magnetic field, or to become elongated in one of more directions at right angles to this direction. In this last case, there may also be a contraction of the crystal in the same direction as the magnetic field.

2.5 Magnetic annealing of cobalt ferrites

The family of Cobalt ferrites with slightly different stoichiometries is known to respond to heat treatment in the presence of strong magnetic fields over long periods of time [1 - 2]. Figure 2.12 reveals the unit cell of the spinel lattice of cobalt ferrite [30 and 31]. The site that is being surrounded by a tetrahedral arrangement of oxygen ions is called A site, whereas the cobalt ions sites that are surrounded by six oxygen ions in the form of octahedral is called site B.

The magnetic moment of cations occupying octahedral sites (B sites) is antiparallel to that of cations in tetrahedral sites (A sites), and the magnetization is the net magnetic moment between the A site and the B site [32].Cobalt ferrite has the so-called inverse spinel structure, with one-half of ferrite ions on the A sites and the rest, together with cobalt ions, on B sites at room temperature [33]. The cation distribution of the cobalt ferrite however has been reported to be changed by heat treatment [34].

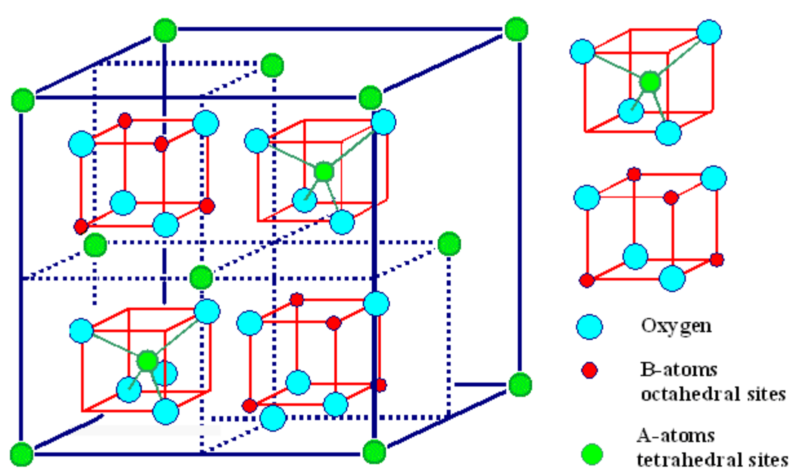

Figure 2.12: Unit cell of spinel lattice of cobalt ferrite [31]

During the annealing operation, the cobalt ions gain sufficient energy to change sites and orientations and to redistribute themselves among the tetrahedral and octahedral sites, and as a result, the domains which are aligned most closely with the external field will grow while all other domains will be reduced in size. Depending on the orientation of the crystal, there will be some cases where electron orbital cannot become aligned to the direction of the external magnetic field without a change taking place in the distances between the atoms or ions. These distances must increase to allow the orbital to become aligned, and as a result not only the domains on a temporary basis, but also the easy axis of magnetization on a more permanent basis, have a preferred direction which is parallel to the magnetic field. Also taking place is the more common annealing effect, in which creep at these temperatures relieves stresses, set up between non-aligned crystals.

A sample, which has been magnetically annealed, will show almost zero magnetostriction when placed in a magnetic field which is aligned along its easy axis of magnetization. It will also show almost no magnetostriction when the magnetic field is in the opposite direction. However when placed in a magnetic field whose direction is not aligned with either of these directions, its magnetostriction properties are significantly greater than would be true for a sample which had received no annealing treatment.

2.6 Measurements of magnetostriction

Magnetostriction measurement techniques can be broadly classified as either direct or indirect, depending on whether the strain is measured directly or the magnetostriction is deduced from a measurement of some other property dependent upon strain [35]. Direct methods enable the magnetostrictive strain to be measured as a function of the applied field, whereas indirect methods are suitable only for measuring the saturation magnetostriction λ_{sat}. Direct methods covered are measurements with strain gauges, capacitance dilatometer, tunnelling tip, and optical methods. The most common indirect methods are ferromagnetic resonance (FMR), small angle magnetization rotation (SMAR), and strain modulated ferromagnetic resonance (SMFMR).

2.6.1 Direct measurements

For crystalline materials, the use of strain gauges is the most common method; they are easy to handle, but limited in sensitivity. The most sensitive method is the capacitance method [35]. Direct methods require a special sample preparation. The most common techniques are:

a. Strain gauge method [36 - 41].

b. Three terminal capacitance dilatometer [42 - 46].

c. Optical interferometry [47 - 51].

d. Tunnelling tip dilatometer [52].

e. Laser method [53].

2.6.2 Indirect measurements

Indirect measurements are techniques based on the Villari effect, which is the inverse of Joule magnetostriction. A stress applied to a sample will produce a change in the magnetic permeability of that sample. These techniques are designated as indirect measurements of magnetostriction because they do not produce a direct measure of the sample length change. Several techniques based on this effect have been used in the measurement of magnetostriction. The most common techniques are:

a. Ferromagnetic resonance (FMR) [54].

b. Small-angle-magnetization rotation (SAMR) [55 - 56].

c. Strain modulated ferromagnetic resonance (SMFMR) [57].

2.7 Applications of magnetostriction

One advantage of magnetostriction transducers over other types is that their driving voltages can be very low which is useful in medical applications, and in general simplifies the amplifier design.

When a magnetostrictive material is subjected to an alternating magnetic field, the material vibrates at twice the frequency of that field, and this magnetostrictive vibration is the major source of humming sound emitted by transformer. Conversely, if a magnetostrictive material is mechanically vibrated, its magnetization will vary in magnitude because of the inverse magnetostrictive effect, and will induce an alternating emf in a coil wound around the material.

These two effects are exploited in magnetostrictive transducers which are capable of converting electrical energy into mechanical energy and vice versa.
Modern magnetostrictive materials such as Terfenol-D are manufactured with the magnetic moments nearly perpendicular to the rod axis; a mechanical preload is nevertheless required in order to achieve full alignment of all magnetic moments. A mechanically free rod has the magnetic moments aligned randomly and will only produce about half of its maximum magnetostriction and this is because of magnetic moments initially aligned with the rod axis do not contribute to the magnetostriction. The effect of prestress on the dynamic performance of a Terfenol-D transducer has been studied in [58].

2.7.1 Actuator applications

The commercial magnetostrictive material, which is most commonly used in actuation applications, is Terfenol-D. This is because in its performance a high conversion energy density, a large force and a fast response can be achieved over a broad frequency bandwidth. The main applications in actuation are presented below.

a. Sonar transducer

During and after second war, most sonar devices, for echo sounding to determine depth and locate other objects, used magnetostrictive elements (made from nickel alloys) to produce their sound. In order to produce sufficient motion, the magnetostrictive material in these devices is made to resonate by driving it with a pulse of a magnetic field (by passing a current pulse through a coil wrapped around the material) to give it a kick. This makes the material ring in the same way as any metal rod rings when hit with a hammer, and produces the characteristic ping of the sonar signal [59 - 62].

b. Linear motors

From the commercial point of view, there are three available sources of giant magnetostrictive materials (GMM): Etrema products, Inc. [63] found in 1988 produces rods with dimensions varying from 2 to 68 mm in diameter and from 6 to 250 mm in length. Gansu Tianxing Rare Earth Functional Material Co, Ltd (China) [64] found in 1988 produces rods with dimensions varying from 5 to 50mm in diameter and up to 200mm in length. MateriTek Co. Ltd (China) [65] is a third company producing GMM.

Kiesewetter motor produces 1000 N of force, 200 mm of useful stroke, and a speed of 20mm/s [66]. This type of motors is intended for uses such as control of coat weight and fiber distribution in paper industry or valve operation and precision positioners for the machine tool industry.

Energen, Inc. develops and manufactures actuators and linear stepper motors based on GMM. A linear actuator consists of a rod of magnetic material surrounded by an electrical coil. Energizing the coil, with electrical current causes the magnetic material to elongate in relation to the current amplitude. [67].

c. Rotational motors

Smart material motors utilize magnetostrictive materials because they are simpler, and, more reliable than conventional hydraulic or electromagnetic systems.
J. M. Varnish et al have demonstrated a device of the inchworm type which was highly successful in the achieving record torque output of 12.2 N.m for its size and in precision microsteps of 800 micro-radians [68].

In addition to high holding torques, such motors possess good position accuracy but their efficiency is very low which tends to limit their number of applications. Much of the efficiency limitation has been overcome in the resonant rotational motors proposed by Claeyssen et al [69]. This resonant magnetostrictive motor is reported to provide a maximum torque of 2 N.m and a maximum speed of 17 r.p.m.

d. Hybrid magnetostrictive/piezoelectric devices

This type of devices is based on combing a magnetostrictive material and piezoelectric material in the same device. This concept has been implemented for linear inchworm motors [70 - 72] and rotational motors.

2.7.2 Sensor applications

The term sensor is used in a broad sense to indicate the attributes of magnetostrictive materials which facilitate generation of electrical signal in response to mechanical excitation such as force or magnetic excitation such as magnetic field. The most common sensors are described below.

a. Torque sensor

Magnetostrictive non-contact torque meters are based on the principle that torque applied to a shaft generated stresses of opposite sign $+\tau$ and $-\tau$ oriented at $\pm 45°$ from the shaft axis. If the shaft is made of a magnetostrictive material, then the magnetic properties along the directions $+\tau$ and $-\tau$ will change, and can be measured by a set of perpendicular coils, or through a single hall effect or similar magnetic field strength sensor as shown figure 2.13(a) [73].This type of sensor usually employed in automotive and industrial applications. Figure 2.13(b) depicts another type of non contact sensor, in which the difference in output voltages from the two sensing coils varies in proportion to the applied torque in the cutting direction [74].

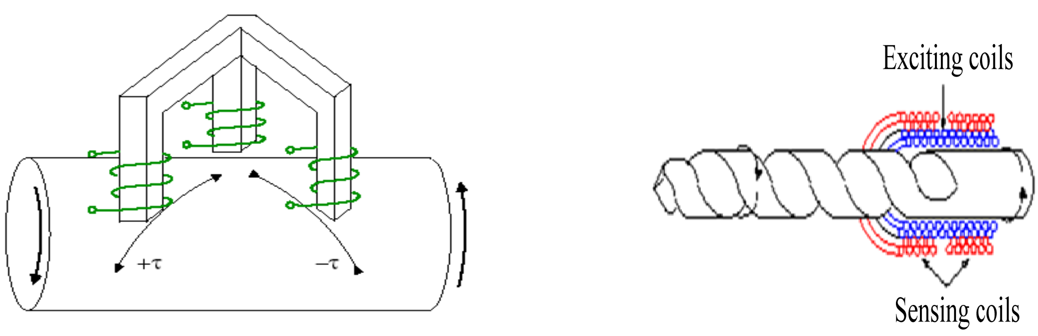

(a) (b)

Figure 2.13: Magnetostrictive non-contact torque sensors [26].

b. Position sensor

A magnetostrictive material can be employed as acoustic waveguide for position detection. Such a device is shown in figure 2.14.

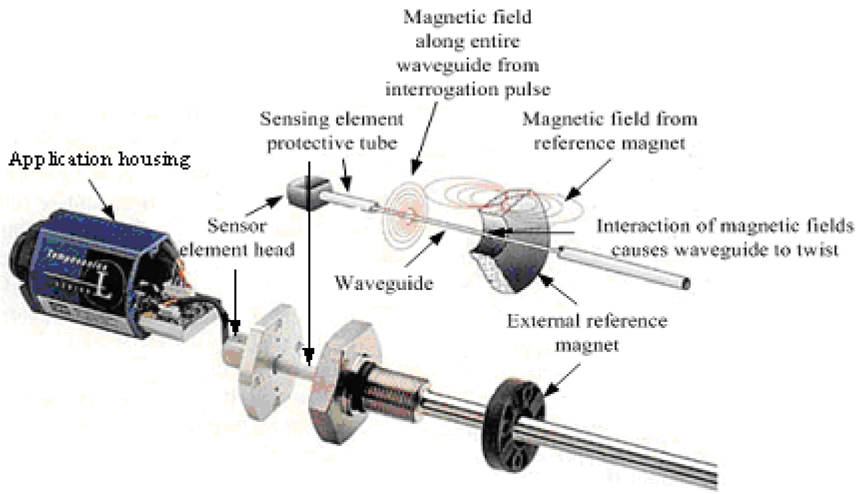

Figure 2.14: Magnetostrictive position sensor [75].

A pulse is induced in a waveguide by the momentary interaction of two magnetic fields, one from a reference magnet and the other from a current pulse launched along the waveguide. The interaction produces a strain pulse that travels along the waveguide and is detected at the sensor head. The position of the magnet is determined by measuring the elapsed time between the launching of the electronic pulse and the arrival of the strain pulse [76]. This type of sensor is usually used in fluid level measurements, medical application such as controlling hospital bed adjustment, positioning dental chair, and improving the durability of a wheelchair lift [77].

c. Force sensors

Force sensors are basically based on the Villari effect, which refers to the changes in magnetization that a magnetostrictive material undergoes when subjected to an applied uniaxial stress [26]. A simple design is illustrated on figure 2.15, which consists of two magnetostrictive elements, one surrounded by an excitation coil, while the other one surrounded by pick-up coil. Once an Ac voltage is applied to the excitation coil, a magnetic field will be generated in the coil, which is picked-up by the sensing coil. As an external force applied, changes in the magnetic flux will occur, which is sensed as a proportional voltage change in the pick-up coil. Also, to maintain a constant voltage at the pick-up coil, changes in the excitation voltage in relation to the applied force is required.

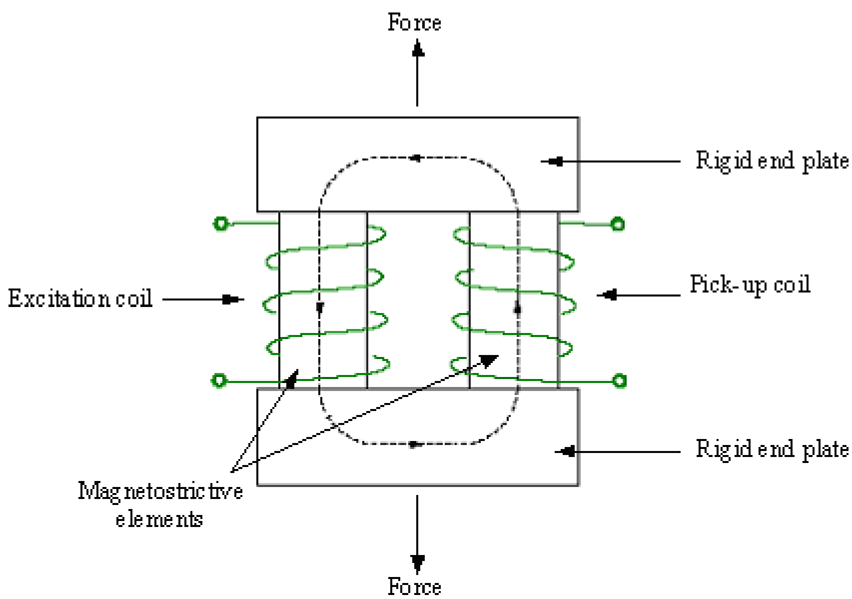

Figure 2.15: Force sensor based on magnetostrictive elements [26].

The advantage of force sensors over other conventional types is that they are simpler to design, more rugged, and require simpler electronic circuitry [26].

2.8 Summary of chapter 2

The general knowledge about magnetic materials, their behaviour and properties are discussed. Theory of magnetism is also discussed in some details. A description of the magnetostriction effects, and an explanation why it occurs and a list of a number of devices where the properties have been put to use, and a range of methods which have been used to measure these properties are also described. Finally a brief description about magnetic annealing of cobalt ferrite is also discussed.

CHAPTER 3

COIL DESIGN PROCEDURE

3.0 Introduction

Two alternative solenoid designs were developed: Firstly there was an air-core coil design where the coil was built around a spool with only air inside the spool and secondly a C-shape coil design where coils were built around a magnetic material and this magnetic material was arranged to form a C shape. The coils were designed to be capable of generating strong and static magnetic fields in various samples of magnetic materials. In the case of the first design, the sample would be placed in the central air space. In the second design, the sample would be placed in part of the "jaws" of the "C" shape, so that the magnetic circuit would be made nearly complete by the insertion of the sample. It was intended that either of the rigs would be used firstly to cause magnetic annealing and then to measure the magnetostriction strain of annealed cobalt ferrite and Terfenol-D based materials, and to do this, it was thought that magnetic flux densities of the order 1.6 tesla would be needed in the air-gap. However after carrying out preliminary calculations for the air-core design, it was realized that very high electrical currents (38kW) would be required, with the result that complex systems would be needed to remove the heat being generated. This design was therefore abandoned. Detailed descriptions of the air-core coil design can be found in appendix A.

3.1 C-shape coil design

This design was comprised of a C-shape structure designed to generate strong magnetic field strengths. The sections of the C-structure were individual solenoids made from copper-wound low carbon steel. These sections were connected such that the overall structure formed a continuous conduit for the magnetic flux and concentrated the magnetic field into an air gap. The sample being tested was placed in the "jaws" of the C-shaped, and completed the magnetic circuit. A cooling system, which was composed of copper tubes, was required to minimize the effect of the heat generated in each coil. Air was forced through the tubes. Figure 3.1 shows the construction of the C-shaped coil.

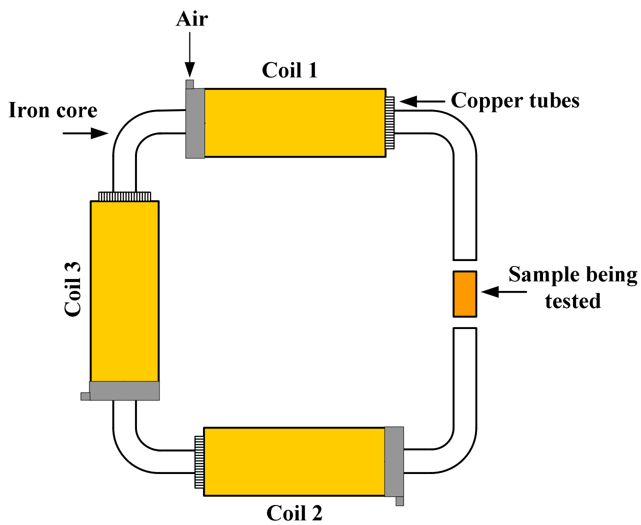

Figure 3.1: Construction of the C-shaped coil design.

3.1.1 C-shape design concept

To generate large and concentrated magnetic fields, a coil of N turns can be constructed by wrapping a conductor around an iron core. The magnetic field strength was directly proportional to the number of turns as well as the current it carries. The magnetic field around each turn of wire links with the fields produced in the adjacent turns when a current passes through the coil. The combined influence of all the turns produces a two pole field similar to that of a simple bar magnet. One end of the coil is a north pole and the other end is a south pole.

There can be a thousandfold increase in the efficiency involved in the generation of a magnetic field if the coil was wrapped around a core made of iron [6]. Iron was said to guide a magnetic flux around a circuit, analogous to the way in which a copper conductor conducts an electric current around a circuit.

In order to provide a magnetic flux density B in the air gap, a certain number of ampere-turns ($N \times I$) were required in the winding [6].

3.1.2 Choice of the magnetic materials to be used for most of the components of the C-shape

A selection must be made for magnetic material to be used as the core in the C-shaped circuit.

a. The core material

The initial C-shape circuit design consisted of three separate coils wound around core made from a low-carbon steel material (30 mm in diameter). The magnetic properties of this type of material are illustrated in figure 3.2. This type of material usually saturates at approximately 2.3 T [78].

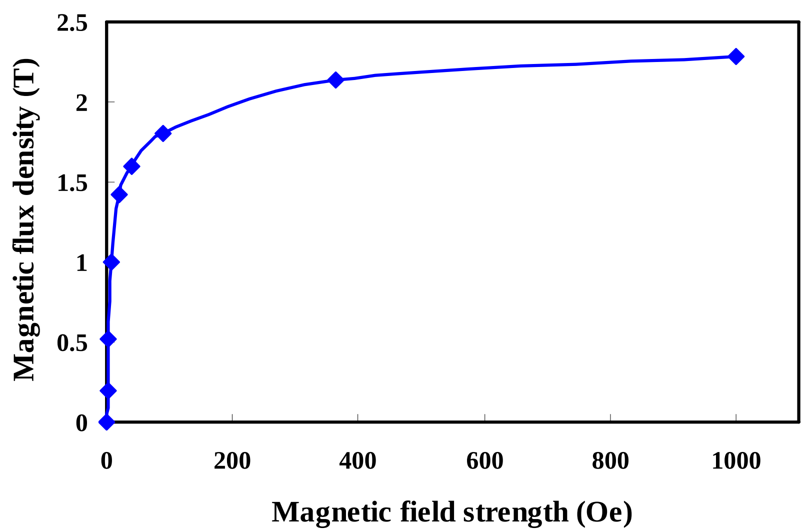

Figure 3.2: Magnetic properties of 1020 low carbon steel [78].

b. Materials used in the air gap

Three different materials have been used in the experimental measurements and simulation. These samples were cobalt ferrite which was prepared in-house [79], Terfenol-D ($Tb_{0.27}Dy_{0.73}Fe_2$) (Etrema Ltd., USA) [63], and low carbon steel (Impact Ireland Metals Ltd) [80]. All samples were cylindrical rods measuring 50 mm in length and 30 mm in diameter as shown in figure 3.3.

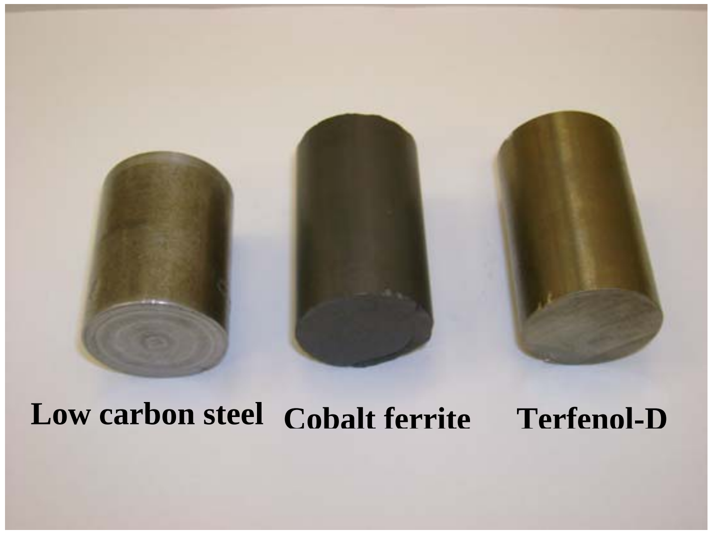

Figure 3.3: Picture of surface detail of the 1020 low carbon steel, cobalt ferrite ($CoFe_2O_4$), and Terfenol-D ($Tb_{0.27}Dy_{0.73}Fe_2$) samples.

c. Corners

Three different corners have been used in the experimental measurements and simulation to form a continuous conduit for the magnetic flux. These corners were gradual curved corners made of 1020 low carbon steel, abrupt right-angle corners made of 1020 low carbon steel, and large-diameter component with circular cross-sections made of pure iron. A picture of these corners is shown in figure 3.4.

(a)

(b)

(c)

Figure 3.4: Picture of surface detail of the gradual curved, abrupt right-angle, and large-diameter component with circular cross-sections corners.

3.1.3 Air-gap considerations

During magnetostrictive strain testing and magnetic annealing, a cobalt ferrite, sample would be held in the space between the "jaws" of the C-shaped. For this reason, the magnetic properties of the cobalt ferrite sample would play a large part in determining the magnetic field strength which would be formed in the "jaws" of the C-shaped.

It was assumed as an initial hypothesis that the flux in the iron core had the same value as the flux in the air gap and in the sample. This was equivalent to the assumption that there was no flux leakage. Therefore, if both the sample and the iron core had the same diameter, the flux density was also the same. If the air gap was very narrow in comparison to this diameter, the flux density B in the air gap was approximately the same also. However, the magnetic field strengths in the air gap and in the iron core were different. They were related to the energy required to establish the magnetic flux and in iron this energy was very much smaller than that required in air. Applying Ampere's circuital law of magnetism [9]

$$N \times I = \oint H dl \tag{3-1}$$

where N is the number of turns in the coil, I is the current, H is the magnetic field strength and l is the length of each component in the circuit. Splitting the circuit into its component parts

$$N \times I = \oint H dl = (H_c \times l_c) + (H_g \times l_g) + (H_s \times l_s) \tag{3-2}$$

where the subscripts c, g and s refer to the iron core, the air gap and the sample being tested, respectively. But by definition

$$H_c = \frac{B}{\mu_{r_c} \times \mu_o} \tag{3-3}$$

$$H_g = \frac{B}{\mu_o} \tag{3-4}$$

$$H_s = \frac{B}{\mu_{r_s} \times \mu_o} \tag{3-5}$$

where

$B =$ Magnetic flux density

μ_r is the relative permeability

μ_{r_g} = Relative permeability of air in the gap, assumed to be equal to 1

μ_o = Permeability of free space = $4\pi \times 10^{-7}$

If flux leakage was neglected, B would be constant. It follows that

$$N \times I = \frac{B}{\mu_o}\left[\left(\frac{l_c}{\mu_{r_c}}\right) + l_g + \left(\frac{l_s}{\mu_{r_s}}\right)\right] \tag{3-6}$$

It was a requirement of the test system being developed, that the sample being tested (50 mm in length by 30 mm in diameter) should experience a magnetic field strength of 9,000 Oe, which is equivalent to 716 kA/m. However to carry out the design it was necessary to know the magnetic properties of the cobalt ferrite sample at this magnetic field strength. Ideally, these properties should be measured by experiment. If the flux density, *B* in the sample could be measured when a magnetic field strength of 9,000 Oe was generated, a value for *B* could be determined. Then the relative permeability of the sample material could be estimated using the following formula

$$\mu_{r_s} = \frac{B}{H_s \mu_o} \tag{3-7}$$

Also, once the flux density, *B*, had been estimated, experimental data could also be used to provide an estimate for the relative permeability of the specific iron alloy used to make the core at the required flux density. This gives a value for μ_{r_c} .

3.1.4 Estimation of magnetic properties of cobalt ferrite

The cobalt ferrite sample has been analyzed by the Cedrat Company to provide the hysteresis loop *B-H* curve [81]. A sample of this data is shown in appendix B.

The *B-H* curve given by Cedrat Company goes through the points, from 129.360512 kA/m down to -129.883392 kA/m and its *B*'s counterpart values were 0.472610652 T down to -0.486498833 T. However since 9000 Oersteds was required in the design, it was essential to estimate the value of *B* where *H* is 9000 Oe (716.197 kA/m), by extrapolating from this data.

The data received from Cedrat has values with a large statistical scattering as shown in figure 3.5(a). This data was first put in ascending order then averaged, so that the data was arranged from the lowest negative point to the highest positive point as illustrated in figure 3.5(b), and the small hysteresis effect was removed. It can still be improved by selecting the first 100 data points, adding them together and dividing by

100, then selecting points 2 to point 101, adding them and dividing by 100 again and so on. When this was done the scattering was reduced considerably as depicted in figure 3.5(c).

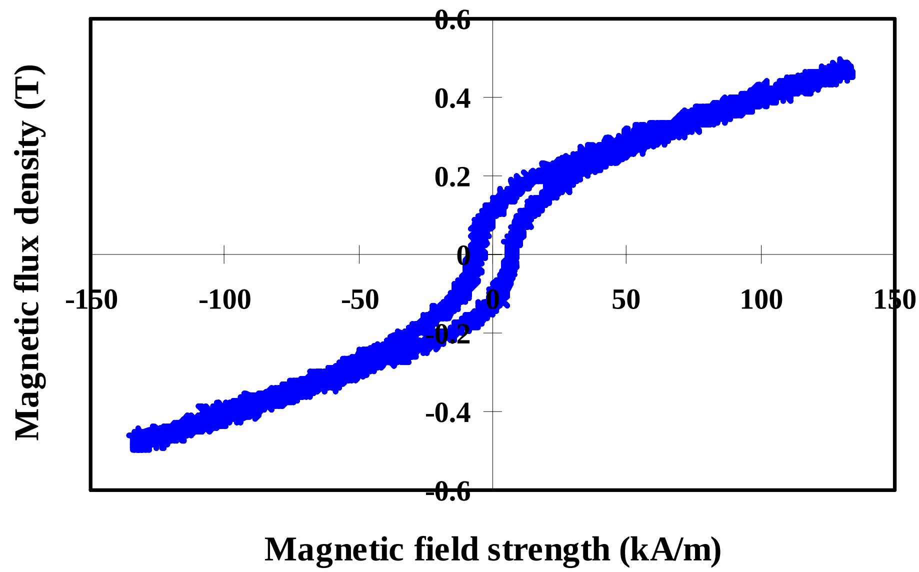

(a)

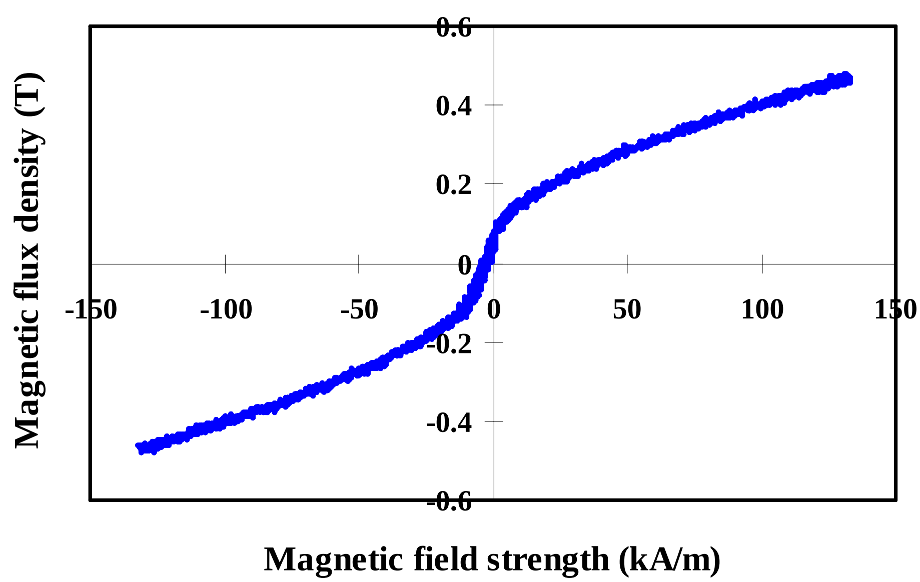

(b)

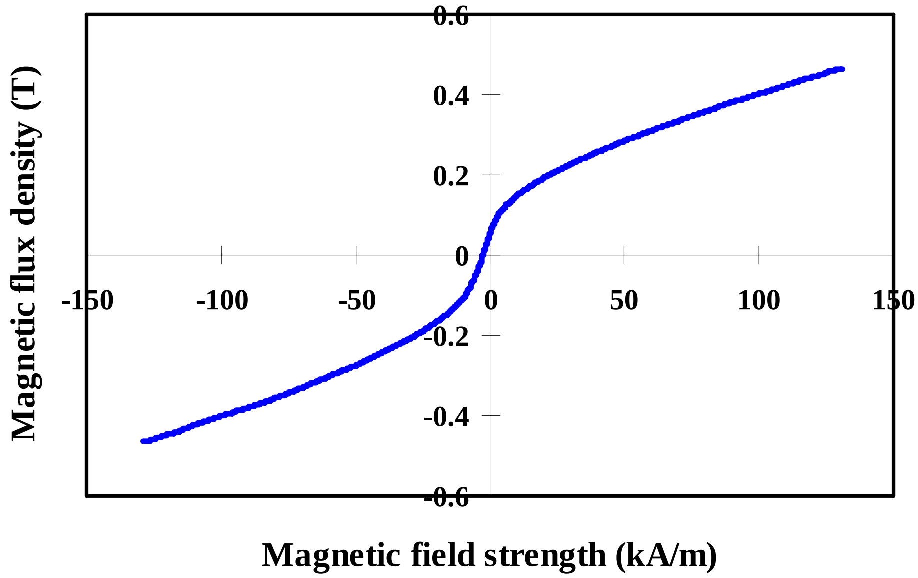

(c)

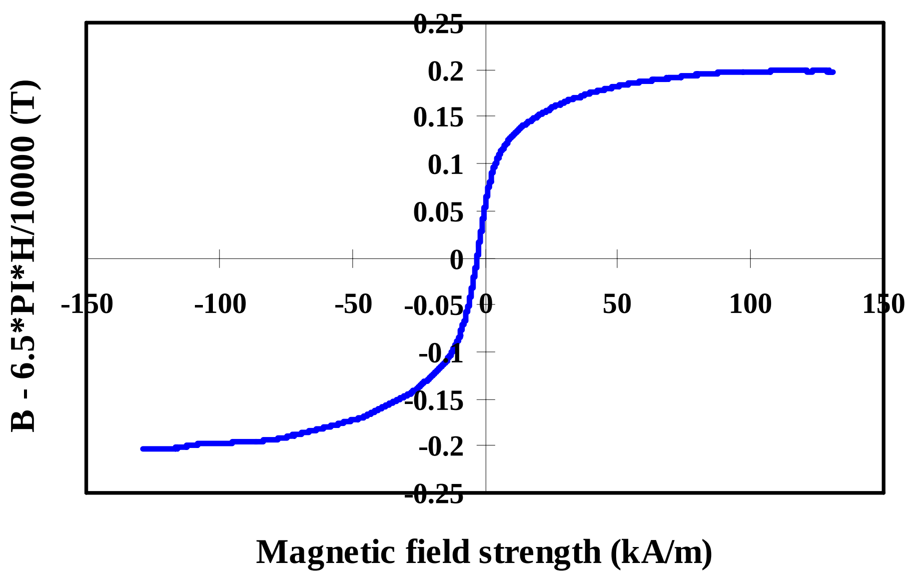

(d)

Figure 3.5: Manipulation of *B-H* data for cobalt ferrite sample.

It was normally assumed that as the values of flux density were increased well above the values in the data, they would follow a line parallel to the *B-H* curve for free space. Therefore, if the values for *B* in tesla were modified by subtracting the contribution of free space to the flux density, the data for high values of flux density should follow a line parallel to the x axis. Results are listed in appendix C. The best result is illustrated in figure 3.5(d).

The extrapolation was based on the equation $\frac{M}{M_s} = \coth(AH) - \frac{1}{AH} = f(H)$, where M is the magnetization, M_s is the saturation magnetization, H is the magnetic field strength, and A is a constant. This is called the Langerin function. It can be derived theoretically for paramagnetic materials but it gives quite good results even for ferromagnetic materials [82].

It is shown in figure 3.6 (a). All data points fall between -1 and +1. It can be modified by inserting a multiplying factor to make it appropriate to the *B-H* relationship for cobalt ferrite. When this was done, curve 3.6 (b) was obtained.

However this did not work out for the data obtained from Cedrat. In fact a much better fit was obtained by subtracting $6.5\pi \times \frac{H}{10000}$ (where H is in Oersteds) than $4\pi \times \frac{H}{10000}$. One can speculate that this result was due to the complicated magnetic structure of cobalt ferrite, where the magnetic effects of some of the ions partially compensate for the opposite magnetic effects of other ions. This might suggest a two-stage magnetic saturation relationship. After the first-stage magnetic saturation, the *B-H* curve might follow a permeability relationship of $6.5\pi \times 10^{-7}$, and only after the second-stage saturation, the curve would follow the more normal $4\pi \times 10^{-7}$ relationship. There was no way of knowing were the second magnetic saturation might occur and therefore the only approach possible was to extrapolate the data available and assume the $6.5\pi \times 10^{-7}$ relationship extended to values of the magnetic field strength of 9000 Oersteds. Details of curve fitting processing are provided in appendix D.

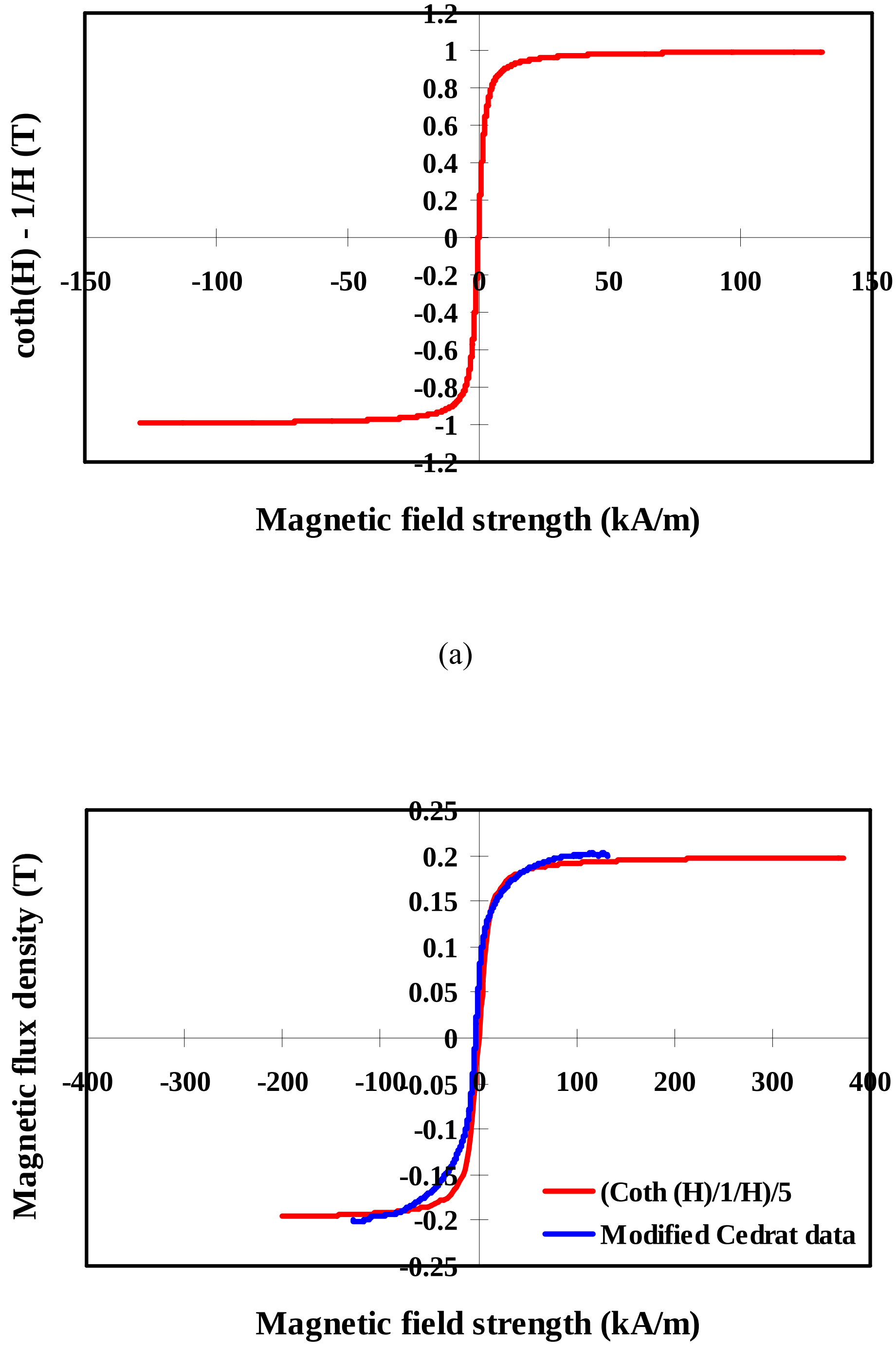

(a)

(b)

Figure 3.6: Curve fitting of *B-H* data for cobalt ferrite.

Therefore values for B can be calculated as follows

$$B = \frac{\coth(H) - \frac{1}{H}}{5} + 6.5\pi \times H/10{,}000 \text{ T} \tag{3-8}$$

The specific value for B at a magnetic field strength of 716.197 kA/m can be estimated as follows

$$B = \frac{\coth(716.197) - \frac{1}{716.197}}{5} + 6.5\pi \times 716.197/10{,}000 = 1.662221\,\text{T} \tag{3-9}$$

From this extrapolation, it was estimated that the flux density B in the sample must reach a value of 1.662221 T when the magnetic field strength was 9,000 Oe. This value was used to calculate estimates for the permeability and relative permeability. Since these values were only extrapolated from experimental data and were not actual experimental data, they introduced some uncertainty into the design procedure. It was only by actually building the equipment and measuring the magnetic properties that the system can be made to provide the conditions specified as the design criteria. However, it was anticipated that there would be scope in the design to modify the factors producing the magnetic field strength, for instance by increasing or decreasing the current in the coil. Therefore, it was expected that the equipment could be modified to realise the design requirements. Applying the flux density value, B, the magnetic field strength in the air gap would be

$$H_g = \frac{B}{\mu_o} = \frac{1.662221}{4\pi \times 10^{-7}} = 1322.7534\,\text{kA/m} \tag{3-10}$$

From the literature (1020 low carbon steel B-H data), the magnetic field strength required to produce a flux density of 1.662221 T in the iron core was about 4300 A/m [78]. This gives the permeability of the iron to be

$$\mu_c = \frac{B}{H} = \frac{1.662221}{4300} = 0.000387 \text{ Tm/A} \tag{3-11}$$

It follows that the relative permeability of the iron core is:

$$\mu_{r_c} = \frac{\mu_c}{\mu_0} = \frac{0.000387}{4\pi \times 10^{-7}} = 307.6171 \qquad (3\text{-}12)$$

Permeability of the cobalt ferrite sample can be calculated as follows

$$\mu_s = \frac{B}{H} = \frac{1.662221}{716197} \qquad (3\text{-}13)$$

It follows that the relative permeability of the cobalt ferrite is:

$$\mu_{r_s} = \frac{\mu_s}{\mu_o} = \frac{1.662221}{716197} \times \frac{10^7}{4\pi} = 1.8469 \qquad (3\text{-}14)$$

3.1.5 Estimation of electrical current and number of turns

The straight sections of the core were 814 mm, 814 mm, 815 mm and 815 mm. Each of the corners was identical, and the centre-line of each corner was 142.5 mm long. The total length of the core was therefore 3,828 mm.

The ampere-turn $N \times I$ required by the system was also an important consideration. Calculation of this parameter was carried using equation (3-6). Results presented in table 3.1 show that the higher the number of turns the lower the current required. Also, the lower the length of the core, the lower the current required. An energy efficient solution for the system to achieve 9000 Oe was to have 24,000 turns, and a core length of 3.828 meters.

Values were thus available to complete the right-hand side of equation (3-6), since l_c = 3.828 m, l_s = 0.05 m and l_g = 0.002 m. Input of these geometric values therefore allows an estimate for the left-hand side of equation (3-6), to be arrived at, where $N \times I$ was the product of the current and the number of turns in the coil.

Table 3.1: Calculation of number of turns and current required by the system.

Length of iron core (m)	No. of turns	$N \times I$ (Ampere-turn)	Current (Amps)
1	9000	42755.6	4.750623
	15000	42755.6	2.850374
	18000	42755.6	2.375311
	24000	42755.6	1.781484
2	9000	47055.6	5.2284
	15000	47055.6	3.13704
	18000	47055.6	2.6142
	24000	47055.6	1.96065
3	9000	51355.6	5.706178
	15000	51355.6	3.423707
	18000	51355.6	2.853089
	24000	51355.6	2.139817
3.828	9000	54916	6.101778
	15000	54916	3.661067
	18000	54916	3.050889
	24000	54916	2.288167

As an example, the total number of turns has already been established at 24,000, and so the current I can be estimated. Therefore, the ampere-turns $N \times I$ required by the system can be calculated as follows

$$N \times I = = 1322.7534 \times 1000 \left(\frac{3.828}{307.6171} + 0.002 + \frac{0.05}{1.8469} \right) = \quad (3\text{-}15)$$

54916

It follows that the current I is

$$I = \frac{54916}{24000} = 2.2882 \text{ Amps} \quad (3\text{-}16)$$

This calculation, however, was not complete until the power requirements of the system have been estimated, and this depends on the value of the total resistance of the copper wire in the coils which was carried out in the next section.

Rather than continuously wind 24,000 turns around the iron core, it was more practical to construct three individual coils, each consisting of 8000 turns. The windings were constructed in 10 layers with 800 turns in each layer. The coils were made from polyurethane-coated copper wire described in table A.1 in appendix A. Winding of the wire was carried out using a computer numerical control (CNC) lathe machine. A schematic of one coil is illustrated in figure 3.7.

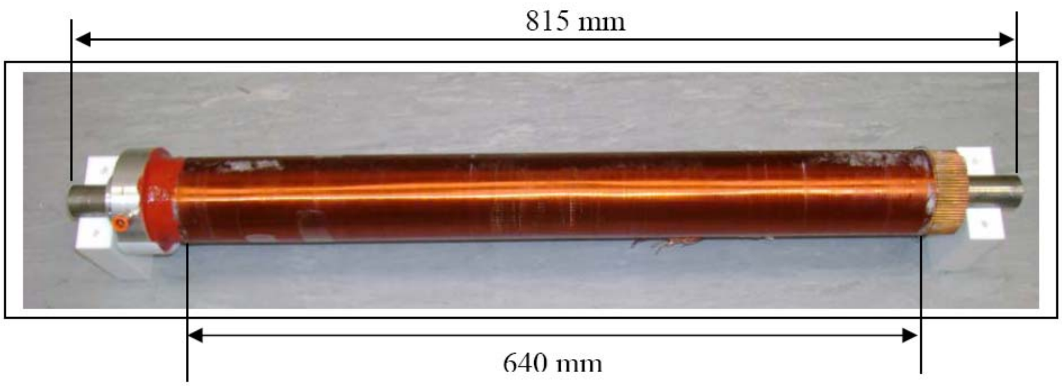

Figure 3.7: Dimensions of one coil.

3.1.6 Estimation of electrical resistance of copper wire

The resistance of each layer in each coil can be calculated using the following formulae

$$R = \frac{\rho \times l}{A} \tag{3-17}$$

where: ρ is the resistivity, l is the length of wire in each layer, and A is the cross sectional area of copper wire.

Table 3.2 shows the length of wire in each layer as well as the resistances of each layer at room temperature. The total length of wire needed to form one coil was about 1326 meters.

Table 3.2: Length of copper wire of each layer in one coil.

Layer No.	**Radius (m)**	**Circumference (m)**	**Length of 800 turns (m)**	**R when ρ @ $20°C$**
1	0.0154	0.0967	77.3485	3.2821
2	0.0192	0.1204	96.3288	4.0875
3	0.0199	0.1253	100.2294	4.2530
4	0.0237	0.1490	119.2096	5.0584
5	0.0245	0.1539	123.1102	5.2239
6	0.0283	0.1777	142.0905	6.0293
7	0.0290	0.1825	145.9911	6.1948
8	0.0328	0.2062	164.9713	7.0002
9	0.0336	0.2111	168.8719	7.1657
10	0.0374	0.2348	187.8522	7.9711

To estimate the total resistance of each coil, layers in each coil can be connected either in series, in parallel or in a combination of both, a semi series/semi parallel arrangement.

a. Series connection

If the10 layers in each coil were connected in series, then the total resistance would be given by

$$R_T = R_{l_1} + R_{l_2} + R_{l_3} + R_{l_4} + R_{l_5} + R_{l_6} + R_{l_7} + R_{l_8} + R_{l_9} + R_{l_{10}} \qquad (3\text{-}18)$$

The total resistance in each coil would be about 56.266Ω, and the potential difference across the coil would be about 129.4 V if, for instance, the current was 2.3 Amps. If the three coils were connected in series the total potential difference would be 388.2 volts.

b. Semi series / semi parallel arrangement

To simplify calculations it was necessary to ensure that each layer in each coil would receive the same amount of current (2.2882 Amps). The wiring arrangements shown in figure 3.8 fulfil this requirement because

$R_{AF} = R_{l_1} + R_{l_{10}} = 11.2532\Omega$

$R_{BG} = R_{l_2} + R_{l_9} = 4.0875 + 7.1657 = 11.2532\Omega$

$R_{CH} = R_{l_3} + R_{l_8} = 4.2530 + 7.0002 = 11.2532\Omega$

$R_{DI} = R_{l_4} + R_{l_7} = 5.0584 + 6.1948 = 11.2532\Omega$

$R_{EJ} = R_{l_5} + R_{l_6} = 5.2239 + 6.0293 = 11.2532\Omega$

This proves that $R_{AF} = R_{BG} = R_{CH} = R_{DI} = R_{EJ}$, and so all sections of the coil have the same current.

Therefore, the total resistance of each coil would be

$$\frac{1}{R_{total}} = \frac{1}{R_{AF}} + \frac{1}{R_{BG}} + \frac{1}{R_{CH}} + \frac{1}{R_{DI}} + \frac{1}{R_{EJ}} = 0.44432\Omega^{-1} \tag{3-19}$$

Therefore $R_T = 2.25064\ \Omega$ for one coil. For Three coils $R_T = 6.7519\ \Omega$

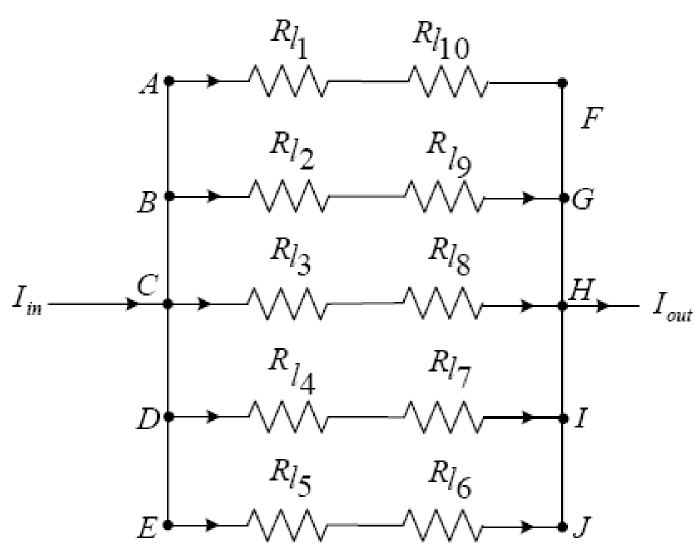

Figure 3.8: Semi series / semi parallel wiring arrangement.

Resistivity of copper increases with temperature. A temperature correction can be made using the following relationship for moderate temperature differences

$$\rho = \rho_{r.t.}\left[1+\alpha\left(T - T_{r.t.}\right)\right] \tag{3-20}$$

where: T is the temperature in centigrade, and the subscripts *rt*. indicates the resistance at a reference temperature

$\rho_{r.t.} = 1.78 \times 10^{-8}\,\Omega m$

$T_{r.t.} = 20°C$ = reference temperature

$\alpha = 0.00381°C^{-1}$ = temperature coefficient of resistance of copper at 20°C

The apparatus was designed to have a maximum working temperature of about 150°C; the resistivity at that temperature can be calculated using equation 3-20:

$$\rho = 1.78 \times 10^{-8}\left[1+0.00381(150-20)\right] = 2.661634 \times 10^{-8}\,\Omega m \tag{3-21}$$

Inserting the new value of Resistivity, this altered the value of the resistance of each layer. The new values are shown in table 3.3.

Table 3.3: Changes in resistance values due to changes in temperature.

Layer No.	**R when** ρ **@** $150°C$	**R when** ρ **@** $20°C$
1	5.1999	3.2821
2	6.4759	4.0875
3	6.7381	4.2530
4	8.0141	5.0584
5	8.2763	5.2239
6	9.5523	6.0293
7	9.8145	6.1948
8	11.0905	7.0002
9	11.3527	7.1657
10	12.6287	7.9711

Therefore the total resistance of the system would be

$$\frac{1}{R_{total}} = \frac{1}{R_{AF}} + \frac{1}{R_{BG}} + \frac{1}{R_{CH}} + \frac{1}{R_{DI}} + \frac{1}{R_{EJ}} = 0.09348\Omega^{-1} \tag{3-22}$$

Therefore $R_T = 10.6972\Omega$

The total current, and power required by the system would be

$$I_{in} = I_{out} = 5 \times 2.2882 = 11.441 \text{ Amps} \tag{3-23}$$

The power is equal to

$$(11.441)^2 \times 10.6972 = 1400.2258 \text{ watts} \tag{3-24}$$

Potential difference across all the coils is equal to

$$11.441 \times 10.6972 = 122.3867 \text{ volts} \tag{3-25}$$

The series connection arrangement was ruled out in favour of semi-series / parallel, as the latter arrangement gave a lower potential difference across each coil. This was a safer arrangement. This analysis suggests that the rig can be a practical solution because its length, coil winding, current, voltage and power were not excessively large or expensive.

3.1.7 The Cooling system and the controls associated with it.

To minimise the effect of heat generated in each coil, it was necessary to insert layers of copper tubes with outside diameters of 3 mm between every two layers of windings as shown in figure 3.9.

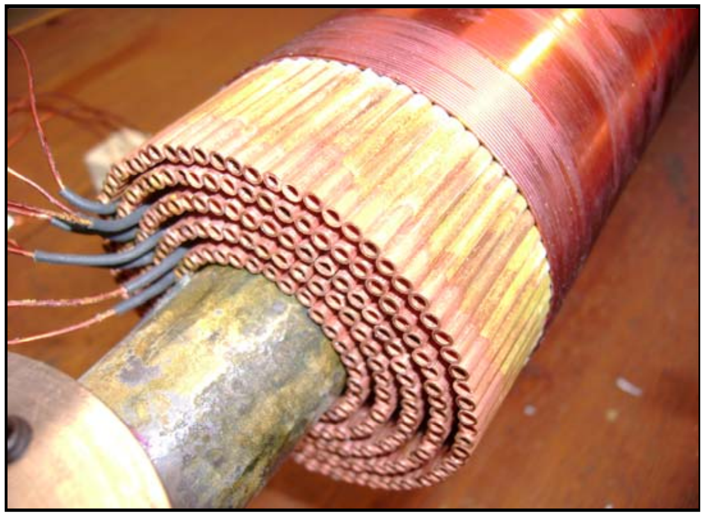

Figure 3.9: Distribution of copper tubes.

Compressed air was forced through the tubes at a pressure of 4 bar. In each coil, two temperature probes (thermocouple type K) were positioned; one between the first and second layer of windings, and the other probe between the fifth and sixth layer. The temperature probes were interfaced with an NI PCI_6024E data acquisition card (DAQ) and Lab-View software. This DAQ card was used to export the temperature data, and also to control the current which was fed to the coils. A schematic diagram of the proposed experimental set-up is depicted in figure 3.10.

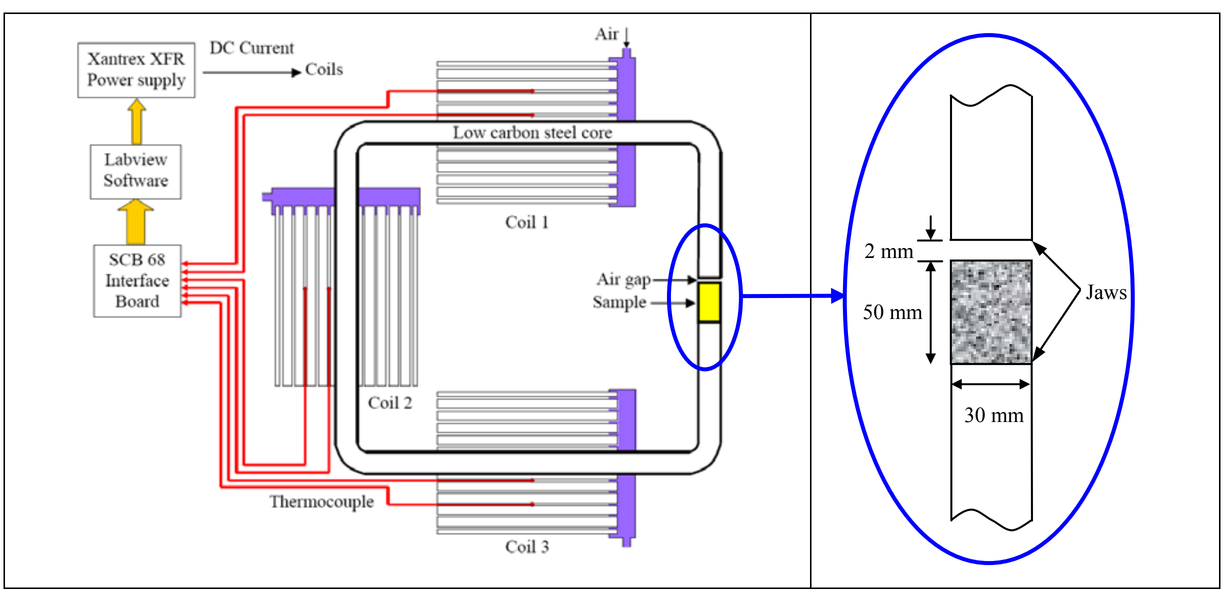

Figure 3.10: Proposed experimental set-up.

3.1.8 Adopted design of C-shaped coil

The adopted design of “C-shaped” coil was mainly composed of the following:

- Four sections of one meter long low carbon mild steel type 1020 arranged to form C-shape.

- Three coils, where each coil consisted of 8000 turns, so the total number of turns was 24000 turns. Each coil was based on 10 layers of windings with 800 turns in each layer.

- Five layers of copper tubes in each coil were used as an air cooling system, in order to minimise the effect of heat generated in each coil.

- To continuously monitor the temperature of each coil, it was essential to use at least two thermocouples in each coil, one inserted at the centre of the first layer, and second one at the centre of the coil.

- Semi series / parallel wiring as shown in figure 3.8 was used to wire the layers of the three coils.

3.1.9 Advantages and disadvantages of C-shape coil design

The “C” Shaped coil design has the following advantages:

- Less power consumption, and therefore less heat generated in the coils.

- It consumed less copper wire compared to “Air-core” coil design.

- Easier to implement copper tubes for cooling system.

- Easier in winding the copper wire around the iron core.

One disadvantage of the system was the difficulty in measuring the magnetostriction coefficient using the displacement laser sensor. However a strain gauge method could be used instead.

3.2 Summary of chapter 3

The C-shape coil design was described in some detail, and the advantages and disadvantages of this design has been listed. The intended practical work would be carried out using the C-shaped coil design which would require less electrical power, and an adequate cooling system capable on minimizing the effect of heat generated by the coils.

CHAPTER 4

EXPERIMENTAL PROCEDURE AND RESULTS

4.0 Introduction

The first sections of this chapter describe the hardware setup, process layout, and the electrical and mechanical components utilized in the experimental work. Moreover, the control of the system is also explained. Preliminary tests and a required modification of the system are also explained.

Finally, different experimental procedures are described for each testing system, and overall processes are summarized at the end of this chapter.

4.1 Process layout

The process layout is shown in figure 4.1. The system was processed using a controlling PC. The PC was used to automatically control the current supplied to the coils. This was established via RS232 communication between the PC and Xantrex$_{TM}$ power supply. It was also used to continuously monitor the temperature rise of the system.

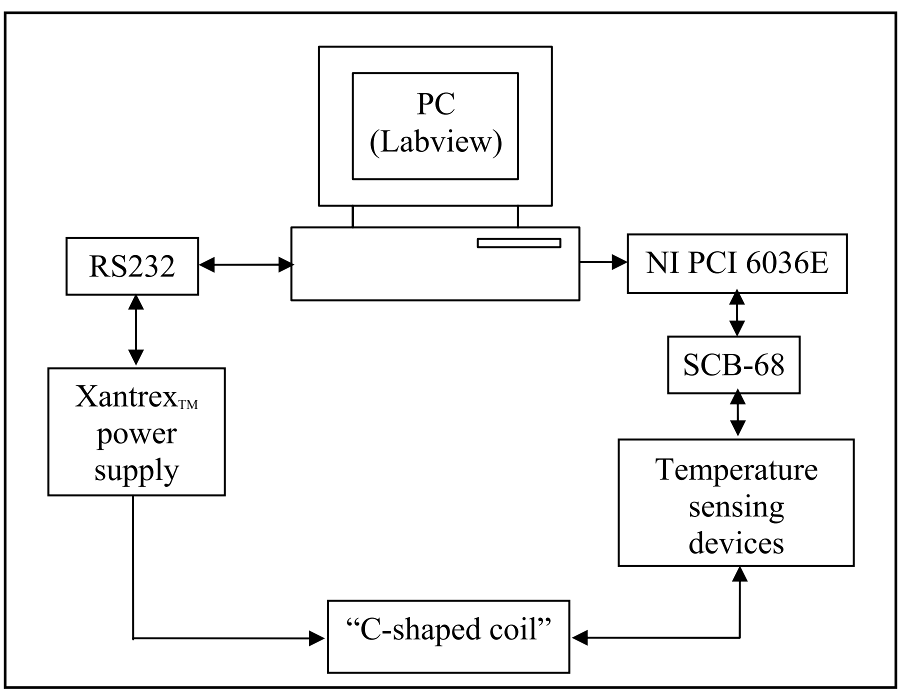

Figure 4.1: The complete system components.

4.2 Electrical and mechanical components used

This section discusses the electrical components, and mechanical components utilised in the practical work.

4.2.1 Electrical components

1. DC power supply

Xantrex$_{TM}$ XFR 150v, 18 Amps DC power supply (figure 4.2) was used in the experimental work [83]. It was provided with RS-232 interface card, which gives remote digital control of the system as illustrated in figure 4.3.

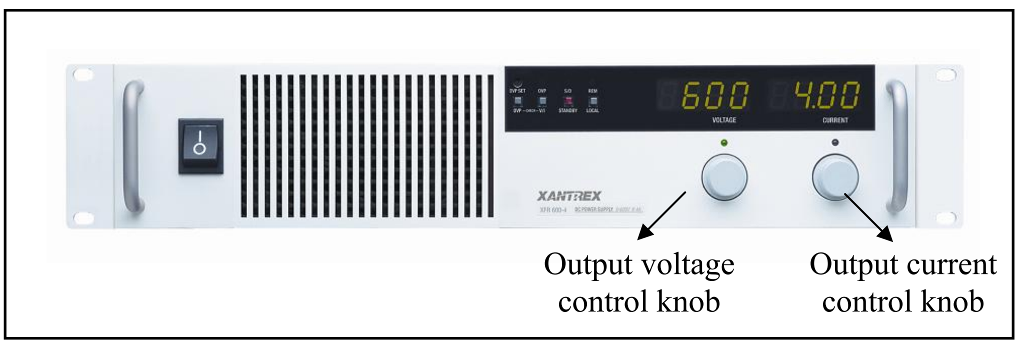

Figure 4.2: Xantrex$_{TM}$ power supply front panel.

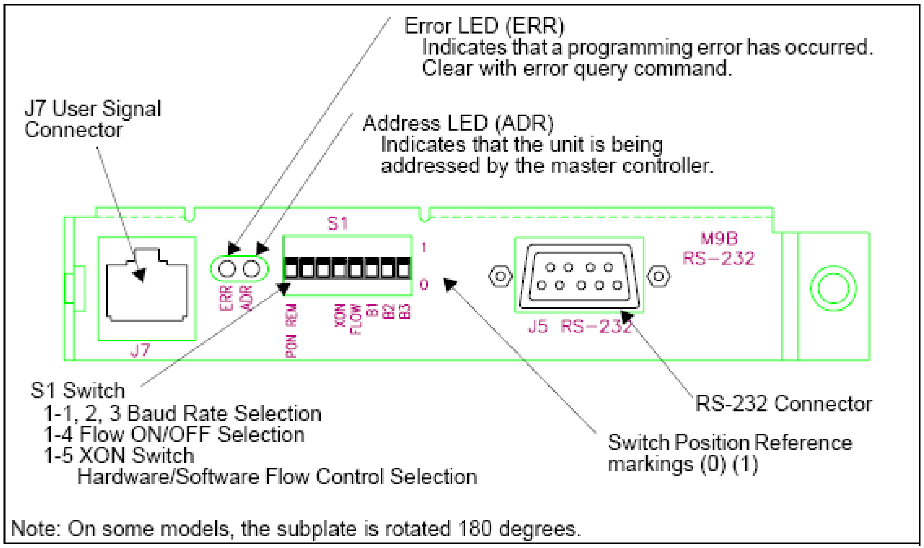

Figure 4.3: RS-232 interface subplate (located on power supply rear panel).

The PC used was a Dell with a P4 processor and Windows XP as the operating system. Xantrex$_{TM}$ DC power supply was connected to the PC via the RS232 communication cable. The RS232 port on the power supply was designed to plug directly into the computer. Communication set up procedure is described as follows:

Serial Port Configuration

Serial transmission sends and receives data in bit streams at fixed bit rates. Both the computer and the interface must have the same bite rate setting for the communication to properly take place. Switches B_1, B_2, and B_3 on the rear panel S_1 switch are set tot 1 in order to have 9600 baud rate (transmission speed).

Flow Control selection

Flow control signals regulate data flow for proper communication. Flow switch on the rear panel S_1 switch was set to “disable flow control”. With flow control enabled either software or hardware protocols can be used to control flow rate. The data flow was “hardware flow controlled”.

RS-232 pin connections

9-pin (DB9) to 9-pin parallel cable was used to connect the interface card to the serial port of the host computer. Pin configuration is shown in table 4.1.

Table 4.1: Transmit/receive pin connections.

Host DB-9	Signal	Description	RS-232
2	RXD	Receive Data	2
3	TXD	Transmit Data	3
5	GND	Ground	5

Communication with Xantrex$_{TM}$ XFR power supply

An instrument driver was developed for Xantrex$_{TM}$ XFR, XHR, XPD, HPD, XT products by National instrument [84]**.** This instrument driver is a set of high-level functions that control and communicate with Xantrex$_{TM}$ power supply hardware using Labview software package. Each of these high level functions provides some functionality on the instrument ranging from initialization and configuration to triggering and acquisition. Figure 4.4 illustrates the front panel of this driver.

Initial values of the operation parameters such as voltage and current can be set on the front panel of the driver, and correspondingly the Xantrex$_{TM}$ power supply will provide the desired current or voltage.

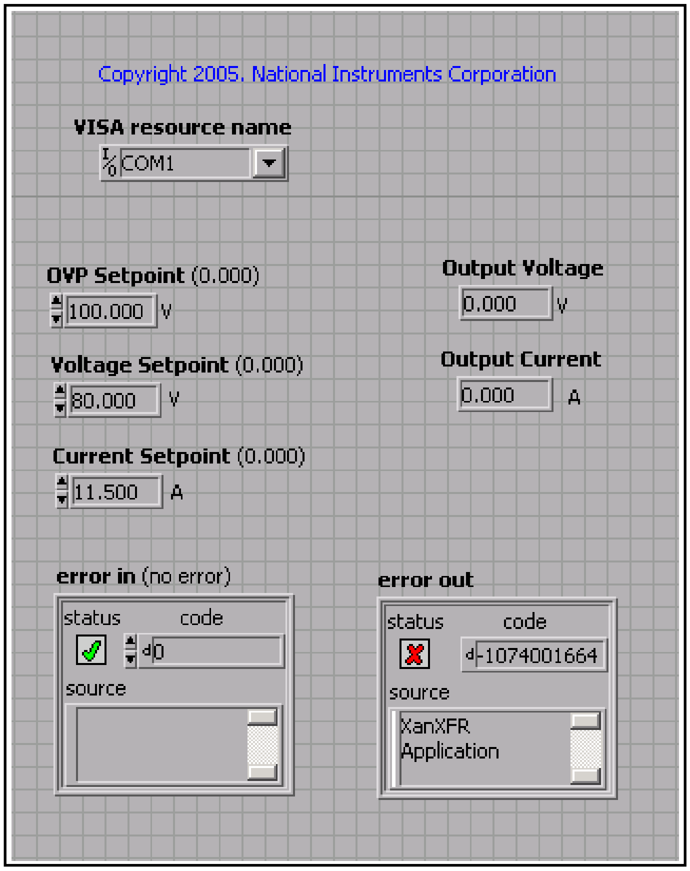

Figure 4.4: Front panel of the Xantrex$_{TM}$ power supply settings Before Operation.

2. Control software and data acquisition

National Instruments™ has a range of interfacing boards, the PCI 6024E interfacing board [85] and the SCB-68 external connector [86] were used as the means of communication between the control PC and the rig. Using this card, it was possible to control the current that was supplied to the coils. Temperature sensing devices (Thermocouples) are also connected to this card in order to continuously monitor the temperature of the coils as depicted in figure 4.5. Technical specification of this data acquisition card can be found in [87].

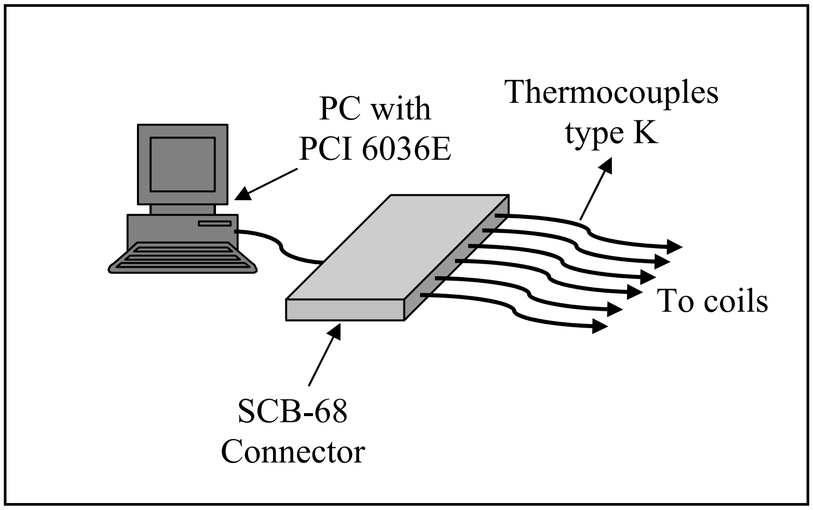

Figure 4.5: Schematic connection of thermocouples to the control PC.

3. Temperature sensing devices

Radionics offers different types of thermocouples which are capable of measuring over very wide temperature ranges. Type K thermocouple or nickel chromium/nickel aluminium is the most widely used. It is basically nickel doped with aluminium and nickel doped with chromium. In this project, eight (type K) thermocouples are used to continuously monitor the temperature of the coils [88]**.** Two thermocouples are used to detect the temperature in each coil. One was inserted between the first and second layers of winding, and the second thermocouple was located between the fifth and the sixth of layers of winding. All thermocouples are then connected to SCB-68 external connector as shown in figure 4.5. The IC sensor of the SCB-68 connector board was configured to do cold junction compensation (CJC). Channel 0 was selected to be the virtual channel which was dedicated to the CJC sensor on SCB-68 as shown in figure 4.6.

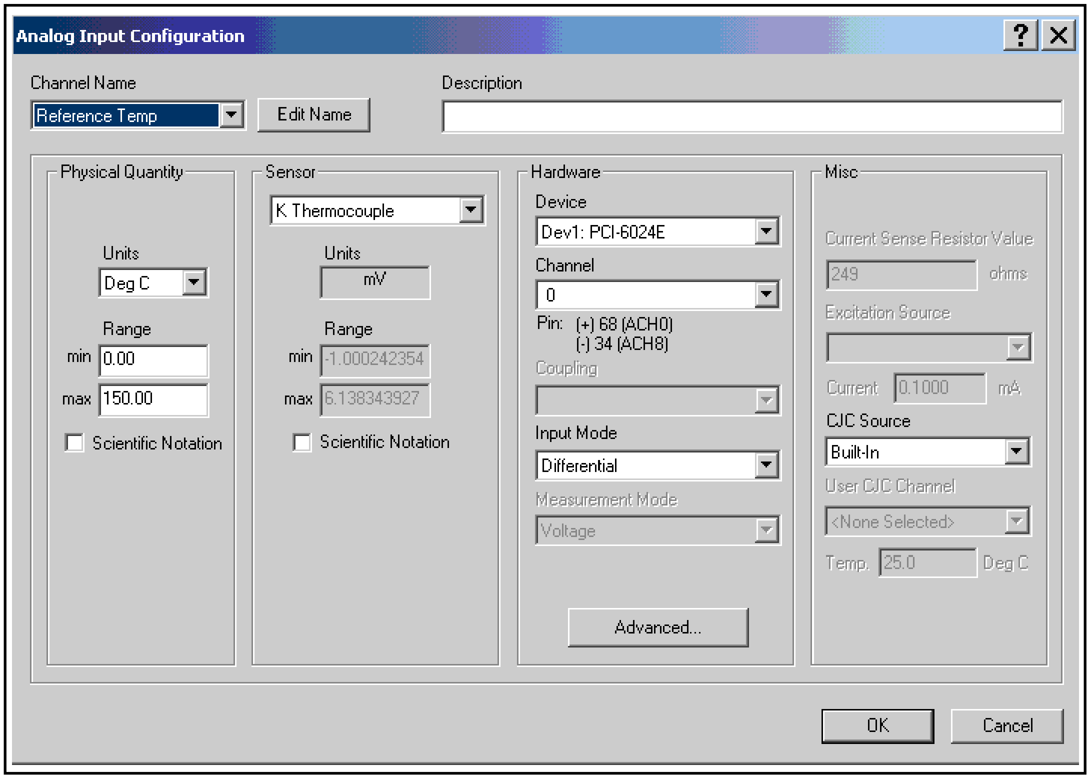

Figure 4.6: Built in CJC virtual channel.

Source code for temperature monitoring

A source code has been built in Labview in order to control the temperature of the system as shown in figure 4.7. The rig was designed to have a maximum working temperature of 150 °C, therefore any of the sensing devices (thermocouples) reads a temperature above 150 °C, as a result, zero current will be fed to the coils.

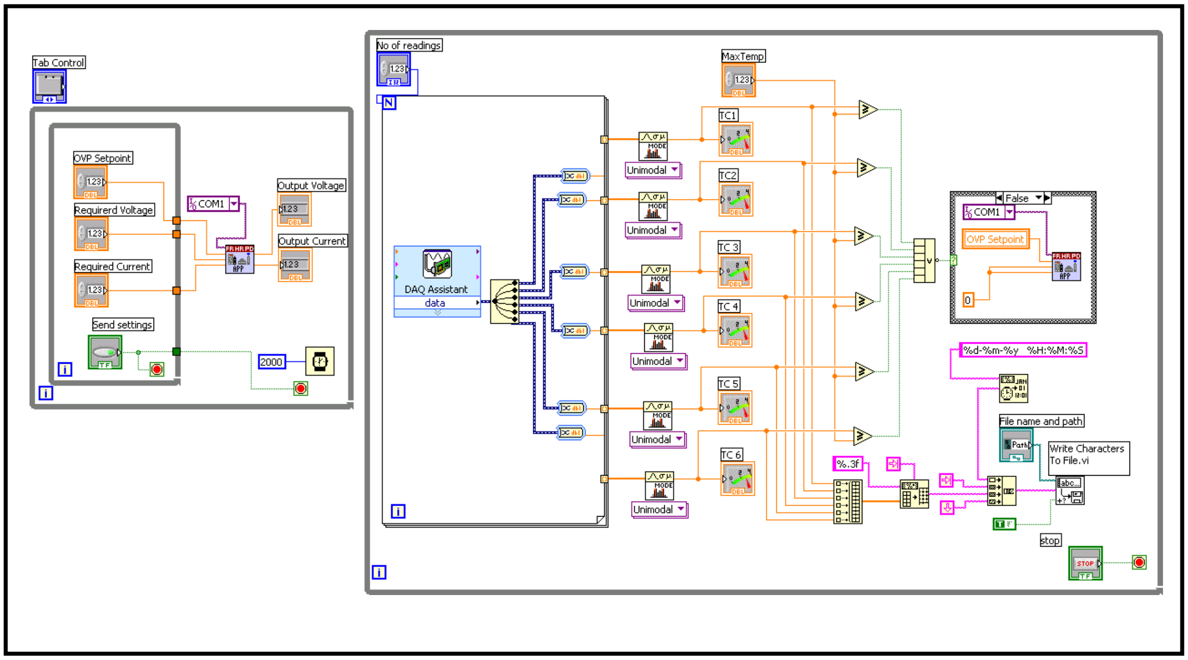

Figure 4.7: Temperature monitoring source code

4. Gauss/Tesla meter

A hand-held 5000 series gaussmeter (F.W Bell) supplied by Sypris Test and Measurement as shown in figure 4.8, was used to validate the results of the FEMM software package for the air gap in terms of the magnetic field intensity generated by the coils. This meter can measure magnetic field intensity of up to 20 kilogauss, and was equipped with a built-in software package to eliminate the requirement for complex calibration procedures [89]. The resolution of this meter is 0.001 T.

Another hand held DC magnetometer (Gaussmeter) supplied by AlphaLab Inc was used in the measurement of magnetic field intensity (figure 4.9) [90].This meter can measure magnetic field intensity of up to 20 kilogauss. The DC Magnetometer has a minimum resolution of 0.01 gauss.

It was very difficult to be sure that either instrument was not faulty, because there was no standard magnetic field to use to verify its accuracy. Therefore it was more convenient to use more than one instrument, and check whether measurements obtained by the two instruments are consistent with each other.

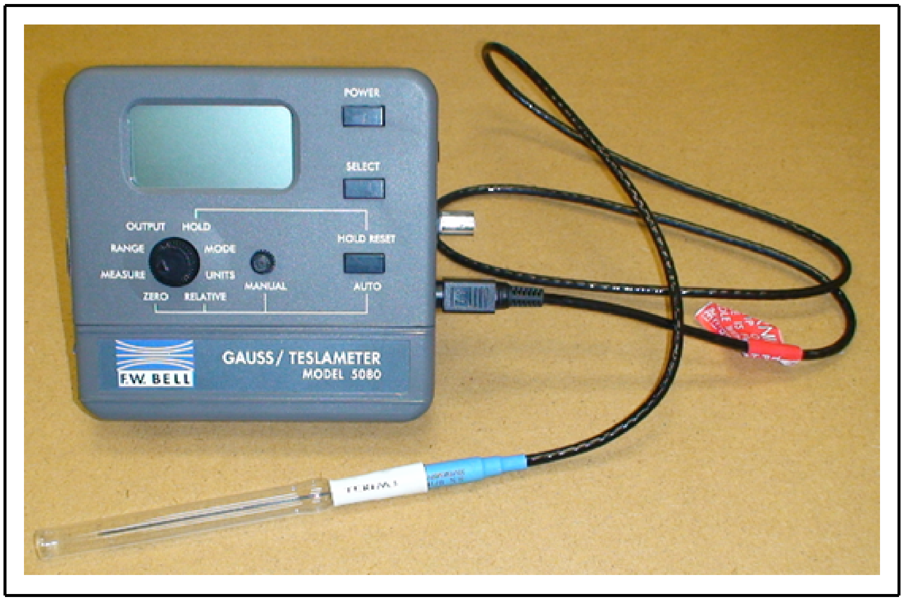

Figure 4.8: The 5080 series hand-held gaussmeter (F.W Bell).

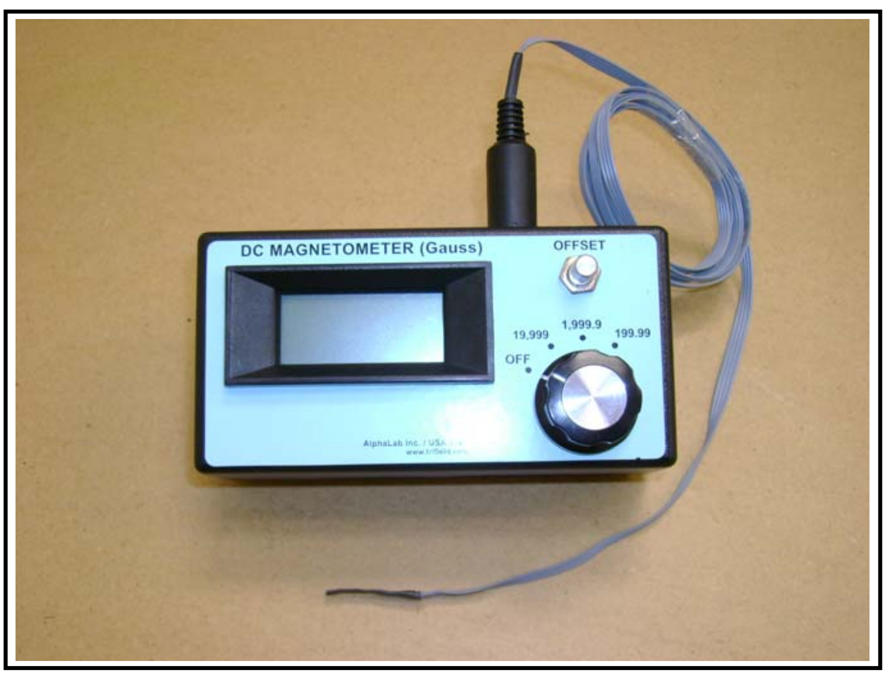

Figure 4.9: Hand-held DC magnetometer (AlphaLab Inc).

4.2.2 Mechanical components design and fabrications

From the early stages of the system design it was clear that a table to hold the coils and other system parts was a necessity. The design of the table was such that a maximum work piece size of 1300 by 1300 mm could be accommodated. The system parts are made of some individual components which are to be rigidly assembled. The rigidity will ensure that the displacement due to flexing of any part was minimized so that it will not impact the minute displacements of the measurement system. Where possible, the use of ferrous or magnetically susceptible components must be avoided. This was to reduce the possibility of distorting the magnetic field. The candidate material should be rigid with a low thermal expansion coefficient.

The mechanical drawings of the sub-assemblies are attached in appendix E. Schedule for the mechanical drawings are listed in the table 4.2.

Table 4.2: Schedule for the mechanical drawings.

1.	Standoffs for iron core (Top)
2.	Standoffs for iron core (bottom)
3.	Standoffs for samples to be tested
4.	End-cap for inserting copper tubes
5.	End-cap for air cooling system
6.	Teflon plastic spacer
7.	Large-diameter with cross-section component corner

4.2.3 Results of the measurement of magnetic properties of the low carbon steel material, carried out by an independent laboratory

A sample of the low carbon steel used as a core for winding the coils was sent to an independent Laboratory (Magnetic Instrumentation Calibration Laboratory Inc, USA) to characterize its magnetic properties [91]. Results shown in appendix F indicate that the maximum magnetic flux density measured was 2.1851 T.

4.3 Preliminary experiments

These preliminary experiments carried out on the electromagnetic rig were aimed to verify its functionality and suitability for the measurements of the magnetostrictive coefficient and the magnetic annealing process which requires a magnetic flux density of 1.662 T in the centre of the air gap in the C-shape circuit.

The procedure of carrying out these preliminary experiments is listed below.

- Measurements of the resistance of each coil separately.

- Measurements of magnetic flux density produced by each coil separately in open circuit.

4.3.1 Resistance measurements and continuity tests

Resistances of each layer of each coil were measured using a digital multimeter (Tektronix DMM 912) and showed reasonable agreement with the calculated theoretical values carried out in section 3.1.6. Figure 4.10 reveals the values of resistance of layers for each coil.

A continuity test for each layer was also carried out to make sure that no short circuit was encountered, and to have well isolated layers and to prevent any possibility of current leakage.

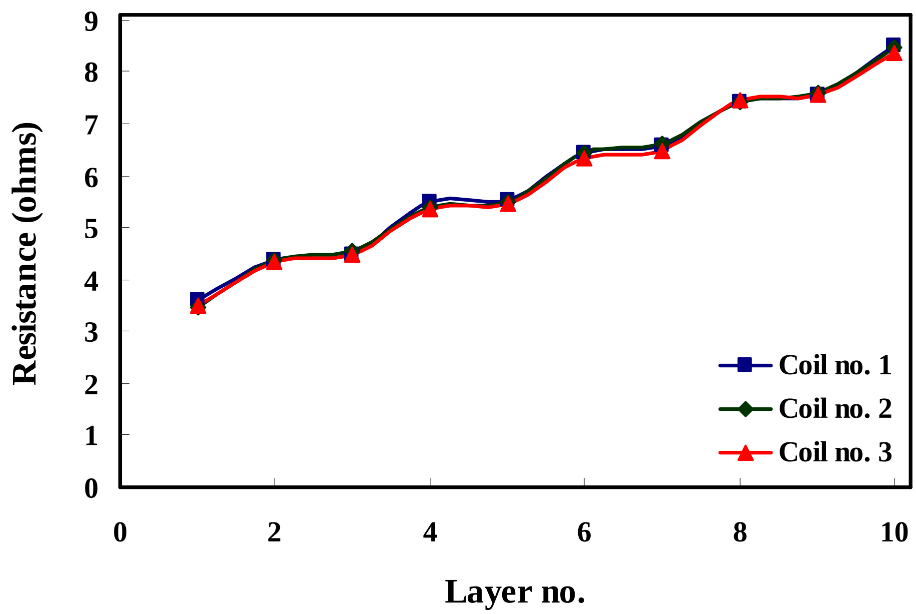

Figure 4.10: Resistance value of each layer for each coil.

As expected, the outer layers of the coils consist of longer sections of copper wire and so the resistances are greater. As described in chapter three, copper tubes were inserted to allow for cooling between layers one and two, three and four, five and six, seven and eight and nine and ten.

4.3.2 Measurements of magnetic flux density in open circuit

The "open circuit" refers to the magnetic circuit when all components are tested in place. The C-shape allows the circuit to be complete by placing a suitable sample in the "jaws" of the C-shape. In these tests, the different components of the C-shape were tested on their own and so the magnetic circuit was not complete.

Different experiments were carried out on each coil. The objective of these experiments was to understand and analyse the magnetic properties of each coil in open circuit, and to establish using the flux density instrument that each layer produces a flux in the same direction.

At the beginning of this work, each of the layers of each of the coils was checked, to investigate whether the coil could have been made in the wrong direction. More over, it was essential to zero the hall probe that is the meter in a zero gauss chamber so that there were no stray or residual fields before making any new measurements. The procedure of carrying out these experiments is listed below.

a. Measurements of magnetic flux density produced by each layer

Each coil was analysed separately in open circuit with different values of dc current being applied to each layer one at a time. A hand-held, Hall Effect, gaussmeter was used to measure the magnetic flux density. A Xantrex$_{TM}$ XFR 150v, 18 Amps DC power supply was used as the current source. It was provided with a RS-232 interface card, which gives remote digital control of the system. A maximum current of 3 amps was passed through each layer. For each measured value of magnetic flux density, the corresponding magnetic field strength was calculated using the following equation:

$$H = \frac{NI}{l} \tag{4-1}$$

where N is the number of turns of each layer which was approximately equal to 800 turns, I is the current supplied, l is the effective length of the coil which was equal to 0.64 mm.

Results of the measurement of magnetic flux densities of layers for each coil are presented in appendix G. Figure 4.11, shows the magnetic flux density produced by each layer for each coil. It can be seen that in each coil, the flux density produced by individual layers have almost the same values.

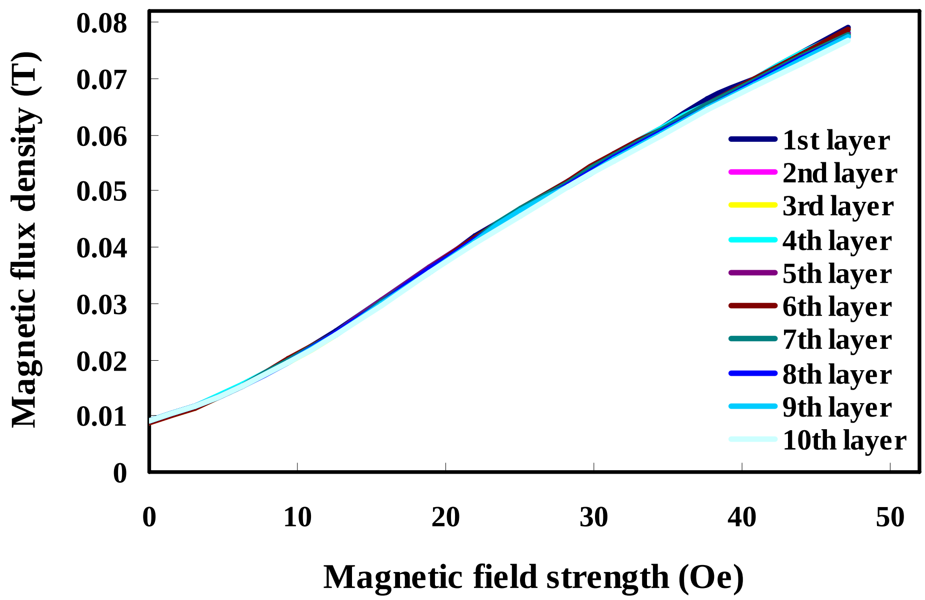

Magnetic flux density (T)
0.08
0.07
0.06
0.05
0.04
0.03
0.02
0.01
0
0
10
20
30
40
50
Magnetic field strength (Oe)
1st layer
2nd layer
3rd layer
4th layer
5th layer
6th layer
7th layer
8th layer
9th layer
10th layer

(a)

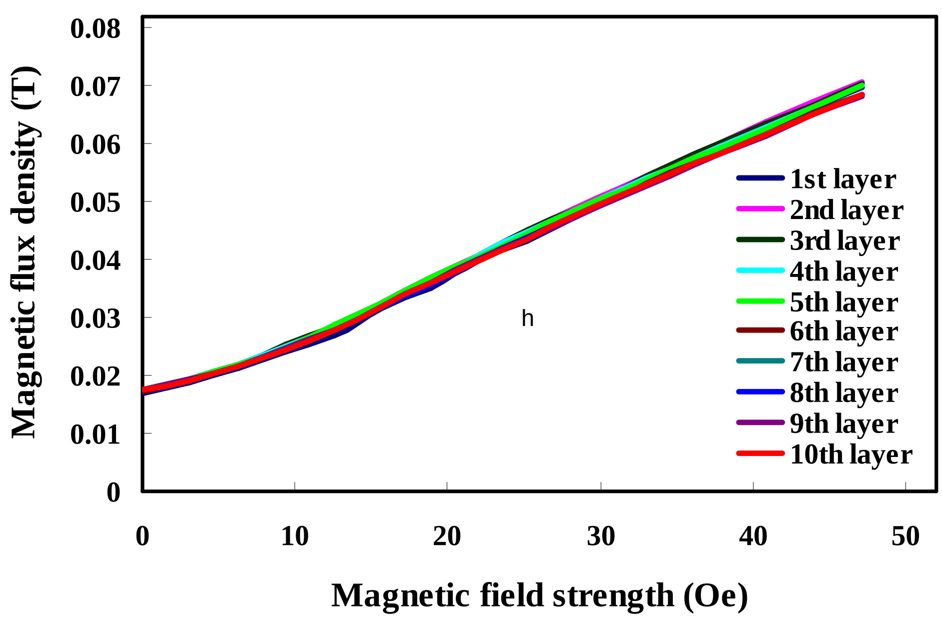

Magnetic flux density (T)
0.08
0.07
0.06
0.05
0.04
0.03
0.02
0.01
0
0
10
20
30
40
50
Magnetic field strength (Oe)
h
1st layer
2nd layer
3rd layer
4th layer
5th layer
6th layer
7th layer
8th layer
9th layer
10th layer

(b)

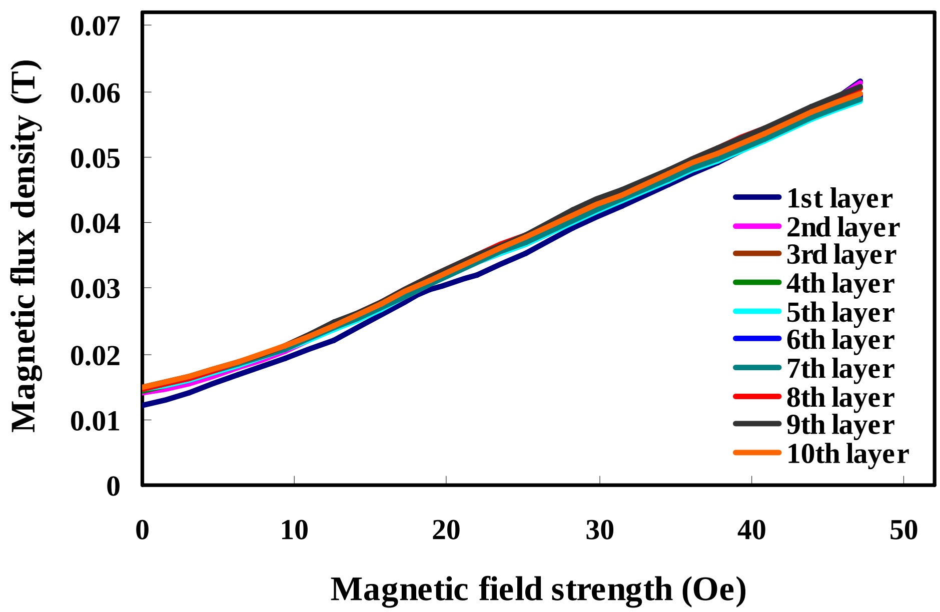

(c)

Figure 4.11: Magnetic flux densities produced by layers for (a) coil no. 1, (b) coil no. 2, and (c) coil no. 3.

b. Measurements of magnetic flux density produced by series layers

As mentioned in a previous chapter, the layers in each coil are combined in a special way to ensure that all layers receive the same current; the first layer was connected in series with the tenth layer, the second layer in series with the ninth layer, the third layer in series with the eighth layer, the forth layer in series with the seventh layer, and finally the fifth layer in series with the sixth layer. A current was applied in the same direction to each combination of two individually. The results are listed in appendix G. These results ensure that all layers produce almost the same magnetic flux density as shown in figure 4.12.

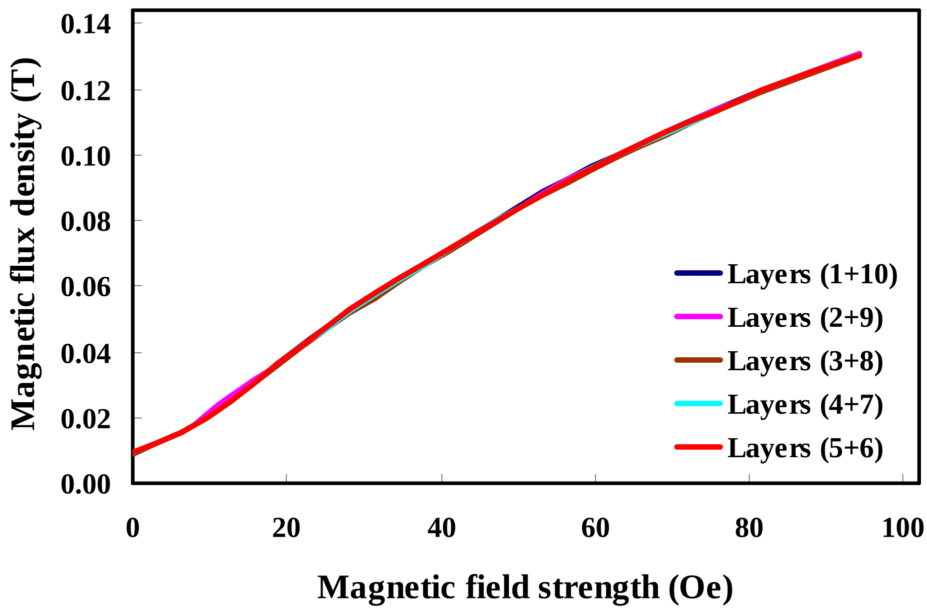

Magnetic flux density (T)
0.14
0.12
0.10
0.08
0.06
0.04
0.02
0.00
0
20
40
60
80
100
Magnetic field strength (Oe)
Layers (1+10)
Layers (2+9)
Layers (3+8)
Layers (4+7)
Layers (5+6)

(a)

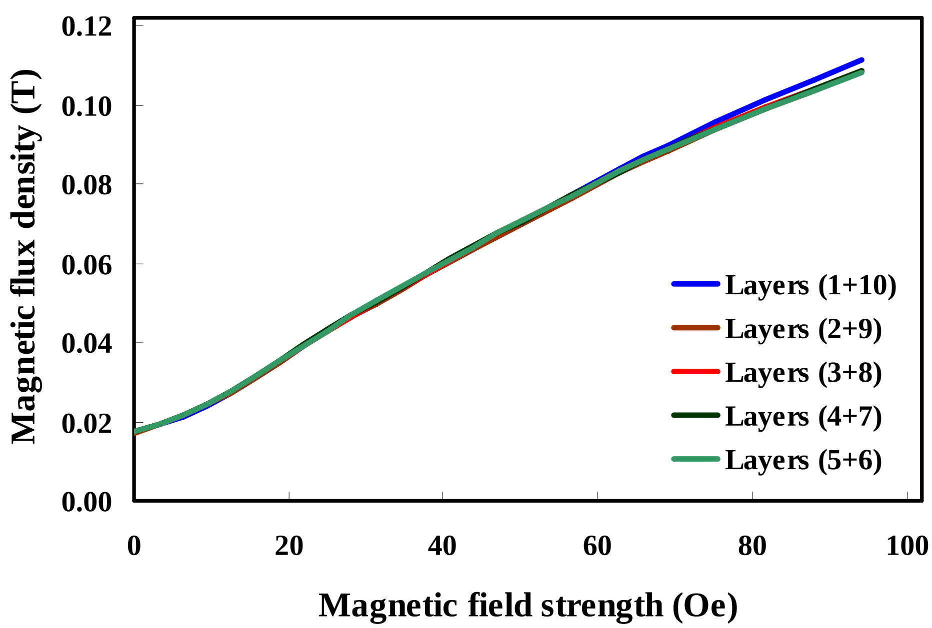

Magnetic flux density (T)
0.12
0.10
0.08
0.06
0.04
0.02
0.00
0
20
40
60
80
100
Magnetic field strength (Oe)
Layers (1+10)
Layers (2+9)
Layers (3+8)
Layers (4+7)
Layers (5+6)

(b)

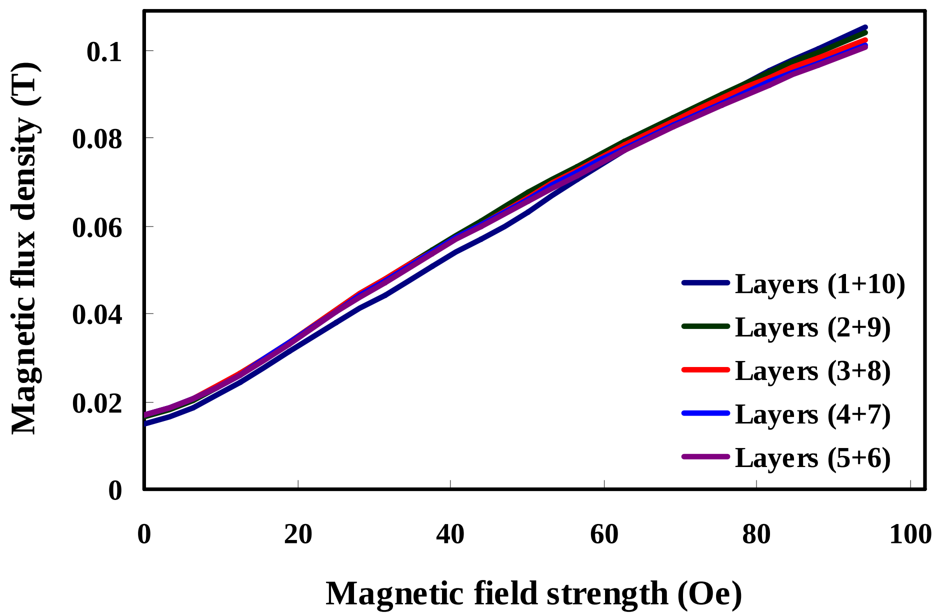

(c)

Figure 4.12: Magnetic flux densities produced by series layers for (a) coil no. 1, (b) coil no. 2, and (c) coil no. 3.

c. Measurements of magnetic flux density produced by each coil individually

Each coil was analysed separately. A maximum current of 15 amps was passed through each coil. The current was always applied in the same direction to investigate whether the coil could have been made with winding in the opposite direction. The magnetic flux density produced by each coil is shown in figure 4.13. The measurement results are listed in appendix G. These results indicate that each layer in each coil produced a flux in the same direction.

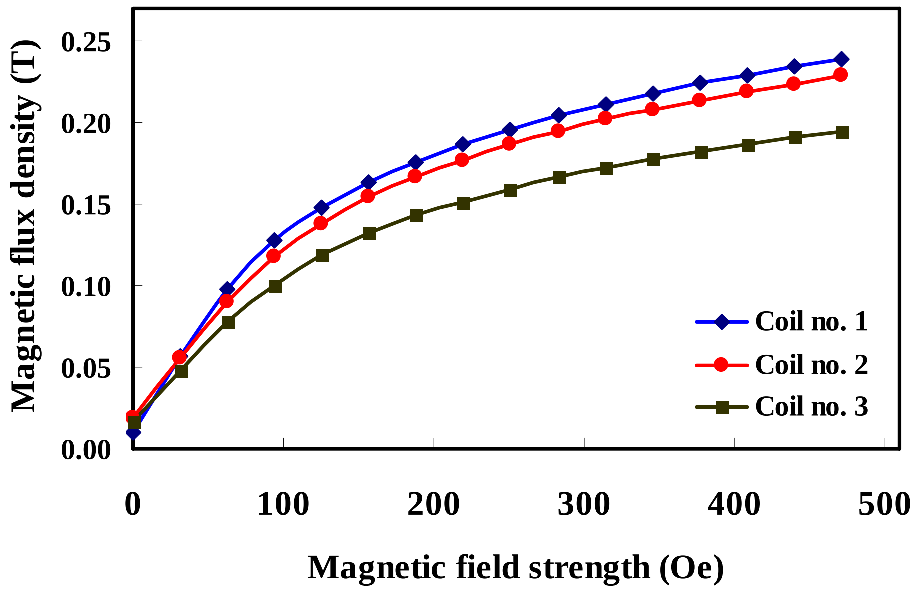

Figure 4.13: Magnetic flux density produced by each coil.

4.4 C-shape circuit using curved corners

The electromagnetic rig structure was assembled into two different configurations. In configuration "A", the C-shape circuit consisted of three coils only. In Configuration "B", the C-shape circuits comprised of four coils. Figure 4.14 depicts the experimental work procedure.

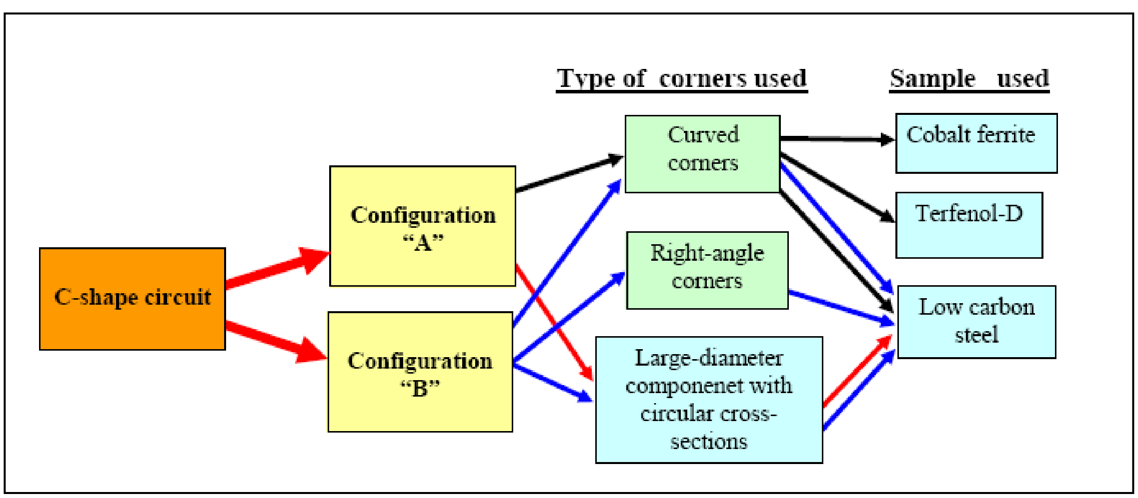

Figure 4.14: Experimental work procedure.

The corners shown in figure 3.4 were used in both configurations in all experiments.

In this section, configuration "A" was analysed using curved corners as shown in figure 4.15. The previously tested coils were connected together using the curved corners, so that it forms a continuous conduit for the magnetic flux, except for a gap of 2 mm on one of the sides. The various sections of the core are joined together tightly using bolts, with almost no gaps, or cracks.

The three coils are electrically connected in series. A Teflon (PTFE) plastic disc was made, measuring 2 mm in thickness by 30 mm in diameter. This custom-made plastic disc was placed and held in the 2 mm air-gap. It has a notch which could accommodate the tip of the DC gaussmeter transverse probe. This ensured the same probe position for successive measurements. A maximum current of 15 amps was passed through each coil, giving a current of 3 amps in each of the layers.

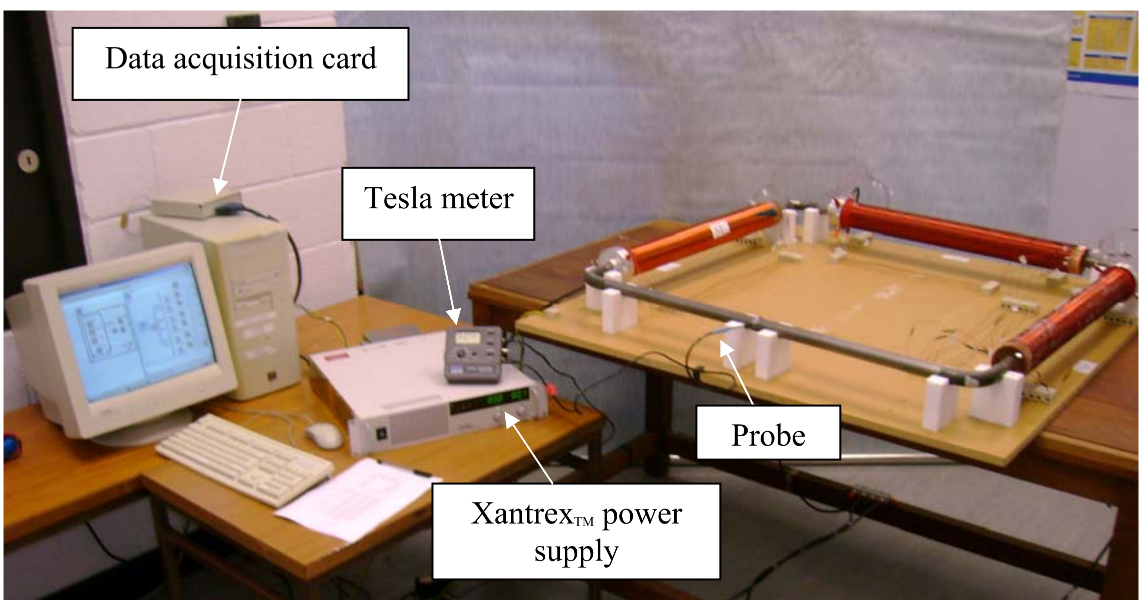

Figure 4.15: Experimental set-up of configuration "A" using curved corners.

The aim of these experiments was to measure the magnetic flux density in the centre of the air-gap when each sample (either the cobalt ferrite sample, or the low carbon steel sample, or the Terfenol-D sample) was placed in the air-gap.

4.4.1 The measurements of magnetic flux density in the air gap using a sample of cobalt ferrite

According to the initial calculation carried out in sections 3.1.4, when introducing the cobalt ferrite sample to the C-shape circuit, this sample should experience 9000 Oe. In other words, the magnetic flux density should be 1.662 T in the centre of the air-gap. However in chapter four it was explained that this initial calculation did not take flux leakage into account.

The cobalt ferrite sample was placed in the "jaws" of the C-shaped. With the sample in place the magnetic circuit was completed. Current was applied to the coils, and slowly it was increased to 15 amps. Then the current was slowly reduced back to zero. The results are listed in appendix I. Figure 4.16 reveals the magnetic flux density measured at the centre of the air-gap.

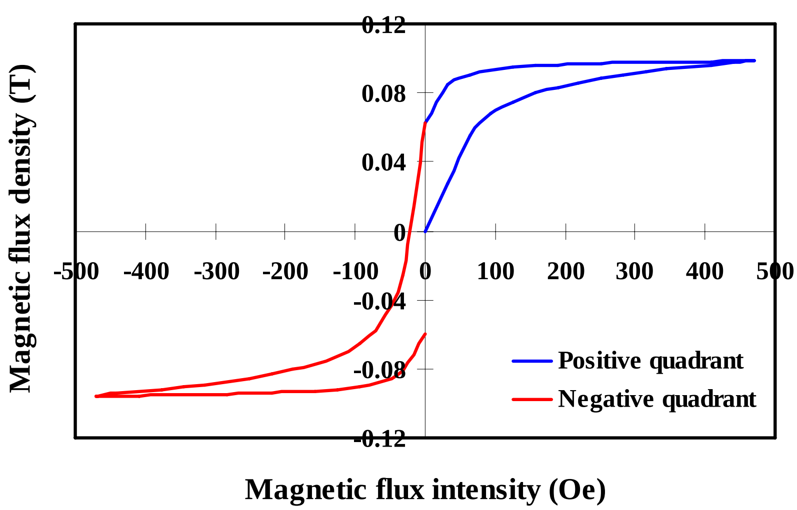

Figure 4.16: Magnetic flux density in the centre of the air gap using cobalt ferrite sample.

An average value for the magnetic flux density B can be calculated by adding the numerical values of positive and negative results as shown in figure 4.17. A considerable difference exists between the theoretical estimation which gives a value of the flux density in centre of the air-gap of 1.662 T, and the experimental measurements which give a value of approximately 0.08 T. However, the initial theoretical estimate did not take flux leakage into account.

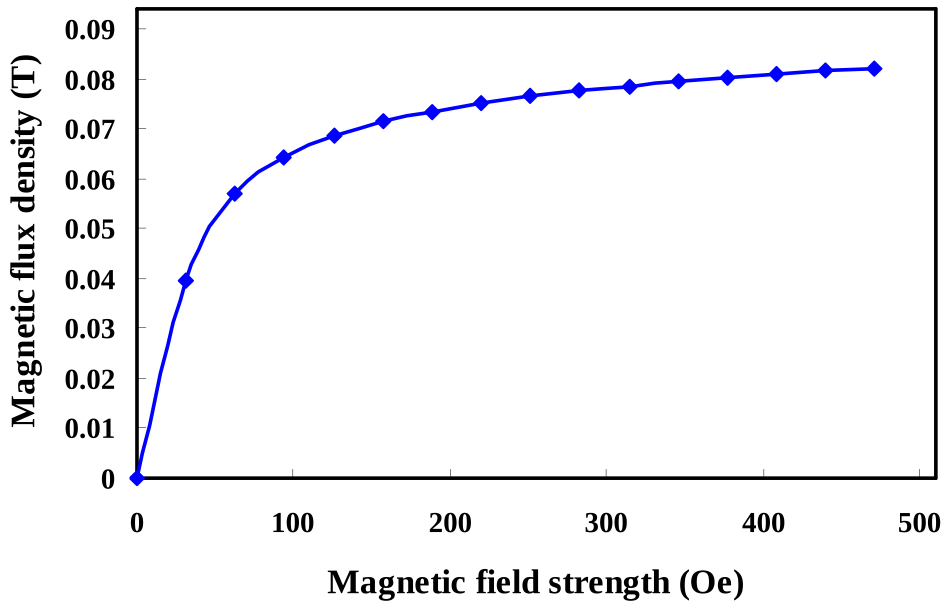

Figure 4.17: Averaged values of magnetic flux density vs. magnetic field strength in the centre of the air gap using the cobalt ferrite sample.

4.4.2 Measurements of magnetic flux density in the air gap using a sample of low carbon steel

The same procedure in taking measurements that carried out in the previous section was followed. The results are presented in appendix G.

Figure 4.18 reveals the magnetic flux density measured at the centre of the air-gap. An average value of the magnetic flux density was shown in figure 4.19. The maximum magnetic flux density measured was approximately 0.25 T in the centre of the air-gap at a current of 15 Amps.

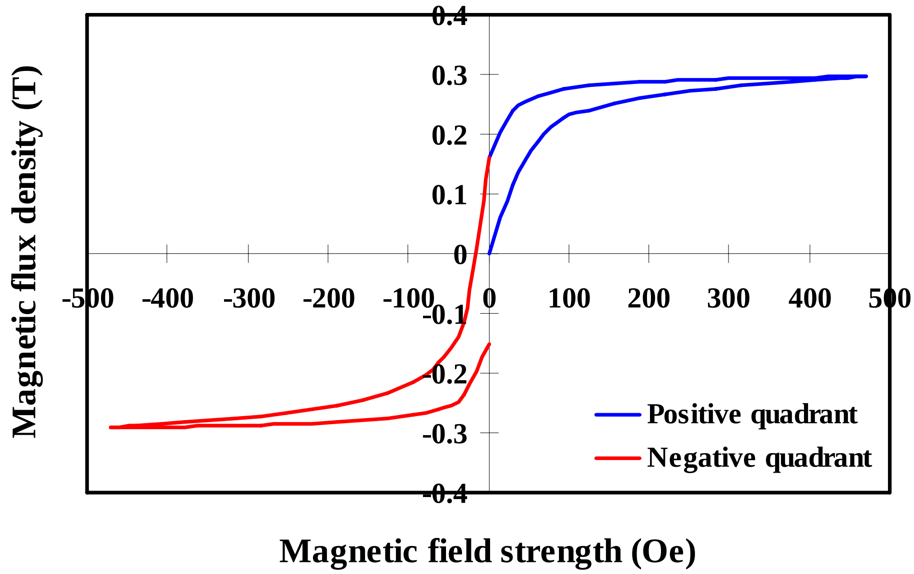

Figure 4.18: Magnetic flux density in the centre of the air gap using the low carbon steel sample.

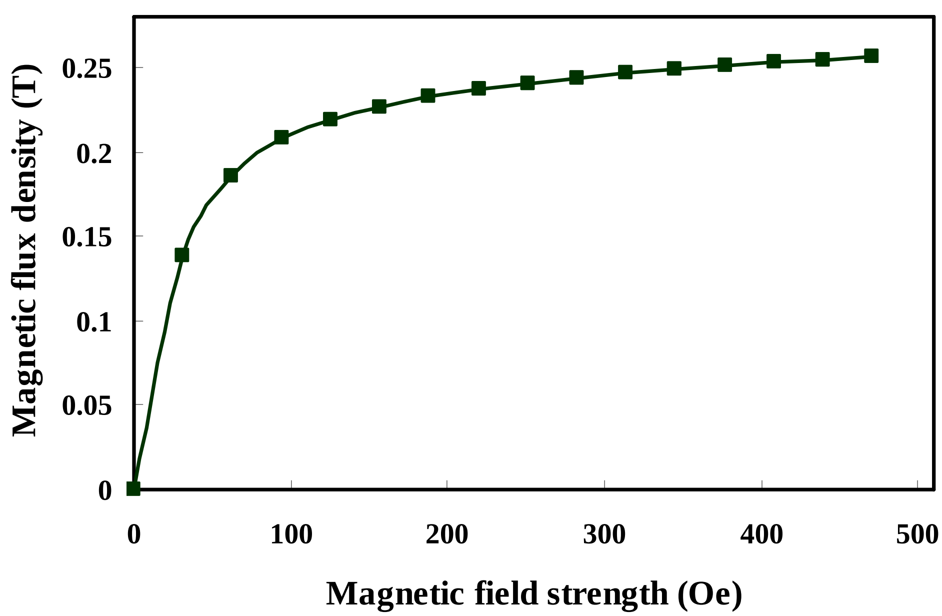

Figure 4.19: Averaged values of magnetic flux density vs. magnetic field strength in the centre of the air gap using the low carbon steel sample.

The problem with these results becomes apparent when the magnetic properties of the core material are considered. According to the magnetic properties of low carbon steel core, a magnetic field strength in the core material will produce a flux density of 2.0095 T. Therefore the measured flux density produced by the three coils was only 0.25 T. The problem therefore was that a theoretical estimation gave the flux density in the core of 2.0095 gauss; while that based on a measurement gave only 0.25 T.

Part of the discrepancy can be explained by the fact that the initial theoretical calculation did not take flux leakage into account. However this explanation is not sufficient to the total discrepancy. Another possible cause of the problem could be that the magnetic properties of some of the samples are unknown. However this does not explain the discrepancy when the sample material is low carbon steel, because its properties are well known.

4.4.3 Measurements of magnetic flux density in the air gap using a sample of Terfenol-D

Figure 4.20 illustrates the values of magnetic flux densities when using Terfenol-D sample in the air-gap. The maximum averaged value measured was approximately 0.24 T as shown in figure 4.21. Measurement results of this experiment are listed in appendix G.

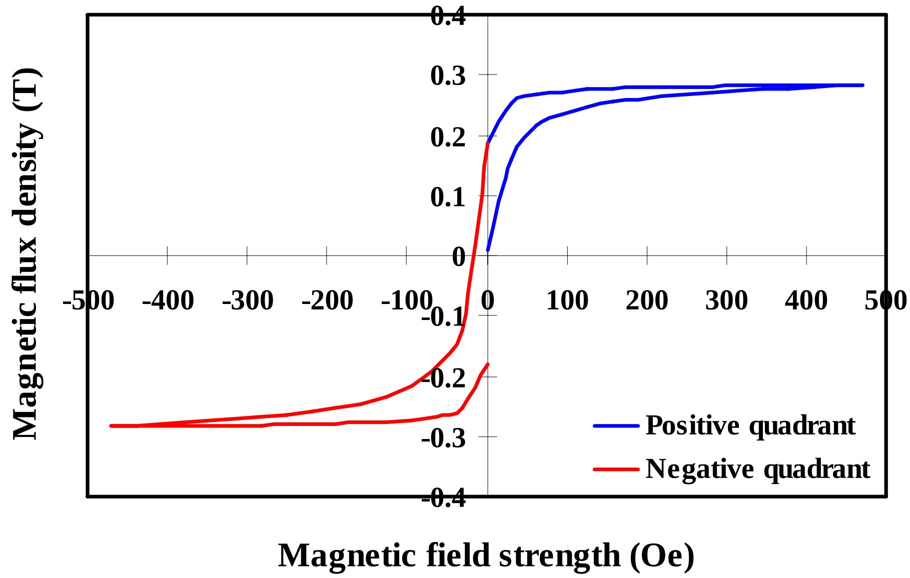

Figure 4.20: Magnetic flux density in the centre of the air gap using Terfenol-D sample.

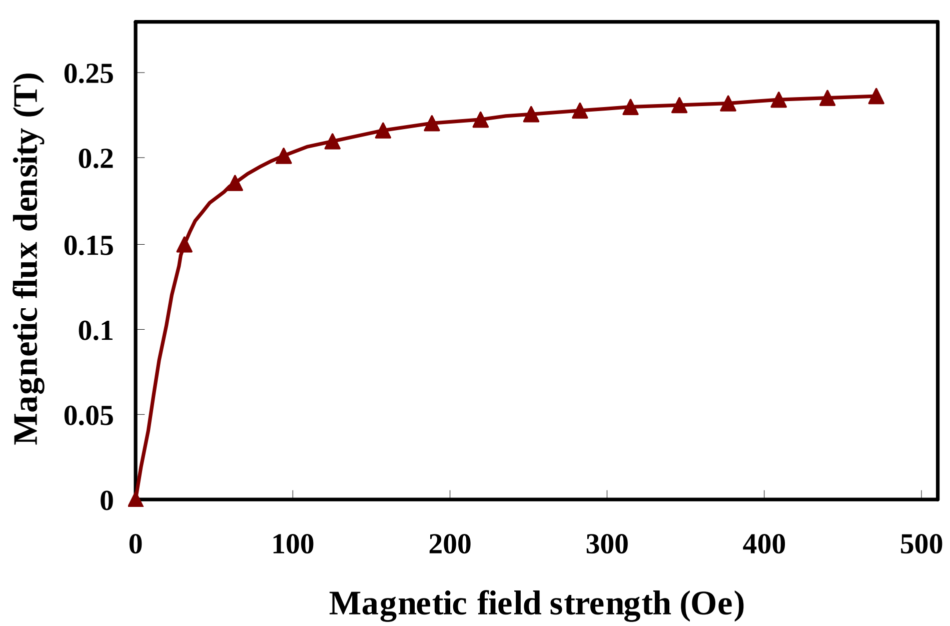

Figure 4.21: Averaged values of magnetic field strength vs. magnetic flux density in the centre of the air-gap using Terfenol-D sample.

4.5 The fabrication of a fourth coil using pure iron as the core material

It is possible that the sample of low carbon steel which was sent for the test could have had superior magnetic properties in comparison with the rest of the core material which was used to construct the system. For this reason a new coil with the same specifications as the previous coils was constructed, but this time pure iron was used as the core. It was supplied by Goodfellow Cambridge Limited [92]. It is of type FE007974 iron and has magnetic properties shown in table 4.3.

This pure iron core coil has also been used in experiments to investigate its functionality using the same procedure carried out in sections 4.3.1 and 4.3.2. The magnetic flux density information produced by single layers, two layers connected in series, and complete coil is presented in appendix G.

Table 4.3: Magnetic properties of pure iron core.

Initial permeability	250
Maximum permeability	5000
Saturation induction	2.1 T
Remanence from	0.8 T
Coercivity	80 A/m
Curie temperature	770 °C

Figure 4.22 illustrates the magnetic flux density produced by single layers, two layers connected in series, and complete coil (coil no. 4) in comparison with the other three coils. It can be seen that the pure iron core has slightly better magnetic properties compared to the other coils. The highest measured magnetic flux density for coil no. 4 was approximately 0.252 T. It follows that the low carbon steel used in constructing the coils has magnetic properties which are almost as good as the pure iron.

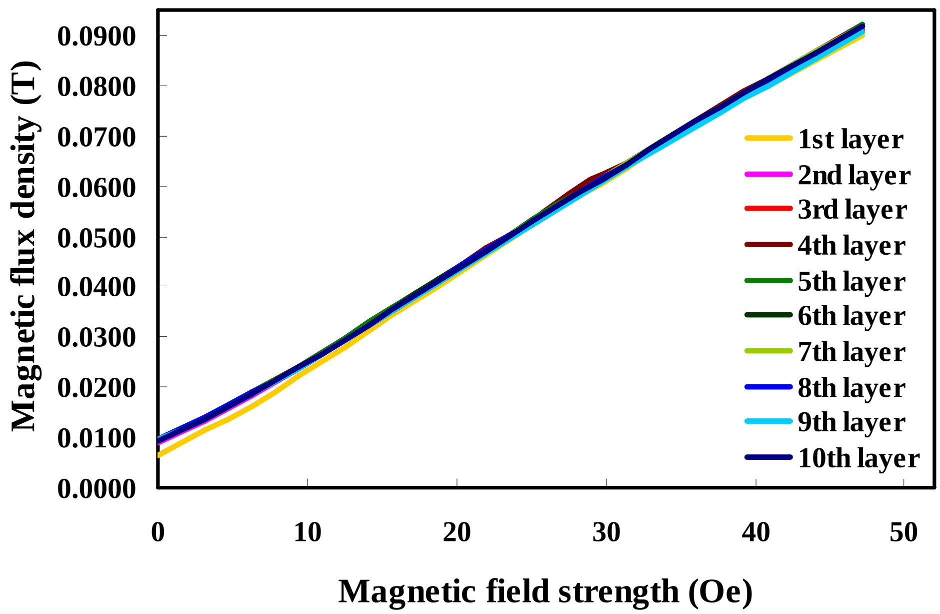
Magnetic flux density (T)
0.0000
0.0100
0.0200
0.0300
0.0400
0.0500
0.0600
0.0700
0.0800
0.0900
0
10
20
30
40
50
Magnetic field strength (Oe)
1st layer
2nd layer
3rd layer
4th layer
5th layer
6th layer
7th layer
8th layer
9th layer
10th layer

(a)

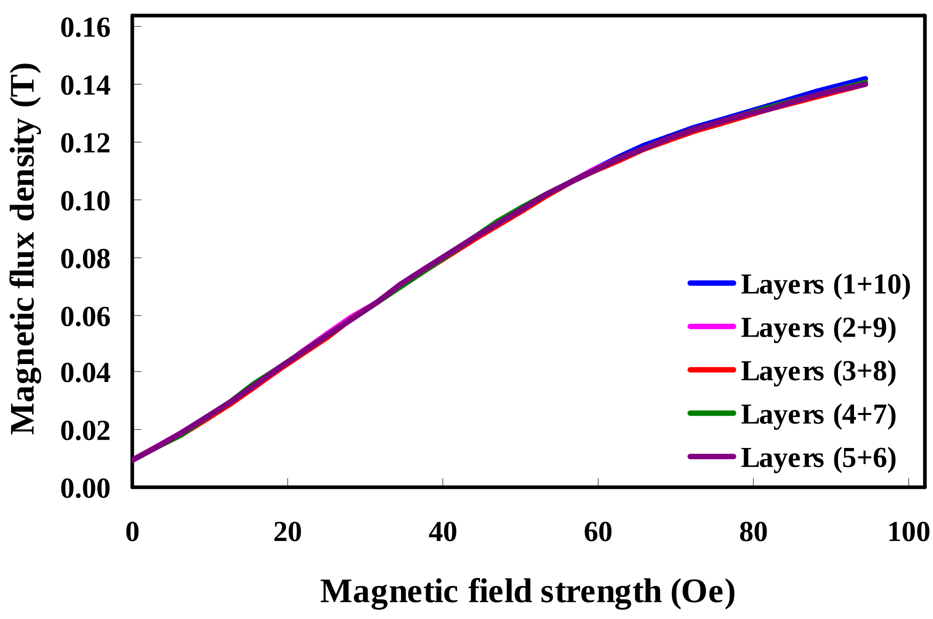
Magnetic flux density (T)
0.00
0.02
0.04
0.06
0.08
0.10
0.12
0.14
0.16
0
20
40
60
80
100
Magnetic field strength (Oe)
Layers (1+10)
Layers (2+9)
Layers (3+8)
Layers (4+7)
Layers (5+6)

(b)

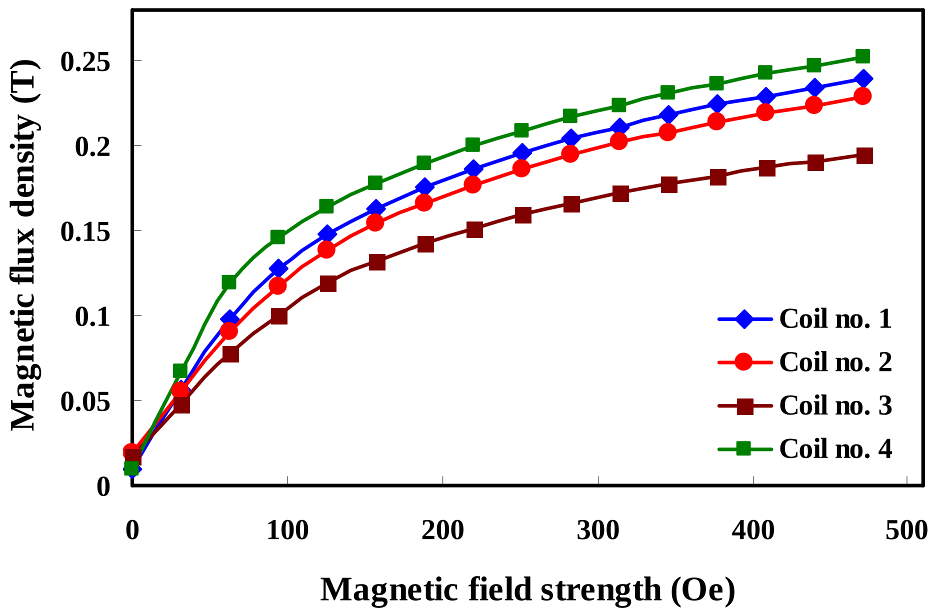

(c)

Figure 4.22: Magnetic flux densities produced by (a) each layer individually (b) series layers (c) coil no. 4 in comparison with other coils.

4.5.1 Configuration "B" using curved corners

It is possible that the magnetic properties of the core material could have been altered when the corners were made. The process used to make these corners involved cutting which produced heat and this heat caused the material to become soft.

Two further experimental modifications were carried out on the system. These experiments were aimed to examine how the flux that was generated by each coil contributes towards the flux measured at the air-gap. The second experiment was to investigate the effect of location of the air-gap with respect to the corners of the C-shaped circuit.

a. Air gap located between two coils

All four coils were incorporated into a slightly different C-shaped circuit. They were connected in series as depicted in figure 4.23. The Tesla probe was located at the end of one core on one side of the air gap. The same procedure was followed in taking measurements of the magnetic flux density as in the previous experiments.

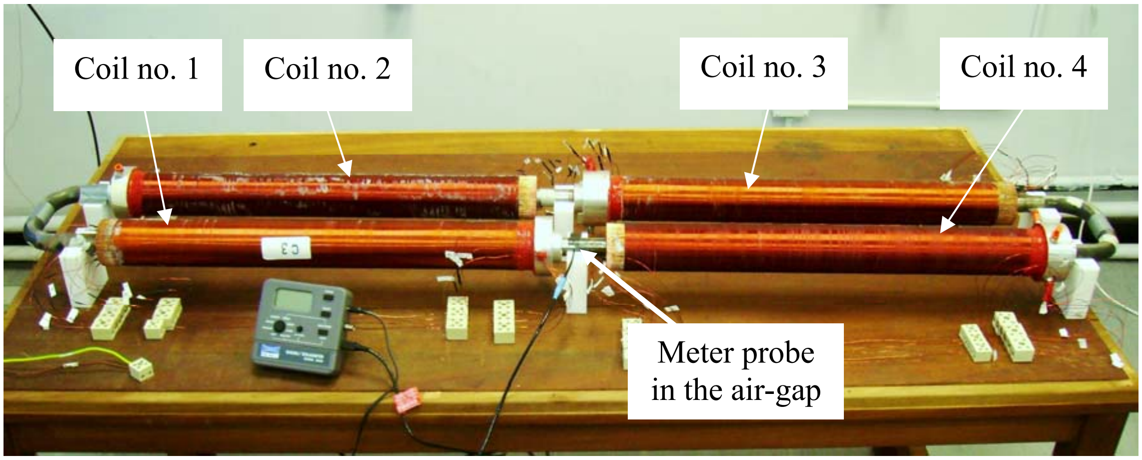

Figure 4.23: Experimental set-up of configuration "B" using curved corners.

The procedure of carrying out these experiments is listed below.

- Measurements of the magnetic flux density in the air-gap produced by each coil separately.

- Measurements of the magnetic flux density in the air-gap produced by a combination of two coils in series.

- Measurements of the magnetic flux density in the air-gap produced by a combination of three coils in series.

- Measurements of the magnetic flux density in the air gap produced by all the coils.

Figure 4.24 shows the measured magnetic flux density results at the edge of the core on one side of the air-gap. Information of magnetic flux densities is tabulated in appendix G.

Magnetic flux density produced by all coils reached about 1.119 T at one side of the air-gap. This is almost the same value produced only by the two coils in-line and closest to the air-gap (coil no. 1 and coil no. 4). In this case, a value of 1.138 T was produced. This suggests that losses could be due to corners which might have poorer magnetic properties or due to leakage across the two rows of coils forming the magnetic circuit. The measured magnetic flux density at one side of the air-gap was the highest achieved at that stage.

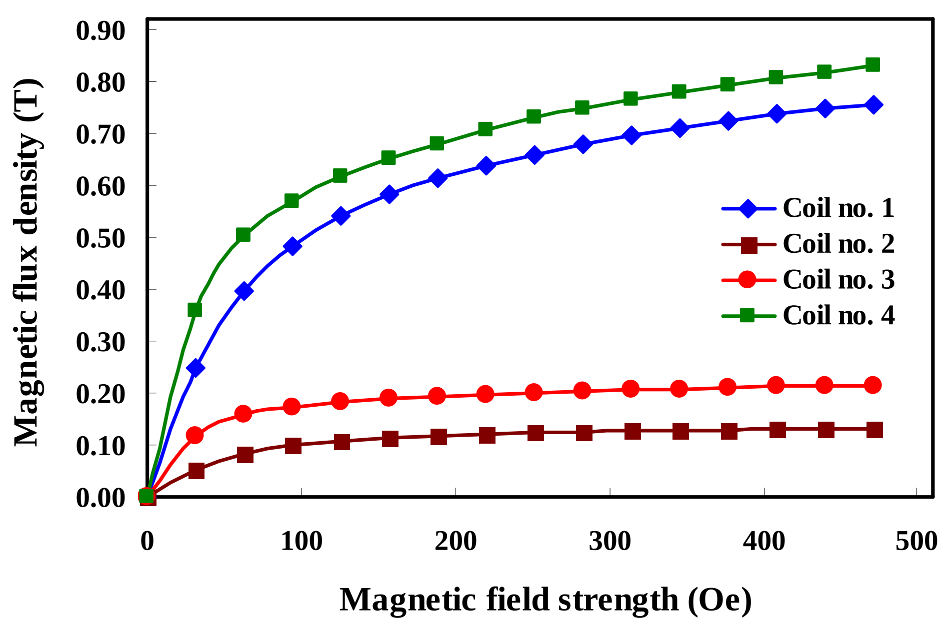

(a)

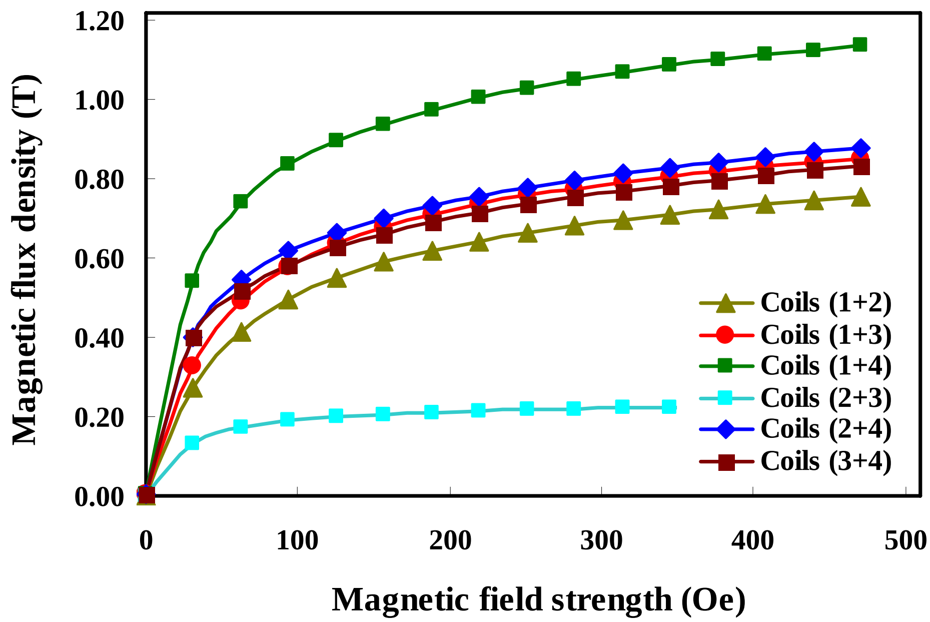

Magnetic flux density (T)
1.20
1.00
0.80
0.60
0.40
0.20
0.00
0
100
200
300
400
500
Magnetic field strength (Oe)
Coils (1+2)
Coils (1+3)
Coils (1+4)
Coils (2+3)
Coils (2+4)
Coils (3+4)

(b)

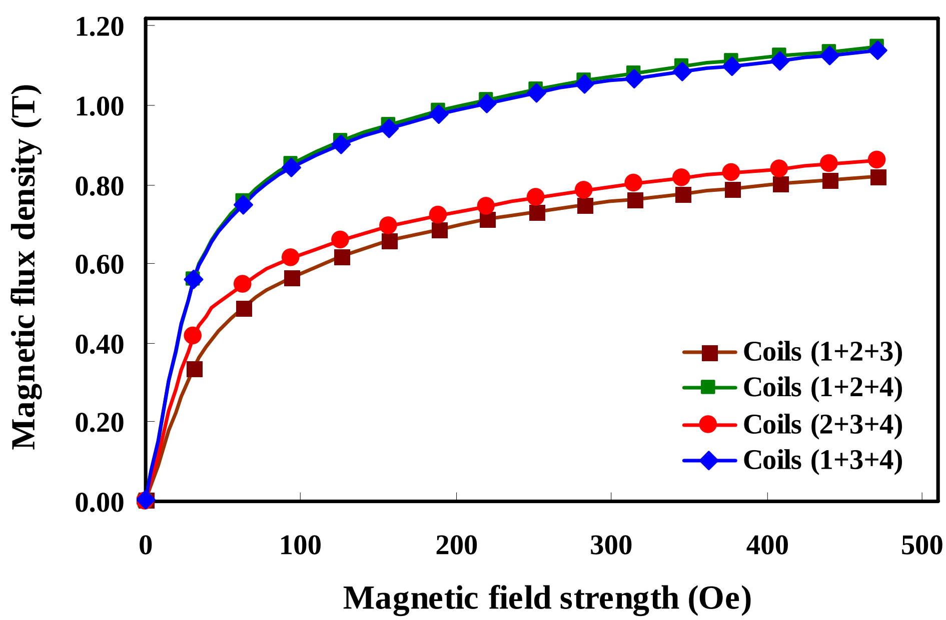

Magnetic flux density (T)
1.20
1.00
0.80
0.60
0.40
0.20
0.00
0
100
200
300
400
500
Magnetic field strength (Oe)
Coils (1+2+3)
Coils (1+2+4)
Coils (2+3+4)
Coils (1+3+4)

(c)

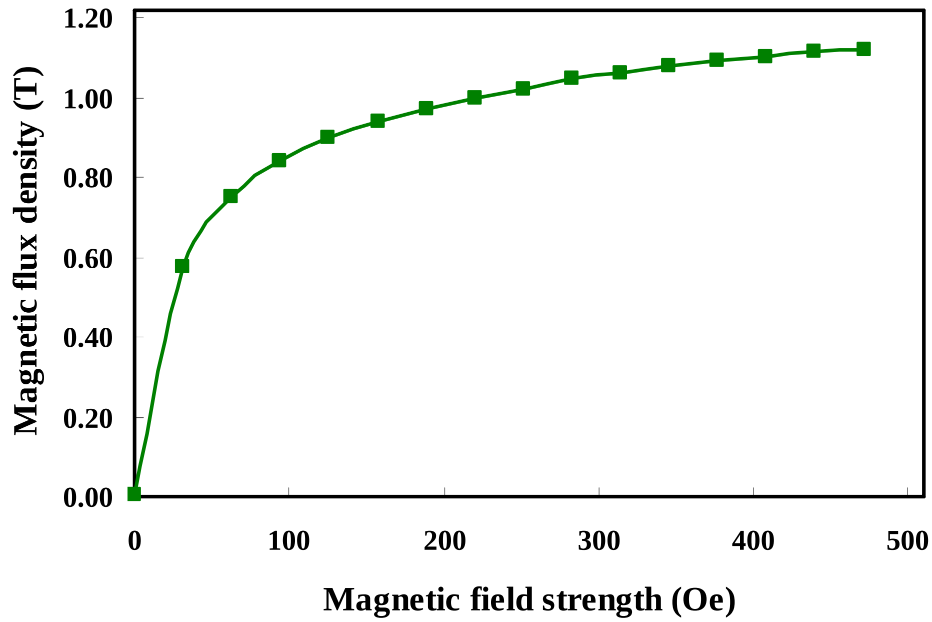

(d)

Figure 4.24: Magnetic flux density of configuration "B" using curved corners produced by (a) each coil individually (b) combinations of two coils (c) combinations of three coils (d) all four coils.

Coils 1 and 4 were in line with and closest to the air-gap. To reach the air-gap, flux generated in coils 2 and 3 had to pass through two curved corners. Figure 4.24 (b) shows that superior flux densities were produced when either coils 1 and 4 were generating flux. On the other hand, inferior flux densities were produced when either coils 2 and 3 were generating flux, and intermediate results were obtained when other coil combinations were used to generate flux.

Again the results depicted in figure 4.24 (c) show some consistent pattern. A higher result occurs when the combination includes both coil no. 1 and coil no. 4. A lower result occurs when the combination includes either coil no. 1 or coil no. 4, but not both.

b. Air gap on one of the sides and close to one of the corners

This experiment is similar to the previous one, except that the air-gap is now on one of the sides and close to one of the corners as shown in figure 4.25. The Tesla probe was located at the edge of core on one side of the air gap. The same procedure was followed in taking measurements of the magnetic flux density as in the previous experiments.

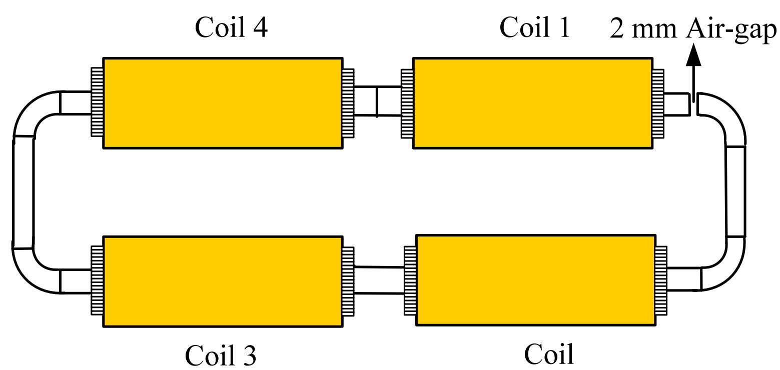

Figure 4.25: Experimental set-up of configuration "B" using curved corners with air-gap close to one corner.

Figure 4.26 shows the measured magnetic flux density at the edge of the core on one side of the air-gap. Information of magnetic flux densities is tabulated in appendix G.

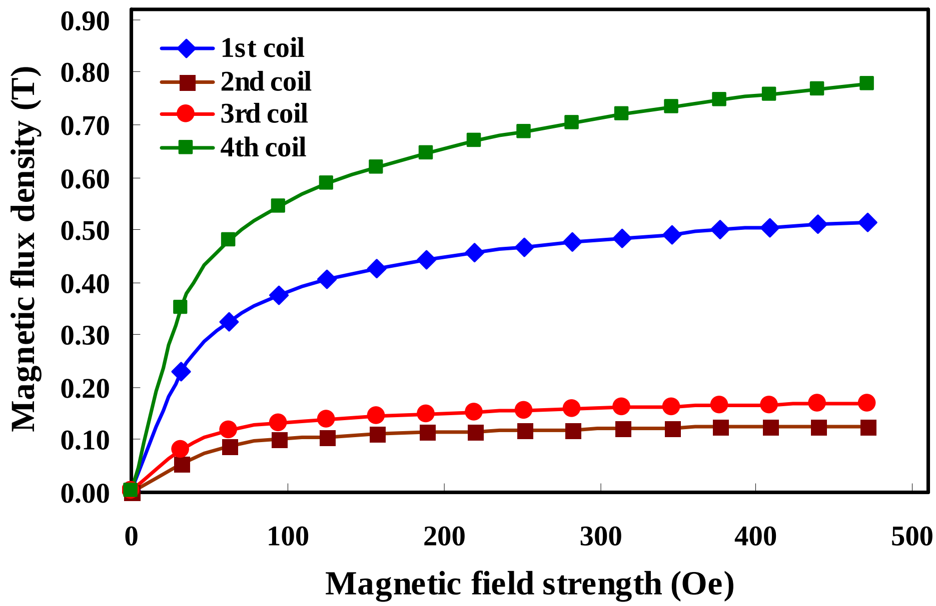

Magnetic flux density (T)
Magnetic field strength (Oe)
1st coil
2nd coil
3rd coil
4th coil

(a)

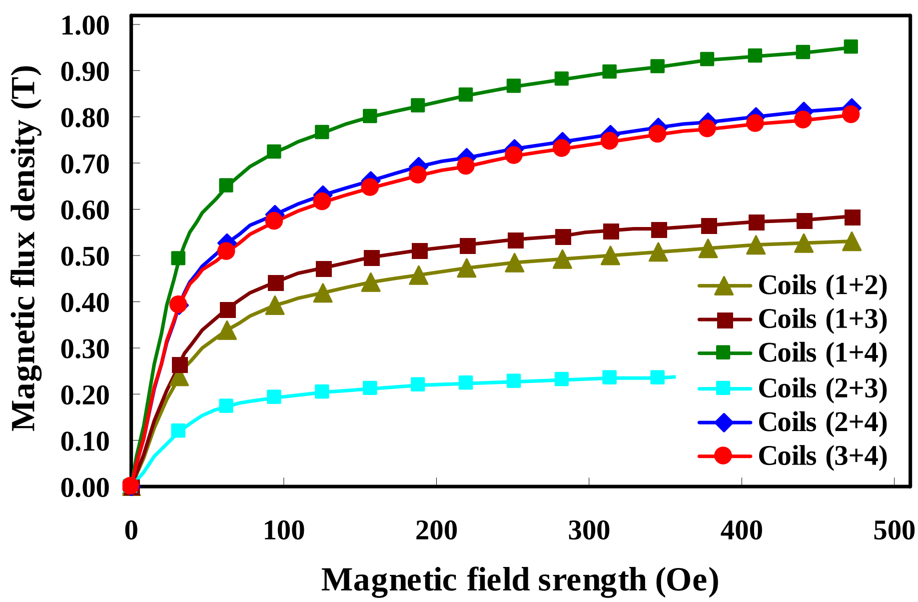

Magnetic flux density (T)
Magnetic field srength (Oe)
Coils (1+2)
Coils (1+3)
Coils (1+4)
Coils (2+3)
Coils (2+4)
Coils (3+4)

(b)

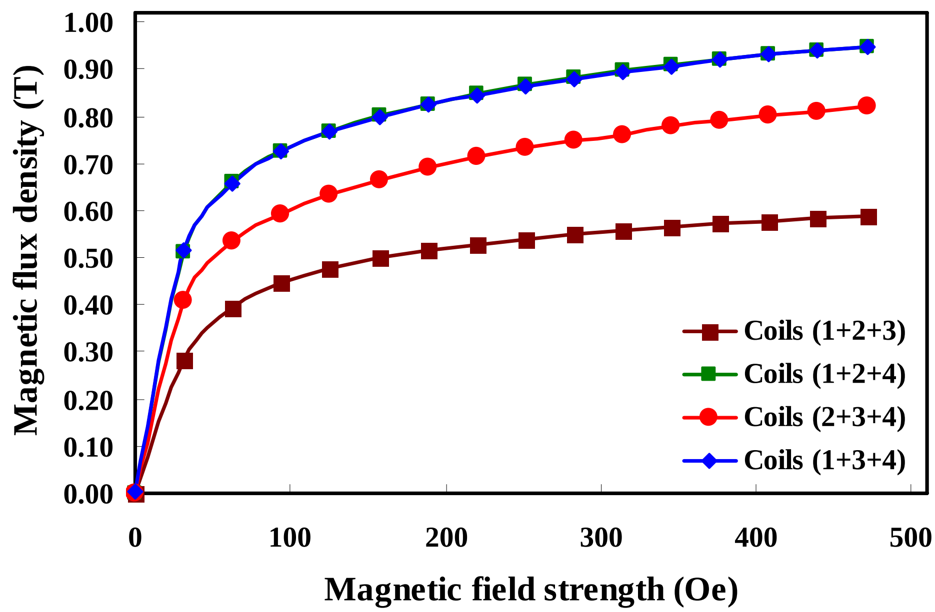

(c)

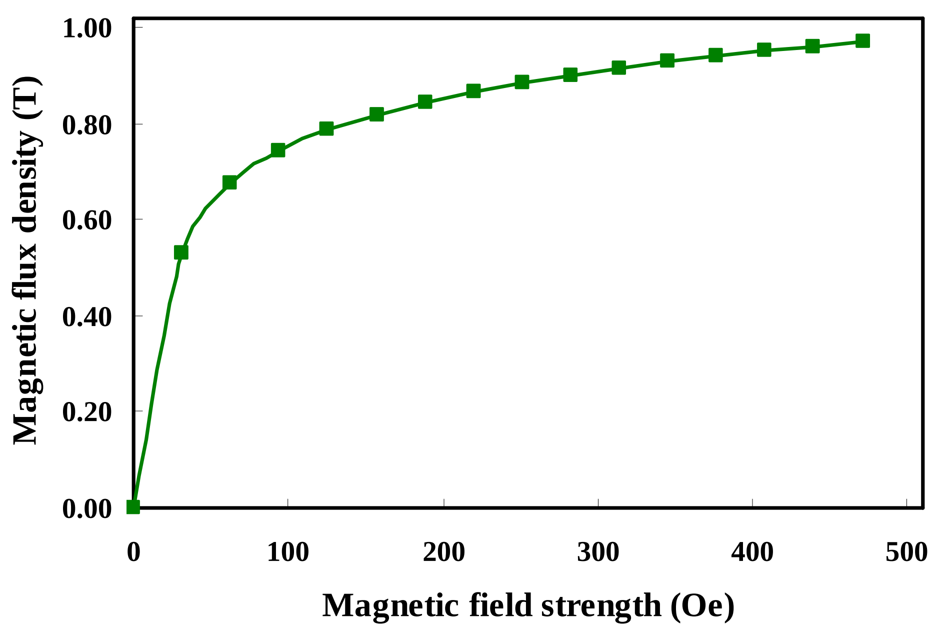

(d)

Figure 4.26: Magnetic flux density of configuration “B” with air-gap close to one corner using curved corners produced by (a) each coil individually (b) combinations of two coils in series (c) combinations of three coils in series (d) all the coils.

Figure 4.26 (a) show that the fourth coil produced the highest magnetic flux density. This was because that this coil was wound around a pure iron core which has much better magnetic properties if compared with low carbon steel core. The second and third coils produced the lowest magnetic flux density. This could be due to leakage in the corners, or the skin effect which is described, in later sections. In general when compared with figure 4.24 (a), the values of flux density are lower and particularly so for coil no. 1, although this was close to the air-gap.

Figure 4.26 (b) shows that coil no. 1 and coil no. 4 produce approximately 0.951 T together whereas all coils produce only about 0.971 T. This emphasises that the contributions of coil no. 2 and coil no. 3 to the C-shape circuit was almost negligible. The magnetic flux density in the centre of the air-gap was 0.486 T. This is half the reading at the edge of the core. This decrease in magnetic flux density value was due to the presence of a screw hole at the centre of the core surface of the air-gap. When compared with figure 4.24 (b), the performance of coil no. 1 is consistently poorer.

Table 4.4 summarises the results achieved by configuration “B”.

Table 4.4: Magnetic flux density produced by configuration “B” using curved corners.

Air-gap location	**Magnetic flux density (T)**	
	At the centre of air-gap	**At the edge of air-gap**
Between two coils	0.556	1.119
On one of the sides and close to one of the corners	0.486	0.971

4.6 C-shape circuit using right-angle corners

The C-shape circuit was assembled as the same circuit depicted in figure 4.23, except that right-angle corners shown in figure 3.4 (b) were used to connect the coils.

The Tesla probe was also located at the edge of core on one side of the air gap. Information about the values of flux densities can be found in appendix I. Figure 4.27 shows the maximum magnetic flux density produced by all coils in comparison with value achieved when using curved corners.

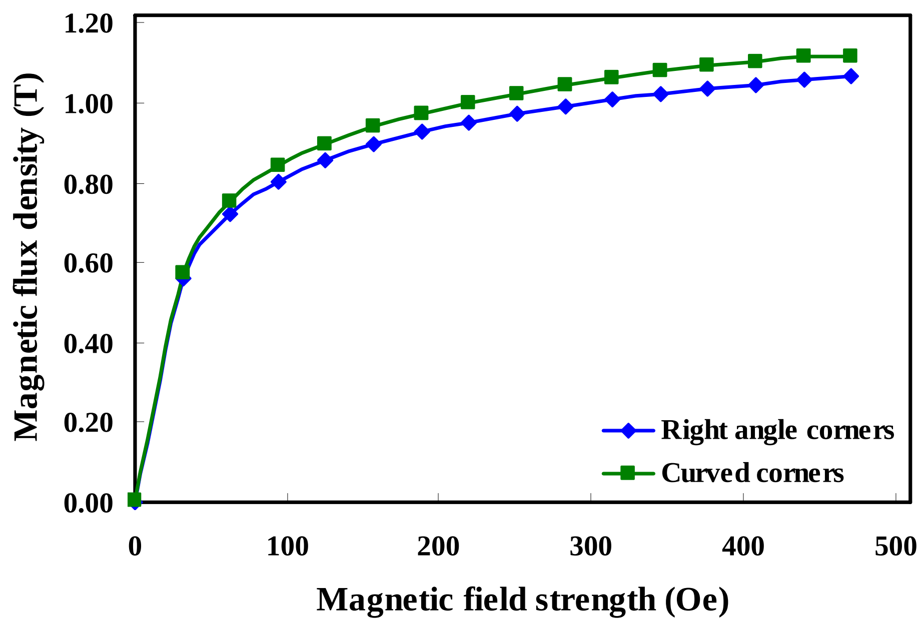

Figure 4.27: Magnetic flux density of configuration “B” using right-angle corners.

It can be seen that, using right-angle corners, the magnetic flux density reached 1.067 T. This is slightly less than the value achieved using curved corners (1.119 T) This indicates that the right-angle corners might have more reluctance to magnetic flux lines than curved corners.

4.7 C-shape circuit using large-diameter component with circular cross-sections

Two types of corners had been tested on the electromagnetic rig at this point; the curved corners and the right-angle corners. In these experiments, new type of corner was introduced to both configuration, configuration “A” and configuration “B”. As shown in figure 3.4 (c), these corners have circular cross-sections measuring 80 mm in diameter, and 50 mm in length. They are made of pure iron, the same material discussed in section 4.5.

These experiments were aimed to investigate the effect of using different types of corner to guide the magnetic flux around the corners with the minimum of flux losses.

4.7.1 Using configuration "A"

Figure 4.28 shows the experimental set-up for configuration "A" using large-diameter components. There are no screw holes either side of the air-gap, and all measurements of flux density were taken at the centre of the air-gap and the edge of the air-gap.

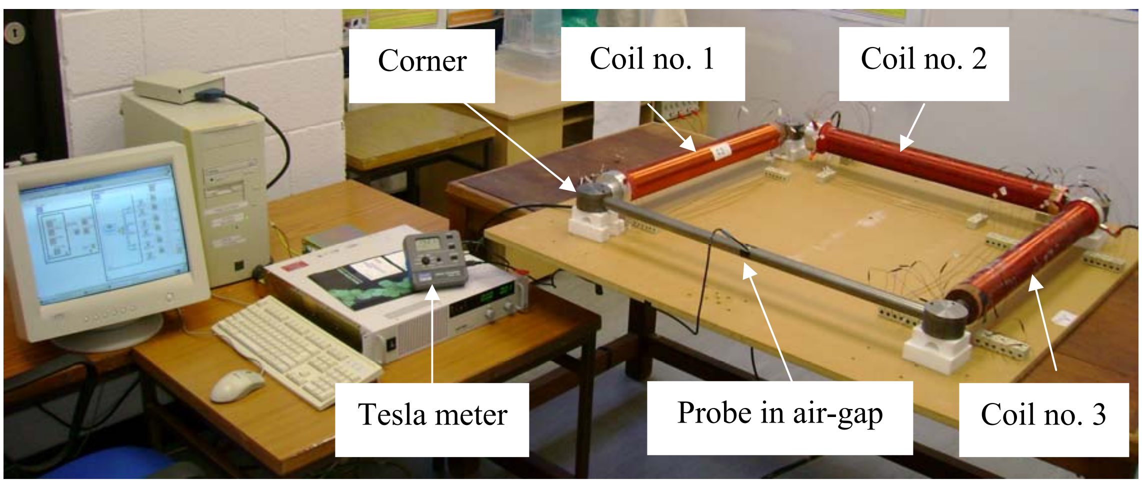

Figure 4.28: Experimental set-up of configuration "A" using large-diameter components with circular cross-sections.

The maximum measured magnetic flux density at the centre of the air-gap was 0.393 T. It reached 0.391 T at the edge of the air-gap as shown in figure 4.29. Magnetic flux densities information is listed in appendix G.

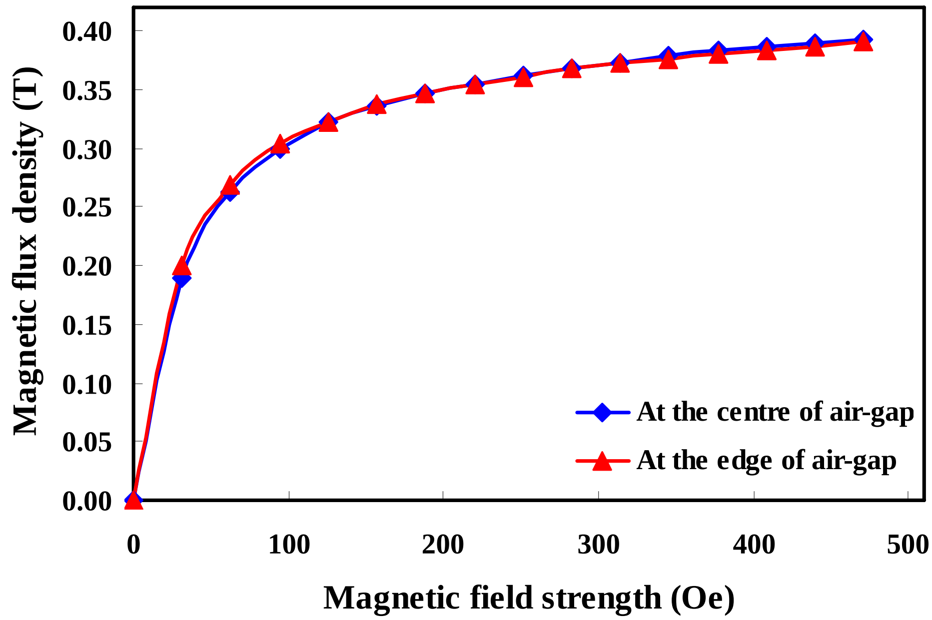

Figure 4.29: Magnetic flux density of configuration "A" using large-diameter components with circular cross-sections.

On the other hand, this value is higher than when curved corners were used in the same configuration (figure 4.19). This could be that these corners guide the flux lines with less reluctance.

4.7.2 Using configuration "B"

The same experimental set-up of configuration "B" shown in figure 4.23 was used in these experiments, except large-diameter components with circular cross-sections were used instead of curved corners.

Three experiments were aimed to investigate the arrangement of coils with respect to the location of the air-gap and also the effect of screw holes either side of the air-gap, or even buried screw holes near the air-gap.

a. Screw holes on the surfaces on either side of the air-gap

In this experiment, the air-gap was located between coil no. 1 and coil no. 4 with screw holes on either side of the air-gap. The magnetic flux density was found to vary according to the position of the meter probe tip. The measured magnetic flux density reached ~ 0.641 T in the centre of the air-gap and 1.169 T at the edge of the air-gap (figure 4.30). Both values are more than the value recorded for the configuration “A” using three coils.

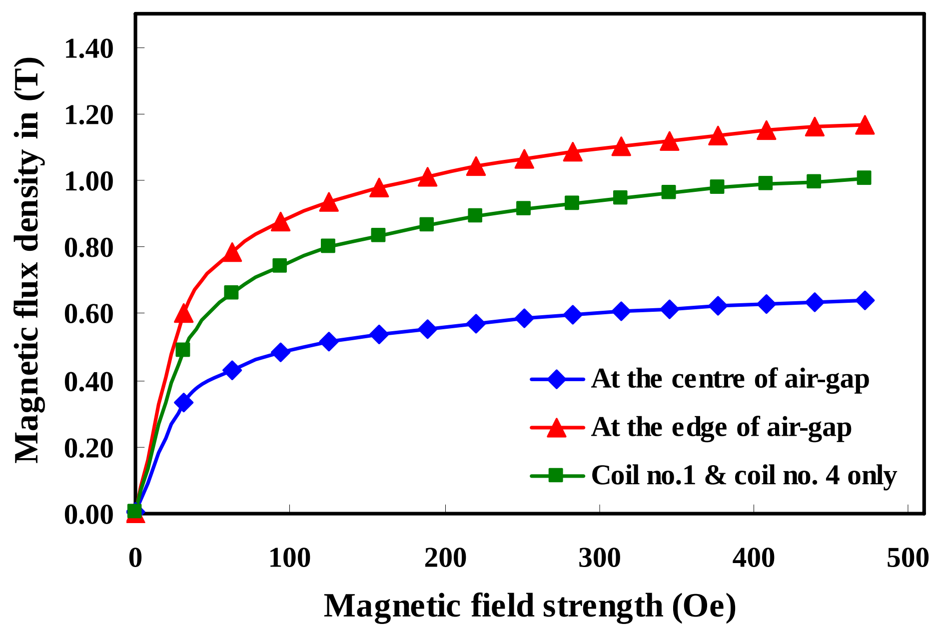

Figure 4.30: Magnetic flux density of configuration “B” using large-diameter components with circular cross-sections with screw holes in the flat surfaces either side of the air-gap.

To investigate the contribution of the back coil (coil no.2 and coil no. 3), a maximum current of 15 amps was only supplied to the coils in line with the testing element (coil no. 1 and coil no. 4). As a result, the magnetic flux density reached 1.008 T (figure 4.30). This value is almost the same value achieved when activating all four coils. This indicates that the back coils make almost no contribution to flux in the C-shape circuit. Values of measured magnetic flux densities can be found in appendix G.

b. Flat surfaces on either side of the air-gap with buried screw holes

In an attempt to assess the impact of buried screw holes beneath the surfaces on either side of the air-gap, flat spacers were added to cover both screw holes. In all other aspects, the same circuit was used as in sub section immediately above.

The result of this change was as follows. The magnetic flux density increased to 0.895 T at the centre of the air-gap, but decreased to 0.913 at each side of the air-gap as shown in figure 4.31 (d). These values are more than double the values achieved in configuration "A" using the same type of corners (and using only three coils).

It can be seen that coil no.2 and coil no. 3 produce very low magnetic flux densities with respect to the other coils as depicted in figure 4.31 (a). To investigate whether these coils could produce more flux, coil no. 1 was swapped with coil no. 2, and analysed individually. The result shows that both coils seem to produce much higher fluxes when placed close to the air-gap. The magnitudes of the fluxes are shown in figure 4.32.

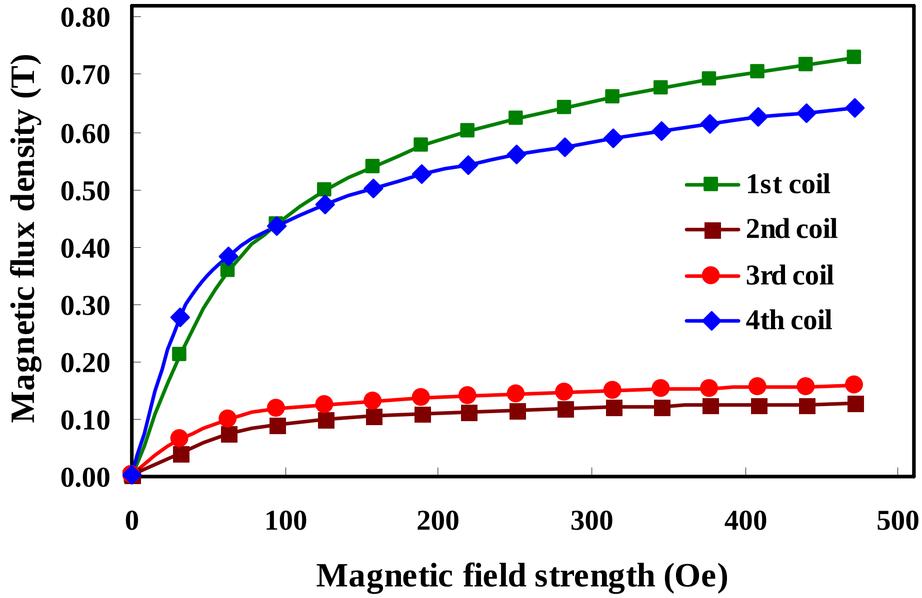
Magnetic flux density (T)
0.80
0.70
0.60
0.50
0.40
0.30
0.20
0.10
0.00
0
100
200
300
400
500
Magnetic field strength (Oe)
1st coil
2nd coil
3rd coil
4th coil

(a)

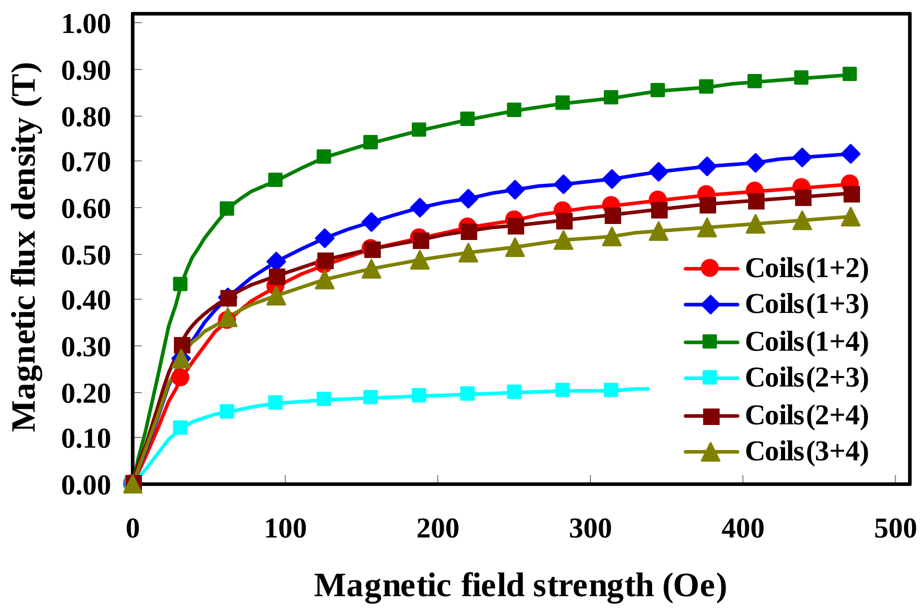
Magnetic flux density (T)
1.00
0.90
0.80
0.70
0.60
0.50
0.40
0.30
0.20
0.10
0.00
0
100
200
300
400
500
Magnetic field strength (Oe)
Coils(1+2)
Coils(1+3)
Coils(1+4)
Coils(2+3)
Coils(2+4)
Coils(3+4)

(b)

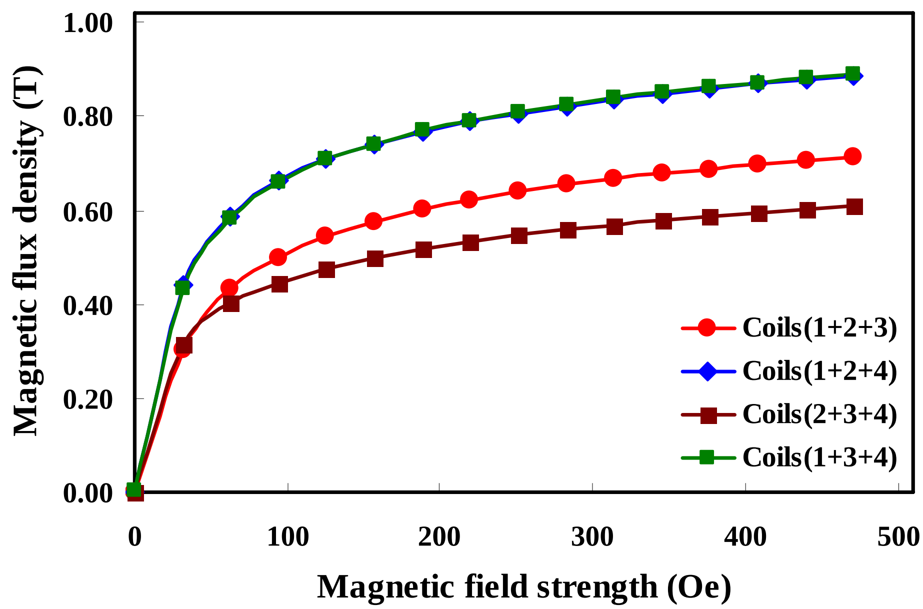

(c)

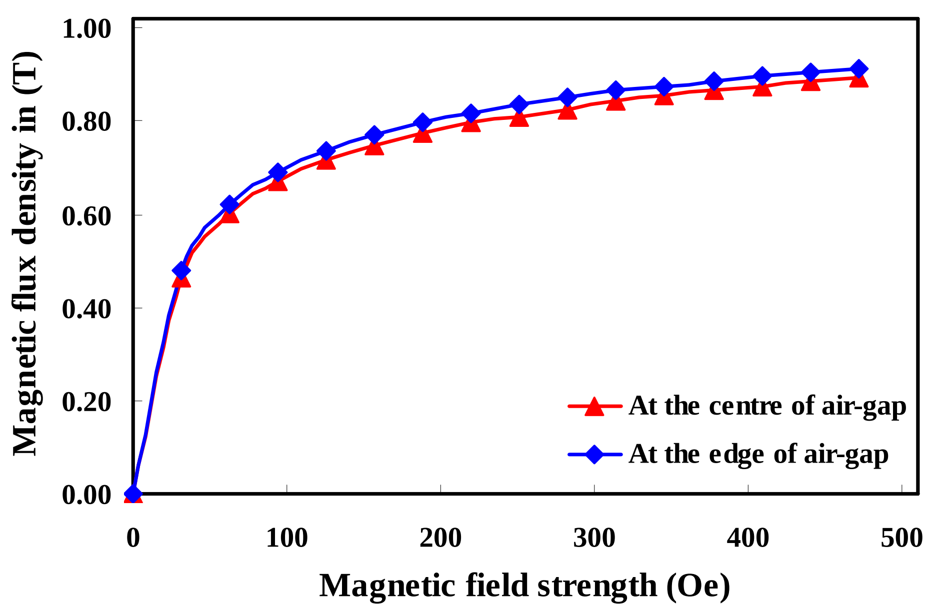

(d)

Figure 4.31: Magnetic flux density of configuration "B" using large-diameter components with circular cross-sections with buried screw holes in the flat surfaces either side of the air-gap produced by (a) each coil individually (b) combinations of two coils (c) combinations of three coils (d) all the coils.

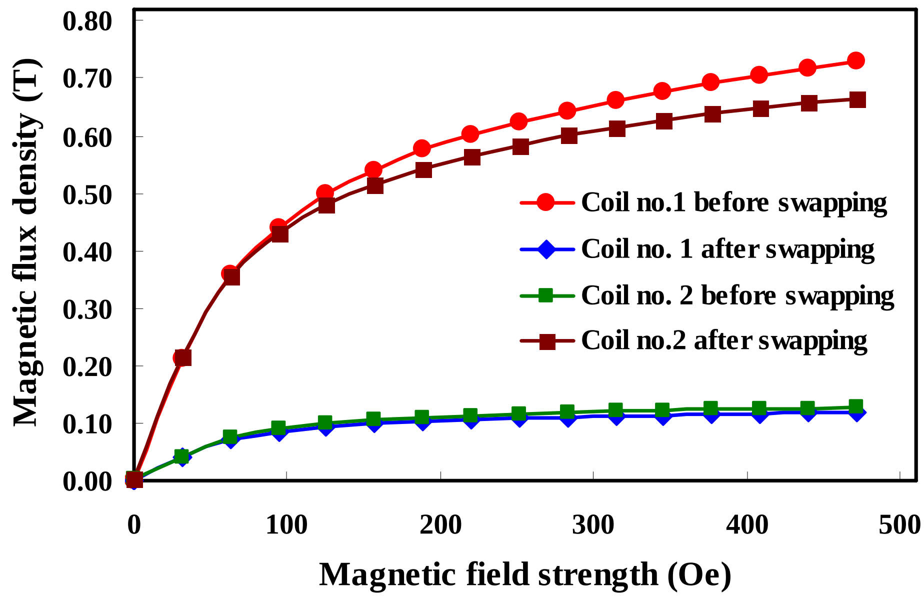

Figure 4.32: Magnetic flux density of configuration "B" using large-diameter components with circular cross-sections with buried screw holes in the flat surfaces either side of the air-gap produced by coil no. 1 and coil no. 2 before and after swapping.

Figure 4.33 also reveals the magnetic flux densities produced only by the coils in line with the testing element (coil no. 1 and coil no. 4) in comparison with magnetic flux density produced only by other coils (coil no. 2 and coil no. 3). It is apparent that, coils in line with the air-gap always produce almost as much magnetic flux density as that produced by all coils. Magnetic flux density information from these experiments is listed in appendix G.

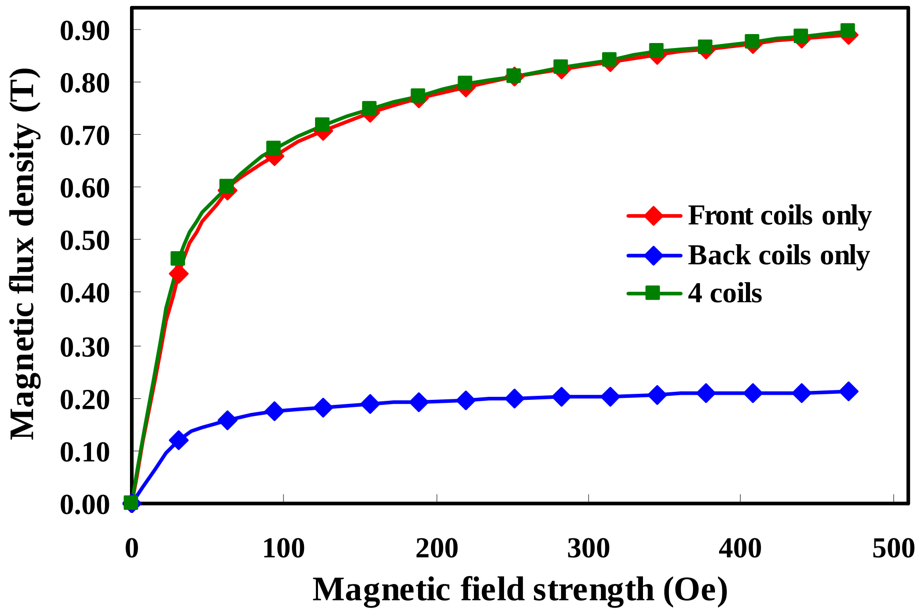

Figure 4.33: Magnetic flux density of configuration "B" using large-diameter components with circular cross-sections with screw holes in the flat surfaces either side of the air-gap.

c. Flat surfaces on either side of the air-gap with no buried screw holes

To eliminate the effect of screw holes altogether, the air-gap was located between coil no. 2 and coil no. 3 where the surfaces either side of the air-gap are flat with no buried screw holes near. Series measurements of magnetic flux density were taken produced by different combinations of coils as shown in figure 4.34. Values of these measurements can be found in appendix G.

The measured magnetic flux density produced by all the coils at the centre of the air-gap and at the edge of the air-gap increased to 1.03 T (figures 4.34 (d)). This increase in the magnetic flux density must be due the absence of any screw holes in the core near the air-gap, with the result that the magnetic flux can penetrate the air-gap region with less reluctance.

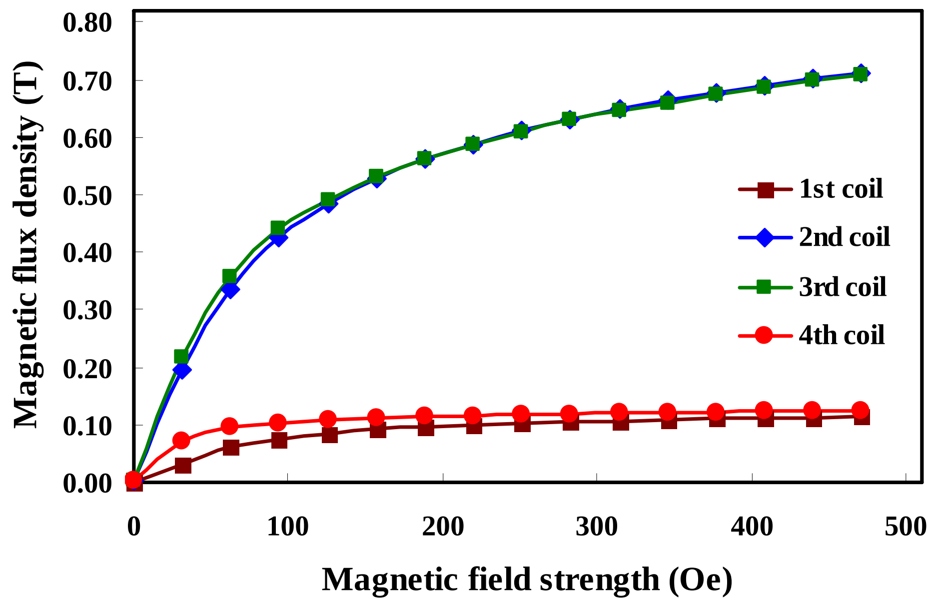
0.80
0.70
0.60
0.50
0.40
0.30
0.20
0.10
0.00
Magnetic flux density (T)
0
100
200
300
400
500
Magnetic field strength (Oe)
1st coil
2nd coil
3rd coil
4th coil

(a)

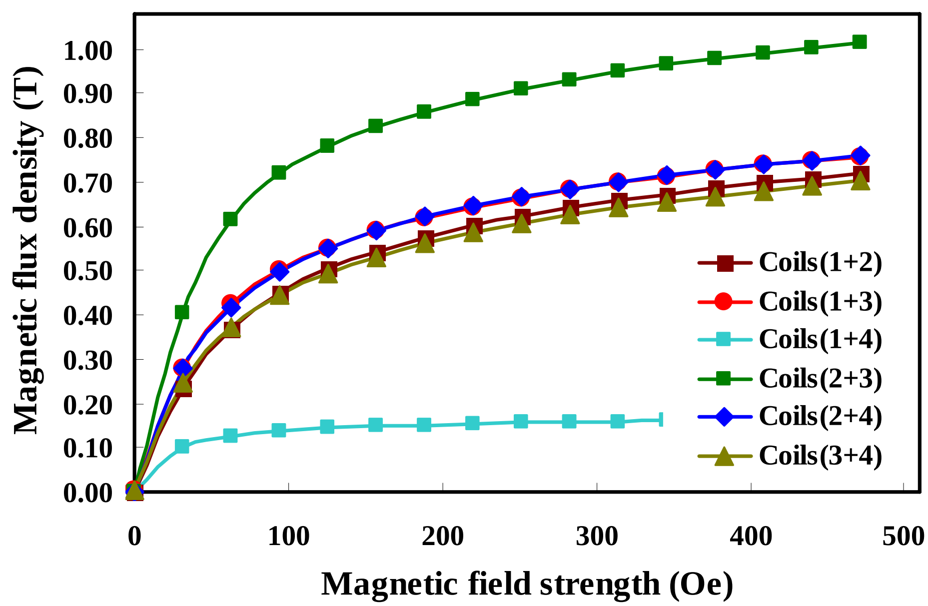
1.00
0.90
0.80
0.70
0.60
0.50
0.40
0.30
0.20
0.10
0.00
Magnetic flux density (T)
0
100
200
300
400
500
Magnetic field strength (Oe)
Coils(1+2)
Coils(1+3)
Coils(1+4)
Coils(2+3)
Coils(2+4)
Coils(3+4)

(b)

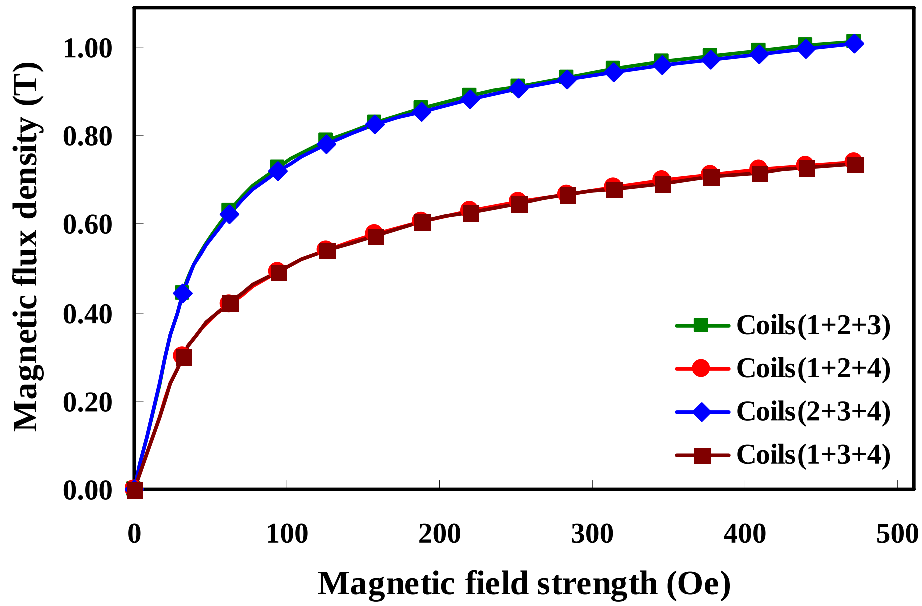

(c)

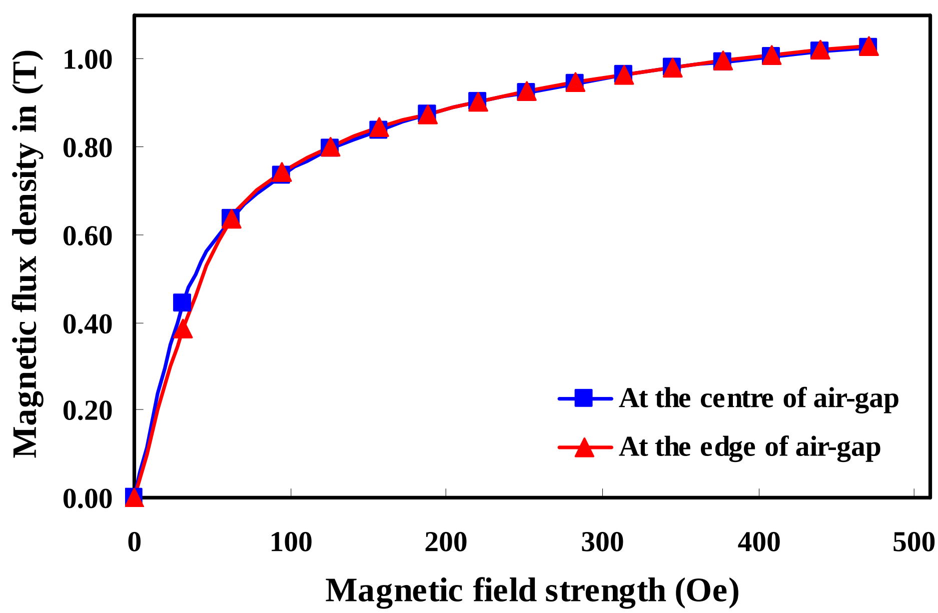

(d)

Figure 4.34: Magnetic flux density of configuration "B" using large-diameter components with circular cross-sections with no buried screw holes near the flat surfaces either side of the air-gap produced by (a) each coil individually (b) combinations of two coils (c) combinations of three coils (d) all the coils.

4.8 Measurement of magnetic flux density in the air-gap produced by coils in line with the testing element in "open circuit"

This test is similar to the experiment carried out in section 4.7 (c), except that coils no.1 and 4 were completely removed from the C-shape circuit. This was done to verify the earlier indications of the reluctance of corners and to investigate whether there was any need to form a "closed circuit" in order to maximise the magnetic flux density produced by an electromagnetic rig. Figure 4.35 illustrates the experimental set-up for the measurement of magnetic flux density produced only by coils in line with the testing element. Only coils no. 2 and coil no. 3 are connected in series and supplied by a maximum current of 15 amps. This resulted in only a minor reduction in flux density at the centre of the air-gap to 0.943 T as shown in figure 4.36. The "closed circuit" result was 1.03 T.

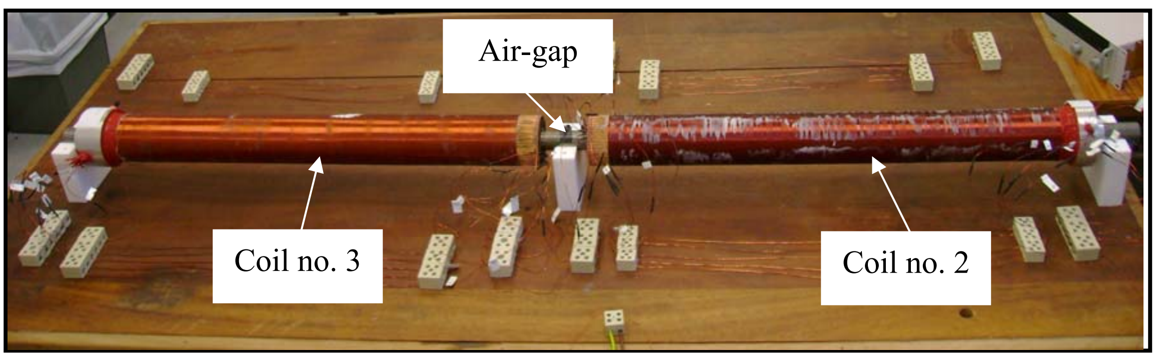

Figure 4.35: Experimental set-up for the measurement of magnetic flux density produced only by coils in line with the testing element.

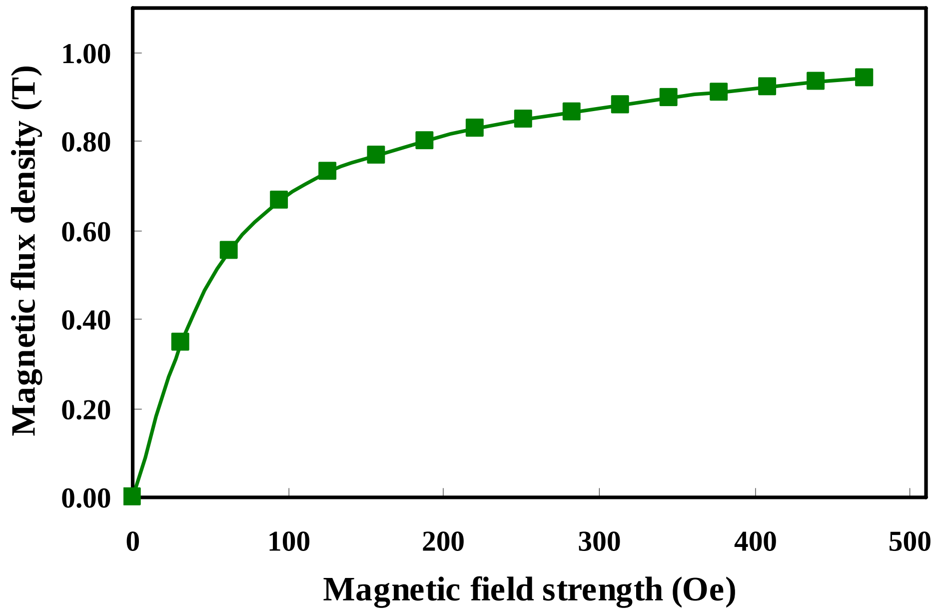

Figure 4.36 Magnetic flux density in the air-gap produced only by coils in line with the testing element.

4.9 Summary of chapter 4

Experimental trials were performed on the C-shape circuit. The circuit was mainly assembled into two configurations; configuration "A" and configuration "B". In each configuration, different types of corners were used in order to establish which was best in producing a high magnetic flux. Experimental results emphasized that configuration "A" produced higher magnetic flux density when large-diameter components with circular cross-sections were used. Configuration "B" showed even better results than configuration "A". Results also showed that the efficiency of the electromagnetic rig in producing high magnetic fields can be decreased due to holes in the material for screws and probably also due to effects related to drilling and machining of the steel cores, especially when drilling is carried out near or at the air-gap. Other reasons for discrepancies include flux leakages across the corners and other components in the "C-shape circuit".

CHAPTER 5

MAGNETIC FIELD SIMULATION OF THE C-SHAPE CIRCUIT

5.0 Introduction

This chapter presents the computer generated simulation results for the magnetic fields generated by the C-shape design with different configurations.

Finite Element Method Magnetics (FEMM) computational modelling software [78] was used to predict magnetic field strengths generated by the electromagnetic rig.

This program is specifically designed to solve electromagnetic problems on two-dimensional planar and axisymmetric domains. It has been employed by various researchers in simulation analysis relevant to magnetic field problems [93 - 95].

Planar models were employed in the FEMM software package for the magnetostatic problems in 2-Dimensional spaces. The magnetostatic problems are problems in which the fields are time-invariant. In this case, the magnetic field intensity *H* must comply with

$$J = \nabla \times \vec{H} \tag{5-1}$$

In 3- Dimensional spaces, the current density is

$$J = \frac{\partial \vec{H}}{\partial x} + \frac{\partial \vec{H}}{\partial y} + \frac{\partial \vec{H}}{\partial z} \tag{5-2}$$

In planar, the component $\frac{\partial \vec{H}}{\partial z}$ can be considered as zero, it follows that:

$$J = \frac{\partial \vec{H}}{\partial x} + \frac{\partial \vec{H}}{\partial y} \tag{5-3}$$

Where, ∇ is the divergence operator (1/m) and J is the current density (Amps/m^2). In another case, according to Gauss's law for magnetism, in the absence of magnetic monopoles, the magnetic flux density *B* must comply with

$$0 = \nabla \cdot \vec{B} \tag{5-4}$$

Where, *B* is the magnetic flux density (Tesla).

Equations 5-1 and 5-4 are subject to a constitutive relationship between magnetic flux density *B* and magnetic field intensity *H* for each material; same as in equation (2-10)

$$\vec{B} = \mu\vec{H}$$

If a material is nonlinear, for instance saturating iron, the permeability μ is actually a function of magnetic flux density *B*,

$$\mu = \frac{\vec{B}}{\vec{H}\left(\vec{B}\right)} \tag{5-5}$$

After nonlinear materials have reached the saturation points, the values of magnetic flux density will remain the same as magnetic field intensity increases.

FEMM goes about finding a field that satisfies equations (2-10) (5-1), and (5-4) via a magnetic vector potential approach. The magnetic flux density is written in terms of the vector potential *A* (magnetic vector potential) as [96]

$$\vec{B} = \nabla \times \vec{A} \tag{5-6}$$

It follows that:

$$J = \nabla \times \left(\frac{1}{\mu\left(\vec{B}\right)} \right) \nabla \times \vec{A} \tag{5-7}$$

For a linear isotropic material (and assuming the Coulomb gauge $\nabla \cdot A = 0$), equation (5-7) reduces to [90]

$$J = -\frac{1}{\mu}\nabla^2\vec{A} \tag{5-8}$$

In practice, FEMM uses equation (5-7) so that magnetostatic problems with a nonlinear *B-H* relationship can be solved.

A is a vector with three components in the 3-Dimensional case. However, in 2-dimensional planar and axisymmetric cases, only one component was left in one direction while the other two components are zero. There was an advantage in using vector potential formulation because all the conditions can be fulfilled and combined into a single equation. If *A* is found, *B* and *H* can then be calculated by differentiating *A*.

For boundary conditions in the FEMM software package, a Robin boundary condition was selected where this boundary was sort of a mix between Dirichle*t* and Neuman*n*, prescribing a relationship between the value of *A* and its normal derivative at the boundary. A Dirichlet boundary condition was applicable if the value of vector potential *A* was explicitly defined on the boundary, for example $A = 0$ along a boundary to keep the magnetic flux from crossing the boundary, while a Neumann boundary condition specified the normal derivative of potential along the boundary. The homogeneous Neuman*n* boundary condition $\partial A/\partial n = 0$ was defined along a boundary to force the flux to pass the boundary condition at exactly 90° angle to the boundary and applicable for a very high permeability metal. Therefore, by using the Robin boundary condition, the magnetic field produced by the coil could be modelled in an unbounded space while still only modelling a finite region of that space. For an asymptotic boundary condition, the coefficients in a boundary condition can be represented by

$$\frac{1}{\mu_r \mu_0} \frac{\partial \vec{A}}{\partial n} + C_0 \vec{A} + C_1 = 0 \tag{5-9}$$

Where, μ_r is the relative magnetic permeability of the region adjacent to the boundary, μ_0 is the permeability of free space and n represents the direction normal to the boundary.

Coefficients C_0 and C_1 are specified by

$$C_0 = \frac{1}{\mu_r \mu_0 R} \tag{5-10}$$

$$C_1 = 0 \tag{5-11}$$

Where, *R* is the outer radius of a sphere problem domain.

5.1 Magnetic field simulation of C-shape using gradual curved corners

The C-shape circuit was modelled in to two different configuration, configuration "A" and configuration "B". In each configuration different corners were applied to the magnetic circuit as shown in figure 5.1.

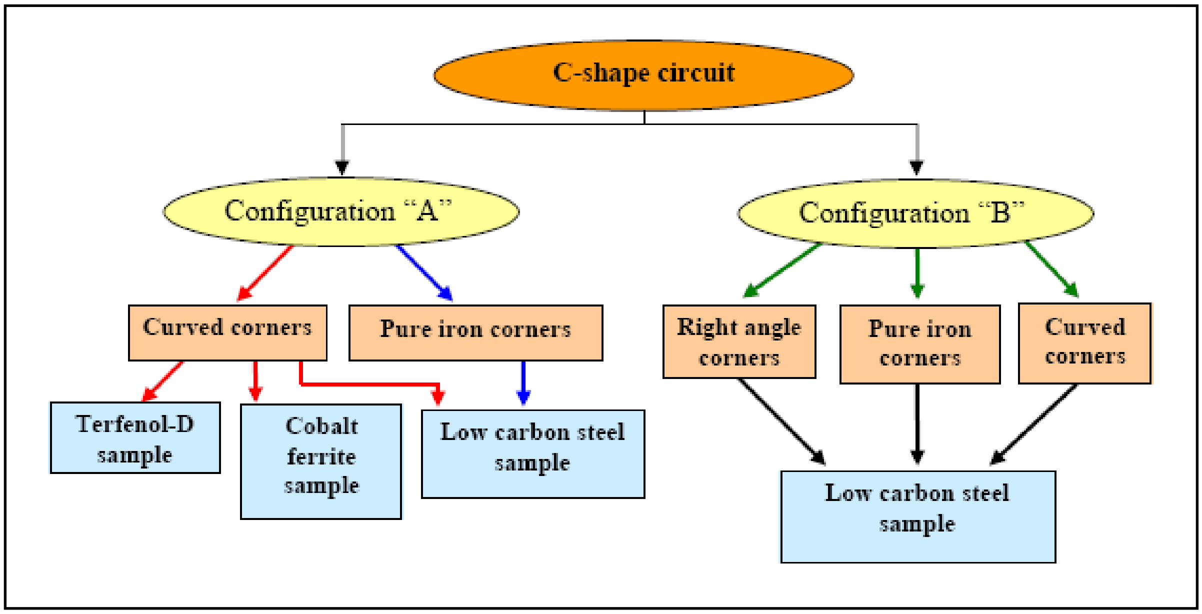

Figure 5.1: Simulation procedure**.**

In this analysis of the magnetic field generated by different configurations using curved corners was performed using FEMM. The magnetic properties of the non-magnetic materials were assumed to be linear such as stainless steel, copper wire and air. The magnetic properties of the magnetic materials such as low carbon steel, low carbon steel sample, and Terfenol-D sample were assumed to follow the *B-H* curves given in the software package, whereas magnetic properties of the cobalt ferrite sample were assumed to follow the *B-H* curve obtained from extrapolating the data from Cedrat. Simulation results were based on using planar model for each simulation trial.

5.1.1 Magnetic field simulation results of configuration "A"

This configuration consists of three coils wound around three magnetic core sections which are rod-shaped and form the sides of a square. Four curved corners were used to connect the three coils to form a continuous conduit for the magnetic flux, except for a gap of 52 mm, where 50 mm would be filled with a sample being tested. The three coils are identical and consist of 8,000 turns.

a. Configuration "A" with cobalt ferrite sample placed in the air gap

This model was entered in FEMM with cobalt ferrite placed in the air-gap as shown in figure 5.2. Table 5.1 shows the data used in FEMM.

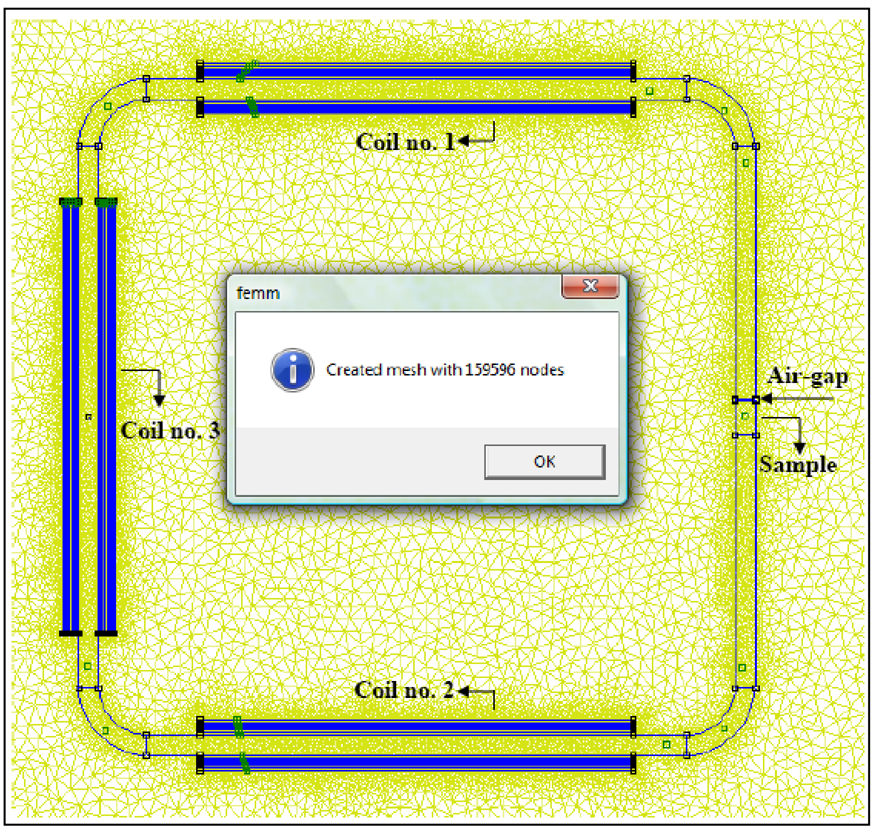

Figure 5.2: Configuration "A" with cobalt ferrite sample placed in the air gap.

Table 5.1: Data entered in FEMM using cobalt ferrite sample in the air-gap.

Problem type	Mesh size		Current in each layer
Planar	Air	20	3 Amps
	Core	5	
	Coils	1	
	Cobalt ferrite sample	5	

The magnetic flux density distribution in this configuration and details regarding the magnetic flux density distribution within the air gap and the cobalt ferrite sample are shown in figures 5.3 and figure 5.4 respectively. The magnetic flux density along the centre of the air gap is illustrated in figure 5.5.

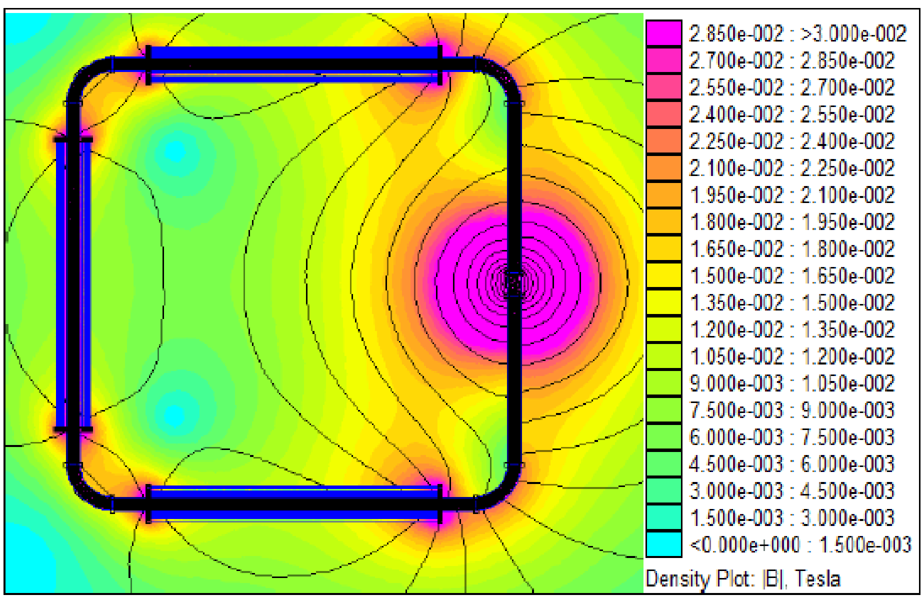

Figure 5.3: Simulated magnetic flux density distribution around the C-shape circuit using configuration “A” with cobalt ferrite sample in the air-gap.

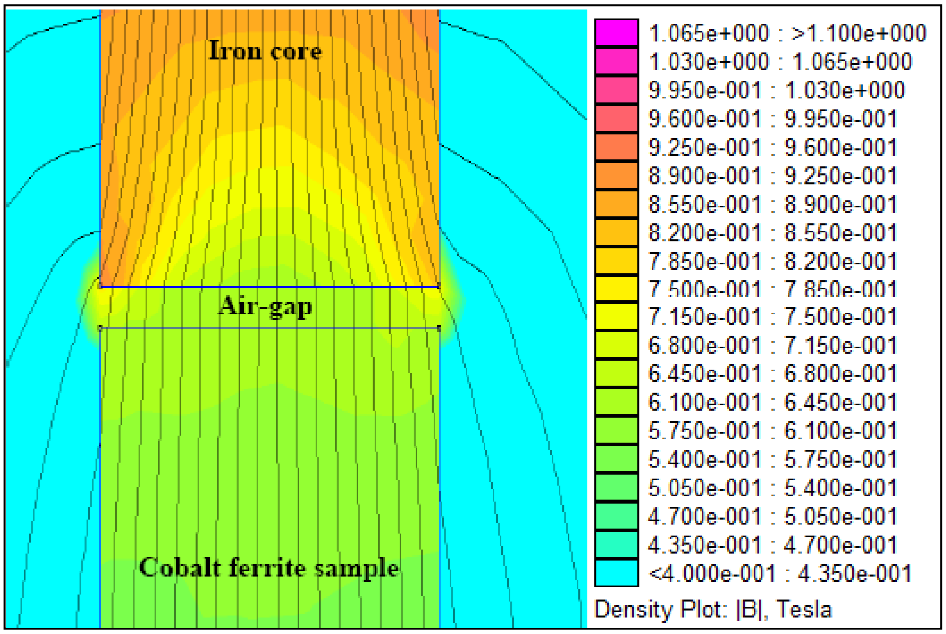

Figure 5.4: Simulated magnetic flux density distribution across the air-gap and cobalt ferrite sample.

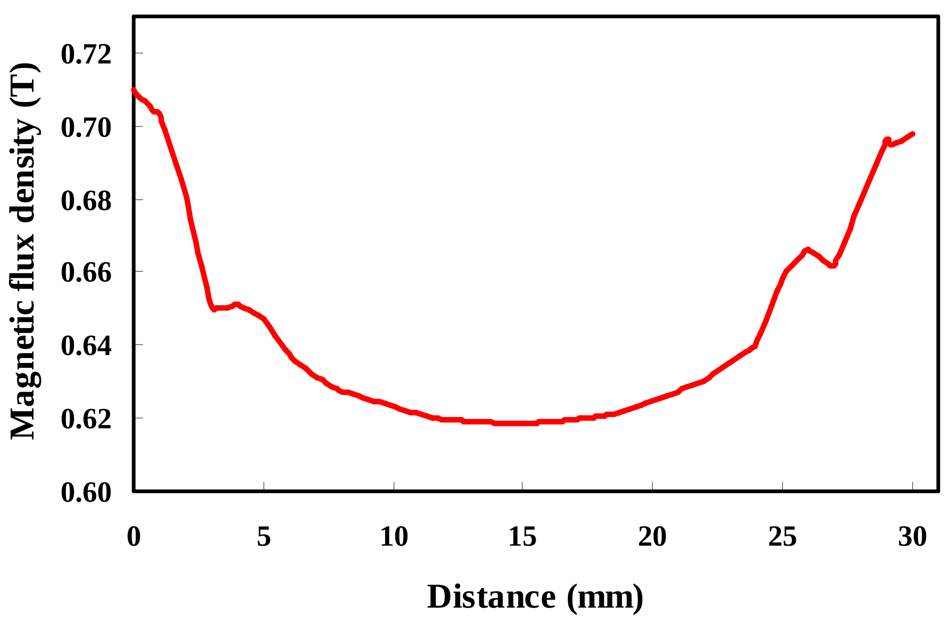

Figure 5.5: Simulated magnetic flux density across the centre of the air-gap with cobalt ferrite sample in the air-gap.

As can be seen from figure 5.5, the magnetic field intensity reached 0.618 T in the centre of the air gap, and 0.71 T at the both ends of the air-gap. This is much smaller than the density predicted in the theoretical estimation which is 1.66 T. There is an obvious explanation for this discrepancy. The derivation of equation 3-9 assumes a constant magnetic flux flows through the whole of the "C" shape including its "jaws". However, Figure 5.3 indicates that this is not strictly true. There is leakage of flux at various points in the circuit. There is some leakage at the corners of the iron core, but the largest leakage occurs across the two ends of the C-shape, where magnetic flux lines can be seen to by-pass the sample. The extent of the flux leakage is difficult to estimate from the diagram, because the depiction tends to exaggerate the amount of leakage, making it difficult to visualise the amount of concentrated flux passing along the iron core. It is therefore not at all surprising that the more detailed and realistic FEMM predicts a magnetic field strength at the air gap, in comparison with the simpler prediction with its ideal assumption of no flux leakage. As a result of this discrepancy between the FEMM predictions and the prediction based on equation 3-9, it is expected that the equipment will not yield the required 9,000 Oersteds of magnetic field strength in the sample.

Also in figure 5.5, it can be seen that the magnetic field strength increases at each side of the air-gap. It is a feature of these plots that variation of the magnetic field strength often occurs at each side of the air-gap, some times greater and some times smaller than the value at the centre of the air-gap. The reason for these variations is not fully understood. Some times it could be due to flux leakage, but some times it could be the result of the FEMM software.

In an attempt to investigate the effect of mesh size on results, the data shown in table 5.1 were altered. The new values of mesh size (roughly half the original values) shown in table 5.2 were used to simulate the same FEMM model shown in figure 5.2.

Table 5.2: New values of mesh size

Problem type	Mesh size		Current in each layer
Planar	Air	10	3 Amps
	Core	3	
	Coils	0.5	
	Cobalt ferrite sample	3	

The magnetic flux density reached 0.618 T at the centre of the air-gap as shown in figure 5.6. This is the same value achieved with mesh size data shown in table 5.1.

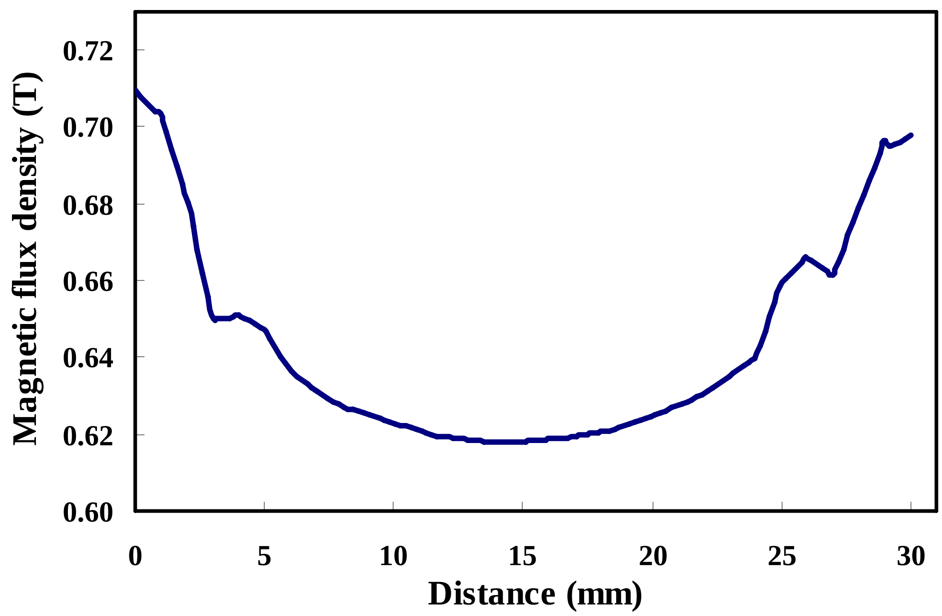

Figure 5.6: Simulated magnetic flux density across the centre of the air-gap with cobalt ferrite sample in the air-gap using different mesh size.

b. Configuration "A" with Low carbon steel sample placed in the air gap

Similar to the previous simulation trial carried out in section (a), the same model and the parameter values listed in table 5.1 were used in the FEMM, except that a sample of low carbon steel is placed in the air-gap.

Figure 5.7 reveals the flux density distribution around the magnetic circuit. Less leakage was observed around the air-gap when compared with figure 5.3. As can be seen, the magnetic flux lines seemed to penetrate the air-gap with less reluctance as shown in figure 5.8. Therefore, higher values of magnetic flux density were observed when low carbon steel sample was used. As shown in figure 5.9, the magnetic flux density reaches about 1.36 T in the centre of the air-gap, and 1.353 T at both edges of the air-gap. This value is more than double the value achieved with the cobalt ferrite sample. The reason for this is that low carbon steel has higher magnetic properties (higher permeability) than the cobalt ferrite sample. Other reasons for discrepancies include flux leakages especially around the air-gap.

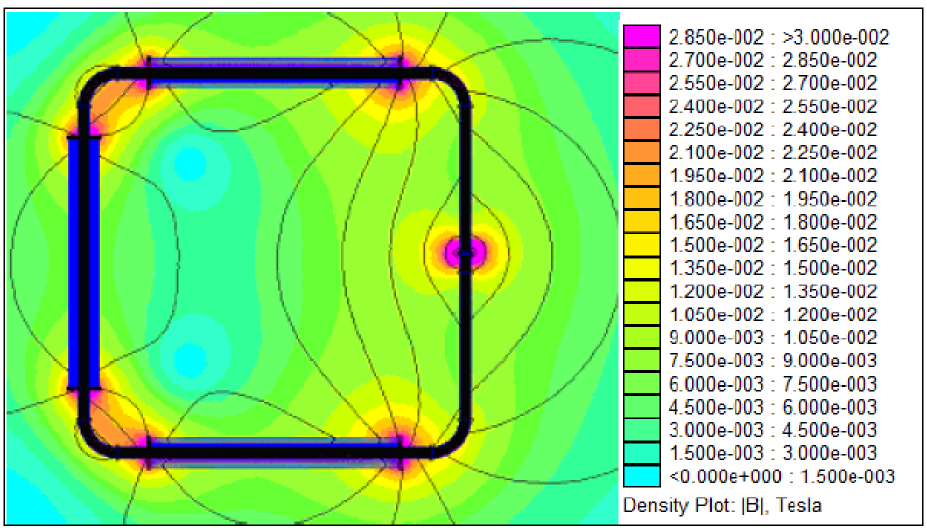

Figure 5.7: Simulated magnetic flux density distribution around the C-shape circuit using configuration "A" with low carbon steel sample in the air-gap.

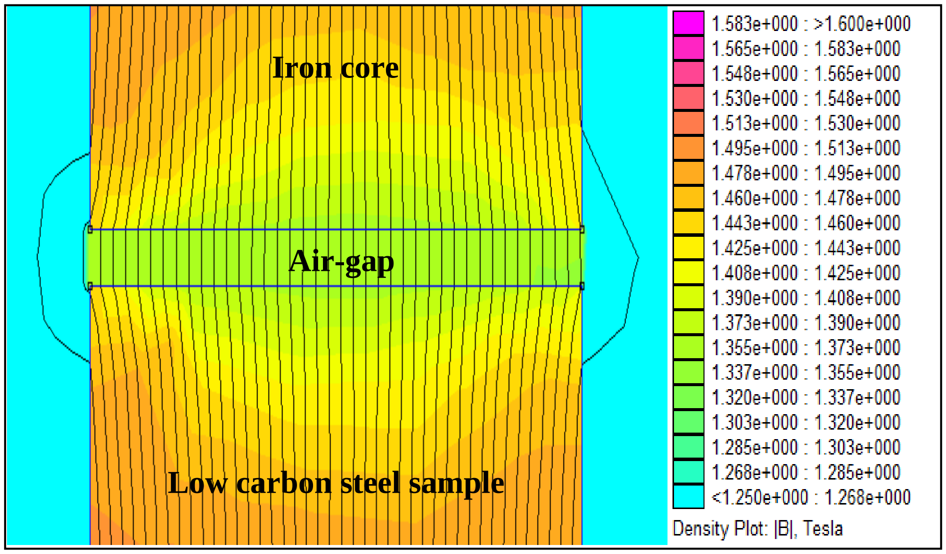

Figure 5.8: Simulated magnetic flux density distribution across the air-gap and low carbon sample.

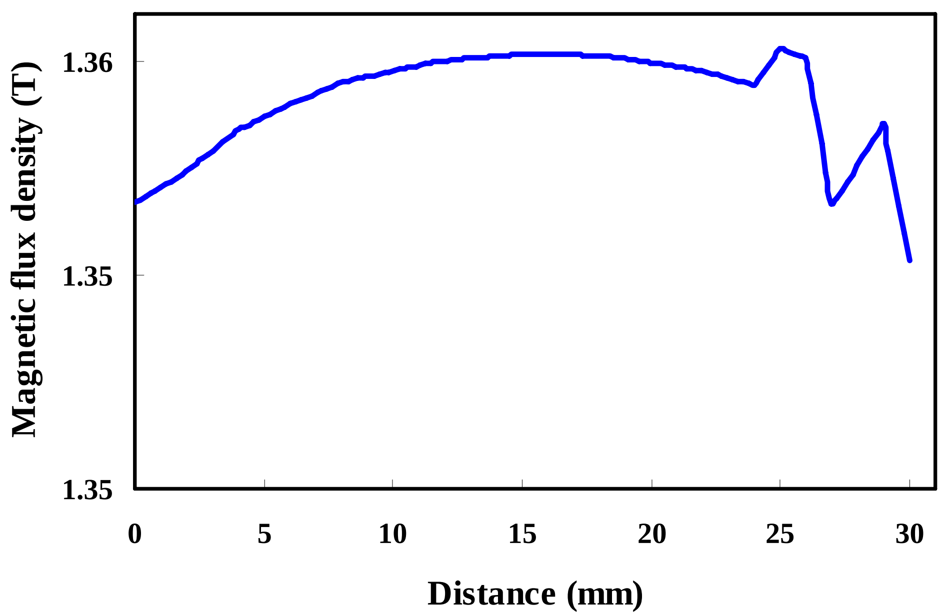

Figure 5.9: Simulated magnetic flux density across the centre of the air-gap with low carbon steel sample in the air-gap.

c. Configuration “A” with Terfenol-D sample placed in the air gap

In this simulation trial, Terfenol-D sample was placed in the air-gap. Figure 5.10 shows the flux distribution around the magnetic circuit. Similar to low carbon steel sample, the flux lines seemed to penetrate the air gap more easily than in the case of the cobalt ferrite sample as depicted in figure 5.11. The magnetic flux density at the centre of the air-gap reached about 1.08 T, and 1.06 at the edges of the core (figure 5.12). This value is much higher than in the case of cobalt ferrite sample, and a bit smaller than the case of low carbon steel sample. This is again because the low carbon steel has higher permeability than both cobalt ferrite and Terfenol-D.

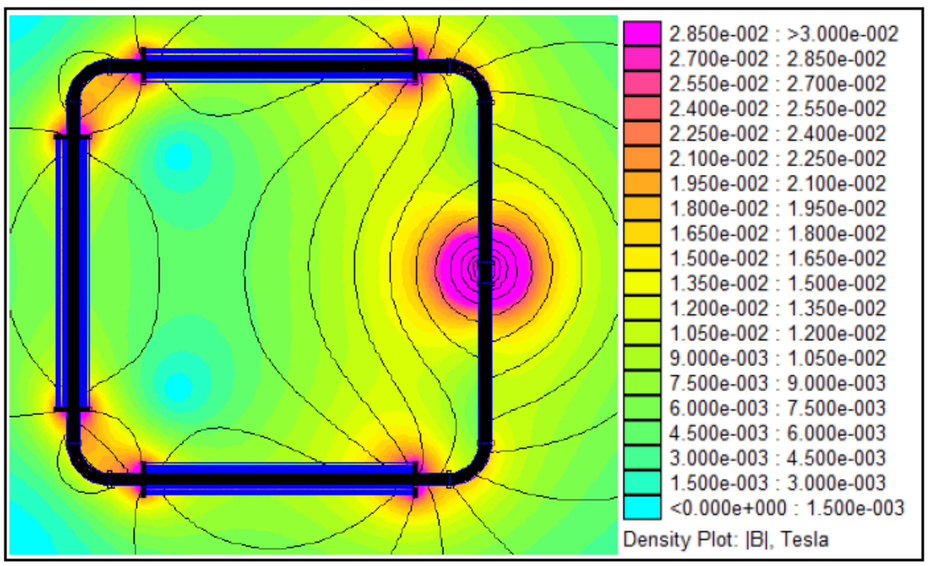

Figure 5.10: Simulated magnetic flux density distribution around the C-shape circuit using configuration “A” with Terfenol-D sample in the air-gap.

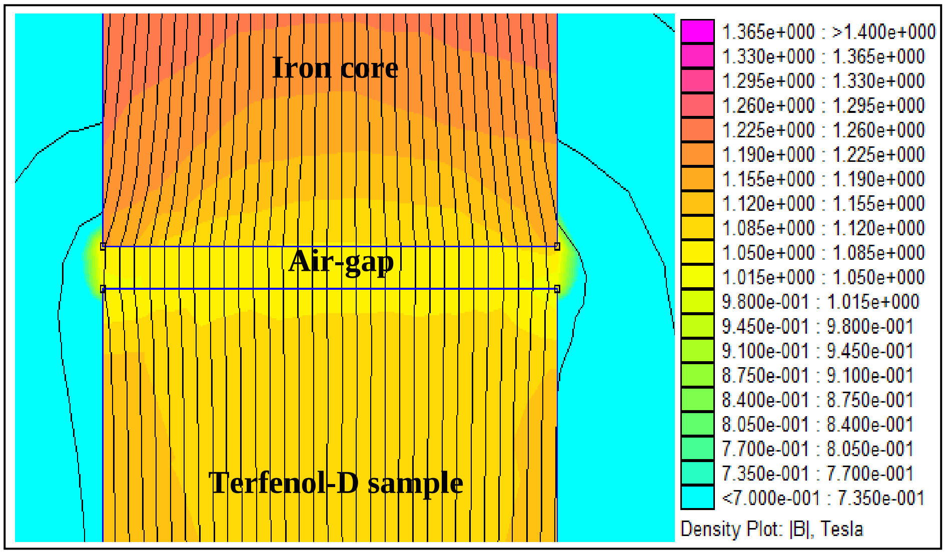

Figure 5.11: Simulated magnetic flux density distribution across the air-gap and Terfenol-D sample.

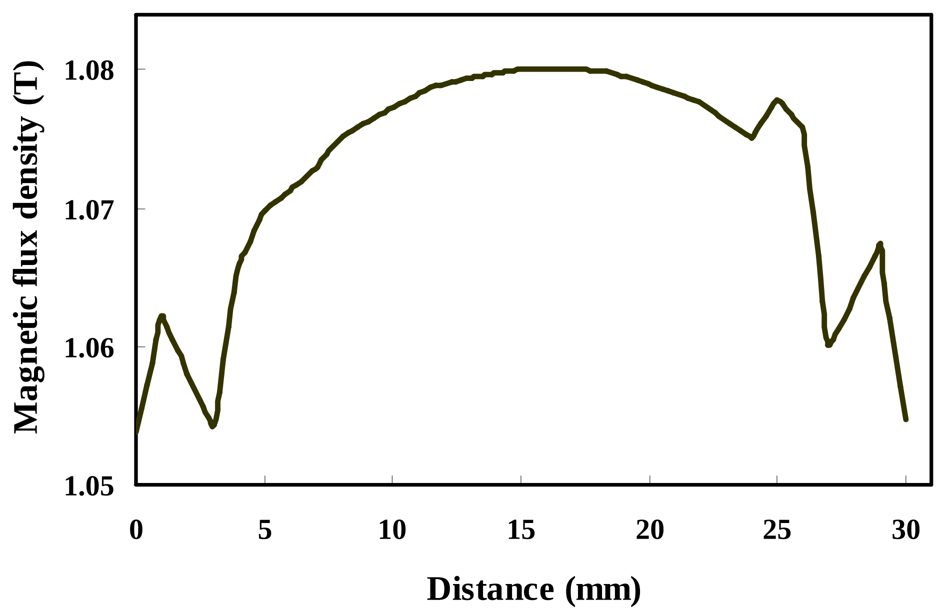

Figure 5.12: Simulated magnetic flux density across the centre of the air-gap with Terfenol-D sample in the air-gap.

Table 5.3 presents a comparison between simulated results and experimental results.

Table 5.3: Comparison between simulated results and practical results of magnetic flux density produced by configuration “A” using curved corners.

Sample	**Value of magnetic flux density (T) when current is 3 amps**		
	Simulation results		**Experimental results**
	At the centre of air-gap	**At the edge of air-gap**	
Cobalt ferrite	0.618	0.71	0.08
Low carbon steel	1.36	1.353	0.25
Terfenol - D	1.08	1.06	0.24

It can be seen that the experimental results fell far short of both the calculated magnetic field strengths in all cases and the values predicted by the software.

5.1.2 Magnetic field simulation results of configuration “B”

In an attempt to assess the impact of the arrangement of the coils in the magnetic circuit, the coils were arranged closer to the air-gap as shown in figure 5.13.

In this configuration, the cobalt ferrite sample and the Terfenol-D sample were not used in the simulation. Therefore it is assumed that a low carbon steel sample is placed in position beside the air-gap of 2mm.

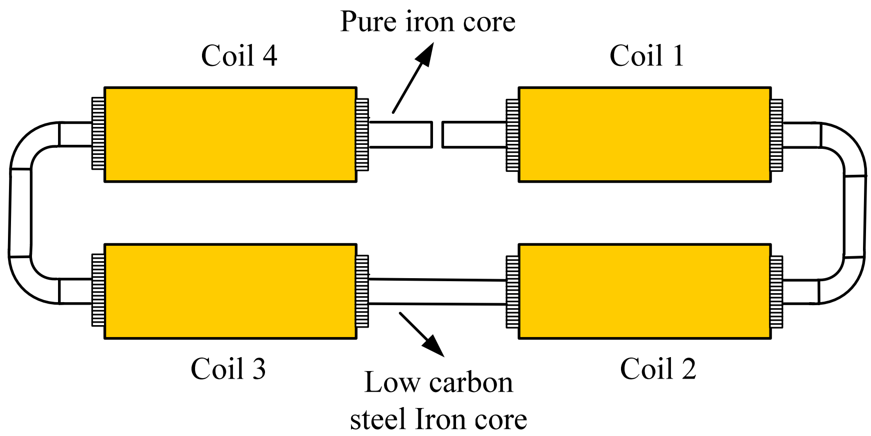

Figure 5.13: Structure of configuration "B" using curved corners.

Table 5.4 depicts the data entered in FEMM. As a result, the magnetic flux density in the centre of the air-gap reached approximately 1.53 T, and 1.19 T and 1.50 T at the edges of the centre of air-gap as depicted in figure 5.14.

Table 5.4: Data entered in FEMM for configuration "B".

Problem type	**Mesh size**		**Current in each layer**
Planar	Air	10	3 Amps
	Cores	1	
	Coils	1	
	Corners	1	

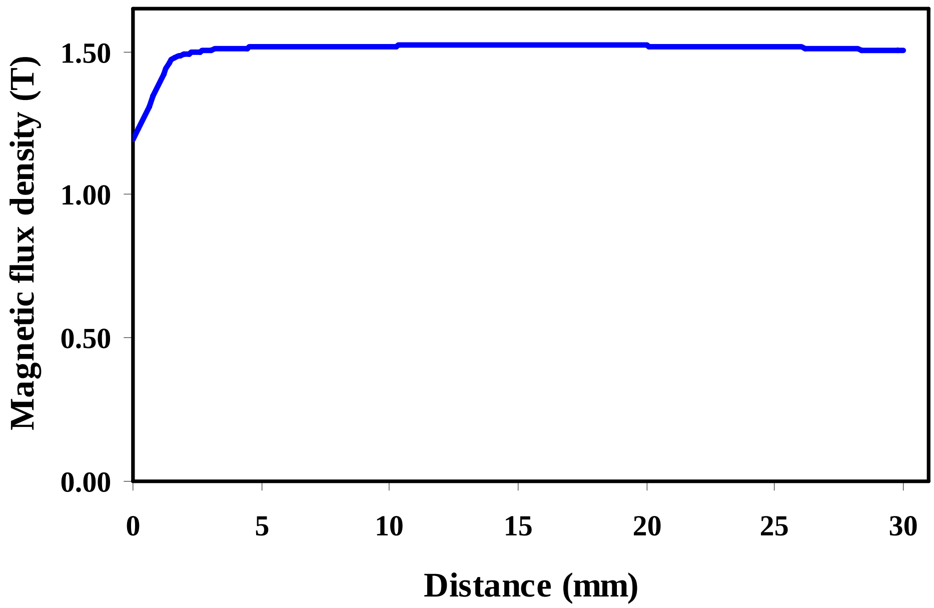

Figure 5.14: Simulated magnetic flux density across the centre of the air-gap using configuration "B".

This value is slightly bit higher than the value achieved in the first configuration using low carbon steel sample (1.36 T). This is believed due to the proximity of the coils to the air-gap, or to the fact that leakage occurs at the corners.

5.2 Magnetic field simulation of C-shape using abrupt right-angle corners

5.2.1 Magnetic field simulation results of configuration "B"

Right-angle corners were used in this simulation as shown in figure 5.15. The same data in table 5.4 was used in this simulation trial. Magnetic flux density in the centre of the air-gap reached approximately 1.53 T, and 1.13 T and 1.15 T at the edges of the centre of air-gap as depicted in figure 5.16.

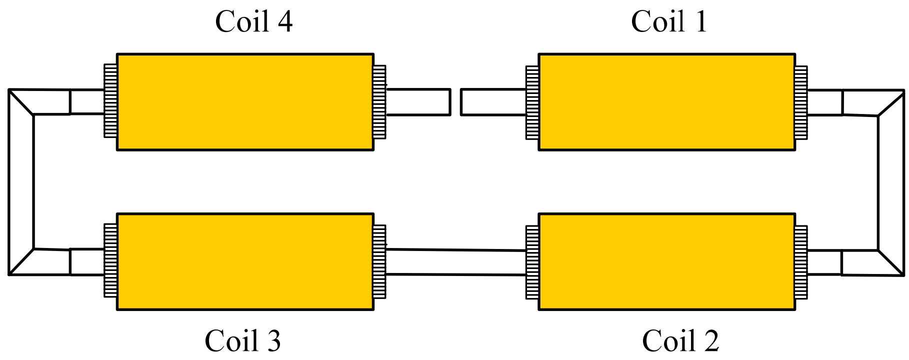

Figure 5.15: Structure of configuration "B" using abrupt right-angle corners.

These results are almost the same as the ones achieved in the previous simulation using curved corners.

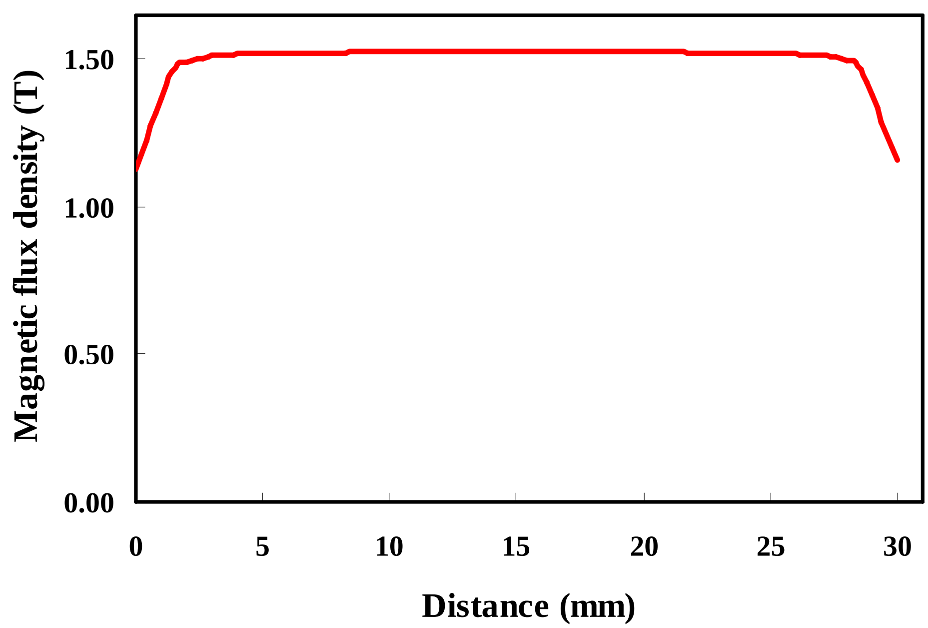

Figure 5.16: Simulated magnetic flux density across the centre of the air-gap using right-angle corners.

5.3 Magnetic field simulation of C-shape using larger-diameter component with circular cross-sections

The same data used as in the previous simulations in section 5.2.1, except using different corners. Configurations “A” and “B” have been analysed as described in the following sections.

5.3.1 Magnetic field simulation results of configuration “A”

The C-shape circuit used in this simulation is shown in figure 5.17. The flux density predicted at the centre of the air-gap reached about 1.36 T using FEMM (figure 5.18). Clearly, this is the same value achieved using curved corners that was carried out in section 5.1.1 (figure 5.9).

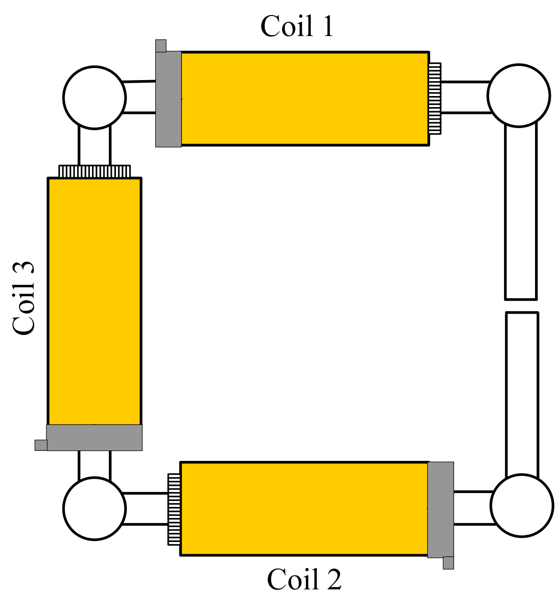

Figure 5.17: Structure of configuration “A” using large-diameter component with circular cross-sections.

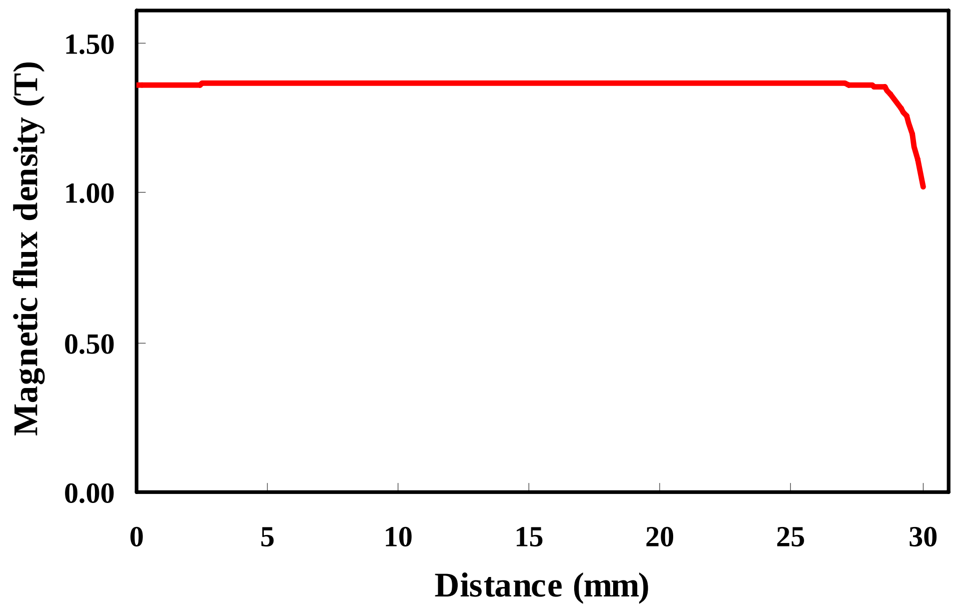

Figure 5.18: Simulated magnetic flux density across the centre of the air-gap using large-diameter component with circular cross-sections.

5.3.2 Magnetic field simulation results of configuration "B"

Larger-diameter with circular cross-sections corners were used to connect the four coils and to guide the magnetic flux around the corners with the minimum of flux losses as depicted in figure 5.19. The same data in table 5.4 was used in this simulation trial. The magnetic flux density in the centre of the air-gap reached approximately 1.52 T, and 1.19 T and 1.16 T at the edges of the centre of air-gap as depicted in figure 5.20.

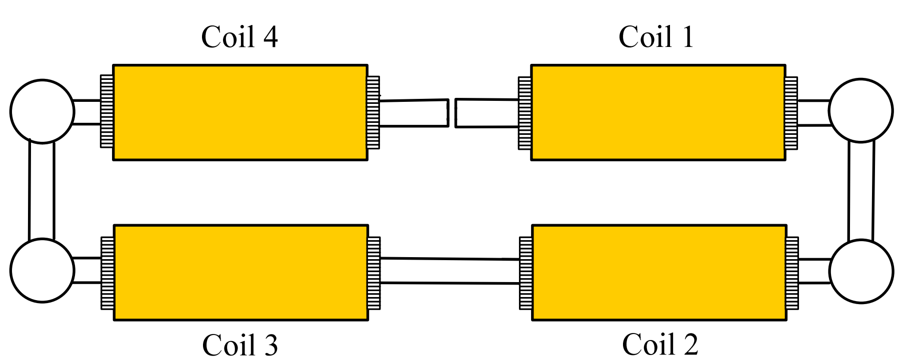

Figure 5.19: Structure of configuration "B" using large-diameter component with circular cross-sections.

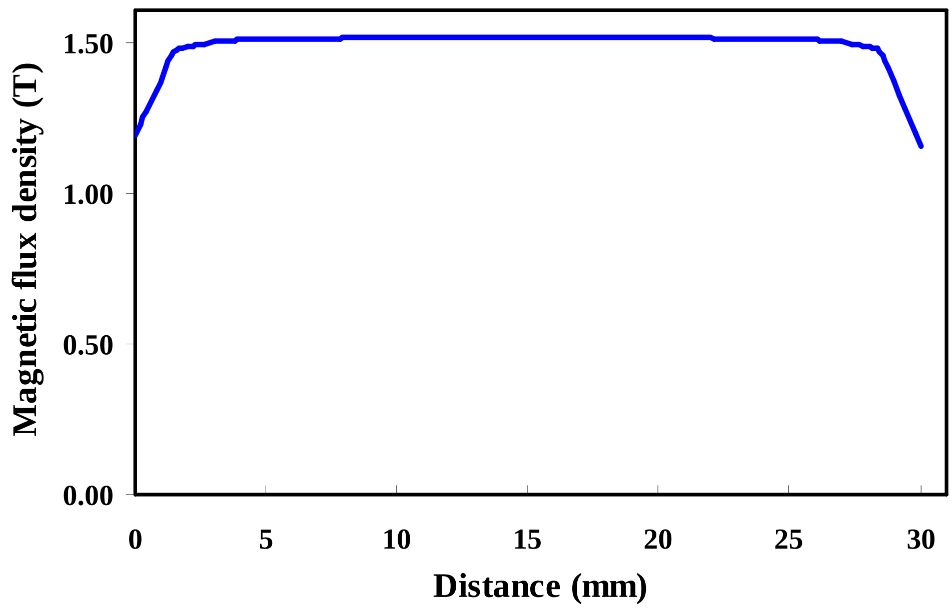

Figure 5.20: Simulated magnetic flux density across the centre of the air-gap using large-diameter component with circular cross-sections.

5.4 Simulation of screw holes and skin effect on the C-shape performance

The following simulation results explore the impact of buried screw holes and skin effect on the performance of the magnetic circuit.

5.4.1 Simulation results of configuration "B" with screw holes either side of the air-gap

To investigate the true impact of machining, screw holes measuring 6 mm in diameter were introduced to the model either side of the air-gap and corners as shown in figure 5.21.

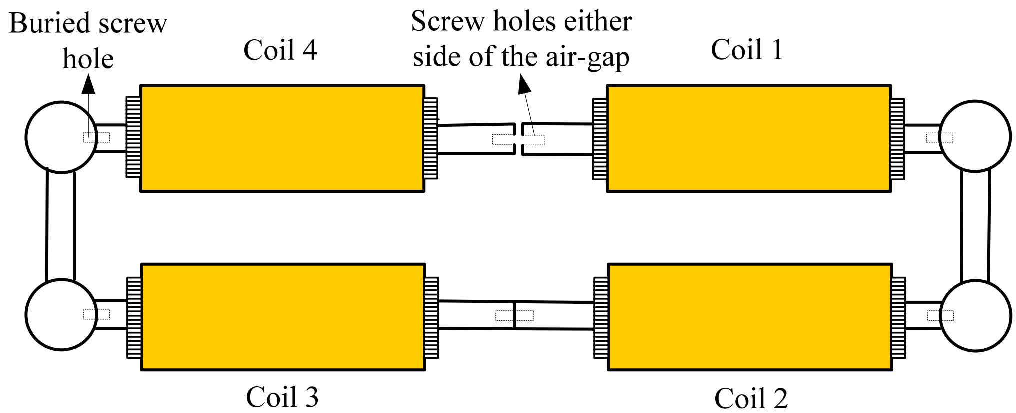

Figure 5.21: Structure of configuration “B” with screw holes in the flat surfaces either side of the air-gap.

The predicted magnetic flux density in the centre of the air-gap reached 0.49 T where it is 1.19 T and 1.20 T at the sides of the air-gap as shown in figure 5.22. The magnetic flux lines seemed to by-pass the screw holes (figure 5.23), causing the flux density to drop down to approximately 0.5 T at the centre of the air-gap.

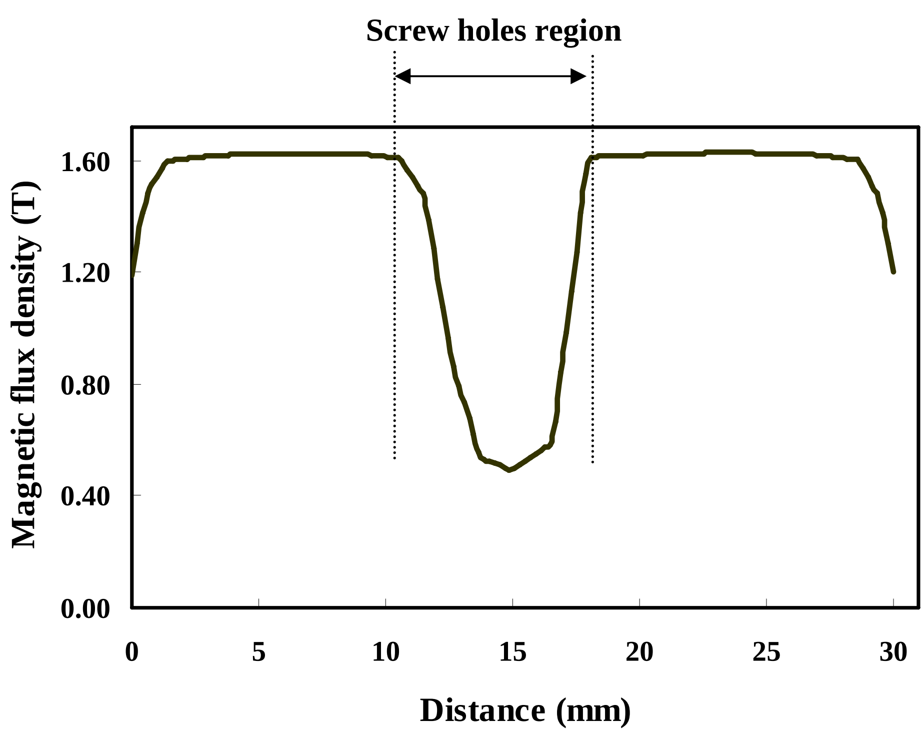

Figure 5.22: Simulated magnetic flux density across the centre of the air-gap with screw holes either side of the air-gap.

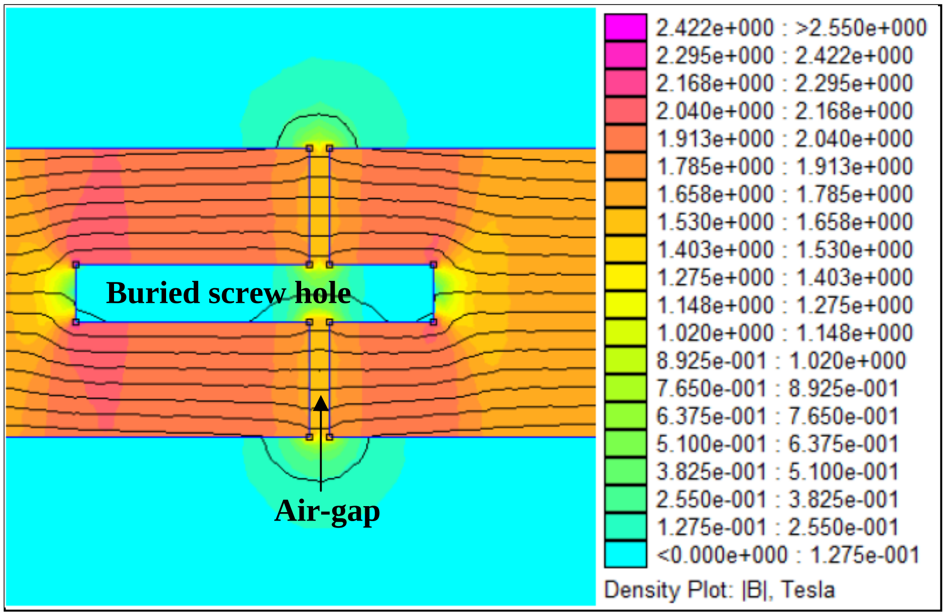

Figure 5.23: Simulated magnetic flux density distribution across the air-gap with screw holes either side of the air-gap.

Figure 5.24 shows the distribution of the flux along one of the corners and a buried screw hole. The flux always seemed to by-pass the hole since it is easier to travel along the core where permeability is higher than air. Therefore, screw holes can be considered as an obstacle to flux lines or in other words that the reluctance in the screw holes is very high.

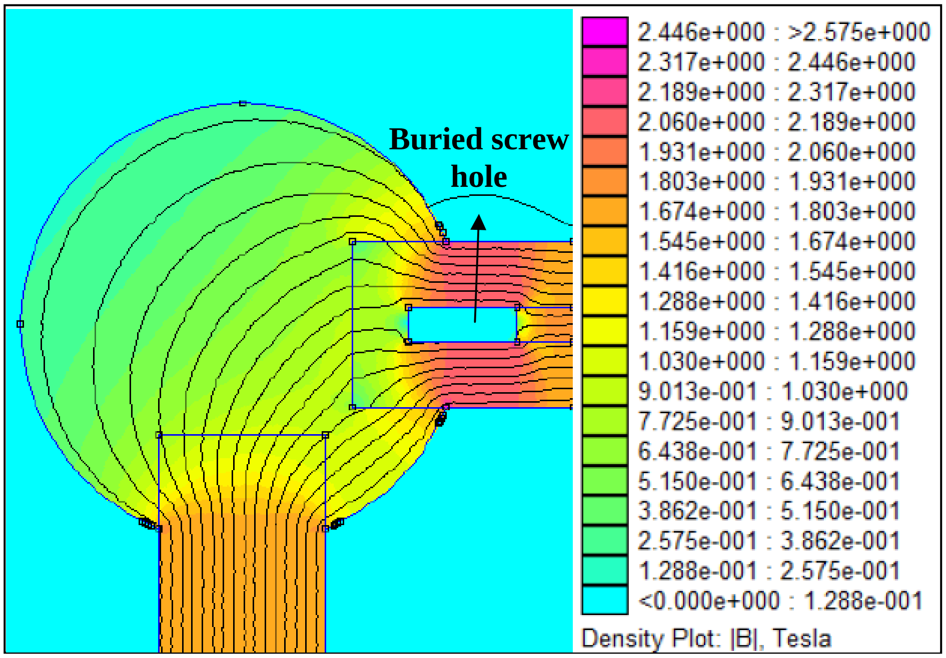

Figure 5.24: Simulated magnetic flux distribution around one corner and buried screw hole.

5.4.2 Simulation results of configuration "B" with buried screw holes near the surfaces of the air-gap

To investigate the impact of buried screw holes between the surfaces either side of the air-gap, flat spacers were added to cover both screw holes as shown in figure 5.25. In addition, an attempt to assess the impact of prior machining on the iron core, a skin effect was also introduced into the outer 2.5 mm around corners, cores and bolted areas to the same model in FEMM shown in figure 5.21; a process which has been investigated by Bas and Molins [17]. In the 2.5 mm nearest to the surface, the material is assumed to be non-magnetic. As a result, the predicted magnetic flux density increased to 0.67 T in the centre of the air-gap but fell to 0.5 T at both the edges of the air-gap which could be due to skin effect (figure 5.26).

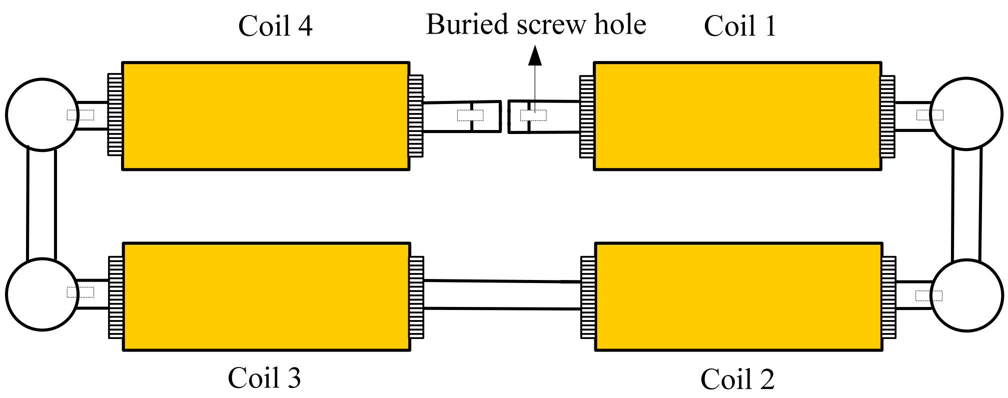

Figure 5.25: Structure of configuration "B" with buried screw holes near the flat surfaces either side of the air-gap.

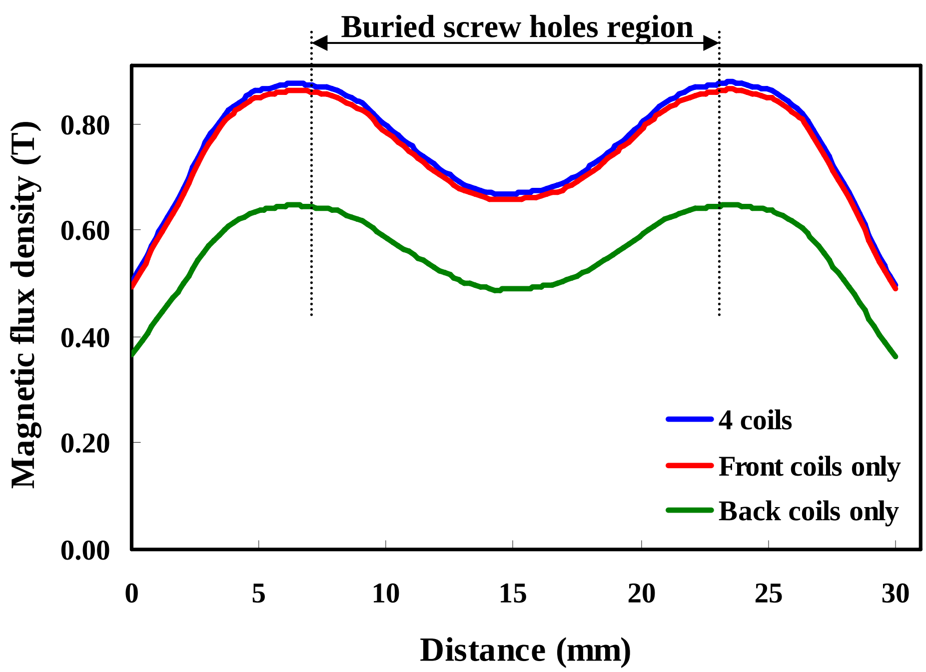

Figure 5.26: Simulated magnetic flux density across the centre of the air-gap with buried screw holes near the flat surfaces either side of the air-gap.

Figure 5.26 reveals that by only activating the coils in line with the air-gap, the predicted magnetic flux density is approximately 0.66 T, whereas it is 0.49 T when only the coils not in line with the air-gap are activated. Therefore the contribution of the flux generated by the back coils with respect to the position of the air-gap is almost insignificant since all coils produce almost the same amount of flux density as when activating only the two front coils which are in line with the air-gap.

5.4.3 Simulation results of configuration "B" with no-buried screw holes near the surfaces of the air-gap

To eliminate the effect of the buried screw holes, the air-gap was located between the second coil and third coil where the surfaces either side of the air-gap are flat with no buried screw holes as shown in figure 5.27. The predicted magnetic flux density at the centre and edge was increased to 0.97 T and 0.54 respectively (figure 5.28).

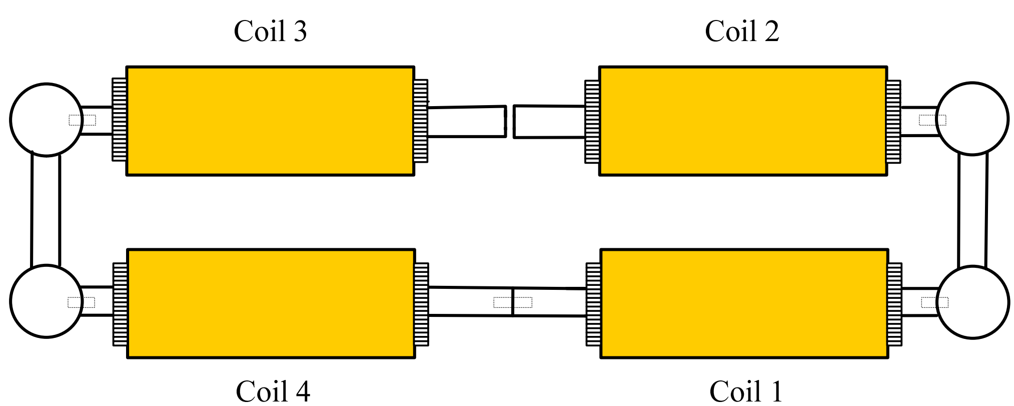

Figure 5.27: Structure of configuration "B" with no-buried screw holes near the flat surfaces either side of the air-gap.

This increase in the magnetic flux density is due the absence of any screw holes in the core near the air-gap, and the magnetic flux lines can penetrate the air-gap with less reluctance.

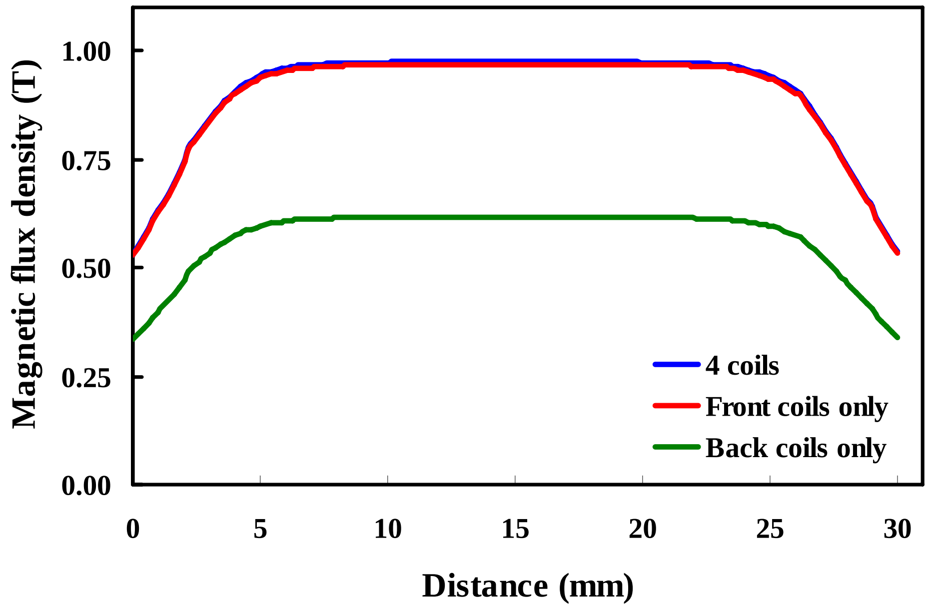

Figure 5.28: Simulated magnetic flux density across the centre of the air-gap with no-buried screw holes near the flat surfaces either side of the air-gap.

Table 5.5 summarizes the results in this section and compares simulated results and experimental results produced by configuration “B” using large-diameter components with circular cross-sections. It can be seen that there is quite good agreement between experimental and simulated results predicted by FEMM. Perhaps the lower results obtained by FEMM indicates that the details of the skin effect need to be modified.

Table 5.5: Comparison between simulated and experimental results produced by configuration "B" using large-diameter components with circular cross-sections.

Air-gap	Magnetic flux density (T)			
	Simulated results		Experimental results	
	At the centre of the air-gap	At the edge of the air-gap	At the centre of the air-gap	At the edge of the air-gap
Screw holes on the surfaces either side of the air-gap	0.49	1.19 / 1.20	0.641	1.169
Flat surfaces with buried screw holes either side of air-gap	0.67	0.50	0.895	0.913
Flat surfaces on either side of the air-gap with no buried screw holes	0.97	0.54	1.03	1.03

5.5 Magnetic field simulation results of coils in line with the testing element in "open circuit"

This simulation trial is similar to the previous one carried out in section 5.4.3 (figure 5.27) except that coil no. 1 and coil no. 4 in were completely removed from the model as shown in figure 5.29.The is done is to investigate whether there is a need to form a "closed circuit" in order to maximise the magnetic flux density produced by the rig. The same data shown in table 5.4 were used in this simulation. This model provides an opportunity to compare the planar and axisymmetric approaches to the simulation.

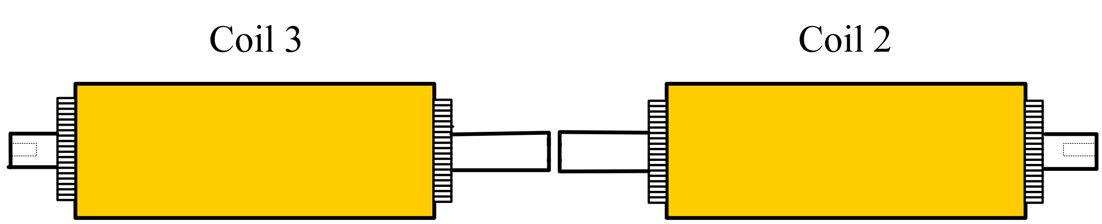

Figure 5.29: Structure of the "open circuit".

When this model was simulated as planar model, the magnetic flux density reached about 0.815 T at the centre of the air-gap as illustrated in figure 5.30. This is about 94% of the value achieved by closed circuit. The drop in flux density at both sides of the air-gap was due to skin effect introduced to the model.

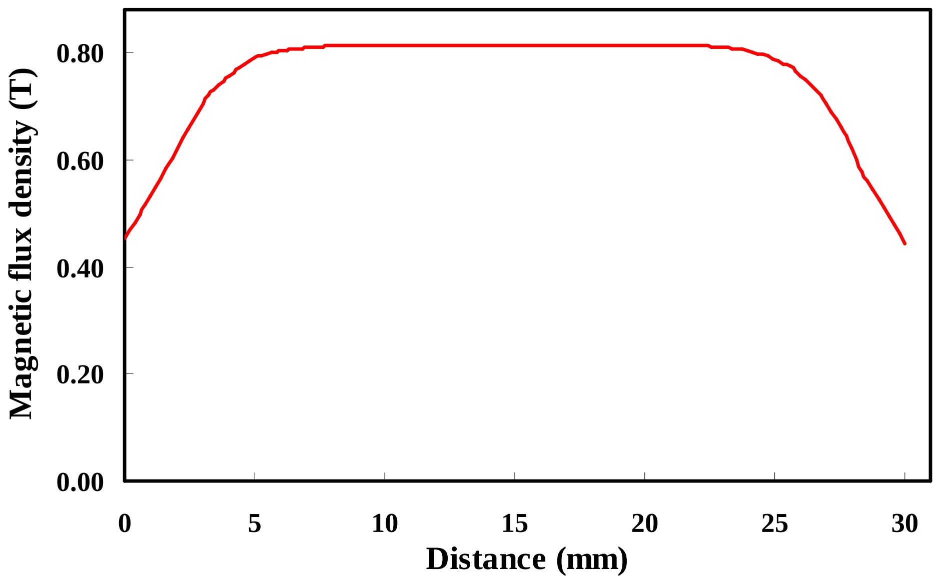

Figure 5.30: Simulated magnetic flux density of the open circuit across the centre of the air-gap using planar model.

When this model was simulated as axisymmetric, the magnetic flux density reached about 0.433 T at the centre of the air-gap. This indicates a disappointing lack of agreement between the two approaches. However for most of the work, it was necessary to use the planar approach.

5.6 Summary of chapter 5

Finite Element Method Magnetics (FEMM) computational modelling software was used to predict magnetic field strengths generated by an electromagnetic rig. Two different configurations were investigated. In this way, the arrangement of the coils was shown to greatly affect the resultant magnetic field strength. By arranging the coils closer to the air-gap, greater field strengths were recorded. According to FEMM analysis, the efficiency of the electromagnetic rig in producing high magnetic fields can be decreased due to effects related to drilling and machining of the steel cores, especially when drilling is carried near or at the air-gap. Other reasons for discrepancies include flux leakages and skin effects in the core material.

CHAPTER 6

EFFECTS OF VARIOUS FACTORS

6.0 Introduction

This chapter presents the effects of various factors such as different corners, the arrangements of coils with respect to the location of air-gap, and drilling and machining especially when it is carried out near or at the air-gap.

The highest magnetic flux density measured at the centre of the air-gap was 1.03 T. The problem therefore is that a theoretical estimation gives the flux density in the core of 20,095 gauss (2.0095 T), while that based on a measurement gives only 1.03 T.

This chapter also includes discussions of each factor that contributes to effects on the performance of the electromagnetic rig in producing high magnetic fluxes. The discussion is intended to support the knowledge gained in all the previous chapters. A brief conclusion with respect to the results and discussions is presented at the end of the chapter.

6.1 Problem definition

The problem with the efficiency of the rig in producing a high magnetic flux was encountered first when placing the cobalt ferrite sample in the air-gap. This gave a reading of 0.08 T at the centre of the air-gap using configuration “A” with curved corners to joint the three coils together (section 4.4.1). The problem with this result becomes apparent when the magnetic properties of the core material are considered. According to the calculation carried out in section 3.1.4 regarding estimation of magnetic properties of cobalt ferrite, the magnetic field strength in the core material should produce a flux density of 1.662 T at the centre of the air-gap.

If the same magnetic flux is flowing through both the core material and the combination of the probe of the meter and the plastic disc which is used to hold the meter probe, the flux density measured by the probe in the plastic disc can be used to estimate the flux density in the core. In fact since both the core and the combination of probe and disc have the same cross-sectional area, they must have the same flux density.

Therefore the flux density in the core must also be 0.08 T. The problem therefore is that a theoretical estimation gives the flux density in the core to be 1.662 T, while that based on a measurement gives only 0.08 T. Some features of the system which might be the causes of the problem are described in the following sections.

6.2 Current leakage in the coils

Each of the layers of each of the coils was rechecked, to investigate whether the coil could have been made in the wrong direction. The flux density instrument was used to establish that each layer produced a flux in the same direction. The resistance in each layer of the coils was measured. These values were compared with the resistivity of copper knowing the length of the copper wires in each layer and the average diameter of the wire. There was a very small current leakage effect because of the less-than-perfect insulation layer on the wire. This does have an effect on the calculation using the number of turns of the coils, but the effect is very small, and can only be responsible for about a 2% discrepancy between the theoretical estimation and the experimental result.

There is also a possibility that the copper used in the air cooling tubes being a commercial product may contain small amounts of magnetic materials such as iron. This would have an effect on the magnetic flux densities produced by the rig. It is considered that this is a very small effect.

6.3 The flux density instrument is faulty

The instrument is a Gauss/Tesla meter model 5180 supplied by Sypris Test and Measurement. The resolution of this meter is 0.001 T. It is very difficult to be sure that the instrument is not faulty, because there is no standard magnetic field to use to verify its accuracy. However two different instruments have been used in taking measurements; the 5080 series hand-held gaussmeter (F.W Bell) and hand-held DC magnetometer with a minimum resolution of 0.01 gauss (AlphaLab Inc). Both instruments have given results which are consistent with each other.

There is a small amount of variation and this seems to be due to the probes used and the exact angle between the probe and the flux.

6.4 The magnetic properties of the core material

In an attempt to characterise the magnetic properties of the core material used in the electromagnetic rig, a sample of the same core material (low carbon steel) was sent to Magnetic Instrumentation Calibration Laboratory Inc in USA. The magnetic properties of the sample of the core material are shown in figure 6.1.

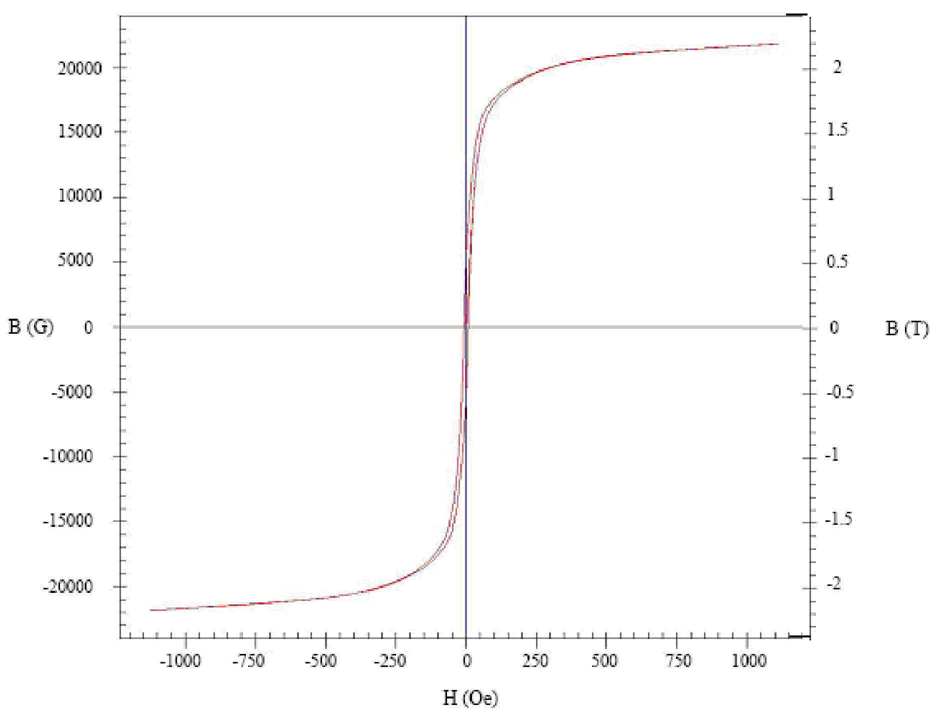

Figure 6.1: Magnetic properties of low carbon steel core characterised by an independent supplier.

There is no means of independently verifying that the testing work, carried out by this laboratory, followed standard procedures. It is also possible that the sample which was sent for the test could have had superior properties in comparison with the rest of the core material which was used to construct the system. To eliminate all doubt a new coil with the same specifications as the previous coils was constructed around a different pure iron supplied by Goodfellow of Cambridge Limited. While the newer coil should have slightly better properties in comparison with the original coils, the effect was far too small to explain the difference between theoretical predictions and experimental results.

6.5 The corners could have poor magnetic properties

It is possible that the magnetic properties of the core material could have been altered when the corners were made. This involved some cutting which produced heat. It also involved heating the material to a sufficiently high temperature to bend it to form the corners.

Three different corners have been used in the experimental work. These corners were introduced to the C-shape circuit using either configuration “A” or configuration “B” as discussed in the previous chapter.

In all experiments, coils which are in line with the testing elements always produce a magnetic flux density almost as high as the one produced by all coils. In other words, the contribution of the coils which were not in line with the testing element was very small. For instance, figure 6.2 illustrates the flux produced by coils in line with the testing element (coil no. 1 and coil no. 4) which is almost the same as the flux produced by all coils.

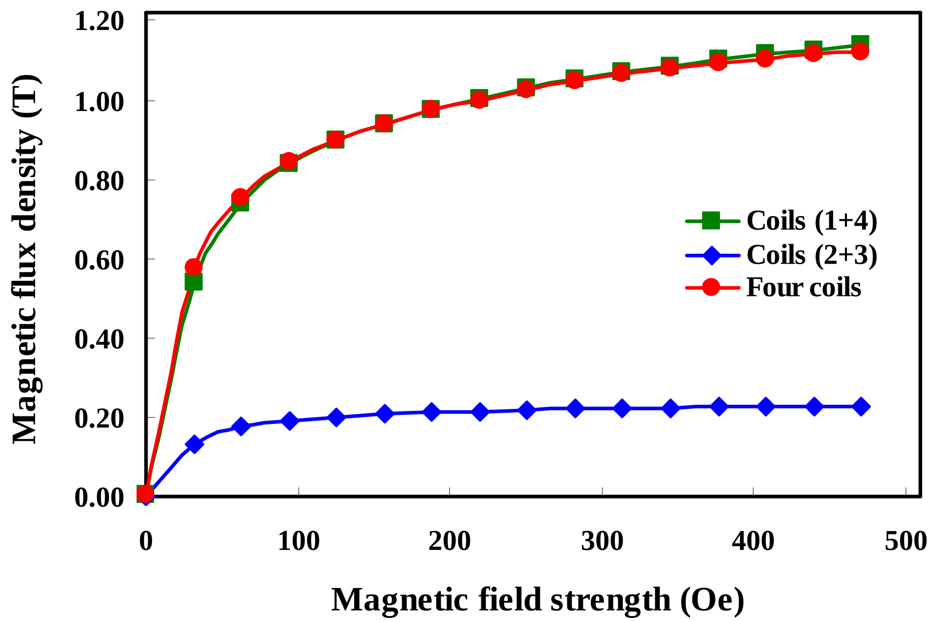

Figure 6.2: Magnetic flux density of configuration "B" using curved corners produced by all four coils in comparison with the coils in line with the testing element.

This indicates that both coil no. 2 and coil no. 3 contribute almost nothing to the magnetic flux density measured by the probe. When the position of the coils were changed (figure 4.32), it is always true that the coils not in-line with the testing element always make a small contribution to the magnetic flux as measured by the probe in the air-gap. This could be due to poor magnetic properties of corners

6.6 The effect of coils arrangement with respect to the air-gap location

The air-gap position has a great impact on the efficiency of the C-shape circuit. Figure 6.3 is an example which shows the effect of the arrangement of coils with respect to the location of the air-gap. The magnetic flux density reached 0.393 T and 0.391 T at the centre of the air-gap and at the edge of the air-gap respectively when the C-shape circuit was assembled to configuration "A" using large-diameter components with circular cross-sections as depicted in figure 4.28. The air-gap was on one side of the C-shape circuit while the other sides were occupied by the coils. On the other hand when the C-shape circuit was assembled to configuration "B" using the same type of corners, the magnetic flux density increased to 1.03 T at both; centre of the air-gap and at the edge of the air-gap. This is about a 60% increase in the magnetic flux density for a change from three coils to four coils.

The effect of the air-gap location with respect to the arrangement of coils can also be seen when the C-shape circuit was assembled in configuration “B” using curved corners. When the air-gap was located between two coils (figure 4.23), the magnetic flux density at the centre of the air and the edge of the air-gap reached to 0.556 T and 1.119 T respectively. When the air-gap was moved to one of the sides and close to one corner (figure 4.25), the magnetic flux densities decreased to 0.486 T and 0.971 T at the centre of the air-gap and the edge of the air-gap respectively as shown in figure 6.4. These results show that the highest value of magnetic flux density then can be achieved is when the coils are arranged as close to the air-gap as possible.

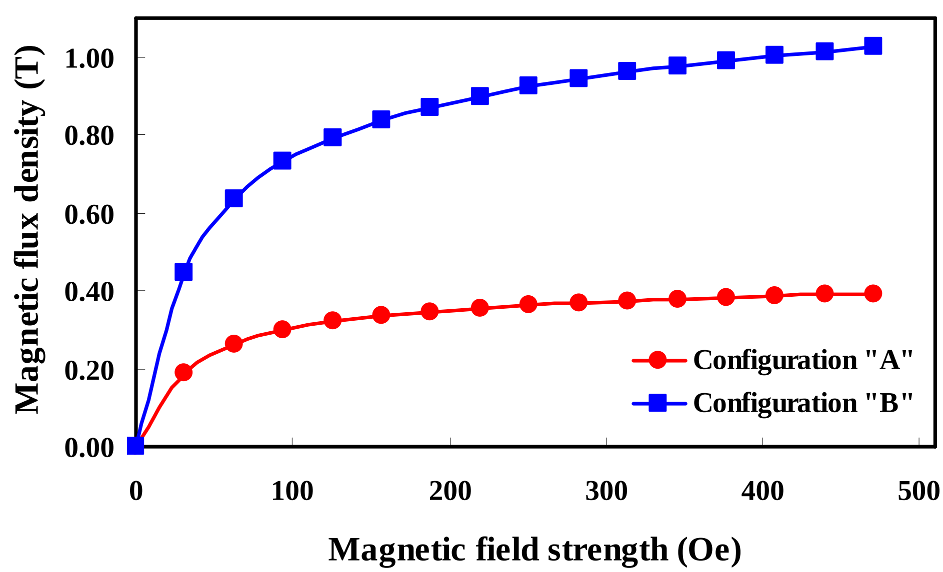

Figure 6.3: Comparison between magnetic flux density of configuration “A” and configuration “B” using large-diameter components with circular cross-sections.

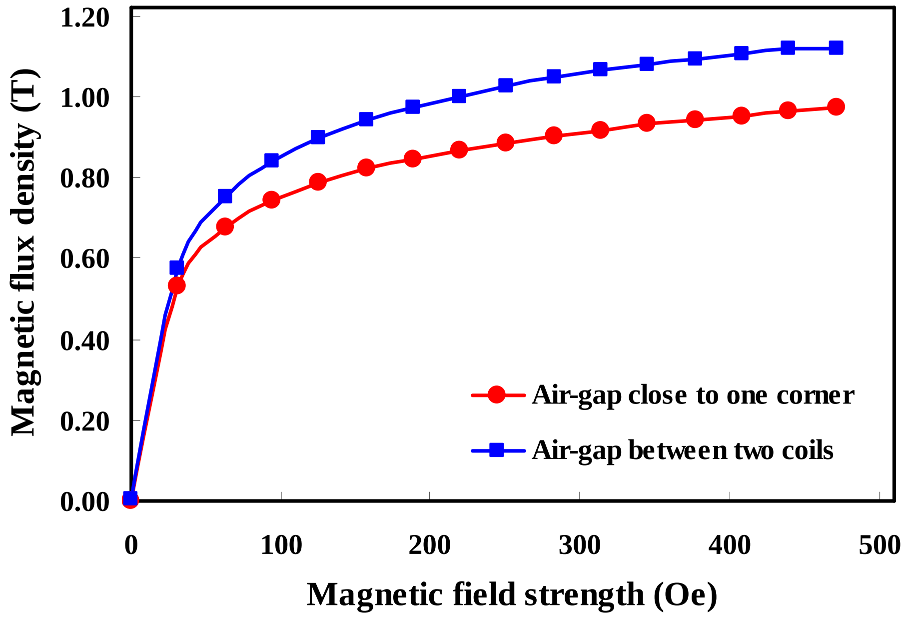

Figure 6.4: Comparison between magnetic flux density of configuration "B" using curved corners with air-gap on one of the sides and close to one corner and air-gap between two coils.

6.7 Flux leakage

In magnetic circuits and particularly those containing air-gaps, there is a tendency for the flux to "leak out" of the magnetic path or spread out. The spreading out of the flux in the air-gap is called the fringing effect. This is not useful since it spreads the flux over a relatively large area, thus in effect reducing the flux density in the air-gap.

Figures 5.3, 5.7, and 5.10 are good examples of flux leakage accruing during the simulation of the C-shape circuit. There is flux leakage at various points in the circuit. There is some leakage at the corners of the iron core, but the largest leakage occurs across the air-gap. Moreover, this leakage is a function of the air-gap thickness (the bigger the air-gap, the higher the flux leakage). It is a function of the magnetic properties of the sample that is placed close to the air-gap. If this sample has high magnetic properties, the flux lines can then easily penetrate the sample. Figure 5.4 reveals that magnetic flux lines can be seen to by-pass the cobalt ferrite sample leading to more flux leakage around the sample and air-gap (figure 5.3), whereas less leakage occurred around the air-gap when low carbon steel and Terfenol-D samples were placed close to the air-gap (figures 5.8 and 5.11).

In general, the extent of the flux leakage is difficult to estimate from the diagrams, because the depiction tends to exaggerate the amount of leakage, making it difficult to visualise the amount of concentrated flux passing along the iron core.

6.8 Effect of machining and drilling on the C-shape performance

The operations of drilling and machining have great impact on the magnetic properties of many materials and thereby alter their performance in certain applications. Changes in the magnetic properties are a function of the type and degree of machining as well as the thickness of the machined parts. As reported in section 2.1.6, a researcher investigated the drilling operation on the magnetic properties of several magnetic materials [13 - 14]. They concluded that this type of operation could result in the following:

- The coercive force increased with a reduction in thickness of the materials.
- Permeability and magnetic flux density decreased as the number of machining operations increases.
- The depth of alteration of magnetic properties differs depending on the degree of drilling and machining.
- Machining increased the electrical resistivity of the material up to 54%.

In this work, three experiments were mainly aimed to investigate the effect of machining and drilling on the efficiency of the electromagnetic rig in producing high magnetic fields. These experiments were carried out in section 4.7.2

In the first experiment, screw holes were made at the centre of the surfaces on each side of the air-gap, measuring 6 mm in diameter and 10 mm in length. Measurements showed that the magnetic flux density reached 0.6 T in the centre of the air-gap and 1.2 T at the edge of the air-gap (figure 4.30). The difference in values is due to the presence of the screw holes in the surfaces on each side of the air-gap. These experimental results are in good agreement with the values predicted by FEMM, where the magnetic flux density in the centre of the air-gap reached 0.5 T and 1.19 T and 1.20 T at the sides of the air-gap.

The reason for the low experimentally-measured values could also include losses of flux at each of the core joints due to screw holes where the corners are bolted together, or due to prior machining of the core itself. When the system was modelled in FEMM, the magnetic flux lines seemed to by-pass the screw holes (figure 5.23), causing a reduction in the flux density as shown in figure 5.22.

The second experiment is a follow-up of the previous one. Flat spacers were added to cover both screw holes. As a result, the magnetic flux density increased to approximately 0.9 T in the centre of the air-gap and decreased to 0.9 T at the edge of the air-gap (figure 4.31 (d)).

In an attempt to assess the impact of prior machining on the iron core, a "skin effect" was introduced into the outer 2.5 mm of all machined surfaces in FEMM around the corners and bolted areas. This resulted in only a minor reduction in flux density at the centre of the air-gap to 0.7 T, and to 0.5 T at both edges of the air-gap (figure 5.26).

In the third experiment, there were no screw holes at or near the surfaces either side of the air-gap, and as a result the magnetic flux density was increased to 1.03 T at both the centre of the air-gap and at the edges of the air-gap (figure 4.34). This increase can be explained in terms of the absence of drilling carried out at or even near the air-gap. This value is in a good agreement with the predicted value in FEMM which was 1.0T as illustrated in figure 5.28.

6.9 Grid independent study

Section 5.1.1 (a) provides a study which proves that the FEMM simulations give results which are independent of the mesh sizes chosen. This therefore can not be an explanation for discrepency.

6.10 Comparison between axisymmetric and planar approaches in the FEMM simulations

In section 5.5, a detailed comparison was made between these two approaches and it was found that the axisymmetric approaches gave values of magnetic flux densities which where considerably lower (about half) than the planar approach. The axisymmetric approach is probably closer the true experimental situation because it is three dimensional, but it is not always possible to use this approach because of the lack of symmetry. Therefore, the planar approach had to be used for most of this work. This could be an explanation for the discrepancy between the experimental results and the FEMM simulation.

6.11 Summary of chapter 6

Experimental results indicate that the highest magnetic flux density produced by the electromagnetic rig was 1.03 T. This value was achieved when the rig was assembled in configuration “B” using large-diameter components with circular cross-sections. The results also indicate that the arrangement of coils with respect to the air-gap has great influence of the efficiency of the rig. By arranging the coils closer to the air-gap, greater flux densities were obtained (1.03 T). The efficiency of the electromagnetic rig was also strongly affected by the various factors such as flux leakage, and drilling and machining effects. The magnetic flux density was higher when drilling was not carried out on the core in the region of the air-gap. Results also show that only the coils which are in line with the testing element contribute significantly to the total flux produced by the magnetic rig at the air-gap. The contributions of the other coils can almost be considered as negligible.

CHAPTER 7

CONCLUSIONS

7.0 Conclusions

In this study, an investigation of some effects of strong magnetic fields generated by an electromagnetic rig was carried out. Two rigs were designed and then one was assembled in such a way that two different configurations could be studied. Aspects of the study were assisted using a Finite Element Method Magnetics (FEMM) software package. The equipment was capable of producing different magnetic flux densities depending on the configuration and the type of corners used. Different experiments were carried out using three different corners to investigate various effects on the efficiency of the electromagnetic rig. Results, achieved by using both configurations were presented and discussed. The conclusions of the study are listed in the following:

1. The design of the electromagnetic rig
The air-core design required very high electrical power to produce the 9000 Oersteds in a sample chamber measuring 30 mm in diameter by 50 mm long. This high power requirement inevitably leads to a complex system in order to remove the heat generated. The approach was abandoned at the design stage.

2. By comparison the C-shape design using a core with good magnetic properties seemed to be able to achieve the same magnetic field results without requiring high electrical power. The cooling system was therefore much simpler and the design concept could be followed.

3. It was possible to use fabrication techniques to make the components of the C-shape design.

4. Cooling system
The cooling system in the design proved to be adequate to maintain a temperature of $40\,°C$ when a steady current of 3 amps was present in each coil.

5. It is normal to carry out the preliminary stages of the design of an electromagnetic rig, assuming that flux leakage around the magnetic circuit can

be ignored. In the design of this particular electromagnetic rig, where high flux densities are required, this assumption leads to invalid results

6. Even allowing for the above factor, the experimentally determined flux densities were much lower than initial predictions using the FEMM software package. Extra details were needed to be taken into account before the predictions of the software package could be reconciled with the experimental results.

7. The decision to hold the components of the magnetic circuit together by drilling screw holes in the core material and inserting screws led to a very much poorer performance. Some other way to hold the components together to form the C-shape should have been followed.

8. The input data for the software package must include effects which tend to produce poorer magnetic properties in materials with otherwise very good magnetic properties. These effects include machining and drilling which seem to produce a layer in these materials of 2.5 mm thickness. In this layer it seems that the material has no ferro magnetic properties at all. Significant differences were also discovered between the axisymmetric and the planar approaches.

9. The input data also needs to take into account the shape and the size of the probes used to measure the magnetic flux density.

10. In the electromagnetic rig which was used in this study, various components were assembled to complete the magnetic circuit, leaving a small gap of 2mm so that the magnetic flux density could be measured. Every joint between the various components produced losses in magnetic flux. If there was more than one joint between the coils generating the magnetic flux and the air-gap where the magnetic flux density was measured, the contribution of that coil was almost negligible. Therefore components used to conduct the flux around the corners which involved a number of joints made the contribution of some coils of almost no consequence.

11. Various modifications to improve the pathing of the flux around corners made a very slight improvement but the effect was very small.

12. In the electromagnetic rig which was developed in this study, there was almost no benefit in completing a magnetic circuit to allow the flux to build up from one component to another. 94% of the magnetic flux density could be achieved by arranging two of the coils to be in-line with the air-gap, and allowing the rest of the magnetic circuit, from the opposite end of one coil to the opposite end of the other coil, to be completed using air and various other materials in the laboratory which had no ferromagnetic properties.

13. The highest value of magnetic flux density achieved by the electromagnetic rig with a current of 3 amps in each coil was 1.03 T over an area of 7.07 cm^2 (3 cm diameter).

14. The electromagnetic rig did not generate sufficiently high values of flux density to be of use in measuring the magnetostriction strain of annealed cobalt ferrite or Terfenol-D samples.

7.1 Contributions of the thesis

In this thesis, an investigation electromagnetic rig - generated strong magnetic fields has been addressed. The results obtained from this investigation showed that the electromagnetic rig can produce as high as 1.03 T in the centre of the air-gap. However the experimental results often fell far short of both the calculated magnetic field strengths and the values predicted by the software. These differences could be due to changes in the magnetic properties of the core material. Drilling and machining of these components could have produced skin effects and other regions of poor magnetic properties. The contributions of this thesis are listed in the following:

a) This thesis contributed to the design of the electromagnetic rig. Magnetic flux density of 1.03 T was achieved using this constructed rig.

b) The second contribution was related to the cooling system applied to the electromagnetic rig in order to reduce the effect of the heat generated by the coils. This cooling system was adequate for the rig.

c) The third contribution was the description of various factors which have a great effect on the rig efficiency in producing high magnetic fields. These factors were related to drilling and machining of the steel cores, especially when drilling is carried near or at the air-gap. Another reason for poor discrepancy is flux leakages. By building these considerations into the FEMM model, modelled values approached the experimentally measured ones.

7.2 Recommendations for future work

Results in this thesis lay the groundwork for a good understanding of C-shape magnetic circuit. Following these investigations, there are some extensions to this work that would help expand and strengthen the results, involving the modification of the electromagnetic rig:

a) Further study and investigation of the effects of drilling and machining in terms of changes of magnetic properties and grain sizes of the material should be carried out in order to gain more understanding regarding to what extent these changes can affect the performance of the electromagnetic rig. This can be done by using scanning electron microscopy (SEM) to estimate the average grain size, grain size distribution, and the shape and surface morphology of the grains and to study porosity effects.

b) Further investigation should be carried out regarding the contribution of the coils which are not in line with the testing element. Their low contribution could due to poor magnetic properties at the corners or due to large flux leakage effects. Also the effect of heating the corners in order to be formed to compatible shapes should be studied.

c) Further improvement of the test rig design could be made. A new design could be developed in which there would be only two coils in the rig instead of four, having the air-gap between them. Each coil would have 16,000 turns instead of 8000 turns. This arrangement could be adopted to take advantage of the finding regarding the use of the coils in-line with the testing element. The system can also be improved by avoiding any drilling or machining processes carried out on the core material.

REFERENCES

[1] R. Bozorth, Anisotropy and Magnetostriction of Some Ferrites, Physical review, Vol. 99, No. 6, 1955, 1788-1798.

[2] Lo CH, Ring A, Snyder J, Jiles D, Improvement of Magnetomechanical Properties of Cobalt Ferrite by Magnetic Annealing, IEEE, Transactions on Magnetics, Vol. 41, 2005, 3676-3678.

[3] D. R. Askeland, The Science and Engineering of Materials, 3rd Ed., Chapman and Hall, London, 1996.

[4] W. D. Calister, Jr., Materials Science and Engineering, 4th Ed., New York: Wiley, 1997.

[5] F. T. Ulaby, Fundamentals of Applied Electromagnetics, Prentice Hall, Upper Saddle: New Jersey, 1997.

[6] P. F. Ryff, Electric Machinery, 2nd Ed., Prentice Hall Inc., 1994.

[7] Magnetic Fields Around Two Parallel Conductors, http://www.tpub.com/neets/book2/la.htm, 10/02 2006.

[8] J. D. Kraus, Electromagnetics, 2nd Ed., McGraw-Hill, Inc, 1973.

[9] J. D. Krauss, Electromagnetics, 4th Ed.,McGraw-Hill, Inc.,1992.

[10] W. D. Calister, Jr., Materials Science and Eengineering, 3rd Ed., New York: Wiley, 1985.

[11] A. Nicolaides, Electrical and Electronic Principles II, 2nd Ed., PASS Publications, London, 1996.

[12] J. D. Kraus, Electromagnetics, International Edition, 4th Ed., Mc-Graw-Hill Inc., Singapore, 1991.

[13] W. D. Callister, Jr., Materials Science and Engineering: An Introduction, 3rd Ed., John Wiley and Sons, Inc., New York, 1994.

[14] A. Ramesh, M. R. Govindaraju, D. C. Jiles, and S. B. Biner, Magnetic Property Variations in Nickel Caused by Non-Magnetic Inclusions, IEEE Transactions on Magnetics, Vol. 32, No. 5, Part 2, 1996, 4836-4838..

[15] S. Takahashi, L. Zhang and T. Ueda, Magnetic Hysteresis Minor Loops in Fe Single Crystal, Journal of Physics Condensed Matter, Vol. 15, No. 46, 2003, 7997-8002.

[16] A. K. Giri, K. M. Chowdary and S. A. Majetich, AC Magnetic Properties of Compacted FeCo Nanocomposites, Materials Physics and Mechanics, Vol. 1, 2000, 1-10.

[17] J. A. Bas, C. Jr Molins, Effect of Machining Procedures on the Magnetic Properties of Several Sintered Soft Magnetic Materials, in proceedings of the conference on Powder Metallurgy, Greece, 1986, 407-410.

[18] R. Maxime, Dubois, P. Lemieux, C. Cyr, and D. Massiocotte, Effect of Machining on the Properties of Resin-Based Soft Magnetic Composites, in proceedings of the XVIIth International Confernce on Electrical Machines, Greece 2006, 1-5.

[19] J. K. Watson, Applications of Magnetism, New York:Wiley, 1980.

[20] F. V. Hunt, Electroacoustic, The analysis of Transduction and its Historical Background, American Institute of Physics for the Acoustical Society of America, 1953.

[21] A. E. Clark, In Ferromagnetic Materials, E. P. Wohlfarth, North Holand Publishing, Co., Amsterdam, 1980.

[22] M. Goodfriend, Applications of Magnetostrictive Terfenol-D, Actuator 94, in proceeding of the 4th International conference on New Actuators, Bremen, Germany, AXON Technologie, 1994.

[23] G. Engdahl, Hand Book of Giant Magnetostrictive Materials, San Diego USA, Academic Press, ISBN 012238640X, 2000.

[24] AR. Piercy, The Changing Shape of Magnetostriction, Physics Education, Vol. 32, 1997, 160-163.

[25] GP. Mcknight, GP. Carman, Large Magnetostriction on Terfenol-D Particulate Composites With Preferred [112] Orientation, in proceeding of SPIE, 2001, 4333, 178-183.

[26] M. Dapino, Magnetostrictive Materials: Their Use in Smart Structure Applications, Encyclopedia of Smart Materials, , J. A. Harvey, Ed., John Wiley & Sons, Inc, New York, 2000, 600-620.

[27] A. G. Olabi, A. Grunwald, Design and Application of Magnetostrictive Materials, Journal of Materials and Design, 2007, Vol. 29, Issue 2, 2008, 469-483.

[28] E. W. Lee, Magnetostriction and Magnetomechanical Effects, Reports in Physics, 18, 1955, 184-220.

[29] B. D. Cullity, Introduction to Magnetic Materials, Addison Welsey, 1972.

[30] E. C. Snelling, Soft Ferrites, Properties and Applications, Iliffe Books Ltd, 1969.

[31] Unit cell of spinel lattice of cobalt ferrite,

http://www.tf.uni-kiel.de/matwis/amat/def_en/kap_2/basics/b2_1_6.html, 01/08/2006.

[32] J. G. Na, Effects of Cation Distribution on Superexchange Interaction in Cobalt Ferrite, IEEE Transaction on Magnetics, Vol. 31, No. 6, November 1995.

[33] J. G. Na, Effects of Cation Distribution on the Magnetic and Electrical Properties of Cobalt Ferrite, IEEE Transaction on Magnetics, Vol. 28, No. 5, September 1992.

[34] G. A. Sawatzky, Cation Distributions in Octahedral & Tetrahedral Sites of the Ferromagnetic Spinel $CoFe2O_4$, Journal of Applied Physics, Vol. 39, 1968, 1204-1206.

[35] R. Grossinger, Accurate Measurement of the Magnetostriction of Soft Magnetic Materials, Technical Report, Institute of Experimental Physics, Technical. University, Vienna, Austria.

[36] P. T. Squire, Magnetomechanical Measurements of Magnetically Soft Amorphous Materials, Review article, School of Physics, University of Bath, Bath UK, Measurements Society Technology, Vol. 5, 1994, 67-81.

[37] National Instruments, Strain gauges, http://zone.ni.com/devzone/conceptd.nsf/webmain/C83E9B93DE714 DB08625686600704DB1#1, 20/01/2006.

[38] J. E Goldman, Magnetostriction of Annealed and Cold Worked Nickel Rods, Physics Review, 72, 529, 1947.

[39] E. Tremolet de Lacheisserie, Magnetostriction Theory and Applications of Magnetoelasticity, CRC Press, Inc., Boca Raton, Florida, 1993, 328.

[40] J .A. Ricodeau, Apparatus for the Measurement of Magnetostriction in Pulsed Magnetic Fields, Journal of Physics E: Society of Instrumentations, Vol.5, 1972.

[41] M.A. Chaudhri, A Microcomputer-Controlled System for the Measurement of Magnetostriction with a 13 T Superconducting Solenoid, Journal of Physics E: Society of Instrumentations, Vol. 17, 1984.

[42] G. K White, Measurement of Thermal Expansion at Low Temperatures, Cryogenics, 151, March 1961.

[43] N. Tsuya, Magnetostriction Measurement by Three-Terminal Capacitance Method, Japanese Journal of Applied. Physics, Vol. 13, 1974, 1808.

[44] R.R. Birss, A Capacitive Instrument for the Measurement of a Large Range of Magnetostriction at Low Temperatures and High Magnetic Fields, Journal of Physics E: Society of Instrumentations, Vol. 11, 1978.

[45] J. Heremans, A Capacitive Instrument for the Measurement of Magnetostriction in Pulsed Fields, Journal of. Physics E: Society of Instrumentations, Vol. 16, 1983.

[46] M. S. Boely, Capacitance Bridge Measurements for Magnetostriction, Journal of Applied Physics, Vol. 91, No. 10, 2002.

[47] H. Samanta, New Optical Technique for Bulk Magnetostriction Measurement, Journal of Magnetism and Magnetic Materials, Vol. 212, 2000, 355-360.

[48] T. Giallorenzi, Optical Fiber Sensor Technology, Microwave Theory and Techniques, IEEE Transactions, Vol. 82, Issue 4, 1982, 472-511.

[49] A. Shimamoto, Optical Fiber Bundle Displacement Sensor Using an AC-Modulated Light Source With Subnanometer and Low Thermal Drift, Applied. Optics, Vol. 34, 1995, 5854.

[50] P.T. Squire, Magnetostrictive Response of Metallic Glasses, Journal of Applied Physics, Vol. 61, 1987, 3784-3786.

[51] G. Bellesis, Magnetostriction Measurement by Interferometry, IEEE Transactions On Magnetics, Vol. 29, No. 6, 1993.

[52] R. Brizzolara, Magnetostriction Measurements Using a Tunneling-Tip Strain Detector, Journal of Magnetism and Magnetic Materials, Vol. 88, 1990.

[53] A. Rafferty, S. Bakir, D. Brabazon, T. Prescott, A Laser-Based Magnetostriction Measurement System, in proceedings of the 22nd International Manufacturing Conference, 2005, 141–150

[54] A. B. Smith, R. V. Jones, Magnetostriction Constants From Ferromagnetic Resonance, Journal of Applied Physics, 34, 1283, 1963.

[55] K.Narita, Measurement of Saturation Magnetostriction of a Thin Amorphous Ribbon By Means Of Small Angle Magnetization Rotation, IEEE Transactions On Magnetics, Vol. 16, No. 435, 1980.

[56] A. Hernando, Modification of the Saturation Magnetostriction Constant After Thermal Treatments For the $Co_{58}Fe_5Ni_{10}B_{16}Si_{11}$ Amorphous Ribbon, Journal of Magnetism and Magnetic Materials, Vol. 37, No. 161, 1983.

[57] J. Henning, Magnetostriction Measurement By Means Of Strain-Modulated Ferromagnetic Resonance (SMFMR), Journal Of Applied Physics, Vol. 16, No. 353, 1978.

[58] F. T. Calkins, Effect of Prestress on the Dynamic Performance of a Terfenol-D Transducer, in proceeding of SPIE Smart Structures and Materials, Vol. 3041, 1997, 293-304.

[59] G .A. Steel, A 2 Khz Magnetostrictive Transducer, In Transducers for Sonic and Ultrasonics, Lancaster, PA Technomic Inc., 1993, 250-258.

[60] J. B. Restorff, Magnetostrictive Materials and Devices, In Encyclopedia of Applied Physics, Vol. 9, VCH Publishers, Inc., 1994, 229-244.

[61] M. J. Dapino, Magnetostrictive Devices, in proceeding of the 22nd. Encyclopedia of Electrical and Electronics Engineering, Ed. J.G. Webster, John Wiley & Sons, Inc., Vol. 12, 1999, 278-305.

[62] L. Kiesewetter, The application of Terfenol in Linear Motors, in proceeding of the 2nd International Conference On Giant Magnetostrictive Alloys, Marbella, Spain, October 12-14 1988.

[63] Etrema Products Inc., www.etrema-usa.com.

[64] Gansu Tianxing Rare Earth Functional Material Co, Ltd (China), www.txre.net

[65] MateriTek Co. Ltd (China), www.materitek.com

[66] R. C. Roth, The elastic Wave Motor-a Versatile Terfenol Driven, Linear Actuator With High Force and Great Precision, in proceeding of the 3rd International Conference on New Actuators, Bremen, Germany, Axon Technology, 1992, 138-141.

[67] C. H. Joshi, Compact Magnetostrictive Actuators and Linear Motors, in proceeding of the Actuator 2000 Conference, Bremen, Germany, June 2000.

[68] J. M. Vranish, Magnetostrictive Direct Drive Rotary Motor Development, IEEE Transaction on Magnetics, Vol. 27, 1991, 5355-5357.

[69] C. N. Lhermet, Design and Construction of a Resonant Magnetostrictive Motor, IEEE Transaction on Magnetics, Vol. 32, No. 5, 1996, 4749-4751.

[70] J.E. Miesner, Piesoelectric/Magnetostrictive Resonant Inchworm Motor, in Proceeding of SPIE Smart Structures and Materials, Vol. 2190, Orlando, Florida, 1994, 520-527.

[71] B. Clephas, New Linear Motor With Hybrid Actuator, in proceeding of SPIE Smart Structures and Materials, Vol. 3041, San Diego, CA, March 1997, 316-327.

[72] R. Venkataraman, The Hybrid Motor Prototype: Design Details and Demonstration Results, Technical report, CDCSS, University of Maryland, College Park, MD, CDCSS T.R., 1988, 98-102.

[73] I. J. Garshelis, A Torque Transducer Utilizing Circularly Polarized Ring, IEEE Transaction on Magnetics, Vol. 28, No. 5, September 1992, 2202-2204.

[74] I. Sasada, In Process Detection of Torque on a Drill Using the Magnetostrictive Effect, IEEE Transaction on Magnetics Vol. 30, No. 6, November 1994, 4632-4635.

[75] Acoustic waveguide for position detection http://www.sensorsmag.com/articles/1002/level/main.shtml, 20/02/2006.

[76] J. Russell, New Developments in Magnetostrictive Position Sensors, Sensors, Vol. 14, No. 6, June 1997.

[77] J. Russell, Smaller Lower Cost Magnetostrictive Position Sensors Open up Consumer and Professional Product Applications, MTS Systems Corporation, Technical paper, Part number: 08-02 M1162 Revision.

[78] Meeker DC, FEMM, Software Manual, Finite Elements Method Magnetics User's Manual and Tutorial, Version 4, 2007, http://femm.foster-miller.net.

[79] A. Rafferty, T. Prescott, D. Brabazon, Sintering Behavior of Cobalt Ferrite Ceramics, Ceramics International, Vol. 34, 2008, 15-21.

[80] Impact Ireland Metals Ltd, www.impactirl.ie.

[81] N. Lhermet, Magnetostrictive Material Characterization, Cobalt Ferrite Rod Characterization, Cedrat Technologies, reference contract PO n# 33592, document no. AAE1934/1/1.0, October 2005.

[82] D. Jiles, Introduction to Magnetism and Magnetic Materials, 2nd Ed., CRC Press, 1998.

[83] Xantrex operating manual http://www.elgar.com/products/XHR/downloads/XHR _RS-, 232_User_Guide_RSRF-01XN.pdf, August 1st 2007.

[84] National instruments, Xantrex XFR XHR XPD Series, http://sine.ni.com/apps/utf8/niid_web_display.download_page?p_id_guid=014E15032CB463F6E0440003BA7CCD71.

[85] National Instruments, PCI E Series User Manual, July 2006.

[86] National Instruments. SCB-68 68-Pin Shielded Connector Block User Manual. July 2006.

[87] National Instruments, DAQ technical data http://www.ni.com/pdf/products /us/4daqsc202-204_ETC_212-213.pdf

[88] Radionics, thermocouple technical data http://docs-europe.electrocomponents.com/webdocs /001b/0900766b8001ba88.pdf.

[89] Sypris Test and Measurement, Hand Held Gaussmeter Technical Manual, www.sypris.com/library/documents/5000-Datasheet.pdf.

[90] AlphaLab Inc., http://www.trifield.com/gauss_meter.htm.

[91] Magnetic Instrumentation Calibration Inc., http://www.maginst.com.

[92] Goodfellow Cambridge, http://www.goodfellow.com/csp/active/gfHome.csp.

[93] R. Grossinger, et al., Eddy Currents in Pulsed Field Measurements, Journal of Magnetism and Magnetic Materials, 2002; 242-245, 911-14.

[94] D. Vasic, V. Bilas, D. Ambrus, Pulsed Eddy-Current non-Destructive Testing of Ferromagnetic Tubes, IEEE Transactions on Instrumentation and Measurement,Vol 53, No. 4, 2004, 289-1294.

[95] J. Bohlmark, M. Ostbye, M. Lattemann, H. Ljungcrantz, T. Rosell, U. Helmersson, Guiding the Deposition Flux in an Ionized Magnetron Discharge, Thin Solid Films, Vol. 515, 2006, 1928-1931.

[96] N. Ida, Engineering Electromagnetics, 2nd Ed., Springer Verlag, New York, 2004.

APPENDICES

APPENDIX A

AIR-CORE COIL DESIGN

A.1 Air-core coil design

Figures A.1 pictures the construction of the “Air-core” coil design for annealing process. The laser based magnetostriction measurement is depicted in figure A.2.

Referring to equation 2-4, the magnetic field strength generated by a coil wound around a spool is a function of several factors such as type of wire used, effective length of coil, number of turns and current required to generate the desired magnetic field. The steps of design are described in the next sections starting with selecting the type of copper wire. The highest field strength requires the maximum possible current.

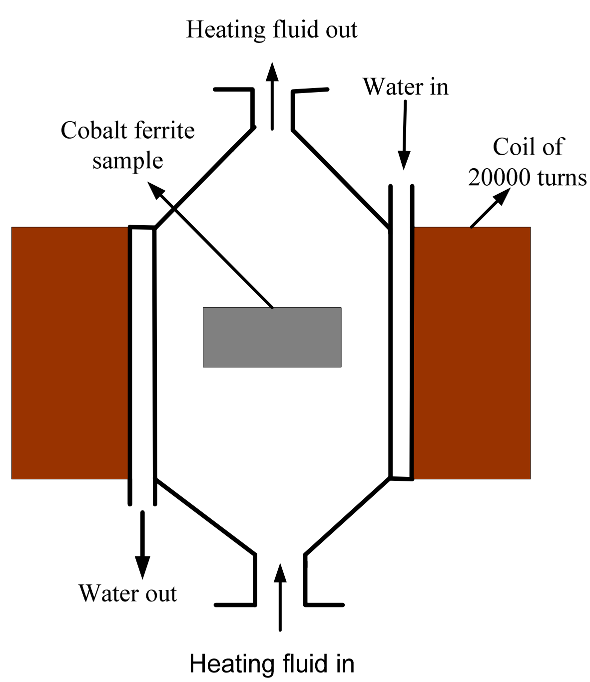

Figure A.1: Construction of air-core coil design for annealing process.

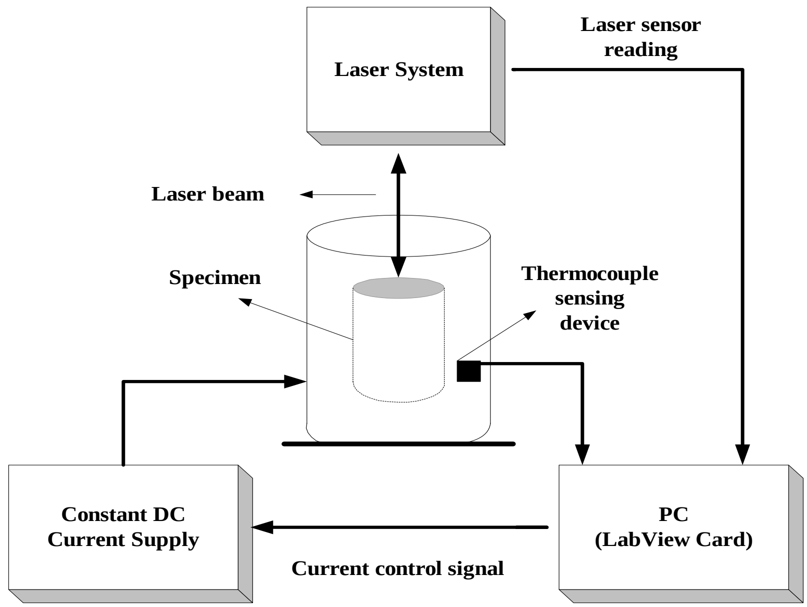

Figure A.2: Laser based magnetostriction measurement [53].

However the current is limited by the insulating properties of the copper wire used. In order to increase the current without damaging the insulation layer of the copper wire, an adequate cooling system (water, oil or air) has to be used to minimize the effect of the heat generated in the coils.

A.1.1 Choice of wire gauge

In this study, copper wire type 22SWG was chosen to be wound around the spool. The specifications of this copper wire are shown in table A.1. 22SWG copper wire was coated with polyurethane to act as an insulator. The same type of wire was also selected by other researchers to make a solenoid where the wire was wound around an air-core and had a current carrying capability sufficient to generate a moderately strong static magnetic field. This type of wire is used normally as a fuse wire for a current limit of 28 Amps.

Table A.1: Specifications of copper wire used to make the coils.

Coil type	Resistivity (nΩm)	Diameter (mm)	Diameter including insulating layer (mm)	Temperature index
22SWG	16.8	0.71	0.776	200 °C

A.1.2 Plastic spool

The copper wire has to fit around a cylindrical plastic spool, with the sample being tested being placed inside; it has to be large enough to allow space for a heating fluid to heat the sample to the correct temperature. The heating is part of the magnetic annealing treatment and is needed to change the magnetic properties of the sample, which will result in a change in its magnetostriction coefficient. It is suggested that this plastic spool will have an outer diameter of 80 mm and an inner diameter of 74 mm. Also the minimum length of the coil has to be larger than the sample's length. An initial suggestion for a value for the length of the coil is 100 mm.

To insure that the heat generated in the coil will not be transferred to the sample, another plastic spool will be placed around the sample to allow a water cooling system between the two spools as shown in figure A.3. The outer diameter of this spool is 68 mm, and its inner diameter is 62mm.

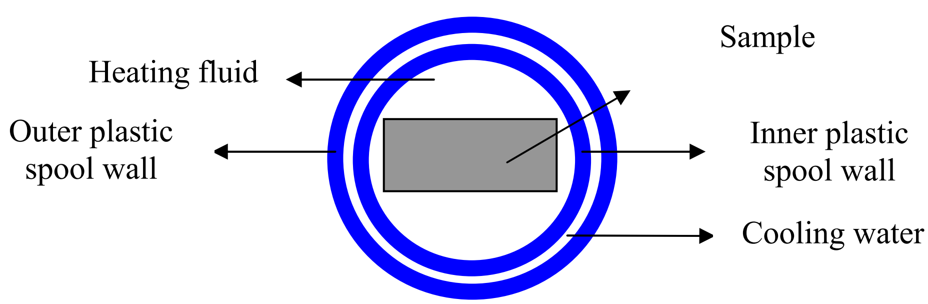

Figure A.3: Plan of arrangement of sample in heating fluid in equipment for magnetic annealing.

A.1.3 Calculation of Power Consumed by the Coil

The required magnetic field strength for this solenoid design is given in the literature as 9000 Oersteds. It depends on the number of loops or turns of the winding, the current that flows in the coil, radius of the coil, and the effective length of the coil, according to equation (2-4) which states that, $H = \frac{NI}{\sqrt{4r^2 + l^2}}$ therefore

$$\frac{H}{I} = \frac{N}{\sqrt{4r^2 + l^2}} \tag{A-1}$$

This equation assumes that the radius of the coil is constant for all the turns of the coil, but for a coil with a large number of turns this is not true because successive layers of wire must be wound around the outside of the inner sections of the coil. Therefore the equation must be modified as follows

$$(H/I)_{total} = \sum_{n=1}^{n=N_1} \frac{N}{\sqrt{4[(n-0.5)\times d_w + r_{in}]^2 + l_c^{\,2}}} \tag{A-2}$$

where

I is the currents that flow in the coil in amps

$r = (n - 0.5) \times d_w + r_{in}$ where n is an integer changing from the value of 1 for the inner most layer to N_1 for the outer most layer.

N = total number of turns

N_1 = total number of layers

d_w = diameter of copper wire including insulation layer

r_{in} = Inner radius of the coil

l_c = length of coil

H is the amperes per meter which can be converted to Oersteds by dividing the value of H by 79.5775.

The number of loops or turns of the first layer of winding is

$N = \frac{l_c}{d_w} = \frac{100mm}{0.776mm} = 128.9 \cong 129$ turns, if the length of the coil is 100 mm.

For example a coil with 13,000 turns in this analytical design could be arranged in 100 layers with each layer consisting of 130 turns. Different values of the number of turns per layer and the number of layers were analysed in order to calculate the lowest power consumed.

Microsoft Excel was used to calculate the total value of $\frac{H}{I}$ generated by different numbers of turns per layer and the number of layers, in order to find the minimum power consumed by the coil for the chosen value of H of 9000 Oersteds. Equation (A-2) was used to calculate the dc current that flows in the coil. Total length of the wire was calculated as follows

$$l_w = 2N\pi \sum_{n=1}^{n=N_1} (r_{in} + (n-0.5) \times d_w) \quad \text{(A-3)}$$

The resistance of the wire was calculated using

$$R = \frac{\rho \times l_w}{A} \quad \text{(A-4)}$$

where

ρ = Resistivity of the copper wire

A= cross-sectional area of the copper wire

The power consumed was calculated using

$$P = I^2 \times R \quad \text{(A-5)}$$

Results are listed in the following tables

Table A.2: Calculation of power when the length of coil is 0.10 m.

Length of coil (m)	No. of turns $N \times N_1$	Length of wire (m)	Resistance (Ω)	Current (Amps)	Power (kW)
0.10	129 X 50	2407	102.15	17.113	29.913
0.10	129 X 75	4201	178.24	12.402	27.417
0.10	129 X 100	6387	271.02	10.041	27.324
0.10	129 X 150	11939	506.61	7.656	29.693
0.10	129 X 200	19064	808.93	6.438	33.523

Table A.3: Calculation of power when the length of coil is 0.14 m.

Length of coil (m)	**No. of turns** ***N X N₁***	**Length of wire (m)**	**Resistance (Ω)**	**Current (Amps)**	**Power (kW)**
0.14	180 X 50	3359	142.53	14.586	30.324
0.14	180 X 75	5861	248.71	10.370	26.747
0.14	180 X100	8912	378.17	8.273	25.880
0.14	180 X 150	16659	706.90	6.178	26.979
0.14	180 X200	26600	1.129 K	5.124	29.633

Table A.4: Calculation of power when the length of coil is 0.15 m.

Length of coil (m)	**No. of turns** $N \times N_1$	**Length of wire (m)**	**Resistance (Ω)**	**Current (Amps)**	**Power (kW)**
0.15	193 X 50	3602	152.83	14.188	30.764
0.15	193 X 75	6285	266.67	10.046	26.912
0.15	193 X 100	9556	405.48	7.987	25.867
0.16	200 X 100	9902	420.18	7.846	25.869
0.15	193 X 150	17862	757.95	5.935	26.701
0.15	193 X 200	28522	1.210 K	4.906	29.132

Table A.5: Calculation of power when the length of coil is 0.16 m.

Length of coil (m)	**No. of turns** $N \times N_1$	**Length of wire (m)**	**Resistance (Ω)**	**Current (Amps)**	**Power (kW)**
0.16	206 X 50	3844	163.12	13.853	31.302
0.16	206 X 75	6708	284.64	9.771	27.173
0.16	206 X 100	10199	432.79	7.744	25.953
0.16	206 X 150	19066	809.01	5.727	26.537
0.16	206 X 200	30443	1.292	4.719	28.763

Table A.6: Calculation of power when the length of coil is 0.17 m.

Length of coil (m)	**No. of turns** ***N X N₁***	**Length of wire (m)**	**Resistance (Ω)**	**Current (Amps)**	**Power (kW)**
0.17	219 X 50	4087	173.41	13.568	31.922
0.17	219 X 75	7131	302.60	9.535	27.513
0.17	219 X 100	10843	460.1	7.535	26.121
0.17	219 X 150	20269	860.06	5.547	26.466
0.17	219 X 200	32364	1373	4.556	28.501

Table A.7: Calculation of power when the length of coil is 0.18 m.

Length of coil (m)	**No. of turns** ***N X N₁***	**Length of wire (m)**	**Resistance (Ω)**	**Current (Amps)**	**Power (kW)**
0.18	232 X 50	4329	183.71	13.323	32.609
0.18	232 X 75	7555	320.56	9.333	27.920
0.18	232 X 100	11487	487.41	7.354	26.357
0.18	232 X150	21472	911.12	5.390	26.473
0.18	232 X200	34285	1455	4.413	28.329

Table A.8: Calculation of power when the length of coil is 0.19 m.

Length of coil (m)	**No. of turns** ***N X N₁***	**Length of wire (m)**	**Resistance (Ω)**	**Current (Amps)**	**Power (kW)**
0.19	245 X 50	4572	194	13.112	33.354
0.19	245 X 75	7978	338.52	9.157	28.382
0.19	245 X 100	12130	514.72	7.196	26.652
0.19	245 X150	22675	962.17	5.252	26.545
0.19	245 X200	36206	1536	4.287	28.233

Table A.9: Calculation of power when the length of coil is 0.20 m.

Length of coil (m)	No. of turns $N \times N_1$	Length of wire (m)	Resistance (Ω)	Current (Amps)	Power (kW)
0.20	258 X 50	4815	204.30	12.929	34.148
0.20	258 X 75	8401	356.49	9.00	28.893
0.20	258 X 100	12774	542.04	7.057	26.996
0.20	258 X 150	23878	1013	5.131	26.672
0.20	258 X 200	38127	1618	4.175	28.200

Table A.10: Calculation of power when the length of coil is 0.20 m.

Length of coil (m)	No. of turns $N \times N_1$	Length of wire (m)	Resistance (Ω)	Current (Amps)	Power (kW)
0.21	271 X 50	5057	214.59	12.768	34.984
0.21	271 X 75	8824	374.45	8.868	29.445
0.21	271 X 100	13418	569.35	6.935	27.382
0.21	271 X 150	25081	1064	5.023	26.847
0.21	271 X 200	40049	1699	4.075	28.223

From these calculated results, it can be seen that coil made up of 20,000 turns (table A.4) is the most suitable. This arrangement was chosen because H, d_w, r_{in}, ρ, A are fixed. N_1 is calculated from $\frac{N}{N_1} = \frac{l_c}{d_w}$, and n must vary between 1 and N_1, and so I, N and l_c are the only true variables. The calculations were performed in groups by choosing a value of l_c and then varying I and N to achieve the given value of H. As a start l_c had to be greater than 100 mm.

Each section in the table shows values of I and N varied to give a minimum of the power. Also all the sections can be arranged to produce a minimum value for the power for the selected value of l_c the length of coil.

A.1.4 Heat removal

In order to allow a copper wire with a diameter of 0.776 mm, to carry a high current, the heat generated must be removed. This must be done to avoid the wire reaching a temperature which is high enough to damage the polyurethane around each wire. If this is not done, the insulation will break down and current leakage across sections of the wire will occur.

- The coil will be immersed in transformer oil to improve the rate of heat transfer.

- A water cooling system should be placed between the sample and the coil to ensure that the heat generated in the coil will not be transferred to the sample.

- The coil has to be split into number of sections to improve the rate of transfer of heat.

The coil must be designed to allow the heat being generated in the coil to be transferred away. Extra features to allow this to take a place are as follows

Firstly a “thermal conductivity” value for the coil must be established so that the heat transfer rates can be calculated.

A.1.5 A Mathematical model used to develop a composite value of thermal conductivity for the copper coil

Thermal conductivity is the quantity of heat flowing per unit time through a wall 1 m^2 in area and 1 m thick when the temperature of the two surfaces differ by 1 °C. Heat can be transferred from a place of higher temperature to a place of lower temperature by either conduction (heat transmission between touching particles in solids, liquid or gaseous bodies), or convection (circulation of warm and cool liquid gas particles) or radiation.

In this analysis, it is assumed that the heat is conveyed by conduction alone, of course there will be some heat transferred by convection in the oil. However it is assumed that there is no heat transferred in this way so that the design can have a safety factor built in.

It is also assumed that the heat is conducted in a straight line. It is necessary to make this assumption because of the complexity of the system. It is unlikely to be strictly true, but the method gives a result which is approximately correct, and again, the design will have a built in safety factor, to allow for this assumption.

Figure A.4 shows two coated copper wires, one on the top of the other. In the coil, there are of course many other coated wires alongside these two above and beneath them. In the diagram, heat is being transferred from the top wire to the bottom one. The flow of heat is therefore in the vertical direction and downwards. The wires alongside are at the same temperatures as their horizontal neighbours, and for them also heat is being transferred vertically downwards.

One quadrant of the upper copper shown in figure A.4 can be split into 388 channels. This number is chosen so that each channel is 1 micron wide and 388 long, arranged side by side. This follows because the diameter of the coated wire is 0.776 mm. The long dimension of the channel is vertical, and the short one is horizontal.

Let the distance that the heat travels in the copper be x. Let the distance in the polyurethane be y, and the distance in the oil be z. Since it is assumed that the heat is conducted in a straight line, there must be perfect heat insulation between each of the channels because no heat travels from one channel to another.

The thermal conductivity for copper is given as 401 W/m°C. For the polyurethane it is 0.21 W/m°C, and for the transformer oil it is 0.136 W/m°C at 273°C, and 0.127 W/m°C at 373°C. The value given at 373 °C will be used in this analysis.

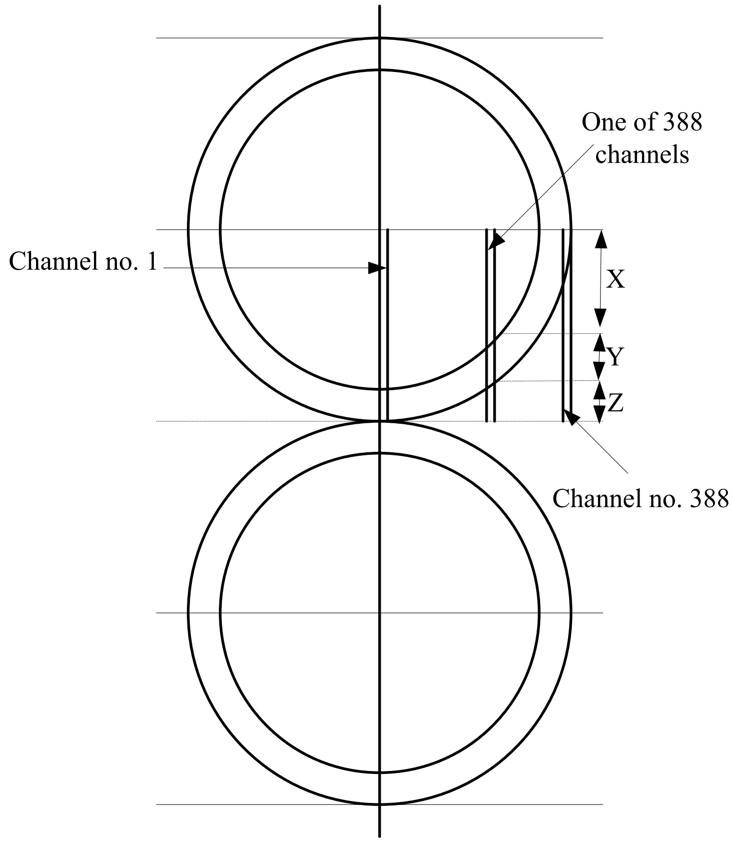

Figure A.4: Two coated copper wires on top of each other.

Each of the channels are numbered with the first one being the one with its corner at the centre of the copper wire, and the 388th one with its corner just touching the outer layer of the coating of the neighbouring wire. For this analysis it can be arranged that the rate of heat flow to be such that the temperature between the centres of the two wires shown in figure A.4 is 2°C. The temperature change, while the heat is flowing through the copper part of the channel, will be designated as ΔT_x.Similarly, the temperature change in the polyurethane and oil parts of the channel will be ΔT_y , and ΔT_z respectively. Therefore

$$\Delta T_x + \Delta T_y + \Delta T_z = 1°\text{C} \tag{A-6}$$

The thermal gradients are therefore $\frac{\Delta T_x}{x}$, $\frac{\Delta T_y}{y}$ and $\frac{\Delta T_z}{z}$.

The cross-sectional area through which the heat is flowing as it flows through each channel will be designated as *A*, the heat flowing will be designated as *Q*, and the time taken for this heat flow will be *t*. The heat flow is proportional to the product of area, time and thermal gradients.

For each channel, the rate of heat flow through the part of the channel in copper will be the same as the heat flow through the part of the channel in polyurethane and in oil. Therefore

$$Q = 401 \times A \times t \times \Delta T_x / \mathrm{x} = 0.21 \times A \times t \times \Delta T_y / \mathrm{y} = 0.127 \times A \times t \times \Delta T_z / \mathrm{z} \tag{A-7}$$

It follows that

$$\Delta T_x = \Delta T_y \left(\frac{0.21x}{401y} \right),\ \Delta T_z = \Delta T_y \left(\frac{0.21z}{0.127y} \right) \tag{A-8}$$

Substituting in equation (3-6)

$$\Delta T_y \left(\frac{0.21x}{401y} \right) + \Delta T_y + \Delta T_y \left(\frac{0.21z}{0.127y} \right) = 1 \tag{A-9}$$

$$\Delta T_y \left(\frac{0.21x}{401y} + 1 + \frac{0.21z}{0.127y} \right) = 1, \text{ therefore} \tag{A-10}$$

$$\Delta T_y = \frac{1}{\left(\frac{0.21x}{401y} + 1 + \frac{0.21z}{0.127y} \right)} \tag{A-11}$$

It follows that

$$\frac{Q}{At} = \frac{0.21}{y} \left(\frac{1}{\frac{0.21x}{401y} + 1 + \frac{0.21z}{0.127y}} \right) \tag{A-12}$$

Since the radius of the copper wire is 355 microns then

$$x + y + z = 388 \tag{A-13}$$

$$x^2 + d^2 = 355^2 \tag{A-14}$$

$$(x + y)^2 + d^2 = 388^2 \tag{A-15}$$

Since each channel is 1 micron wide, and 388 long, then lengths *x*, *y*, and *z* can be computed using the formulas shown above and this gives the following

$$z = 388 - \sqrt{388^2 - d^2} \tag{A-16}$$

$$x = \sqrt{355^2 - d^2} \tag{A-17}$$

$$y = \sqrt{388^2 - d^2} - \sqrt{355^2 - d^2} \tag{A-18}$$

where d = 0.5 for channel 1, and 1.5 for channel 2 and so on.

Equation (A-12) can provide estimates for the rate of heat flow, *Q/t* per unit area A in terms of single variable *d*. Then the sum of all values of Q*/At* can be made for all 388 channels, by allowing *d* to take values from 0.5 to 387.5. This provides an average value which can be found by dividing the sum by 388, and this is composite thermal conductivity of the coil. Microsoft excel was used to calculate a composite thermal conductivity of 0.9339 W/m°C.

A.1.6 Examination of correction factor

It is possible to use these results to test whether the heat is conducted in a straight line. This assumption is that there is no flow of heat from one channel to the neighbours. By calculating the temperature changes for each channel as the heat flows from one point in the channel to another, it can be shown that a very small amount of heat would flow from channels with high numbers (354, 355, 356, etc.) towards channels with low numbers (1, 2, 3 etc.) over the part of the channels in the copper.

An attempt has been made to correct the figures to take this into account. As a result the temperature where the copper touches the polyurethane insulation in each channel will alter. For low channel numbers, the temperature will rise slightly, and for high channel numbers, it will fall slightly. The correction assumes that the temperature gradient is the same for copper parts of each channel.

The following mathematical models were used in order to perform a suitable correction factor for the composite thermal conductivity:

$$\Delta T_x = \left(\frac{\frac{0.21x}{401y}}{\frac{0.21x}{401y} + 1 + \frac{0.21z}{0.127y}} \right) \tag{A-19}$$

Temperature gradient difference in copper channels

$$= \left[\frac{\Delta T_x}{x} \right]_i - \left[\frac{\Delta T_x}{x} \right]_{i+1} \tag{A-20}$$

$$\left(\frac{\Delta T_x}{x} \right)_{corrected} = \frac{\Sigma \left(\frac{\Delta T_x}{x} \right)}{355} \tag{A-21}$$

$$\left(\Delta T_x \right)_{corrected} = \left(\frac{\Delta T_x}{x} \right)_{corrected} \times x \tag{A-22}$$

This yield to a correction factor equals to ΔT_x - $\left(\Delta T_x \right)_{corrected}$

It follows that

$$Q / At = \frac{0.21}{y} \left\{ \left[\frac{1}{\frac{0.21x}{401y} + 1 + \frac{0.21z}{0.127y}} \right] + correction \right\} \tag{A-23}$$

This alters the composite thermal conductivity very slightly to 0.9349 W/m°C.

A.1.7 Analysis of heat transfer through the coil

Initially, it has already been arranged to design a coil consisting of 20,000 turns, and generating a 25.869 KW of heat when producing the required magnetic field.

The initial length of the solenoid, if it is not divided into sections, is therefore

$$l_c = N \times d_w = 200 \times 0.776 = 155.2 \text{ mm} \qquad \text{(A-24)}$$

The coil has an inner radius of 40 mm, and therefore its outer radius is (figure A.5)

$$r_c = r_{in} + N_1 \times d_w = 40 + 100 \times 0.776 = 117.6 \text{ mm} \qquad \text{(A-25)}$$

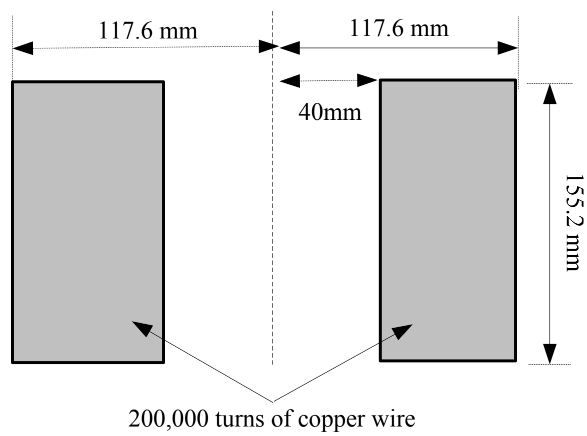

Figure A.5: Initial dimensions of the coil.

With the design shown in figure A.6, the distances between the copper heat conductor discs is likely to be much smaller than the distance between the innermost section of the coil and the outmost section of the coil. Therefore, with this feature, it is obvious that the analysis will only take into account that heat being conducted upwards and downwards and heat being conducted a radial direction can be ignored.

Now consider the surfaces formed when the coil was made by winding the copper wire around the spool. The spool must have flanges to allow the winding of the coil to form. If the spool is a cylindrical with a vertical axis, it will have flanges at the top and bottom as shown in figure A.6.

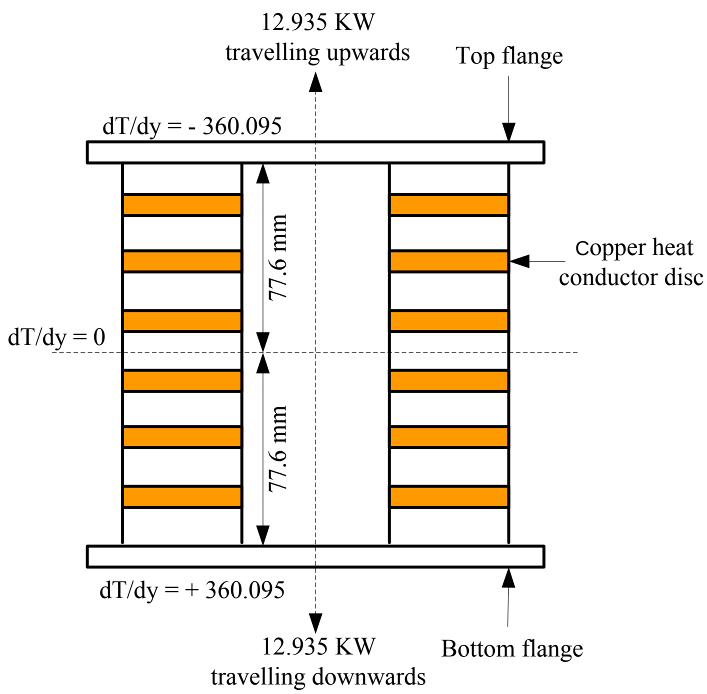

Figure A.6: Coil with top and bottom flanges and copper heat conductor discs.

It is also assumed that half the heat generated in the coil travels vertically upwards by conduction, and the other half travels vertically downwards, also by conduction. Therefore the amount of heat travelling upwards from the coil will be

$$Q_{up} = P \times 0.5 = 25.869 \times 0.5 = 12.935\,\text{KW} \tag{A-26}$$

The area at the top of coil, through which this heat must travel, is

$$A_l = \pi(117.6^2 - 40^2)\,\text{mm}^2 \text{ or } \pi(117.6^2 - 40^2)/1{,}000{,}000\ \text{m}^2 \tag{A-27}$$

The thermal gradient at the top of coil can be estimated. It is given by *dT/dy*, where y is a vertical distance.

$$\frac{dT}{dy} = -\frac{Q_{up}}{K_{tc} \times A_1} = -\frac{12935}{0.9349 \times \pi(117.6^2 - 40^2)} = -360.095°C/m \qquad \text{(A-28)}$$

where K_{tc} is the composite thermal conductivity calculated in section A.1.5.
The minus sign denotes that the temperature decreases as the height y increases.

Since an assumption has been made that the heat must travel rather upwards or downwards, it is also true that a horizontal plane must also exist through the centre of the coil, where there will be no heat travelling upwards or downwards and so at this level $\frac{dT}{dy} = 0$ *°C/mm*.

Vertical distances above and below this line can be defined by making $y = 0$ at this plane. This means that y can vary from -77.6 mm at the bottom of the coil to +77.6 mm at the top of the coil (figure A.6). Also the value of $\frac{dT}{dy}$ varies between +360.095 °C/mm at the bottom of the coil to -360.095 °C/mm at the top of the coil. The equations describing heat conduction are satisfied if the value of $\frac{dT}{dy}$ is proportional to y at each level. Therefore

$$\frac{dT}{dy} = \frac{-360.095y}{77.6} \qquad \text{(A-29)}$$

This equation can be integrated to give

$$\int \frac{dTdy}{dy} = T = -\frac{360.095y^2}{2(77.6)} + C \qquad \text{(A-30)}$$

where, C is the constant of integration. Therefore as y changes, the temperature profile has the same shape as a parabola, and the highest temperature occurs where y is zero, therefore we can define

$T_{\max} = C$, and the equation can now be written as

$$T = T_{\max} - \frac{360.095y^2}{2(77.6)} \qquad \text{(A-31)}$$

At the top of the coil, where y = 77.6 mm, the temperature can be written as

$$T = T_{\max} - \frac{360.095 \times 77.6^2}{2(77.6)} = T_{\max} - 13971.7\,°\mathrm{C} \tag{A-32}$$

This analysis predicts that if the coil described above was constructed with no sections for cooling, the maximum temperature at its centre would be 13971.7°C above the temperature at its top or bottom. Therefore it is essential to provide a cooling system capable of avoiding this extreme temperature difference. This can be done by dividing the coil into sections.

A.1.8 Dividing the coil into sections

As an initial example of this procedure, it is considered that the coil is divided into 40 sections with horizontal copper cooling plates between the sections capable of removing the heat.

The total of 20,000 turns will form 40 sections of 500 turns each. The total vertical height was already calculated using equation (A-24) to be 155.2 mm. Therefore the height of each section will be

$$H_{\mathrm{sec}} = N_2 \times d_w = 5 \times 0.776 = 3.88\ \text{mm} \tag{A-33}$$

where N_2 = number of turns in each layer

In each section of this size, the number of turns in each layer must be five. Again it is assumed that the heat can travel upwards or downwards in each section but not in a radial direction. The heat travelling upwards in these sections will be

$$Q_{up-\mathrm{sec}} = \left(\frac{0.5 \times N_2}{N}\right) \times P = \left(\frac{2.5}{200}\right) \times 25.869KW = 323.363\text{Watts} \tag{A-34}$$

Each section will have the cross-sectional area, through which the heat must pass, as the original coil with no sections. Therefore the temperature gradient at the top of each section will be

$$\left[\frac{dT}{dr}\right]_{\text{sec}} = \frac{Q}{K_{tc} \times A_1} = \frac{323.363}{0.9349 \times \pi((117.6^2 - 40^2)}$$

$$\left[\frac{dT}{dr}\right]_{\text{sec}} = 9002.38°\text{C/m} \tag{A-35}$$

The equations describing heat conduction are satisfied if the temperature gradient varies linearly with the vertical height from the centre to the surface. Therefore the temperature difference between the hottest part of the section of the coil (centre), and the surface of the section will be half the thermal gradient multiplied by the distance

$$\left[T_{\max} - T\right]_{\text{sec}} = 0.5 \times 9.00238 \times \frac{3.88}{2} = 8.73231°C \tag{A-36}$$

A.1.9 Calculation of the width of copper heat conductors

The copper conductor must draw the heat being generated by the upper half of the coil section below it and the heat being generated by the lower half of the coil section above it.

Let the thickness of the copper heat conductor (which is also the distance between sections of the coil) be Y_c.

For the innermost section of the wire, the distance to the centre of the equipment is 40 mm, and so the length of one loop or turn of the wire is $2\pi \times 40mm$. For the outmost section of the wire, the distance to the centre of the equipment is 117.6 mm, and the length of each loop is $2\pi \times 117.6$ mm. The heat generated by each section of the coil is

$$Q_{\text{sec}} = \left(\frac{1}{40}\right) \times P = \left(\frac{5}{200}\right) \times 25.869KW = 646.725\text{Watts} \tag{A-37}$$

This is also the total amount of heat which must be conducted away by the copper heat conductor. The cross-sectional area through which the heat must flow for the outside surface of the disc shaped copper conductor will be

$$A_2 = Y_c \times 2\pi \times 117.6 \times 10^{-6} \tag{A-38}$$

Therefore

$$\frac{dT}{dr} = -\frac{646.725}{401 \times Y_c \times 2\pi \times 117.6 \times 10^{-6}} = -\frac{2182.67}{Y_c}\ \text{°C/m} \tag{A-39}$$

The negative sign indicates that as the radius increases, the temperature decreases. The thermal gradient at the other end of the conductor must be zero, since no heat is generated at this point.

Half-way along the conductor, the heat generated by the turns of the coils closer to the centre of the equipment must be conducted through the copper heat conductor so that it can be drawn away, but heat generated by the turns of the coils further away from the centre of the equipment will not pass through this part of the copper heat conductor. The copper heat conductor will have the shape of a disc as shown in figure A.7. Therefore a point half-way along the conductor will have a radius of $40 + 77.6/2 = 78.8$ mm.

The heat generated in the turns closer to the centre of the equipment where the radius is less than 78.8 mm will be proportional to the area of the disc.

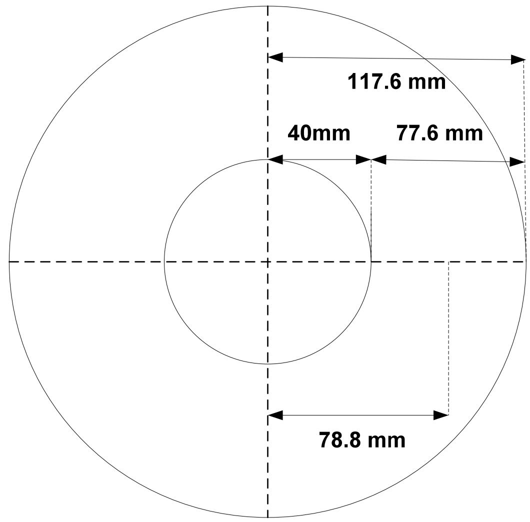

Figure A.7: Dimensions of copper heat conductor disc.

Therefore the heat generated by the turns closer to the centre of the equipment is

$$Q_1 = 646.725 \times \frac{\pi(78.8^2 - 40^2)mm^2}{\pi(117.6^2 - 40^2)mm^2} = 243.75 \text{ Watts} \tag{A-40}$$

A similar calculation can be made to estimate the thermal gradient at this half-way position along the copper conductor

$$\left[\frac{dT}{dr}\right]_{halfway} = -\frac{243.75}{401 \times Y_c \times 2\pi \times 78.8 \times 10^{-6}} \quad -\frac{1227.71}{Y_c} \text{ °C/m} \tag{A-41}$$

Similarly, calculation can be made to estimate $\frac{dT}{dr}$ for a point having a radius of r_n

$$Q_n = 646.725 \times \frac{\pi(r_n^2 - 40^2)}{\pi(117.6^2 - 40^2)} \tag{A-42}$$

This approach can be generalized using the formula

$$\frac{dT}{dr} = \frac{646.725 \times \dfrac{\pi(r_n^2 - 40^2)}{\pi(117.6^2 - 40^2)}}{0.401 \times 2\pi \times Y_c \times r_n} = \frac{-646.725 \times (r_n^2 - 40^2)}{0.401 \times 2 \times Y_c \times r_n \times \pi(117.6^2 - 40^2)}$$

$$\frac{dT}{dr} = -\frac{(r_n^2 - 40^2)}{47.65 \times Y_c \times r_n} \tag{A-43}$$

$$\frac{dT}{dr} = \frac{-K(r^2 - 40^2)}{r} \tag{A-44}$$

where $K = \dfrac{1}{47.65 \times Yc}$

To calculate the temperature change, equation (A-44) must be integrated;

$$\int \frac{dT}{dr} = \int \frac{-Kr^2}{r} + \int \frac{40^2 K}{r}$$

$$T = \frac{-Kr^2}{2} + 40^2 \log_e r + C \tag{A-45}$$

where: C is the integration constant.

The maximum temperature will occur at the innermost part of the copper heat conductor disc, where the radius r is 40 mm. Substituting in equation (A-45) where r = 40 mm. Therefore

$$T_{\max} = \frac{-K40^2}{2} + 40^2 K \log_e 40 + C$$

$$C = T_{\max} + \frac{K40^2}{2} - 40^2 K \log_e 40 \tag{A-46}$$

Substituting equation (A-46) into equation (A-45), therefore

$$T = \frac{-Kr^2}{2} + 40^2 K \log_e r + T_{\max} + \frac{K40^2}{2} - 40^2 K \log_e 40$$

$$T_{\max} - T = \frac{Kr^2}{2} - \frac{K40^2}{2} - 40^2 K \log_e r + 40^2 K \log_e 40$$

$$T_{max} - T = \frac{K(r^2 - 40^2)}{2} - 40^2 K \log_e(\frac{r}{40}) = K\left[\left(\frac{r^2 - 40^2}{2}\right) - 40^2 \log_e\left(\frac{r}{40}\right)\right]$$

Since $K = \dfrac{1}{47.65 \times Y_c}$

Therefore

$$T_{max} - T = \frac{\dfrac{r^2 - 40^2}{2} - 40^2 \log_e\left(\dfrac{r}{40}\right)}{47.65 \times Y_c} \tag{A-47}$$

The greatest temperature difference will occur at the other end of the copper heat conductor disc, on the out side edge, where the radius is 117.6 mm. At this edge

$$T_{max} - T = \frac{\dfrac{117.6^2 - 40^2}{2} - 40^2 \log_e\left(\dfrac{117.6}{40}\right)}{47.65 \times Y_c} = \frac{92.12}{Y_c} \tag{A-48}$$

This is a reasonable approach, for instance if $Y_c = 1$ mm, the quantity $T_{max} - T =$ $92.12\,°C$. This allows one to operate a coil in this way without reaching excessive temperatures.

One further complication needs to be added at this point. For safety reasons, it is considered appropriate to place electrically insulating materials around the copper discs which are being used as heat conductors to draw away the heat being generated in the coil. One possibility is to coat the copper discs with polyurethane varnish, providing a coating similar to the coating around the copper wire forming the coil. Its thickness would be 0.033 mm, and its thermal conductivity would be 0.21 W/m°C. The heat passing through these insulations layers is

$$Q_{ins} = 0.5 \times \frac{5}{200} \times 25.869 = 323.363\text{Watts} \tag{A-49}$$

The temperature gradient of the insulating material is

$$\left[\frac{dT}{dr}\right]_{ins} = \frac{323.363}{0.21\times(\pi(0.04+(100\times 0.000776))^2-(\pi\times 0.04^2))}$$

$$\left[\frac{dT}{dr}\right]_{ins} = 40077.74°\text{C/m} \tag{A-50}$$

The temperature difference across the insulation layers =

$$\left[T_{\max} - T\right]_{ins} = \frac{dT}{dr}\times 0.000033 = 1.323\,°\text{C} \tag{A-51}$$

It is estimated that the outside surface must be maintained at a temperature of at least 40°C by the cooling air flow. The maximum temperature that the coil can withstand is 200°C, and it is probably safe to design the system so that the maximum temperature never exceeds 190°C. Therefore there is a total temperature difference available for the system of 150°C. This is made of three parts

- The temperature difference between the centre of the coil and the outside surface which is calculated in equation (A-36).

- The temperature difference across the insulation surrounding the copper heat conductors which is calculated in equation (A-51).

- The temperature difference between the hottest part of copper heat conductor and its outside edge which is equal to:

$$T_{\max} - T = 150°C - (T_{\max} - T)_{section} - (T_{\max} - T)_{layers}$$

$$T_{\max} - T = 150°C - 1.323°C - 8.73231°C = 139.945°C \tag{A-52}$$

The value for the thickness of copper heat conductor Y_c is obtained by equations (A-48) and (A-52)

$$\frac{92.12}{Y_c} = 139.945 \text{ , and therefore } Y_c = 0.6583\,\text{mm} \tag{A-53}$$

A.1.10 Corrections to calculations to allow for the true height of the coil

Each layer of the coil is made up of 200 turns and there are 100 layers but in each layer the 200 turns are divided into 40 sections, each containing 5 turns. The copper heat conductors separate the 40 sections from each other, and therefore there are 39 of these, which must be taken into account when calculating the total height of the coil.

It is true that the coil will also have copper heat conductors above and below it, to remove some of the heat, so that there will probably be 41 identical copper heat conductors in total. However the top and bottom members of the series have no effect on the dimensions of the coil itself, and therefore they are disregarded in this calculations.
The total length or height of the coil is calculated by multiplying a thickness dimension for each coil section, by the number of sections.

To this must be added the thickness of the copper heat conductors, multiplied by the total number of copper heat conductors, which is 39.
Finally this must be increased still further to allow for the thickness of the insulation on each side of the copper heat conductors. This insulation is 0.033 mm thick, and it will be placed on each side of the copper heat conductors. The total height is therefore:

$$l_{coil} = 200 \times 0.776 + Y_c \times 39 + 39 \times 2 \times 0.033 = 183.448 \text{ mm} \tag{A-54}$$

This value must then be used to adjust the calculation of the magnetic field strength. Originally a value of 155.2 was used as an initial height of the coil. Iterative calculations must be then performed to arrive at a value used as initial value which is produced again in equation (A-54).

Microsoft Excel was used to carry out these calculations. Eventually after 6 iterations, the final value of height of the coil found to be 191.044 mm. The sequence of calculations that are built in Microsoft Excel is as follows:

Equation A.1: Calculation *of H/I*:

$$(H/I)_{total} = \sum_{n=1}^{n=N_1} \frac{N}{\sqrt{[(n-0.5)\times d_w + r_{in}]^2 + l_c{}^2}}$$

Equation A.2: Calculation of total circumference of the magnetic wire:

$$C = \sum_{n=1}^{n=N_1} 2\pi[(n-0.5)\times d_w \times + r_{in}]$$

Equation A.3: Calculation of the current that flows in the coil:

$$I = \frac{9000\times 1000}{4\pi \times (H/I)_{total}}$$

Equation A.4: Calculation total length of the magnetic wire:

$$l_w = N \times C$$

Equation A.5: Calculation of cross sectional area of the magnetic wire:

$$A = \pi(d_{w_{uncoated}} / 2)^2$$

Equation A.6: Calculation of the resistance of the magnetic wire:

$$R = \frac{\rho \times l_w}{A}$$

Equation A.7: Total required power:

$$P = I^2 \times R$$

Equation A.8: Calculation of temperature gradient of each section:

$$\left[\frac{dT}{dr}\right]_{\sec} = -\frac{Q_{up-\sec}}{K_{tc} \times A_2}$$

where: A_2 = surface area of the copper disc

Equation A.9: Calculation of thickness of each section:

$$T_{\sec} = N_2 \times d_w$$

Equation A.10: Calculation of the temperature difference between centre and surface of each section:

$$[T_{\max} - T]_{\sec} = 0.5 \times \left[\frac{dT}{dr}\right]_{\sec} \times \frac{T_{\sec}}{2}$$

Equation A.11: Calculation of heat passing each insulation layer:

$$H_{ins} = 0.5 \times P \times \frac{N_2}{N}$$

Equation A.12: Calculation of temperature gradient of insulating material that coats the copper rings:

$$\left[\frac{dT}{dr}\right]_{ins} = -\frac{Q_{up-\sec}}{K_{poly} \times A_2}$$

where K_{poly} = thermal conductivity of polyurethane

Equation A.13: Calculation of temperature difference across the insulation layer:

$$[T_{\max} - T]_{ins} = \left[\frac{dT}{dr}\right]_{ins} \times T_{ins}$$

where T_{ins} = Thickness of insulation

Equation A.14: Calculation of temperature difference between innermost and outside surface of copper rings, in terms of temperature difference across the insulation layer and temperature difference between the centre and the surface of a section:

$$\left[T_{\max} - T\right]_{rin} = 190 - 40 - [T_{\max} - T]_{ins} - [T_{\max} - T]_{\sec}$$

Equation A.15: Calculation of heat generated by each section:

$$Q_{\sec} = \frac{N_2}{N} \times p$$

Equation A.16: Calculation of temperature difference between innermost and outside surface of copper rings, in terms of Y_c :

$$\left[T_{\max} - T\right]_{rin} = \frac{\frac{r^2 - 40^2}{2} - 40^2 \log_e\left(\frac{r}{40}\right)}{K_a \times Y_c}$$

where $K_a = \frac{K_c \times 2}{Q_{\sec} / A_2}$

r = outer radius of the copper disc

K_c = thermal conductivity of copper

Equation A.17: Calculation of Y_c :

$$Y_c = \frac{\dfrac{\frac{r^2 - 40^2}{2} - 40^2 \log_e\left(\frac{r}{40}\right)}{K_a}}{190 - 40 - [T_{\max} - T]_{ins} - [T_{\max} - T]_{\sec}}$$

Equation A.18: Calculation of total length of coil:

$$L_c = (N_3 - 1) \times Y_c + N \times d_w + (N_3 - 1) \times 2 \times T_{ins}$$

where N_3 = number of sections

A.1.11 Calculation of adopted design of coil's construction

It is now necessary to find the adopted design so that the coil can be constructed with the best geometric dimensions to produce 9000 Oersteds with the minimum of heat generation.

The previous calculation was for a coil arranged as 200 spirals each of 100 turns and the 200 layers were separated into 40 sections of 5 spirals.
Again, Microsoft Excel was used to analyze different values of spirals and sections. However it is possible that an arrangement with sections of 3, and 6 spirals might produce a lower power requirement, but this can not be tested when working with a total of 200 spirals, since 200 when divided by 3, or 6 will not produce an integer. The arrangement with 200 spirals divided into 40 sections each having 100 turns, has the most appropriate power requirement, but due to the critical thickness of the copper heat conductor which is 0.853073 mm, this thickness can not be provided by the market, and once it is altered to 0.9 mm, this causes the power to rise up to 34.640 kW.

The other alternative is to use a coil made of 19,000 turns, where the thickness of the copper heat conductor is 0.902986 mm, and the power consumed by the coil is only 32.890 kW. The arrangement with 190 spirals divided into 38 sections each having 100 turns, has the most appropriate power requirement.

A.1.12 Proposed method of removing heat from the coil

The basic principle is to use air to keep the equipment cool, using a fume cupboard fan. It is necessary to use copper to conduct the heat away from the coil to the air. Up to this point, it has been necessary to concentrate on the need for copper to be inserted between the sections of the coil, to collect the heat and conduct it to the outer edge of the coil. However the outer surface of the coil does not provide enough large surface area for the transfer of heat to the air. It is necessary to increase the surface area between the copper and the air. This has to be done by building a structure in copper outside the outer edge of the coil, so that the air can come into contact with the copper and remove the heat.

However the required rate of removal of heat is so great that there must be a significant fall in temperature between the copper in contact with the outer edge of the coil structure, and the copper in contact with the air. This is a limitation caused by the value of the thermal conductivity of the copper. Because of this factor, it is necessary to re-adjust the design of the coil sections, increasing the thickness of the copper conductors between the coil sections from 0.90 mm to 1.50 mm. This, in turn would have the effect of reducing the magnetic field strength generated by the coil. It is therefore necessary to increase the electric current in the coil, to allow the magnetic field strength to remain at 9,000 Oersteds. As a result, there is an increase in the electrical energy being supplied to the coil, and, of course, an increase in the amount of heat which must be removed. The new values are listed in table A.11.

Other workers have calculated that equipment to remove the heat generated in the rig would consist of 599.8 tonnes of copper having a surface area of 141.64 square meters. It would heat 2.07 cubic meters of air per second from $20\,^{\circ}C$ to about $47\,^{\circ}C$ and this would require the use of fan consuming a power 20 kW of electricity.

Table A.11: Current, resistance, and power values.

Length of wire (m)	**Current (Amps)**	**Resistance (Ω)**	**Power (kW)**	**Thickness of copper discs (mm)**	**Length of coil (m)**
9407	9.75	399.17	37.93	1.50	0.205

A.1.13 Advantages and disadvantages of air-core coil design

No further analysis has been carried out with this design. This is due to the following reasons:

- The system requires very high power of 37.93 kW and 20 kW for the fan.

- From economic perspective, this design is quite costly especially for the annealing experiment which has to run for 72 hours continuously.

- It would be extremely difficult to wind the copper wire in the narrow spaces between each two copper heat conductors, as required in the design to achieve 500 turns in a space of 3.88 mm.

- A complex system required to remove the heat, with very large amounts of high parity copper.

APPENDIX B

SAMPLE OF *B*-*H* DATA RECEIVED FROM CEDRAT COMPANY

Table B1: H/B data received from Cedrat Company

Magnetic field intensity H (kA/m)	Magnetic flux density B (T)
57.5168	0.280258
54.9024	0.288296
57.5168	0.288296
58.824	0.280258
57.5168	0.296334
57.5168	0.288296
61.4384	0.296334
56.2096	0.288296
60.1312	0.296334
58.824	0.288296
58.824	0.280258
57.5168	0.27222
58.824	0.296334
57.5168	0.296334
57.5168	0.288296
58.824	0.296334
57.5168	0.296334
60.1312	0.296334
58.824	0.296334
57.5168	0.280258
62.7456	0.288296
61.4384	0.296334
58.824	0.288296
60.1312	0.296334
58.824	0.296334
60.1312	0.296334
60.1312	0.296334
61.4384	0.304373
60.1312	0.312411
62.7456	0.296334
62.7456	0.304373
61.4384	0.312411
62.7456	0.320449
60.1312	0.304373
62.7456	0.304373
60.1312	0.296334
62.7456	0.296334
64.0528	0.320449
62.7456	0.312411
61.4384	0.288296
64.0528	0.304373

Magnetic field intensity H (kA/m)	Magnetic flux density B (T)
62.7456	0.304373
64.0528	0.280258
64.0528	0.312411
64.0528	0.288296
62.7456	0.312411
65.36	0.288296
62.7456	0.304373
64.0528	0.304373
66.6672	0.304373
62.7456	0.304373
61.4384	0.304373
64.0528	0.312411
67.9744	0.304373
64.0528	0.320449
65.36	0.320449
66.6672	0.320449
65.36	0.320449
64.0528	0.304373
66.6672	0.320449
64.0528	0.304373
65.36	0.296334
67.9744	0.312411
66.6672	0.304373
67.9744	0.304373
67.9744	0.312411
65.36	0.320449
65.36	0.320449
66.6672	0.296334
67.9744	0.312411
65.36	0.304373
67.9744	0.320449
70.5888	0.320449
66.6672	0.320449
69.2816	0.304373
69.2816	0.312411
70.5888	0.312411
70.5888	0.320449
69.2816	0.320449
69.2816	0.320449
67.9744	0.304373
69.2816	0.312411
69.2816	0.320449

Magnetic field intensity H (kA/m)	Magnetic flux density B (T)
67.9744	0.320449
71.896	0.304373
70.5888	0.336525
69.2816	0.312411
73.2032	0.328487
69.2816	0.320449
73.2032	0.328487
71.896	0.312411
70.5888	0.320449
73.2032	0.320449
71.896	0.328487
70.5888	0.336525
71.896	0.312411
74.5104	0.320449
73.2032	0.320449
73.2032	0.328487
71.896	0.328487
75.8176	0.328487
69.2816	0.328487
71.896	0.328487
71.896	0.320449
73.2032	0.320449
74.5104	0.312411
73.2032	0.320449
73.2032	0.328487
74.5104	0.336525
77.1248	0.312411
75.8176	0.336525
75.8176	0.336525
74.5104	0.336525
75.8176	0.336525
75.8176	0.336525
75.8176	0.336525
75.8176	0.336525
74.5104	0.328487
75.8176	0.328487
75.8176	0.328487
74.5104	0.328487
75.8176	0.336525
75.8176	0.344563
75.8176	0.336525
75.8176	0.328487

Magnetic field intensity H (kA/m)	Magnetic flux density B (T)
75.8176	0.328487
77.1248	0.328487
78.432	0.344563
78.432	0.336525
77.1248	0.328487
77.1248	0.344563
78.432	0.328487
75.8176	0.328487
78.432	0.336525
78.432	0.328487
81.0464	0.328487
75.8176	0.336525
78.432	0.344563
77.1248	0.352601
78.432	0.336525
78.432	0.344563
81.0464	0.336525
78.432	0.344563
77.1248	0.336525
81.0464	0.352601
81.0464	0.344563
81.0464	0.344563
78.432	0.328487
79.7392	0.344563
79.7392	0.328487
81.0464	0.352601
79.7392	0.344563
79.7392	0.352601
79.7392	0.336525
82.3536	0.36064
82.3536	0.344563
81.0464	0.36064
81.0464	0.344563
82.3536	0.344563
81.0464	0.336525
82.3536	0.336525
82.3536	0.344563
82.3536	0.344563
81.0464	0.344563
82.3536	0.328487

APPENDIX C

MANIPULATION OF FLUX DENSITY OF COBALT FERRITE DATA

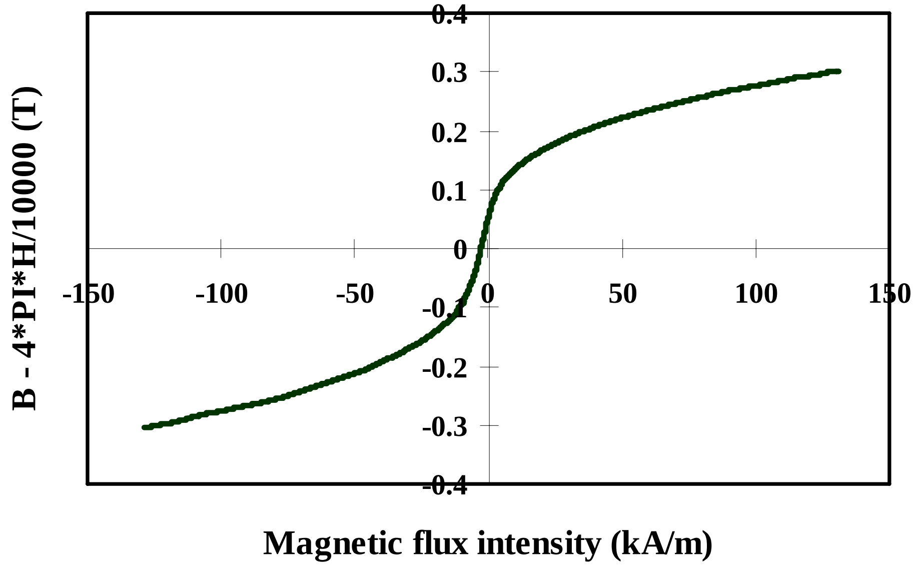

Figure C1: H (kA/m) vs. B - 4*PI*H/10000 (T).

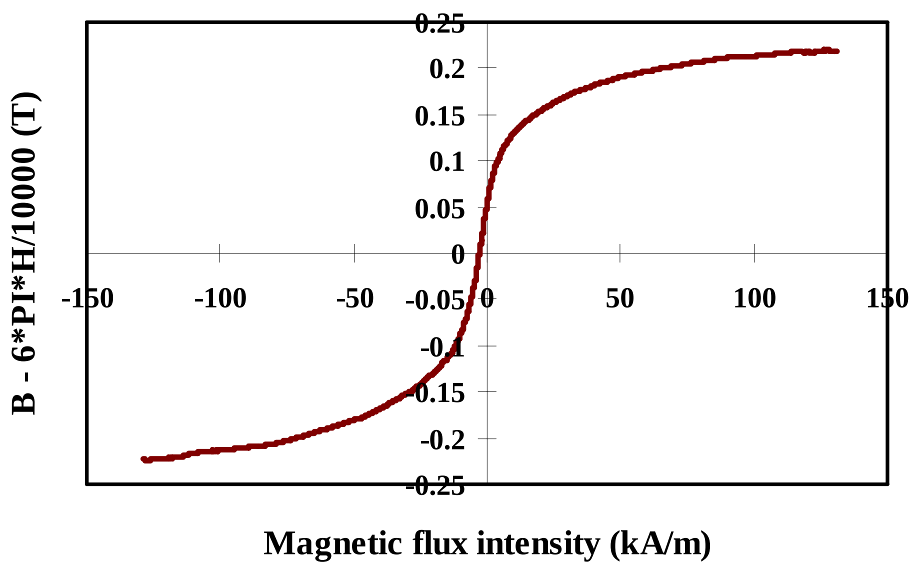

Figure C2: H (kA/m) vs. B - 6*PI*H/10000 (T).

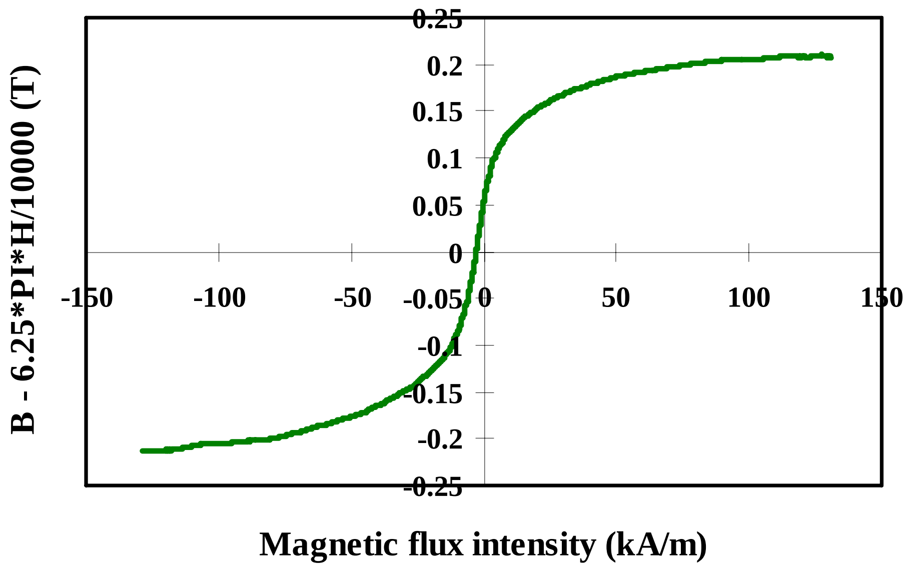

Figure C3: H (kA/m) vs. B - 6.25*PI*H/10000 (T).

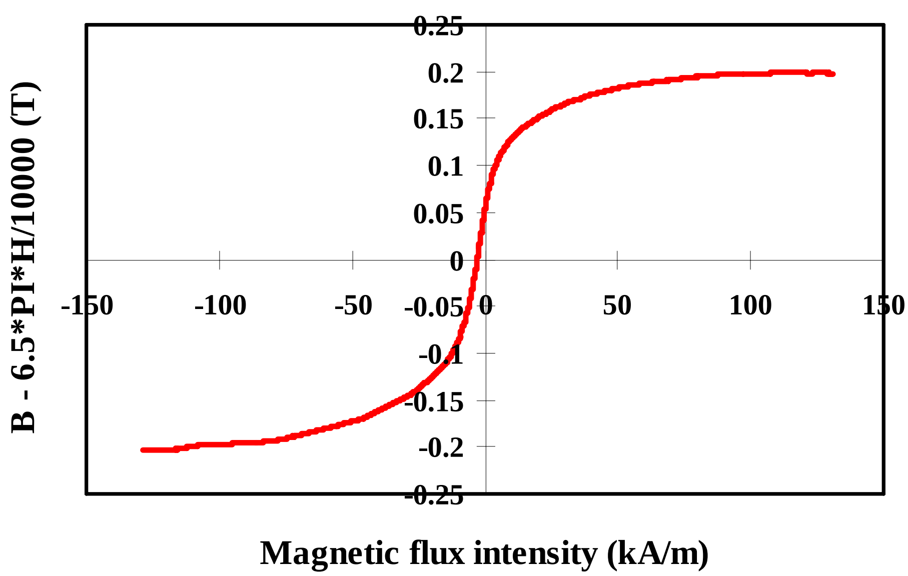

Figure C4: H (kA/m) vs. B - 6.5*PI*H/10000 (T).

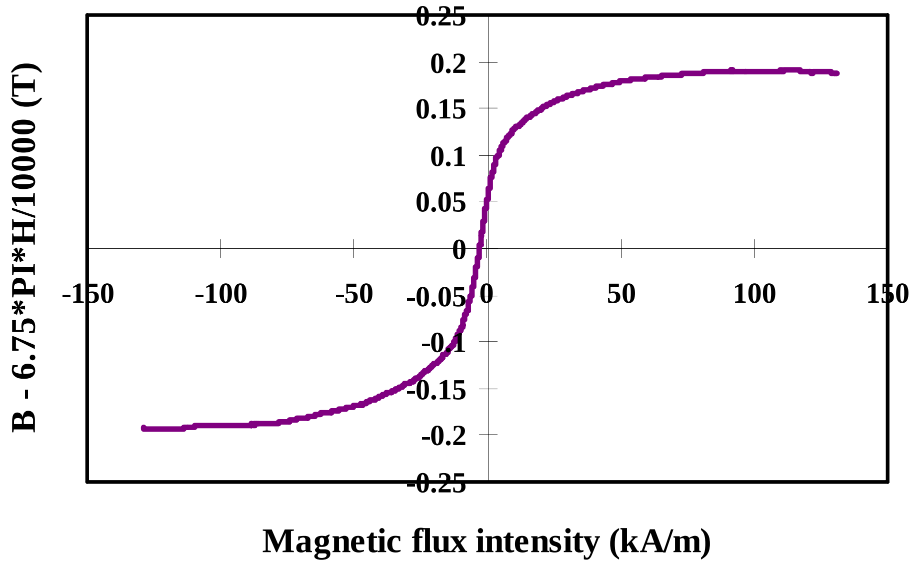

Figure C5: H (kA/m) vs. B - 6.75*PI*H/10000 (T).

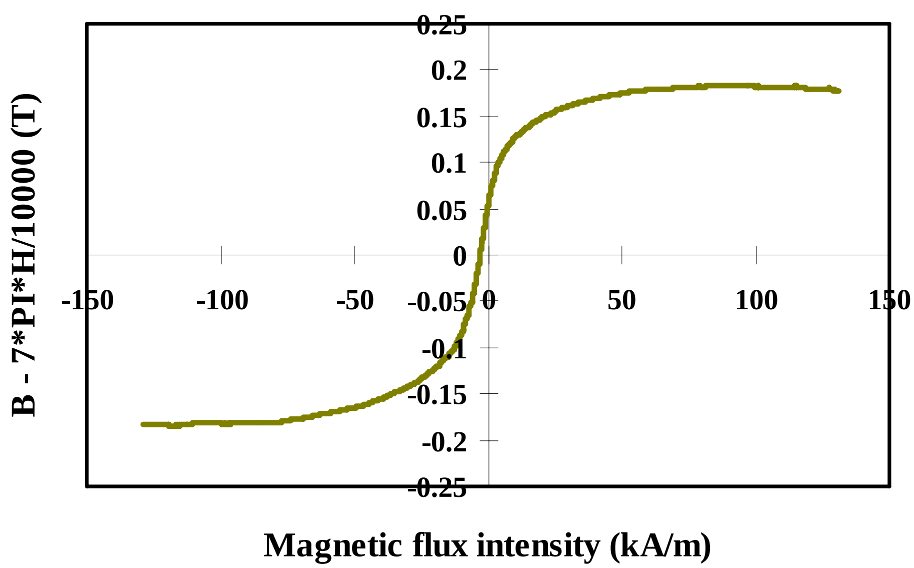

Figure C6: H (kA/m) vs. B - 7*PI*H/10000 (T).

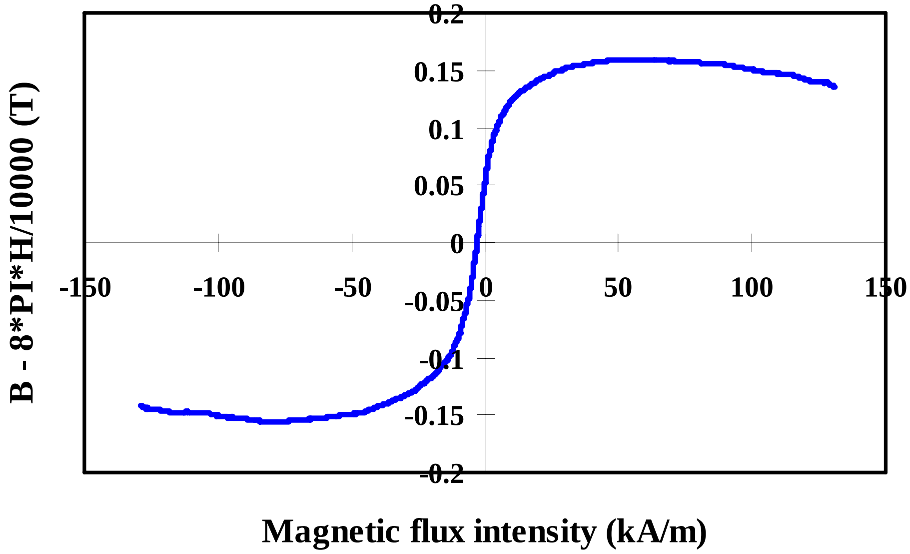

Figure C7: H (kA/m) vs. B - 8*PI*H/10000 (T).

APPENDIX D

CURVE FITTING OF COBALT FERRITE DATA

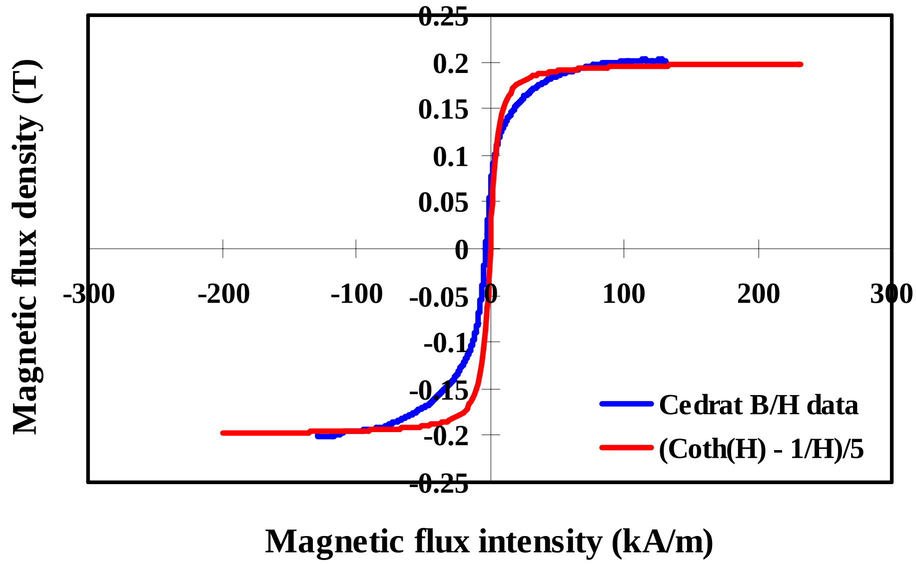

Figure D1: *B-H* curve for $H = 2.5x$, where $x = \{-80, -79, -78\ldots\ 93\}$.

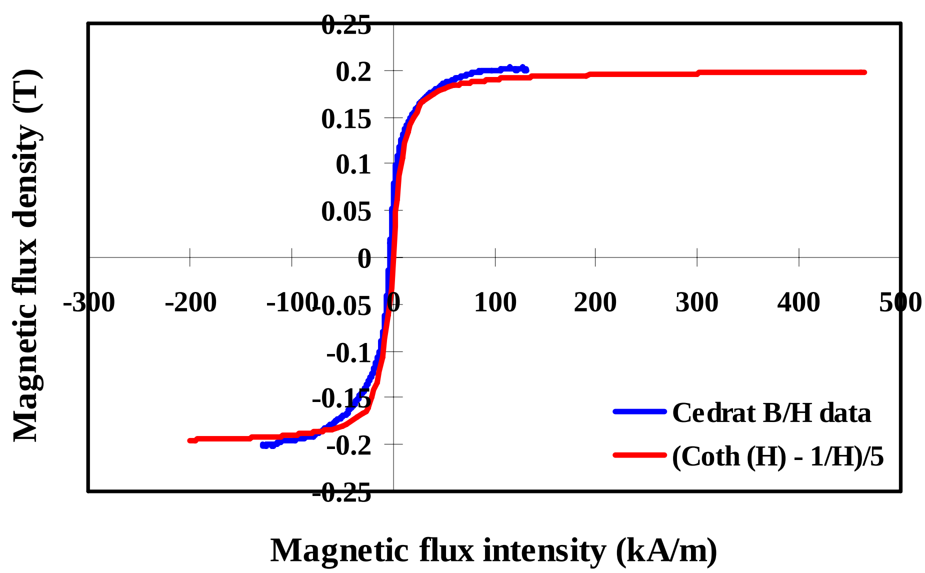

Figure D2: *B-H* curve for $H = 5x$, where $x = \{-40, -39, -38\ldots\ 93\}$.

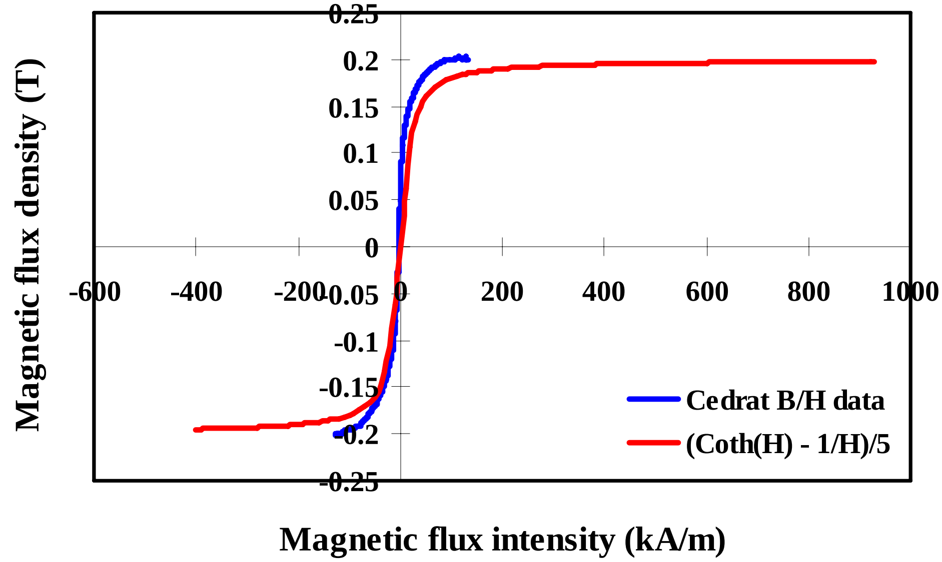

Figure D3: *B*-*H* curve for $H = 10x$, where $x = \{-40, -39, -38 \ldots 93\}$.

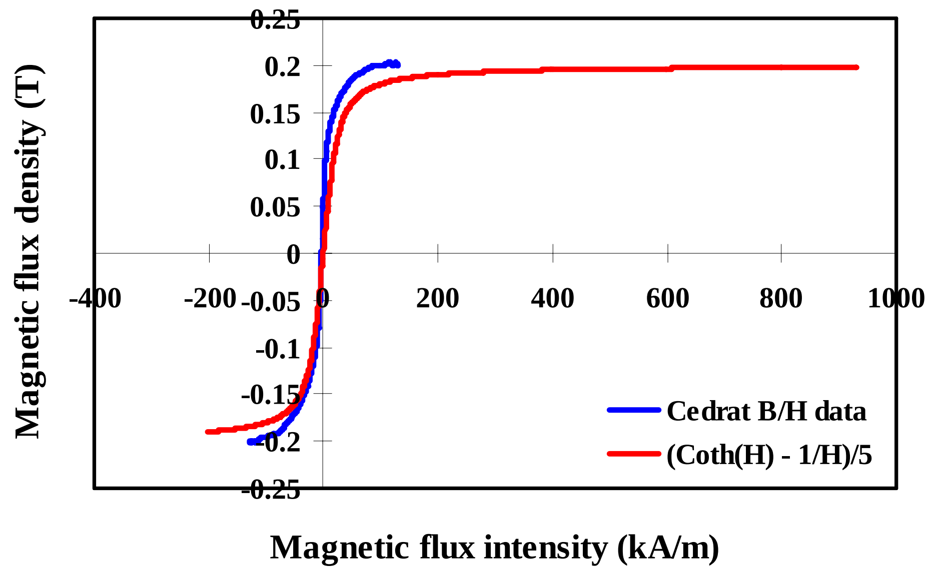

Figure D4: *B*-*H* curve for $H = \dfrac{200x}{20}$, where $x = \{-20, -19.9, -19.8 \ldots 93\}$.

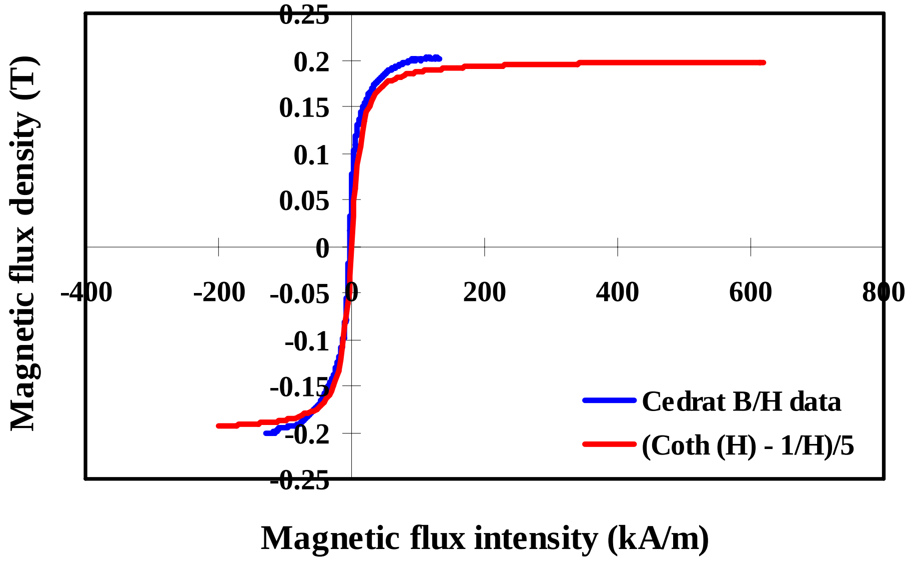

Figure D5: *B*-*H* curve for $H = \dfrac{200x}{30}$, where $x = \{-30, -29, -28\ldots\ 93\}$.

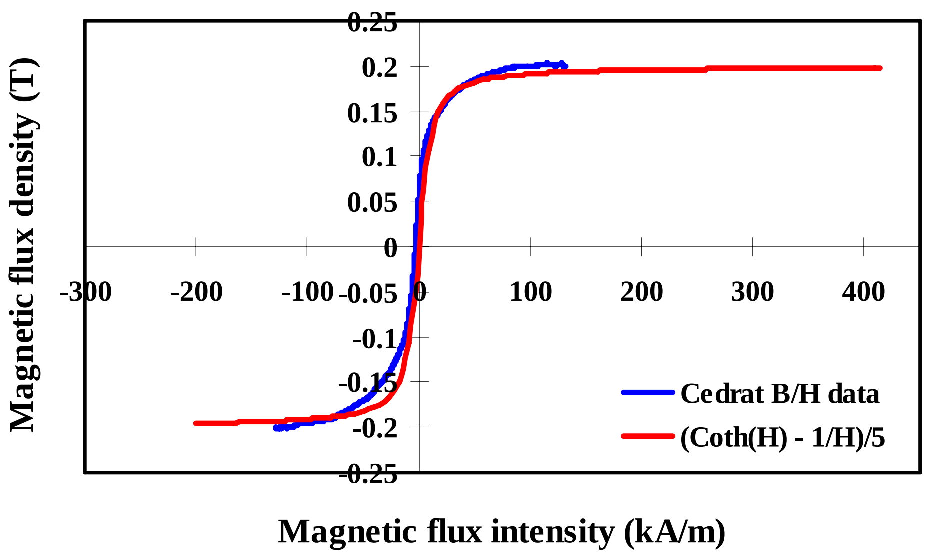

Figure D6: *B*-*H* curve for $H = \dfrac{200x}{45}$, where $x = \{-45, -44, -43\ldots\ 93\}$.

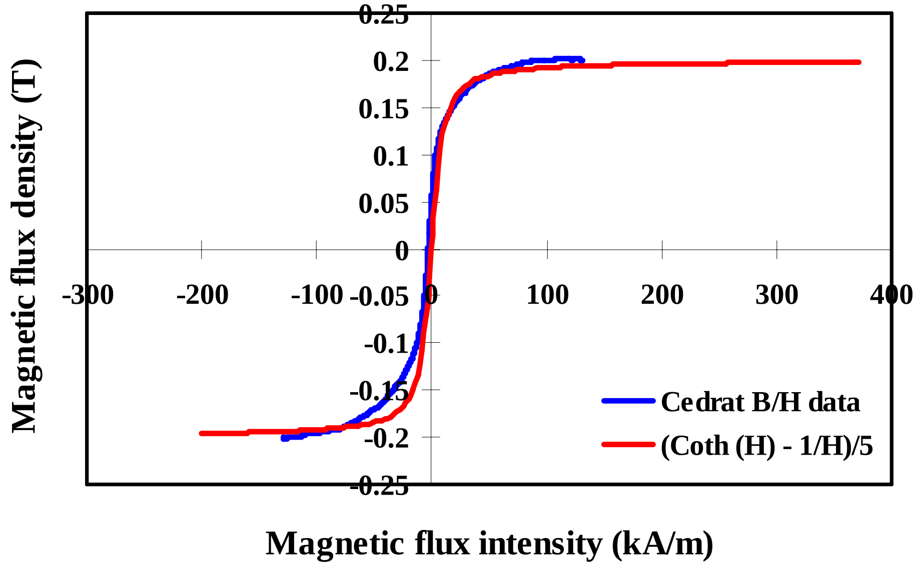

Figure D7: *B*-*H* curve for $H = \dfrac{200x}{50}$, where $x = \{-50, -49, -48 \ldots 93\}$.

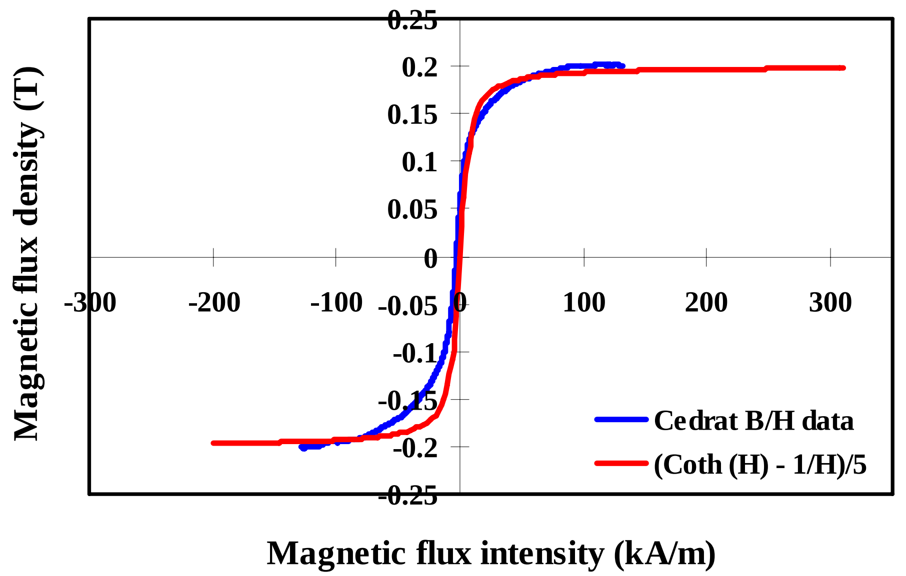

Figure D8: *B*-*H* curve for $H = \dfrac{200x}{60}$, where $x = \{-60, -59, -58 \ldots 93\}$.

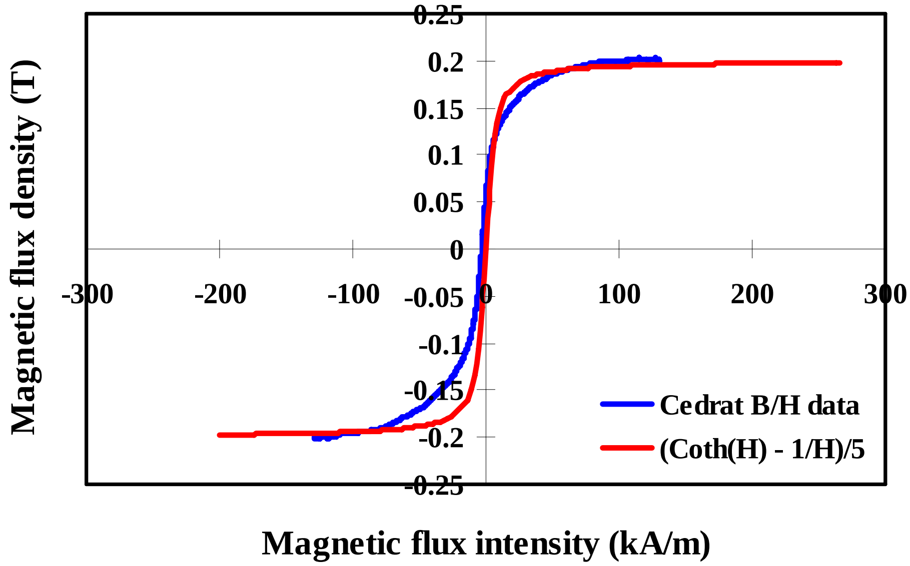

Figure D9: *B-H* curve for $H = \dfrac{200x}{70}$, where $x = \{-70, -69, -68 \ldots 93\}$.

APPENDIX E

CAD DRAWINGS

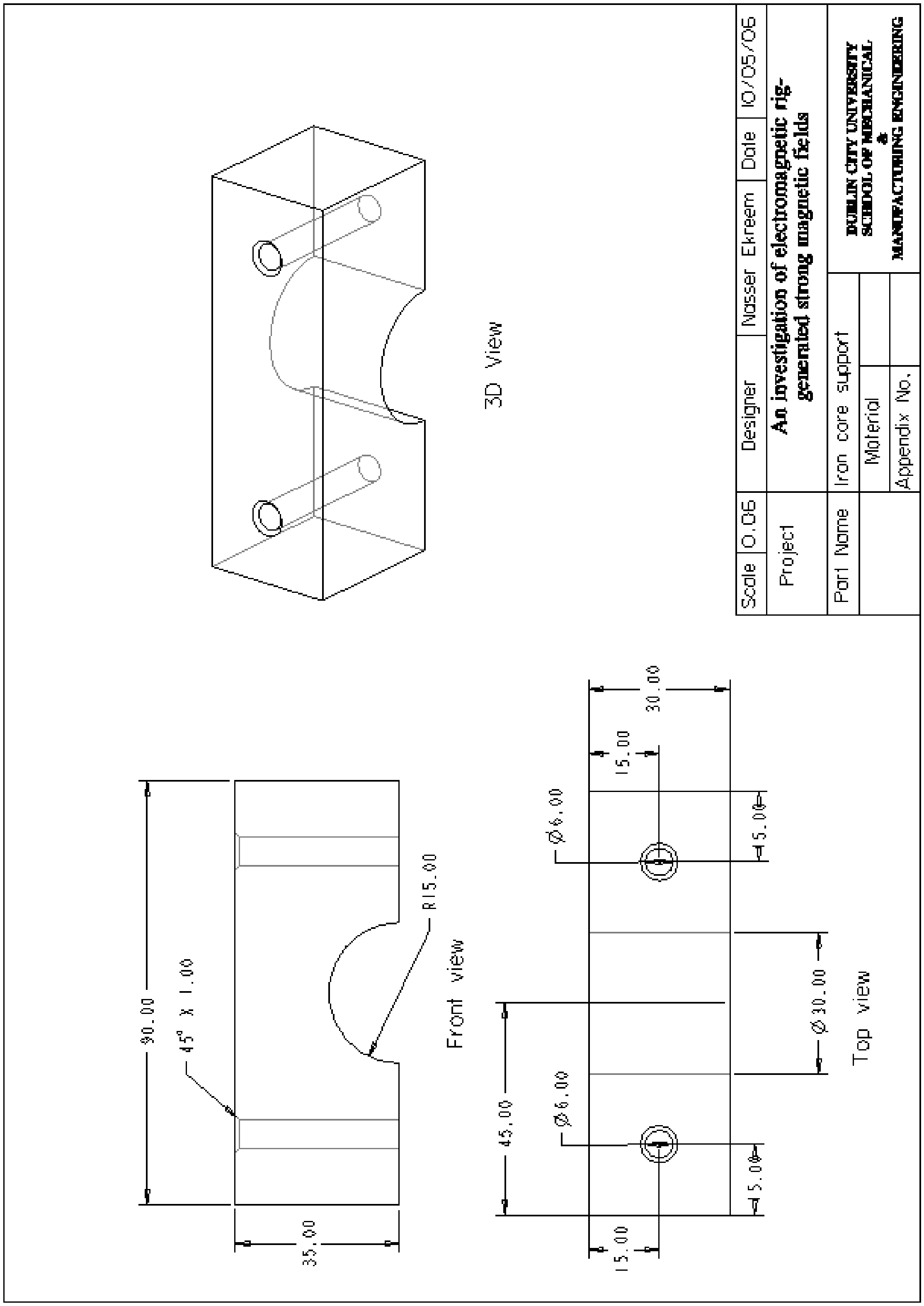

Figure E1: Standoff for iron core (Top).

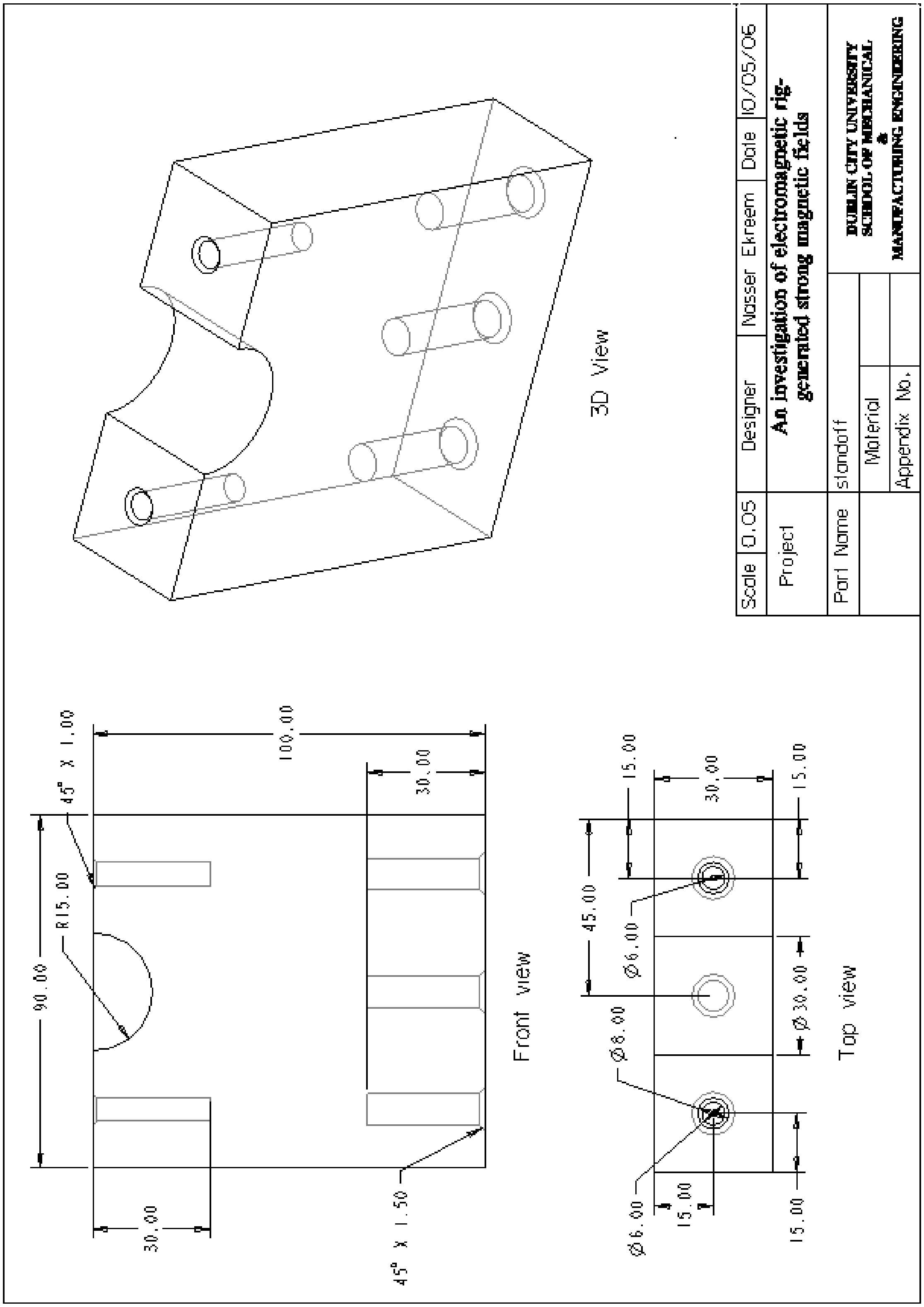

Figure E2: Standoff for iron core (Bottom).

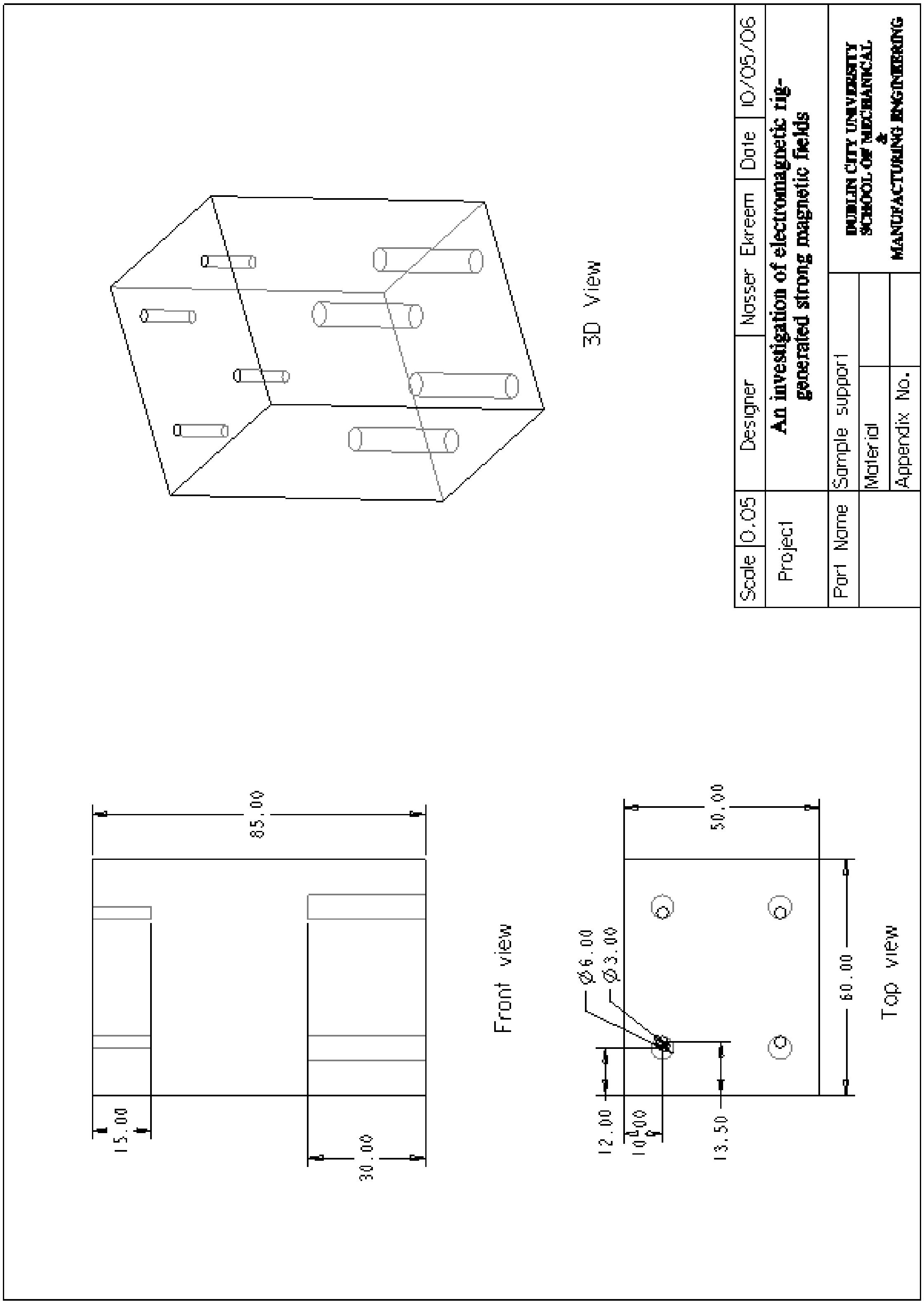

Figure E3: Standoff for samples to be tested.

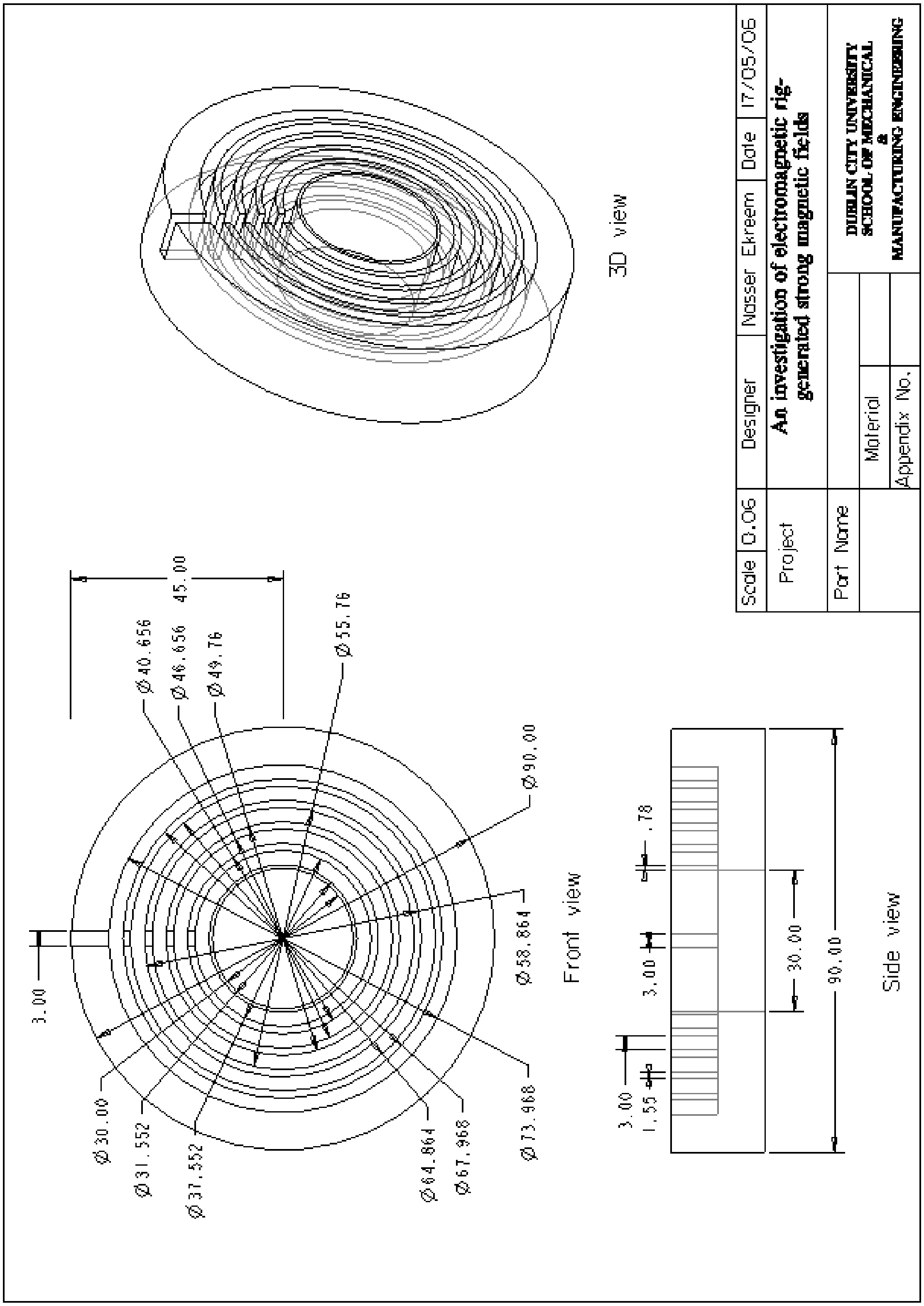

Figure E4: End-cap for inserting copper tubes.

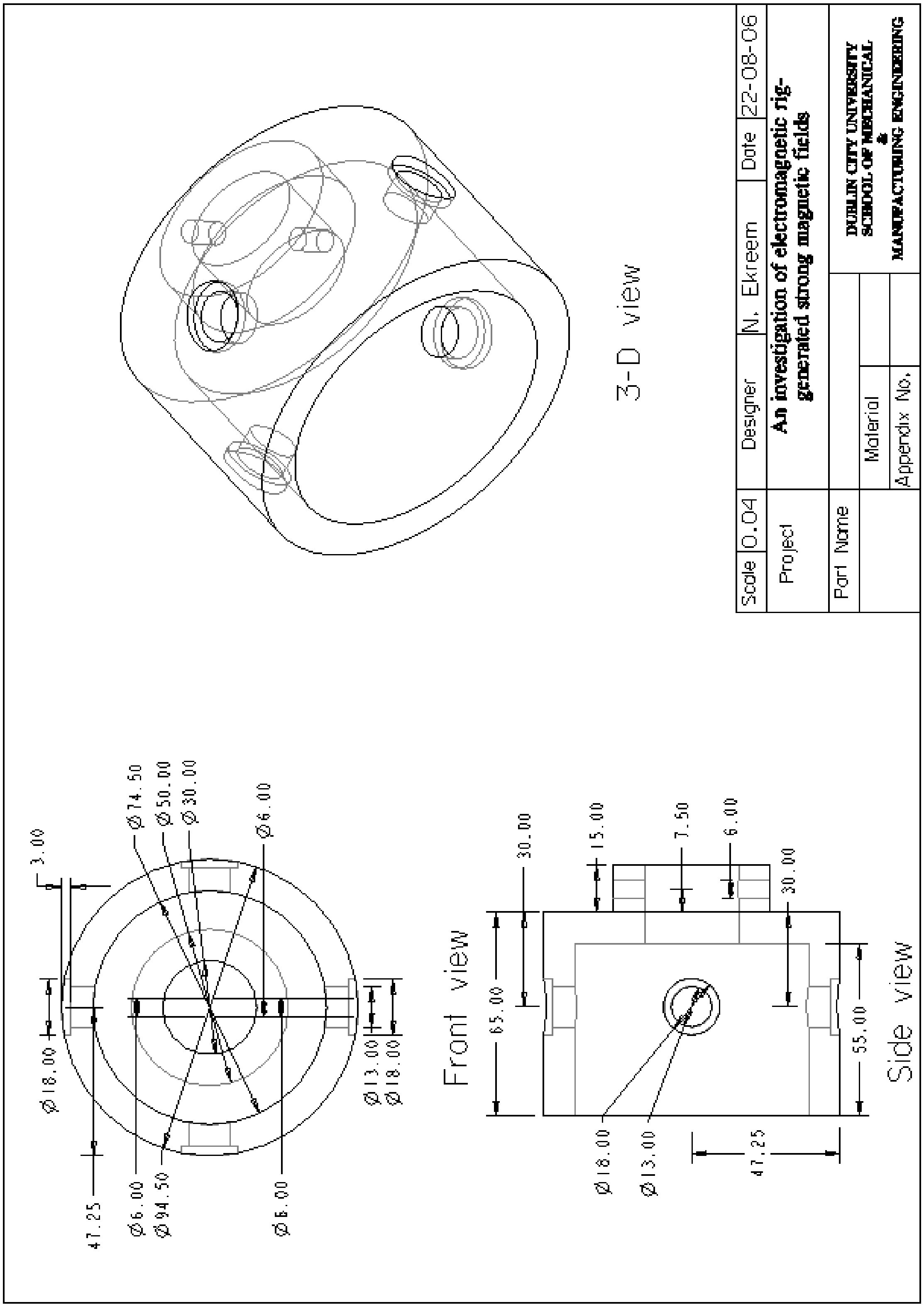

Figure E5: End-cap for air cooling system.

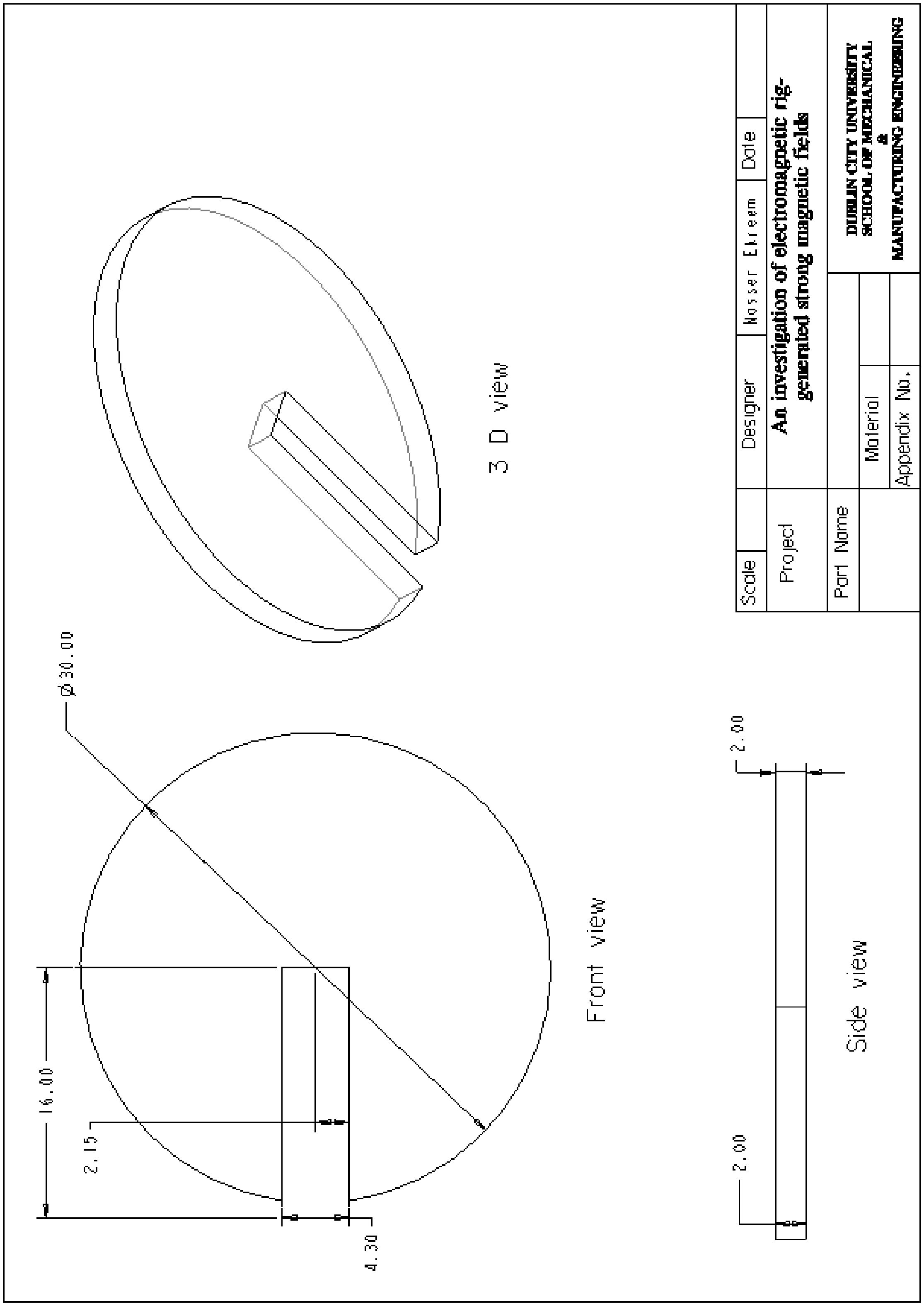

Figure E6: Teflon plastic spacer for holding gaussmeter probe.

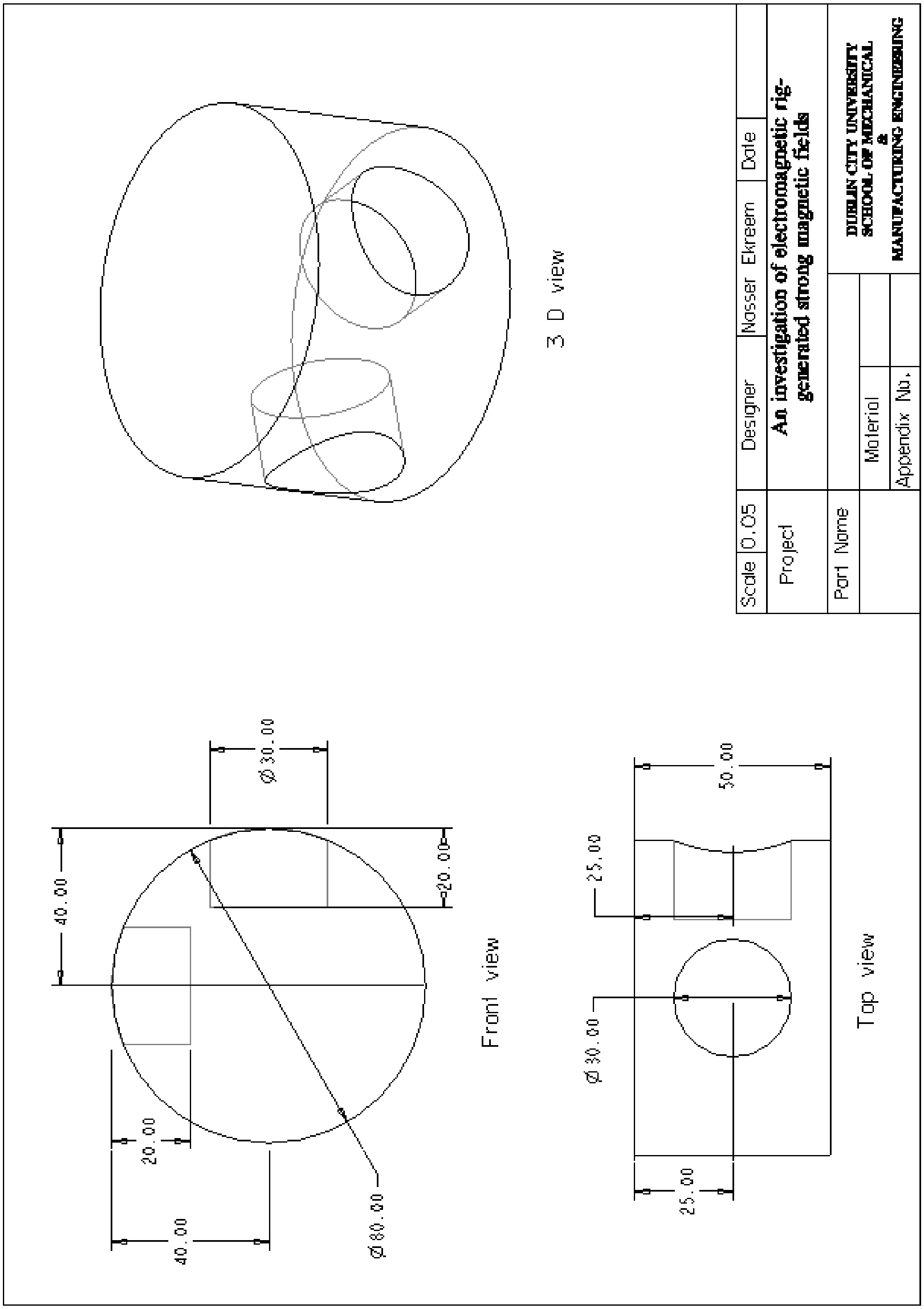

Figure E7: Large diameter component corner.

APPENDIX F

MAGNETIC PROPERTIES OF LOW CARBON STEEL

Results of the measurement of magnetic properties of low carbon steel material carried out by an independent laboratory

magnetic instrumentation inc.

KJS ASSOCIATES

August 13, 2007

Dublin City University, School of Mechanical & Mfg. Engineering
Attn: Alan Meehan
Dublin 9
Ireland

Tel: +353-1-7007718
Fax: +353-1-7005345
email: alan.meehan@dcu.ie
www.

Ref: P.O. 300067685, S.O. 20070995, DC magnetic testing of Mild Steel Bar.

Dear Mr. Meehan,

We have completed the DC magnetic B vs. H testing on one (1) sample bar which we received from Dublin University on 06-Aug-07. The material is identified by our in-house catalog number as follows:

KJS ID	*Customer ID*
MS16332	Sample 1 Mild Steel

The following procedural notes apply to this testing:

1. The physical dimensions of the bar were measured and recorded.
2. A secondary (B) winding of #30AWG magnet wire was applied over 2 layers of 0.002" insulating tape on the bar.
3. The bar under test was placed in a KJS Associates Model YOKE-100 test yoke and clamped. A calibrated Hall probe was placed at the surface of the coil to measure the applied field H. The search coil winding was connected to the system fluxmeter to determine the flux density in the sample.
4. The sample was dynamically demagnetized prior to test.
5. After demagnetizing, the bar specimen was magnetized to a maximum applied field of approximately 1000 oersted in the yoke fixture. Then the full four-quadrant B vs. H curve was measured at room temperature.
6. All measurements were made using a KJS Associates, Inc. Model SMT-600-5 Computer-Automated Soft Magnetic Hysteresigraph System and Model YOKE-100 test fixture, which complies with ASTM A773/A773M-01, "Standard Test Method for D-C Magnetic Properties of Materials Using Ring and Permeameter Procedures with D-C Electronic Hysteresigraphs". Overall system accuracy is approximately $\pm 2\%$ for B and H. The system is due for calibration on 17-Jul-08.
7. Deliverables include this report, the attached original data curves, all test results forwarded by email, and return of all sample material.

8431 Castlewood Drive, Indianapolis, IN 46250 USA
(317) 842-7500 • Fax (317) 849-7600
E-Mail: maginst@maginst.com • www.maginst.com

Thank you for this opportunity to be of service. If you have any questions or comments about the information presented here, please contact me.

Sincerely yours,

KJS Associates Div.
Magnetic Instrumentation, Inc.

Greg M. Umana
KJS Lab Mgr.

cc: file

8431 Castlewood Drive, Indianapolis, IN 46250 USA
(317) 842-7500 • Fax (317) 849-7600
E-Mail: maginst@maginst.com • www.maginst.com

KJS Associates, Inc. Model SMT-600 Hysteresigraph System

File Name	MS16332.csv	Test Date/Time	10 Aug 2007	
Sample I.D.	Sample 1 Mild Steel	Test Procedure	ASTM A773/A773M-01	
Batch I.D.	Dublin City University 20070995	Operator/version	JDC	2.0.3.0
Heat No.		Comments	KJS Associates Div. - Excellence in magnetics since 1968.	

SAMPLE INFORMATION		
Diameter	0.671	in
B Coil Turns	10	
B Coil Resistance	0.2	Ohms
B Coil Wire Thickness	0.022	in
Tape Thickness	0.004	in
Cross Sectional Shape	Circular	
Area Calculation Method	Dimension	
Sample Area	2.2814	cm^2
B Coil Area	2.48997	cm^2

TEST PARAMETERS		
Temperature	25	C
Max. Measured B	21851	G
Max. Measured H	1123	Oe
Step Delay	0.01	s
TEST SUMMARY		
Remanence Br	5421	G
Coercive Field Hc	7.16	Oe
Max. Permeability umax	407.4	
B @ Max. Permeability	6113	G
H @ Max. Permeability	15.006	Oe
Demag. Offset	82	G
Test Type	DC Yoke	

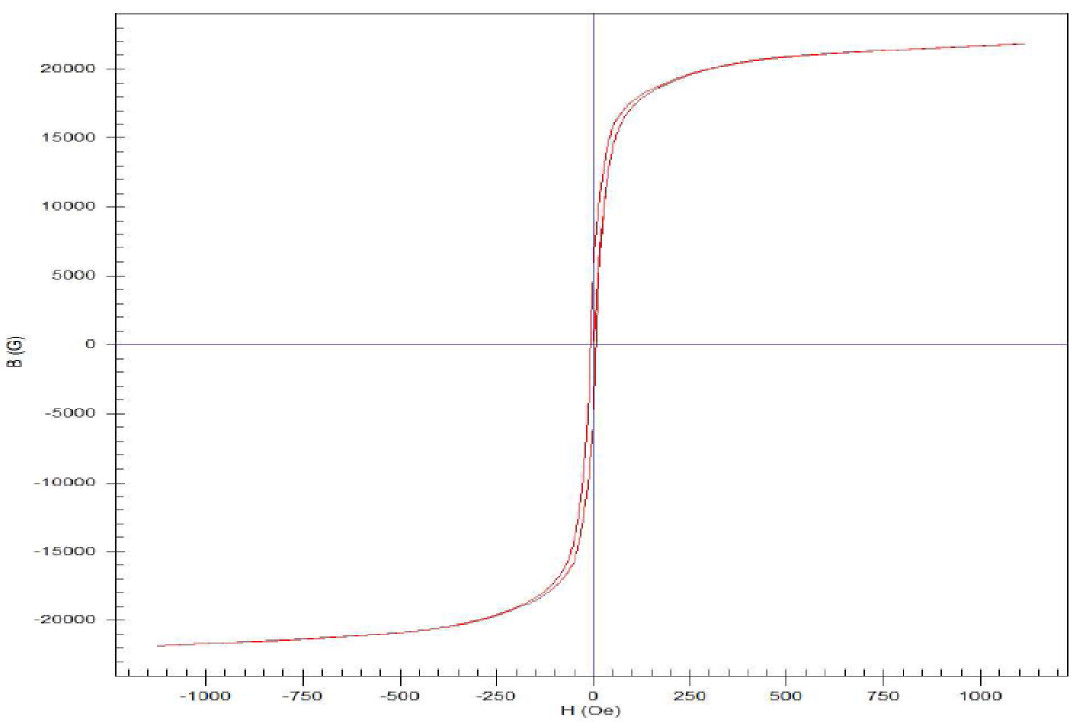

KJS Associates Div. - Excellence in magnetics since 1968.

APPENDIX G

MEASUREMENTS OF MAGNETIC FLUX DENSITY INFORMATIONS

Table G1: Measurement of magnetic flux density produced only by each layer of coil no.1 in open circuit.

Current (Amps)	Magnetic field strength (Oe)	Magnetic flux density (T)									
		Layers									
		1	2	3	4	5	6	7	8	9	10
0	0	0.009	0.0089	0.0089	0.009	0.0091	0.0089	0.009	0.009	0.009	0.009
0.2	3.1416	0.0117	0.0116	0.0114	0.0117	0.0117	0.0115	0.0116	0.0117	0.0118	0.0116
0.4	6.2832	0.0154	0.0153	0.0152	0.0156	0.0154	0.0153	0.0152	0.0154	0.0153	0.0152
0.6	9.4248	0.0198	0.0197	0.0194	0.0198	0.0197	0.0201	0.0199	0.0196	0.0196	0.0194
0.8	12.5664	0.025	0.0246	0.0245	0.0248	0.0247	0.0246	0.0247	0.0246	0.0244	0.0244
1	15.7080	0.0307	0.0302	0.0303	0.0306	0.0307	0.0304	0.0302	0.03	0.0299	0.0297
1.2	18.8495	0.036	0.0359	0.0358	0.0363	0.0363	0.036	0.036	0.0362	0.0355	0.0355
1.4	21.9911	0.042	0.0413	0.041	0.0414	0.0417	0.0417	0.0413	0.0412	0.0411	0.0408
1.6	25.1327	0.0466	0.0465	0.0463	0.0467	0.0464	0.0468	0.0469	0.0462	0.0464	0.0457
1.8	28.2743	0.0518	0.0518	0.0513	0.0518	0.0514	0.0517	0.0514	0.0511	0.0509	0.0508
2	31.4159	0.0565	0.0559	0.0558	0.0564	0.0563	0.0565	0.0562	0.0559	0.0557	0.0552
2.2	34.5575	0.0612	0.0608	0.0606	0.0612	0.0607	0.061	0.0608	0.0604	0.0602	0.06
2.4	37.6991	0.0663	0.0651	0.0653	0.0655	0.0654	0.0655	0.0653	0.0648	0.0648	0.0644
2.6	40.8407	0.0701	0.0696	0.0694	0.0698	0.0698	0.07	0.0696	0.0694	0.069	0.0686
2.8	43.9823	0.0745	0.0743	0.0738	0.0744	0.074	0.0742	0.0738	0.0736	0.0733	0.0727
3	47.1239	0.0792	0.0781	0.0778	0.0783	0.0781	0.0786	0.0779	0.0776	0.0773	0.0768

Table G2: Measurement of magnetic flux density produced only by series layers of coil no.1 in open circuit.

Current (Amps)	Magnetic field strength (Oe)	Magnetic flux density (T)				
		Series layers				
		(1+10)	(2+9)	(3+8)	(4+7)	(5+6)
0	0	0.0091	0.0092	0.0091	0.0093	0.0092
0.2	6.2832	0.0155	0.0155	0.0157	0.0154	0.0156
0.4	12.5664	0.025	0.0263	0.0246	0.025	0.025
0.6	18.8495	0.0361	0.0358	0.0358	0.0362	0.0362
0.8	25.1327	0.0472	0.0471	0.0468	0.0471	0.0473
1	31.4159	0.0571	0.0572	0.0565	0.0573	0.058
1.2	37.6991	0.0666	0.0662	0.066	0.0664	0.0666
1.4	43.9823	0.0757	0.0754	0.075	0.0754	0.0755
1.6	50.2655	0.0843	0.0837	0.0837	0.084	0.0839
1.8	56.5486	0.0925	0.0925	0.0916	0.0919	0.0923
2	62.8318	0.0998	0.0993	0.0993	0.0997	0.0996
2.2	69.1150	0.1069	0.1065	0.1062	0.1067	0.1068
2.4	75.3982	0.1135	0.1134	0.113	0.1132	0.1132
2.6	81.6814	0.1197	0.1194	0.1192	0.1195	0.1195
2.8	87.9646	0.1255	0.1252	0.1247	0.125	0.1255
3	94.2477	0.1306	0.1306	0.1301	0.1302	0.1302

Table G3: Measurement of magnetic flux density produced only by coil no. 1 in open circuit.

Current (Amps)	Magnetic field strength (Oe)	Magnetic flux density (T)
0	0	0.0108
1	31.4159	0.0459
2	62.8318	0.0757
3	94.2477	0.0941
4	125.664	0.1057
5	157.080	0.1138
6	188.495	0.1199
7	219.911	0.1248
8	251.327	0.1292
9	282.743	0.1329
10	314.159	0.136
11	345.575	0.1389
12	376.991	0.1415
13	408.407	0.1438
14	439.823	0.1459
15	471.2439	0.1478

Table G4: Measurement of magnetic flux density produced only by each layer of coil no.2 in open circuit.

Current (Amps)	Magnetic field strength (Oe)	Magnetic flux density (T)									
		Layers									
		1	2	3	4	5	6	7	8	9	10
0	0	0.0169	0.01744	0.01756	0.0176	0.01767	0.01731	0.0174	0.01739	0.01743	0.01742
0.2	3.1416	0.01882	0.01932	0.01942	0.01956	0.01954	0.01921	0.01918	0.01924	0.01928	0.01922
0.4	6.2832	0.02135	0.02195	0.02192	0.022	0.022	0.02156	0.02165	0.02175	0.02175	0.02168
0.6	9.4248	0.02405	0.02502	0.02522	0.0249	0.02488	0.02443	0.02456	0.02457	0.02465	0.02456
0.8	12.5664	0.02703	0.02854	0.02845	0.02841	0.02895	0.02793	0.02786	0.02784	0.02778	0.02785
1	15.7080	0.03173	0.0327	0.0327	0.0325	0.0325	0.0319	0.0319	0.032	0.0319	0.032
1.2	18.8495	0.035	0.0368	0.0366	0.0366	0.0368	0.0361	0.0361	0.0358	0.0361	0.0359
1.4	21.9911	0.0399	0.0408	0.0408	0.0407	0.0405	0.0398	0.0398	0.0397	0.04	0.0398
1.6	25.1327	0.0433	0.045	0.045	0.0447	0.0444	0.0437	0.0436	0.0437	0.0436	0.0436
1.8	28.2743	0.0472	0.0487	0.0486	0.0483	0.0484	0.0475	0.0476	0.0473	0.0473	0.0475
2	31.4159	0.0515	0.0525	0.0522	0.0523	0.052	0.0511	0.0511	0.0509	0.0509	0.0512
2.2	34.5575	0.0554	0.0562	0.0562	0.0558	0.0557	0.055	0.0547	0.0545	0.0545	0.0547
2.4	37.6991	0.0591	0.06	0.06	0.0594	0.0593	0.0583	0.0582	0.0582	0.0583	0.0582
2.6	40.8407	0.0627	0.0637	0.0634	0.063	0.0627	0.0616	0.0616	0.0616	0.0615	0.0618
2.8	43.9823	0.0665	0.0672	0.0668	0.0664	0.0664	0.0654	0.0651	0.0651	0.065	0.0652
3	47.1239	0.0698	0.0708	0.0704	0.07	0.07	0.0684	0.0684	0.0684	0.0683	0.0686

Table G5: Measurement of magnetic flux density produced only by series layers of coil no.2 in open circuit.

Current (Amps)	Magnetic field strength (Oe)	Magnetic flux density (T)				
		Series layers				
		(1+10)	(2+9)	(3+8)	(4+7)	(5+6)
0	0	0.0173	0.01716	0.01763	0.01767	0.01766
0.2	6.2832	0.02138	0.02149	0.02164	0.02168	0.02186
0.4	12.5664	0.02731	0.02725	0.02752	0.02752	0.02764
0.6	18.8495	0.035	0.0352	0.0356	0.0354	0.0353
0.8	25.1327	0.0431	0.0427	0.0428	0.0433	0.0428
1	31.4159	0.0503	0.0497	0.05	0.0503	0.0507
1.2	37.6991	0.0571	0.0569	0.0572	0.0574	0.0574
1.4	43.9823	0.0637	0.0637	0.064	0.0643	0.0641
1.6	50.2655	0.0704	0.0702	0.0707	0.0705	0.0707
1.8	56.5486	0.0773	0.0766	0.077	0.0772	0.077
2	62.8318	0.0838	0.0829	0.0834	0.0829	0.0833
2.2	69.1150	0.0899	0.0886	0.089	0.0888	0.0888
2.4	75.3982	0.0958	0.0941	0.0944	0.094	0.0941
2.6	81.6814	0.1012	0.099	0.0994	0.0991	0.0991
2.8	87.9646	0.1062	0.1038	0.1042	0.1039	0.1038
3	94.2477	0.1112	0.1087	0.1085	0.1085	0.1084

Table G6: Measurement of magnetic flux density produced only by coil no. 2 in open circuit.

Current (Amps)	Magnetic field strength (Oe)	Magnetic flux density (T)
0	0	0.01884
1	31.4159	0.0558
2	62.8318	0.0902
3	94.2477	0.1173
4	125.664	0.1382
5	157.080	0.1541
6	188.495	0.1666
7	219.911	0.1772
8	251.327	0.1864
9	282.743	0.1943
10	314.159	0.202
11	345.575	0.2077
12	376.991	0.2136
13	408.407	0.2189
14	439.823	0.2237
15	471.2439	0.2285

Table G7: Measurement of magnetic flux density produced only by each layer of coil no.3 in open circuit.

Current (Amps)	Magnetic field strength (Oe)	Magnetic flux density (T)									
		Layers									
		1	2	3	4	5	6	7	8	9	10
0	0	0.01205	0.01396	0.01439	0.01444	0.0146	0.01464	0.01462	0.01462	0.01476	0.0148
0.2	3.1416	0.01405	0.01557	0.01593	0.01602	0.01611	0.01619	0.01629	0.0164	0.01645	0.01645
0.4	6.2832	0.0168	0.0178	0.01826	0.01817	0.01828	0.01839	0.01841	0.0187	0.01877	0.01876
0.6	9.4248	0.01923	0.02046	0.02092	0.02095	0.02082	0.021	0.02082	0.02125	0.02135	0.02126
0.8	12.5664	0.02205	0.0239	0.02395	0.02375	0.02382	0.02395	0.02389	0.02452	0.02487	0.02423
1	15.7080	0.026	0.02669	0.02702	0.02698	0.02681	0.02734	0.02706	0.0278	0.02778	0.02763
1.2	18.8495	0.02993	0.0306	0.0307	0.0306	0.0305	0.0309	0.0307	0.0316	0.0316	0.0313
1.4	21.9911	0.032	0.0339	0.0339	0.0338	0.0338	0.0342	0.0339	0.035	0.035	0.0345
1.6	25.1327	0.0353	0.0368	0.0374	0.0371	0.0368	0.0374	0.0371	0.0381	0.0382	0.0378
1.8	28.2743	0.0391	0.0403	0.0404	0.0402	0.04	0.0406	0.0403	0.0413	0.0418	0.041
2	31.4159	0.0424	0.0433	0.0438	0.0433	0.0433	0.0439	0.0435	0.0446	0.0449	0.0442
2.2	34.5575	0.0457	0.0468	0.047	0.0467	0.0463	0.0471	0.0465	0.0478	0.0479	0.0474
2.4	37.6991	0.0492	0.0502	0.0503	0.0497	0.0495	0.05	0.0497	0.0513	0.0514	0.0506
2.6	40.8407	0.0526	0.0532	0.0535	0.0529	0.0525	0.0532	0.0528	0.0543	0.0544	0.0536
2.8	43.9823	0.0562	0.0562	0.0564	0.056	0.0556	0.0562	0.056	0.0574	0.0576	0.0568
3	47.1239	0.0615	0.0612	0.0596	0.0589	0.0585	0.0594	0.0587	0.0604	0.0607	0.0597

Table G8: Measurement of magnetic flux density produced only by series layers of coil no.3 in open circuit.

Current (Amps)	Magnetic field strength (Oe)	Magnetic flux density (T) Series layers				
		(1+10)	(2+9)	(3+8)	(4+7)	(5+6)
0	0	0.01491	0.01656	0.01676	0.01683	0.01686
0.2	6.2832	0.01876	0.02038	0.02046	0.02052	0.02054
0.4	12.5664	0.02433	0.02628	0.02623	0.02601	0.02603
0.6	18.8495	0.0314	0.0336	0.0334	0.0336	0.0332
0.8	25.1327	0.0378	0.0409	0.0409	0.0406	0.0404
1	31.4159	0.0443	0.0478	0.0479	0.0475	0.0472
1.2	37.6991	0.0507	0.0546	0.0542	0.0542	0.0537
1.4	43.9823	0.0571	0.0611	0.0604	0.0603	0.0598
1.6	50.2655	0.0632	0.0676	0.0666	0.0662	0.0658
1.8	56.5486	0.0704	0.0734	0.0727	0.0722	0.0716
2	62.8318	0.0772	0.0791	0.0784	0.0777	0.0772
2.2	69.1150	0.0837	0.0848	0.084	0.0831	0.0825
2.4	75.3982	0.0897	0.0901	0.089	0.0881	0.0876
2.6	81.6814	0.0952	0.0949	0.0937	0.0927	0.0922
2.8	87.9646	0.1003	0.0995	0.0983	0.0971	0.0965
3	94.2477	0.1051	0.1042	0.1024	0.1013	0.1006

Table G9: Measurement of magnetic flux density produced only by coil no. 3 in open circuit.

Current (Amps)	Magnetic field strength (Oe)	Magnetic flux density (T)
0	0	0.0167
1	31.4159	0.0475
2	62.8318	0.0777
3	94.2477	0.1003
4	125.664	0.1188
5	157.080	0.1317
6	188.495	0.1428
7	219.911	0.1516
8	251.327	0.1594
9	282.743	0.1663
10	314.159	0.1722
11	345.575	0.1777
12	376.991	0.1824
13	408.407	0.1869
14	439.823	0.1909
15	471.2439	0.1946

Table G10: Magnetic flux density in the centre of the air gap using cobalt ferrite sample (positive quadrant).

Positive quadrant		
Current (Amps)	**Magnetic field strength (Oe)**	**Magnetic flux density (T)**
0	0	0
1	31.416	0.027
2	62.832	0.0553
3	94.248	0.0679
4	125.66	0.0749
5	157.08	0.0797
6	188.49	0.0833
7	219.91	0.086
8	251.33	0.0884
9	282.74	0.0904
10	314.16	0.092
11	345.58	0.0936
12	376.99	0.095
13	408.41	0.0962
14	439.82	0.0973
15	471.24	0.0983
14	439.82	0.0983
13	408.41	0.0982
12	376.99	0.098
11	345.58	0.0978
10	314.16	0.0976
9	282.74	0.0974
8	251.33	0.097
7	219.91	0.0966
6	188.49	0.0961
5	157.08	0.0955
4	125.66	0.0946
3	94.248	0.0932
2	62.832	0.0907
1	31.416	0.0845
0	0	0.0628

Table G11: Magnetic flux density in the centre of the air gap using cobalt ferrite sample (negative quadrant).

Negative quadrant		
Current (Amps)	**Magnetic field strength (Oe)**	**Magnetic flux density (T)**
0	0	0.0628
-1	-31.416	-0.0251
-2	-62.832	-0.0531
-3	-94.248	-0.0655
-4	-125.66	-0.0724
-5	-157.08	-0.0771
-6	-188.49	-0.0805
-7	-219.91	-0.0833
-8	-251.33	-0.0855
-9	-282.74	-0.0875
-10	-314.16	-0.0892
-11	-345.58	-0.0907
-12	-376.99	-0.092
-13	-408.41	-0.0932
-14	-439.82	-0.0943
-15	-471.23	-0.0957
-14	-439.82	-0.0956
-13	-408.41	-0.0955
-12	-376.991	-0.0953
-11	-345.5751	-0.0951
-10	-314.1592	-0.0949
-9	-282.7432	-0.0946
-8	-251.3273	-0.0943
-7	-219.9114	-0.0939
-6	-188.4955	-0.0934
-5	-157.0796	-0.0928
-4	-125.6637	-0.0919
-3	-94.24775	-0.0905
-2	-62.83183	-0.0878
-1	-31.41592	-0.0814
0	0	-0.0595

Table G12: Averaged values of magnetic flux intensity vs. magnetic flux density in the centre of the air gap using cobalt ferrite sample.

Current (Amps)	Magnetic field strength (Oe)	Magnetic flux density (T)
0	0	0
1	31.416	0.0396
2	62.832	0.0569
3	94.248	0.0644
4	125.66	0.0686
5	157.08	0.0714
6	188.49	0.0735
7	219.91	0.0751
8	251.33	0.0764
9	282.74	0.0776
10	314.16	0.0786
11	345.58	0.07942
12	376.99	0.0802
13	408.41	0.0809
14	439.83	0.0815
15	471.24	0.08213

Table G13: Magnetic flux density in the centre of the air gap using low carbon steel sample (positive quadrant).

Positive quadrant		
Current (Amps)	**Magnetic field strength (Oe)**	**Magnetic flux density (T)**
0	0	0
1	31.416	0.115
2	62.832	0.1883
3	94.248	0.2266
4	125.66	0.2383
5	157.08	0.2501
6	188.50	0.2602
7	219.91	0.2657
8	251.33	0.2714
9	282.74	0.2765
10	314.16	0.2806
11	345.58	0.2845
12	376.99	0.2879
13	408.41	0.2909
14	439.82	0.2938
15	471.24	0.2963
14	439.82	0.2958
13	408.41	0.2953
12	376.99	0.2946
11	345.58	0.2937
10	314.16	0.2928
9	282.74	0.2917
8	251.33	0.2903
7	219.91	0.2886
6	188.49	0.2866
5	157.08	0.284
4	125.66	0.2804
3	94.248	0.2748
2	62.832	0.2648
1	31.416	0.2403
0	0	0.1595

Table G14: Magnetic flux density in the centre of the air gap using low carbon steel sample (negative quadrant).

Negative quadrant		
Current (Amps)	**Magnetic field strength (Oe)**	**Magnetic flux density (T)**
0	0	0.1595
-1	-31.416	-0.1148
-2	-62.832	-0.1831
-3	-94.248	-0.215
-4	-125.66	-0.233
-5	-157.08	-0.245
-6	-188.50	-0.2538
-7	-219.91	-0.2608
-8	-251.33	-0.2666
-9	-282.74	-0.2716
-10	-314.16	-0.2759
-11	-345.58	-0.2798
-12	-376.99	-0.2831
-13	-408.41	-0.2863
-14	-439.82	-0.2891
-15	-471.24	-0.2916
-14	-439.82	-0.2911
-13	-408.41	-0.2906
-12	-376.99	-0.2899
-11	-345.58	-0.289
-10	-314.16	-0.2881
-9	-282.74	-0.2869
-8	-251.33	-0.2855
-7	-219.91	-0.2838
-6	-188.50	-0.2818
-5	-157.08	-0.279
-4	-125.66	-0.2753
-3	-94.248	-0.2697
-2	-62.832	-0.2593
-1	-31.416	-0.2349
0	0	-0.1523

Table G15: Averaged values of magnetic flux intensity vs. magnetic flux density in the centre of the air gap using low carbon steel sample.

Current (Amps)	Magnetic field strength (Oe)	Magnetic flux density (T)
0	0	0
1	31.416	0.1382
2	62.832	0.1858
3	94.248	0.2085
4	125.66	0.2187
5	157.08	0.2265
6	188.49	0.2325
7	219.91	0.2367
8	251.33	0.2404
9	282.74	0.2436
10	314.16	0.2463
11	345.58	0.2487
12	376.99	0.2508
13	408.41	0.2527
14	439.82	0.2544
15	471.24	0.2559

Table G16: Magnetic flux density in the centre of the air gap using Terfenol-D sample (positive quadrant).

Positive quadrant		
Current (Amps)	**Magnetic field strength (Oe)**	**Magnetic flux density (T)**
0	0	0.0085
1	31.416	0.1592
2	62.832	0.2169
3	94.247	0.2352
4	125.66	0.2468
5	157.08	0.2543
6	188.49	0.2598
7	219.911	0.2641
8	251.32	0.2677
9	282.74	0.2707
10	314.15	0.2734
11	345.57	0.2758
12	376.99	0.2779
13	408.40	0.2800
14	439.82	0.2819
15	471.23	0.2833
14	439.82	0.2832
13	408.40	0.2829
12	376.99	0.2825
11	345.57	0.2822
10	314.15	0.2817
9	282.74	0.2811
8	251.32	0.2805
7	219.91	0.2796
6	188.49	0.2786
5	157.08	0.2771
4	125.66	0.2752
3	94.247	0.2721
2	62.831	0.2666
1	31.415	0.2528
0	0	0.1878

Table G17: Magnetic flux density in the centre of the air gap using Terfenol-D sample (negative quadrant).

Negative quadrant		
Current (Amps)	**Magnetic field strength (Oe)**	**Magnetic flux density (T)**
0	0	0.1872
-1	-31.416	-0.1245
-2	-62.832	-0.1822
-3	-94.248	-0.2173
-4	-125.66	-0.2347
-5	-157.08	-0.2453
-6	-188.5	-0.2531
-7	-219.91	-0.2591
-8	-251.33	-0.2641
-9	-282.74	-0.2682
-10	-314.16	-0.2715
-11	-345.58	-0.2748
-12	-376.99	-0.2775
-13	-408.41	-0.2799
-14	-439.82	-0.2820
-15	-471.24	-0.2840
-14	-439.82	-0.2839
-13	-408.41	-0.2836
-12	-376.99	-0.2833
-11	-345.58	-0.2829
-10	-314.16	-0.2824
-9	-282.74	-0.2818
-8	-251.33	-0.2811
-7	-219.91	-0.2802
-6	-188.50	-0.2791
-5	-157.08	-0.2777
-4	-125.66	-0.2756
-3	-94.248	-0.2724
-2	-62.832	-0.2664
-1	-31.416	-0.2514
0	0	-0.1811

Table G18: Averaged values of magnetic flux intensity vs. magnetic flux density in the centre of the air gap using Terfenol-D sample.

Current (Amps)	Magnetic field strength (Oe)	Magnetic flux density (T)
0	0	0
1	31.415	0.1494
2	62.831	0.1855
3	94.247	0.2017
4	125.66	0.2105
5	157.08	0.2160
6	188.49	0.2201
7	219.91	0.2232
8	251.33	0.2258
9	282.74	0.2279
10	314.16	0.2297
11	345.58	0.2313
12	376.99	0.2327
13	408.41	0.2340
14	439.82	0.2352
15	471.24	0.2361

Table G19: Measurement of magnetic flux density produced only by each layer of coil no.4 in open circuit.

Current (Amps)	Magnetic field strength (Oe)	Magnetic flux density (T)									
		Layers									
		1	2	3	4	5	6	7	8	9	10
0	0	0.0064	0.0090	0.0094	0.0096	0.0096	0.0096	0.0096	0.0096	0.0096	0.0094
0.2	3.1416	0.0114	0.0134	0.0136	0.0138	0.0138	0.0138	0.0137	0.0139	0.0137	0.0137
0.4	6.2832	0.0163	0.0183	0.0187	0.0189	0.0189	0.0188	0.0188	0.0188	0.0187	0.0187
0.6	9.4248	0.0222	0.0238	0.0238	0.0239	0.0240	0.0241	0.0240	0.0238	0.0238	0.0239
0.8	12.5664	0.0281	0.0294	0.0293	0.0299	0.0297	0.0295	0.0296	0.0295	0.0294	0.0296
1	15.7080	0.0343	0.0350	0.0353	0.0360	0.0359	0.0354	0.0356	0.0353	0.0353	0.0354
1.2	18.8495	0.0403	0.0409	0.0411	0.0414	0.0413	0.0415	0.0414	0.0414	0.0409	0.0413
1.4	21.9911	0.0463	0.0470	0.0468	0.0478	0.0471	0.0471	0.0472	0.0472	0.0467	0.0470
1.6	25.1327	0.0522	0.0525	0.0528	0.0529	0.0533	0.0529	0.0529	0.0528	0.0522	0.0532
1.8	28.2743	0.0582	0.0583	0.0585	0.0598	0.0589	0.0587	0.0587	0.0587	0.0580	0.0589
2	31.4159	0.0636	0.0641	0.0641	0.0646	0.0646	0.0646	0.0644	0.0643	0.0639	0.0643
2.2	34.5575	0.0696	0.0698	0.0700	0.0702	0.0704	0.0702	0.0704	0.0697	0.0691	0.0701
2.4	37.6991	0.0744	0.0755	0.0752	0.0759	0.0757	0.0758	0.0758	0.0754	0.0747	0.0758
2.6	40.8407	0.0798	0.0809	0.0808	0.0813	0.0813	0.0812	0.0812	0.0809	0.0801	0.0813
2.8	43.9823	0.0851	0.0866	0.0861	0.0866	0.0865	0.0866	0.0867	0.0863	0.0855	0.0865
3	47.1239	0.0899	0.0919	0.0912	0.0922	0.0920	0.0917	0.0917	0.0916	0.0906	0.0919

Table G20: Measurement of magnetic flux density produced only by series layers of coil no.4 in open circuit.

Current (Amps)	Magnetic field strength (Oe)	Magnetic flux density (T)				
		Series layers				
		(1+10)	(2+9)	(3+8)	(4+7)	(5+6)
0	0	0.0095	0.0095	0.0096	0.0096	0.0096
0.2	6.2832	0.0186	0.0187	0.0185	0.0185	0.0186
0.4	12.5664	0.0294	0.0292	0.0292	0.0295	0.0293
0.6	18.8495	0.0411	0.0410	0.0409	0.0413	0.0413
0.8	25.1327	0.0529	0.0531	0.0524	0.0528	0.0528
1	31.4159	0.0644	0.0639	0.0639	0.0643	0.0644
1.2	37.6991	0.0754	0.0752	0.0755	0.0757	0.0759
1.4	43.9823	0.0861	0.0861	0.0861	0.0867	0.0865
1.6	50.2655	0.0969	0.0965	0.0963	0.0971	0.0970
1.8	56.5486	0.1064	0.1059	0.1060	0.1064	0.1060
2	62.8318	0.1150	0.1142	0.1138	0.1143	0.1145
2.2	69.1150	0.1218	0.1209	0.1206	0.1213	0.1210
2.4	75.3982	0.1278	0.1267	0.1265	0.1270	0.1267
2.6	81.6814	0.1328	0.1317	0.1314	0.1320	0.1315
2.8	87.9646	0.1375	0.1361	0.1360	0.1362	0.1361
3	94.2477	0.1418	0.1407	0.1400	0.1405	0.1401

Table G21: Measurement of magnetic flux density produced only by coil no. 4 in open circuit.

Current (Amps)	Magnetic field strength (Oe)	Magnetic flux density (T)
0	0	0.0096
1	31.4159	0.0673
2	62.8318	0.1189
3	94.2477	0.1461
4	125.664	0.1637
5	157.080	0.1780
6	188.495	0.1898
7	219.911	0.2000
8	251.327	0.2088
9	282.743	0.2168
10	314.159	0.2240
11	345.575	0.2305
12	376.991	0.2365
13	408.407	0.2423
14	439.823	0.2473
15	471.2439	0.2520

Table G22: Measurement of magnetic flux density of configuration "B" produced only by each coil with air-gap between two coils using curved corners.

Current (Amps)	Magnetic field strength (Oe)	Magnetic flux density (T)			
		Coils			
		Coil no. 1	Coil no. 2	Coil no. 3	Coil no. 4
0	0.0000	0.0000	0.0016	0.0017	0.0013
1	31.4159	0.2495	0.0510	0.1177	0.3600
2	62.8318	0.3960	0.0843	0.1568	0.5020
3	94.2477	0.4840	0.0996	0.1737	0.5690
4	125.6637	0.5400	0.1080	0.1828	0.6160
5	157.0796	0.5810	0.1132	0.1891	0.6520
6	188.4955	0.6130	0.1171	0.1938	0.6800
7	219.9114	0.6390	0.1202	0.1980	0.7060
8	251.3273	0.6590	0.1227	0.2010	0.7290
9	282.7432	0.6790	0.1246	0.2038	0.7460
10	314.1592	0.6950	0.1264	0.2063	0.7640
11	345.5751	0.7110	0.1278	0.2084	0.7790
12	376.9910	0.7230	0.1292	0.2103	0.7940
13	408.4069	0.7360	0.1303	0.2120	0.8060
14	439.8228	0.7460	0.1313	0.2133	0.8180
15	471.2387	0.7550	0.1321	0.2146	0.8290

Table G23: Measurement of magnetic flux density of configuration "B" produced only by two coils in series with air-gap between two coils using curved corners.

Current (Amps)	Magnetic field strength (Oe)	Magnetic flux density (T)					
		Combination of two coils in series					
		(1+2)	(1+3)	(1+4)	(2+3)	(2+4)	(3+4)
0	0.0000	0.0007	0.0038	0.0056	0.0017	0.0032	0.0026
1	31.4159	0.2735	0.3260	0.5410	0.1320	0.3990	0.3990
2	62.8318	0.4160	0.4920	0.7410	0.1748	0.5450	0.5200
3	94.2477	0.4980	0.5800	0.8390	0.1916	0.6170	0.5840
4	125.6637	0.5490	0.6380	0.8980	0.2004	0.6650	0.6280
5	157.0796	0.5900	0.6790	0.9400	0.2065	0.7020	0.6620
6	188.4955	0.6200	0.7110	0.9760	0.2111	0.7310	0.6900
7	219.9114	0.6440	0.7370	1.0040	0.2147	0.7570	0.7150
8	251.3273	0.6650	0.7580	1.0300	0.2178	0.7780	0.7360
9	282.7432	0.6830	0.7760	1.0520	0.2203	0.7970	0.7540
10	314.1592	0.6980	0.7940	1.0690	0.2224	0.8140	0.7690
11	345.5751	0.7120	0.8080	1.0860	0.2240	0.8290	0.7840
12	376.9910	0.7240	0.8210	1.1010	0.2253	0.8430	0.7980
13	408.4069	0.7360	0.8330	1.1140	0.2260	0.8560	0.8100
14	439.8228	0.7460	0.8440	1.1260	0.2268	0.8680	0.8220
15	471.2387	0.7550	0.8530	1.1380	0.2273	0.8780	0.8330

Table G24: Measurement of magnetic flux density of configuration "B" produced only by three coils in series with air-gap between two coils using curved corners.

Current (Amps)	Magnetic field strength (Oe)	Magnetic flux density (T)			
		Combination of three coils in series			
		(1+2+3)	(1+2+4)	(2+3+4)	(1+3+4)
0	0.0000	0.0056	0.0001	0.0006	0.0042
1	31.4159	0.3370	0.5600	0.4170	0.5620
2	62.8318	0.4870	0.7580	0.5480	0.7470
3	94.2477	0.5670	0.8530	0.6150	0.8430
4	125.6637	0.6200	0.9100	0.6590	0.9020
5	157.0796	0.6580	0.9530	0.6940	0.9440
6	188.4955	0.6870	0.9870	0.7230	0.9780
7	219.9114	0.7120	1.0150	0.7460	1.0060
8	251.3273	0.7310	1.0400	0.7660	1.0300
9	282.7432	0.7480	1.0610	0.7840	1.0520
10	314.1592	0.7640	1.0800	0.8010	1.0690
11	345.5751	0.7780	1.0970	0.8150	1.0860
12	376.9910	0.7900	1.1110	0.8280	1.1010
13	408.4069	0.8010	1.1240	0.8400	1.1140
14	439.8228	0.8110	1.1360	0.8520	1.1260
15	471.2387	0.8210	1.1470	0.8620	1.1380

Table G25: Measurement of magnetic flux density of configuration "B" produced by four coils with air-gap between two coils using curved corners.

Current (Amps)	Magnetic field strength (Oe)	Magnetic flux density (T)
0	0.0000	0.0027
1	31.4159	0.5760
2	62.8318	0.7530
3	94.2477	0.8420
4	125.6637	0.8990
5	157.0796	0.9400
6	188.4955	0.9730
7	219.9114	1.0000
8	251.3273	1.0240
9	282.7432	1.0470
10	314.1592	1.0640
11	345.5751	1.0790
12	376.9910	1.0930
13	408.4069	1.1040
14	439.8228	1.1170
15	471.2387	1.1190

Table G26: Measurement of magnetic flux density of configuration "B" produced only by each coil with air-gap on one of the sides and close to one of the corners using curved corners.

Current (Amps)	Magnetic field strength (Oe)	Magnetic flux density (T)			
		Coils			
		Coil no. 1	Coil no. 2	Coil no. 3	Coil no. 4
0	0.0000	0.0026	0.0013	0.0022	0.0040
1	31.4159	0.2293	0.0554	0.0795	0.3530
2	62.8318	0.3260	0.0876	0.1167	0.4810
3	94.2477	0.3770	0.0998	0.1307	0.5440
4	125.6637	0.4060	0.1064	0.1399	0.5870
5	157.0796	0.4270	0.1105	0.1455	0.6200
6	188.4955	0.4420	0.1135	0.1498	0.6470
7	219.9114	0.4560	0.1160	0.1534	0.6690
8	251.3273	0.4670	0.1179	0.1562	0.6880
9	282.7432	0.4770	0.1197	0.1587	0.7050
10	314.1592	0.4850	0.1211	0.1611	0.7200
11	345.5751	0.4920	0.1225	0.1630	0.7340
12	376.9910	0.4990	0.1236	0.1645	0.7460
13	408.4069	0.5050	0.1249	0.1662	0.7580
14	439.8228	0.5100	0.1257	0.1676	0.7680
15	471.2387	0.5140	0.1267	0.1688	0.7780

Table G27: Measurement of magnetic flux density of configuration "B" produced only by two coils in series with air-gap on one of the sides and close to one of the corners using curved corners.

Current (Amps)	Magnetic field strength (Oe)	Magnetic flux density (T)					
		Combination of two coils in series					
		(1+2)	(1+3)	(1+4)	(2+3)	(2+4)	(3+4)
0	0.0000	0.0002	0.0006	0.0003	0.0003	0.0006	0.0001
1	31.4159	0.2384	0.2646	0.4940	0.1211	0.3920	0.3910
2	62.8318	0.3400	0.3850	0.6520	0.1719	0.5270	0.5100
3	94.2477	0.3910	0.4410	0.7230	0.1932	0.5880	0.5720
4	125.6637	0.4210	0.4730	0.7660	0.2053	0.6330	0.6150
5	157.0796	0.4440	0.4950	0.8000	0.2132	0.6630	0.6450
6	188.4955	0.4590	0.5120	0.8250	0.2190	0.6910	0.6720
7	219.9114	0.4730	0.5250	0.8470	0.2236	0.7120	0.6940
8	251.3273	0.4840	0.5340	0.8650	0.2273	0.7310	0.7150
9	282.7432	0.4940	0.5440	0.8810	0.2305	0.7470	0.7310
10	314.1592	0.5020	0.5540	0.8960	0.2334	0.7620	0.7460
11	345.5751	0.5100	0.5600	0.9100	0.2358	0.7760	0.7610
12	376.9910	0.5160	0.5670	0.9220	0.2379	0.7890	0.7720
13	408.4069	0.5230	0.5730	0.9320	0.2398	0.8010	0.7840
14	439.8228	0.5270	0.5780	0.9410	0.2415	0.8110	0.7940
15	471.2387	0.5310	0.5840	0.9510	0.2430	0.8200	0.8050

Table G28: Measurement of magnetic flux density of configuration "B" produced only by three coils in series with air-gap on one of the sides and close to one of the corners using curved corners.

Current (Amps)	Magnetic field strength (Oe)	Magnetic flux density (T)			
		Combination of three coils in series			
		(1+2+3)	(1+2+4)	(2+3+4)	(1+3+4)
0	0.0000	0.0008	0.0010	0.0015	0.0043
1	31.4159	0.2821	0.5120	0.4080	0.5140
2	62.8318	0.3950	0.6590	0.5330	0.6580
3	94.2477	0.4480	0.7260	0.5920	0.7260
4	125.6637	0.4780	0.7680	0.6350	0.7680
5	157.0796	0.5000	0.8010	0.6650	0.8000
6	188.4955	0.5170	0.8250	0.6910	0.8250
7	219.9114	0.5290	0.8470	0.7130	0.8460
8	251.3273	0.5400	0.8670	0.7330	0.8650
9	282.7432	0.5490	0.8820	0.7480	0.8800
10	314.1592	0.5590	0.8960	0.7620	0.8950
11	345.5751	0.5660	0.9090	0.7780	0.9070
12	376.9910	0.5730	0.9210	0.7890	0.9200
13	408.4069	0.5780	0.9320	0.8010	0.9310
14	439.8228	0.5840	0.9410	0.8100	0.9380
15	471.2387	0.5900	0.9490	0.8200	0.9480

Table G29: Measurement of magnetic flux density of configuration "B" produced by four coils with air-gap on one of the sides and close to one of the corners using curved corners.

Current (Amps)	Magnetic field strength (Oe)	Magnetic flux density (T)
0	0.0000	0.0005
1	31.4159	0.5300
2	62.8318	0.6760
3	94.2477	0.7430
4	125.6637	0.7870
5	157.0796	0.8200
6	188.4955	0.8440
7	219.9114	0.8670
8	251.3273	0.8850
9	282.7432	0.9020
10	314.1592	0.9170
11	345.5751	0.9310
12	376.9910	0.9410
13	408.4069	0.9520
14	439.8228	0.9620
15	471.2387	0.9710

Table G30: Measurement of magnetic flux density of configuration "B" produced by four coils using right-angle corners.

Current (Amps)	Magnetic field strength (Oe)	Magnetic flux density (T)
0	0.0000	0.0002
1	31.4159	0.5590
2	62.8318	0.7220
3	94.2477	0.8050
4	125.6637	0.8580
5	157.0796	0.8960
6	188.4955	0.9280
7	219.9114	0.9520
8	251.3273	0.9730
9	282.7432	0.9920
10	314.1592	1.0080
11	345.5751	1.0220
12	376.9910	1.0360
13	408.4069	1.0470
14	439.8228	1.0570
15	471.2387	1.0670

Table G31: Measurement of magnetic flux density of configuration “A” using large-diameter component with circular cross-sections.

Current (Amps)	Magnetic field strength (Oe)	Magnetic flux density (T)	
		At the centre of air-gap	At the edge of air-gap
0	0.0000	0.0001	0.0002
1	31.4159	0.1897	0.2008
2	62.8318	0.2623	0.2685
3	94.2477	0.2992	0.3040
4	125.6637	0.3220	0.3230
5	157.0796	0.3360	0.3370
6	188.4955	0.3470	0.3470
7	219.9114	0.3550	0.3550
8	251.3273	0.3620	0.3610
9	282.7432	0.3680	0.3680
10	314.1592	0.3730	0.3720
11	345.5751	0.3790	0.3760
12	376.9910	0.3830	0.3800
13	408.4069	0.3860	0.3840
14	439.8228	0.3900	0.3870
15	471.2387	0.3930	0.3910

Table G32: Magnetic flux density of configuration "B" using large-diameter component with circular cross-sections with screw holes in the flat surfaces either side of the air-gap.

Current (Amps)	Magnetic field strength (Oe)	Magnetic flux density (T)	
		At the centre of air-gap	At the edge of air-gap
0	0.0000	0.0032	0.0021
1	31.4159	0.3320	0.6000
2	62.8318	0.4310	0.7830
3	94.2477	0.4820	0.8760
4	125.6637	0.5140	0.9340
5	157.0796	0.5380	0.9790
6	188.4955	0.5560	1.0130
7	219.9114	0.5710	1.0410
8	251.3273	0.5840	1.0640
9	282.7432	0.5950	1.0870
10	314.1592	0.6060	1.1030
11	345.5751	0.6150	1.1200
12	376.9910	0.6220	1.1350
13	408.4069	0.6290	1.1490
14	439.8228	0.6350	1.1600
15	471.2387	0.6410	1.1690

Table G33: Magnetic flux density of configuration "B" produced only by coils in line with the testing element using large-diameter component with circular cross-sections with screw holes in the flat surfaces either side of the air-gap.

Current (Amps)	Magnetic field strength (Oe)	Magnetic flux density (T)
		Coils in line with the testing element
0	0.0000	0.0028
1	31.4159	0.4870
2	62.8318	0.6620
3	94.2477	0.7440
4	125.6637	0.8000
5	157.0796	0.8360
6	188.4955	0.8680
7	219.9114	0.8920
8	251.3273	0.9130
9	282.7432	0.9320
10	314.1592	0.9480
11	345.5751	0.9620
12	376.9910	0.9760
13	408.4069	0.9870
14	439.8228	0.9970
15	471.2387	1.0080

Table G34: Magnetic flux density of configuration "B" produced only by each coil individually using large-diameter component with circular cross-sections with buried screw holes in the flat surfaces either side of the air-gap.

Current (Amps)	Magnetic field strength (Oe)	Magnetic flux density (T)			
		Coils			
		Coil no. 1	Coil no. 2	Coil no. 3	Coil no. 4
0	0.0000	0.0008	0.0021	0.0025	0.0021
1	31.4159	0.2107	0.0419	0.0663	0.2766
2	62.8318	0.3580	0.0758	0.1012	0.3830
3	94.2477	0.4410	0.0919	0.1178	0.4360
4	125.6637	0.5000	0.1002	0.1260	0.4730
5	157.0796	0.5390	0.1061	0.1322	0.5020
6	188.4955	0.5760	0.1104	0.1368	0.5270
7	219.9114	0.6010	0.1136	0.1408	0.5440
8	251.3273	0.6240	0.1163	0.1440	0.5610
9	282.7432	0.6420	0.1186	0.1469	0.5740
10	314.1592	0.6600	0.1205	0.1494	0.5890
11	345.5751	0.6770	0.1221	0.1515	0.6010
12	376.9910	0.6920	0.1235	0.1535	0.6130
13	408.4069	0.7050	0.1248	0.1552	0.6260
14	439.8228	0.7170	0.1256	0.1567	0.6340
15	471.2387	0.7290	0.1266	0.1581	0.6430

Table G35: Magnetic flux density of configuration "B" produced only by a combination of two coils in series using large-diameter component with circular cross-sections with buried screw holes in the flat surfaces either side of the air-gap.

Current (Amps)	Magnetic field strength (Oe)	Magnetic flux density (T)					
		Combination of two coils in series					
		(1+2)	(1+3)	(1+4)	(2+3)	(2+4)	(3+4)
0	0.0000	0.0002	0.0010	0.0006	0.0013	0.0022	0.0014
1	31.4159	0.2307	0.2738	0.4340	0.1197	0.3040	0.2707
2	62.8318	0.3560	0.4060	0.5940	0.1572	0.4030	0.3610
3	94.2477	0.4270	0.4840	0.6580	0.1734	0.4520	0.4080
4	125.6637	0.4740	0.5340	0.7080	0.1821	0.4850	0.4420
5	157.0796	0.5090	0.5700	0.7400	0.1881	0.5100	0.4670
6	188.4955	0.5340	0.5980	0.7680	0.1925	0.5290	0.4850
7	219.9114	0.5550	0.6200	0.7900	0.1960	0.5470	0.5010
8	251.3273	0.5730	0.6370	0.8080	0.1991	0.5600	0.5150
9	282.7432	0.5900	0.6510	0.8240	0.2017	0.5740	0.5280
10	314.1592	0.6030	0.6630	0.8380	0.2041	0.5850	0.5380
11	345.5751	0.6150	0.6770	0.8510	0.2059	0.5960	0.5490
12	376.9910	0.6260	0.6880	0.8620	0.2077	0.6060	0.5570
13	408.4069	0.6350	0.6980	0.8720	0.2093	0.6150	0.5660
14	439.8228	0.6430	0.7080	0.8810	0.2106	0.6230	0.5740
15	471.2387	0.6510	0.7160	0.8890	0.2120	0.6300	0.5800

Table G36: Magnetic flux density of configuration "B" produced only by a combination of three coils in series using large-diameter component with circular cross-sections with buried screw holes in the flat surfaces either side of the air-gap

Current (Amps)	Magnetic field strength (Oe)	Magnetic flux density (T)			
		Combination of three coils in series			
		(1+2+3)	(1+2+4)	(2+3+4)	(1+3+4)
0	0.0000	0.0001	0.0002	0.0017	0.0033
1	31.4159	0.3020	0.4410	0.3130	0.4320
2	62.8318	0.4340	0.5880	0.4010	0.5810
3	94.2477	0.4990	0.6620	0.4460	0.6590
4	125.6637	0.5440	0.7080	0.4770	0.7080
5	157.0796	0.5770	0.7400	0.4990	0.7410
6	188.4955	0.6020	0.7660	0.5180	0.7690
7	219.9114	0.6230	0.7900	0.5330	0.7910
8	251.3273	0.6390	0.8060	0.5470	0.8080
9	282.7432	0.6540	0.8220	0.5590	0.8250
10	314.1592	0.6660	0.8360	0.5690	0.8390
11	345.5751	0.6790	0.8490	0.5800	0.8510
12	376.9910	0.6880	0.8600	0.5880	0.8620
13	408.4069	0.6980	0.8690	0.5950	0.8720
14	439.8228	0.7060	0.8780	0.6030	0.8810
15	471.2387	0.7150	0.8860	0.6090	0.8890

Table G37: Magnetic flux density of configuration "B" produced by four coils using large-diameter component with circular cross-sections with buried screw holes in the flat surfaces either side of the air-gap

Current (Amps)	**Magnetic field strength (Oe)**	**Magnetic flux density (T)**	
		At the centre of air-gap	**At the edge of air-gap**
0	0.0000	0.0009	0.0001
1	31.4159	0.4640	0.4810
2	62.8318	0.6010	0.6200
3	94.2477	0.6720	0.6910
4	125.6637	0.7160	0.7370
5	157.0796	0.7480	0.7690
6	188.4955	0.7730	0.7970
7	219.9114	0.7960	0.8170
8	251.3273	0.8110	0.8350
9	282.7432	0.8260	0.8510
10	314.1592	0.8420	0.8650
11	345.5751	0.8560	0.8750
12	376.9910	0.8650	0.8860
13	408.4069	0.8750	0.8980
14	439.8228	0.8840	0.9060
15	471.2387	0.8950	0.9130

Table G38: Comparison between magnetic flux density of configuration "B" produced only by coils in line with the testing element and back coils using large-diameter component with circular cross-sections with buried screw holes in the flat surfaces either side of the air-gap

Current (Amps)	Magnetic field strength (Oe)	Magnetic flux density (T)	
		Coils	
		Coils in line with the testing element only	Back coils only
0	0.0000	0.0006	0.0013
1	31.4159	0.4340	0.1197
2	62.8318	0.5940	0.1572
3	94.2477	0.6580	0.1734
4	125.6637	0.7080	0.1821
5	157.0796	0.7400	0.1881
6	188.4955	0.7680	0.1925
7	219.9114	0.7900	0.1960
8	251.3273	0.8080	0.1991
9	282.7432	0.8240	0.2017
10	314.1592	0.8380	0.2041
11	345.5751	0.8510	0.2059
12	376.9910	0.8620	0.2077
13	408.4069	0.8720	0.2093
14	439.8228	0.8810	0.2106
15	471.2387	0.8890	0.2120

Table G39: Magnetic flux density of configuration "B" produced only by each coil individually using large-diameter component with circular cross-sections with no buried screw holes near the flat surfaces either side of the air-gap.

Current (Amps)	Magnetic field strength (Oe)	Magnetic flux density (T)			
		Coils			
		Coil no. 1	Coil no. 2	Coil no. 3	Coil no. 4
0	0.0000	0.0010	0.0040	0.0030	0.0030
1	31.4159	0.0300	0.1960	0.2180	0.0700
2	62.8318	0.0610	0.3370	0.3580	0.0970
3	94.2477	0.0760	0.4260	0.4400	0.1040
4	125.6637	0.0850	0.4850	0.4910	0.1080
5	157.0796	0.0920	0.5280	0.5300	0.1110
6	188.4955	0.0960	0.5610	0.5620	0.1140
7	219.9114	0.1000	0.5880	0.5870	0.1150
8	251.3273	0.1030	0.6110	0.6100	0.1170
9	282.7432	0.1050	0.6310	0.6290	0.1190
10	314.1592	0.1070	0.6490	0.6460	0.1200
11	345.5751	0.1090	0.6640	0.6600	0.1210
12	376.9910	0.1110	0.6780	0.6740	0.1220
13	408.4069	0.1120	0.6900	0.6860	0.1230
14	439.8228	0.1130	0.7010	0.6980	0.1240
15	471.2387	0.1140	0.7120	0.7080	0.1250

Table G40: Magnetic flux density of configuration "B" produced only by a combination of two coils in series using large-diameter component with circular cross-sections with no buried screw holes near the flat surfaces either side of the air-gap.

Current (Amps)	Magnetic field strength (Oe)	Magnetic flux density (T)					
		Combination of two coils in series					
		(1+2)	(1+3)	(1+4)	(2+3)	(2+4)	(3+4)
0	0.0000	0.0020	0.0030	0.0000	0.0010	0.0000	0.0040
1	31.4159	0.2350	0.2800	0.1000	0.4050	0.2800	0.2470
2	62.8318	0.3700	0.4230	0.1260	0.6130	0.4150	0.3720
3	94.2477	0.4500	0.5000	0.1370	0.7180	0.4970	0.4460
4	125.6637	0.5050	0.5510	0.1440	0.7810	0.5510	0.4940
5	157.0796	0.5440	0.5890	0.1480	0.8260	0.5900	0.5310
6	188.4955	0.5760	0.6190	0.1510	0.8580	0.6210	0.5610
7	219.9114	0.6020	0.6440	0.1540	0.8860	0.6460	0.5860
8	251.3273	0.6240	0.6640	0.1560	0.9100	0.6670	0.6070
9	282.7432	0.6430	0.6820	0.1570	0.9310	0.6850	0.6260
10	314.1592	0.6590	0.6990	0.1590	0.9490	0.7010	0.6420
11	345.5751	0.6730	0.7130	0.1600	0.9650	0.7160	0.6560
12	376.9910	0.6860	0.7270	0.1610	0.9800	0.7290	0.6690
13	408.4069	0.6980	0.7390	0.1620	0.9920	0.7410	0.6810
14	439.8228	0.7090	0.7480	0.1630	1.0030	0.7490	0.6920
15	471.2387	0.7190	0.7580	0.1640	1.0140	0.7590	0.7020

Table G41 Magnetic flux density of configuration "B" produced only by a combination of three coils in series using large-diameter component with circular cross-sections with no buried screw holes near the flat surfaces either side of the air-gap.

Current (Amps)	Magnetic field strength (Oe)	Magnetic flux density (T)			
		Combination of three coils in series			
		(1+2+3)	(1+2+4)	(2+3+4)	(1+3+4)
0	0.0000	0.0000	0.0000	0.0000	0.0000
1	31.4159	0.4420	0.3010	0.4440	0.2990
2	62.8318	0.6300	0.4200	0.6220	0.4240
3	94.2477	0.7280	0.4930	0.7210	0.4930
4	125.6637	0.7870	0.5420	0.7810	0.5400
5	157.0796	0.8310	0.5790	0.8240	0.5750
6	188.4955	0.8620	0.6080	0.8560	0.6040
7	219.9114	0.8900	0.6320	0.8830	0.6270
8	251.3273	0.9130	0.6510	0.9070	0.6480
9	282.7432	0.9320	0.6690	0.9270	0.6670
10	314.1592	0.9500	0.6850	0.9450	0.6800
11	345.5751	0.9660	0.6980	0.9600	0.6930
12	376.9910	0.9800	0.7110	0.9730	0.7060
13	408.4069	0.9920	0.7220	0.9860	0.7170
14	439.8228	1.0030	0.7320	0.9970	0.7280
15	471.2387	1.0130	0.7420	1.0070	0.7370

Table G42: Magnetic flux density of configuration "B" produced by four coils using large-diameter component with circular cross-sections with no buried screw holes near the flat surfaces either side of the air-gap.

Current (Amps)	Magnetic field strength (Oe)	Magnetic flux density (T)	
		At the centre of air-gap	At the edge of air-gap
0	0.0000	0.0010	0.0000
1	31.4159	0.4450	0.3860
2	62.8318	0.6360	0.6380
3	94.2477	0.7340	0.7420
4	125.6637	0.7950	0.8000
5	157.0796	0.8390	0.8440
6	188.4955	0.8730	0.8760
7	219.9114	0.9010	0.9050
8	251.3273	0.9250	0.9270
9	282.7432	0.9450	0.9480
10	314.1592	0.9630	0.9660
11	345.5751	0.9790	0.9810
12	376.9910	0.9920	0.9960
13	408.4069	1.0050	1.0090
14	439.8228	1.0160	1.0200
15	471.2387	1.0270	1.0310

Table G43: Magnetic flux density in the air-gap produced only by coils in line with the testing element.

Current (Amps)	Magnetic field strength (Oe)	Magnetic flux density (T)
0	0.0000	0.0020
1	31.4159	0.3480
2	62.8318	0.5560
3	94.2477	0.6680
4	125.6637	0.7300
5	157.0796	0.7700
6	188.4955	0.8020
7	219.9114	0.8290
8	251.3273	0.8490
9	282.7432	0.8670
10	314.1592	0.8830
11	345.5751	0.8980
12	376.9910	0.9110
13	408.4069	0.9230
14	439.8228	0.9330
15	471.2387	0.9430